Développement de méthodes numériques et étude des phénomènes couplés d'écoulement, de rayonnement, et d'ablation dans les problèmes d'entrée atmosphérique

James Scoggins

université PARIS-SACLAY

CentraleSupélec

von KARMAN INSTITUTE FOR FLUID DYNAMICS

NNT : 2017SACLC048

Development of numerical methods and study of coupled flow, radiation, and ablation phenomena for atmospheric entry

Thèse de doctorat de l'Université Paris-Saclay, préparée au von Karman Institute for Fluid Dynamics, Aeronautics and Aerospace Department, et à CentraleSupélec, Laboratoire EM2C

École doctorale n°579 Sciences mécaniques et énergétiques, matériaux et géosciences (SMEMAG)
Spécialité de doctorat: Energétique

Thèse présentée et soutenue à Paris, le 29 septembre 2017, par

M. James B. Scoggins

Composition du Jury :

M. Marc Massot Professeur, École Polytechnique (Laboratoire CPAM)	Président
M. Yann Cressault Maître de conférences, Université Toulouse III (Laboratoire LAPLACE)	Rapporteur
M. Sergey Timofeevich Surzhikov Directeur de recherche, Ishlinsky Institute for Problems in Mechanics	Rapporteur
M. Philippe Rivière Chargé de recherche CNRS, CentraleSupélec (Laboratoire EM2C)	Examinateur
M. Nagi Mansour Branch Chief, NASA ARC (NAS Supercomputing Branch)	Examinateur
M. Anouar Soufiani Directeur de recherche CNRS, CentraleSupélec (Laboratoire EM2C)	Directeur de thèse
M. Thierry Magin Associate professor, von Karman Institute for Fluid Dynamics	Co-Directeur de thèse

Thèse de doctorat

To my parents, James and Susan,
who taught me the most important lessons.

Abstract

This thesis focuses on the coupling between flow, ablation, and radiation phenomena encountered in the stagnation region of atmospheric entry vehicles with carbon-phenolic thermal protection systems (TPS). The research is divided into three parts: 1) development of numerical methods and tools for the simulation of hypersonic, non equilibrium flows over blunt bodies, 2) implementation of a new radiation transport model for calculating nonequilibrium radiative heat transfer in atmospheric entry flows, including ablation contaminated boundary layers, and 3) application of these tools to study real flight conditions.

A review of the thermochemical nonequilibrium models and governing equations for atmospheric entry flows is made, leading to a generalized framework, able to encompass most popular models in use today. From this, a new software library called MUlticomponent Thermodynamic And Transport properties for IONized gases, written in C++ (MUTATION++) is developed, providing thermodynamic, transport, chemistry, and energy transfer models, data, and algorithms, relevant to nonequilibrium flows. In addition, the library implements a novel method, developed in this work, for the robust calculation of linearly constrained, multiphase equilibria, which is guaranteed to converge for all well posed constraints, a crucial component of many TPS response codes.

The steady-state flow along the stagnation line of an atmospheric entry vehicle is computed using a one-dimensional, finite-volume tool, based on the dimensionally reduced Navier-Stokes equations. Coupling with ablation is achieved through a steady-state ablation boundary condition using finite-rate heterogeneous reactions at the surface and imposed equilibrium compositions of pyrolysis outgassing.

The High Temperature Gas Radiation (HTGR) database provides accurate line-by-line (LBL) spectral coefficients. From a review of the major mechanisms contributing to the radiative heat flux for atmospheric entry vehicles, several contributions are added to the HTGR database, including H lines, C_3 Swings and UV electronic systems, and photoionization of H, H_2, and CH. The Hybrid Statistical Narrow Band (HSNB) model is implemented to reduce the CPU time required to compute accurate radiative heating calculations when many species are present. New SNB parameters are computed for the H_2 Lyman and Werner systems, by adjusting the Doppler and Lorentz overlap parameters to fit curves of growth for each narrow band. Comparisons with band-averaged LBL transmissivities show excellent agreement with the SNB parameters. It's shown that the HSNB method provides a speedup of two orders of magnitude and can accurately predict wall radiative fluxes to within 5 % of LBL results. A novel spectral grid adaptation is developed for atomic lines and is shown to provide nearly identical results compared to the high-resolution HSNB method with a 20-fold decrease in CPU time. The HSNB model yields greater accuracy compared to the Smeared-Rotational-Band model in the case of Titan entry, dominated by optically thick CN radiation.

The effects of coupled ablation and radiation are studied for Earth entries. It's shown that ablation products in the boundary layer can increase the radiation blockage to the surface of the vehicle. In particular, the C_3 UV and CO 4+ band systems and photoionization of C contribute significantly to absorption when enough carbon is present. An analysis of the Apollo 4 peak heating condition shows coupled radiation and ablation effects reduce the conducted heat flux by as much as 35 % for a fixed wall temperature of 2500 K. Comparison with the radiometer data shows excellent agreement, partially validating the coupling methodology and radiation database. The importance of accurately modeling the amount of carbon blown into the boundary layer is demonstrated by contrasting the results of other researchers.

Résumé

Cette thèse est centrée sur le couplage entre les phénomènes d'écoulement, d'ablation et de rayonnement au voisinage du point d'arrêt de véhicules d'entrée atmosphérique pourvus d'un système de protection thermique de type carbone-phénolique. La recherche est divisée en trois parties : 1) le développement de méthodes numériques et d'outils pour la simulation d'écoulements hypersoniques hors équilibre autour de corps émoussés, 2) la mise en œuvre d'un nouveau modèle de transport du rayonnement hors équilibre dans ces écoulements, y compris dans les couches limites contaminées par les produits d'ablation, et 3) l'application de ces outils à des conditions réelles de vol.

La librairie MUTATION++ a été développée en C++ sur la base d'une formulation générale englobant les modèles hors équilibre thermo-chimique les plus couramment utilisés pour fermer les équations gouvernant les écoulements hypersoniques. Les propriétés thermodynamiques et de transport de gaz ionisés multi-composants sont calculés, ainsi que les taux de production chimique et de transfert d'énergie. Un nouvel algorithme permet un calcul robuste de la composition d'équilibre de mélanges multiphasiques sous contraintes linéaires, garantissant la convergence de la méthode pour les problèmes contraints bien posés, une composante essentielle aux nombreux codes de réponse pour les matériaux.

L'écoulement stationnaire le long de la ligne d'arrêt de l'écoulement autour d'un véhicule spatial est simulé à l'aide d'une méthode de volumes finis appliquée aux équations de Navier-Stokes réduites à une dimension. Le couplage avec l'ablation est réalisé à l'aide d'une condition aux limites utilisant un modèle de chimie hétérogène avec des taux de réaction surfaciques finis et une composition d'équilibre des gaz de pyrolyse.

La base de données de rayonnement des gaz à haute température (HTGR) fournit des propriétés radiatives spectrales précises de type raie-par-raie (LBL). Après évaluation des principaux mécanismes contribuant au flux radiatif à la paroi, plusieurs contributions ont été ajoutées dans HTGR : les raies atomiques de H, les systèmes électroniques de C_3 Swings et UV, et la photoionisation de H, H_2 et CH. Le modèle hybride statistique à bande étroite (HSNB) est mis en œuvre pour réduire le coût CPU nécessaire au calcul précis du transfert par rayonnement en présence de nombreuses espèces. De nouveaux paramètres SNB sont calculés pour les systèmes H_2 Lyman et Werner, en ajustant les paramètres de chevauchement Doppler et Lorentz de façon à reproduire les courbes de croissance pour chaque bande étroite. Les comparaisons avec les transmittivités LBL moyennées par bande montrent un excellent accord avec les résultats SNB. La méthode HSNB fournit une accélération de deux ordres de grandeur avec une précision de 5 % sur les flux radiatifs pariétaux par rapport aux résultats LBL. Une nouvelle méthode d'adaptation de la grille spectrale est développée pour les raies atomiques, fournissant des résultats très proches de ceux obtenus par la méthode HSNB à haute résolution tout en réduisant d'un facteur 20 le coût CPU. Le modèle HSNB apporte aussi une précision accrue par rapport au modèle de gaz gris par bandes dans l'étude d'une entrée dans l'atmosphère de Titan, dominée par le rayonnement optiquement épais de CN.

Les effets du couplage entre l'ablation et le rayonnement sont étudiés pour les rentrées terrestres. Il est démontré que les produits d'ablation dans la couche limite peuvent augmenter le blocage radiatif à la surface du véhicule. Pour les conditions de flux maximum d'Apollo 4, les effets de couplage entre le rayonnement et l'ablation réduisent le flux conductif de 35 %. L'accord avec les données radiométriques est excellent, ce qui valide partiellement la méthode de couplage et la base de données radiatives. L'importance d'une modélisation précise du soufflage du carbone dans la couche limite est également établie.

Acknowledgements

It's probably a bit cliché to recall the famous metaphor Isaac Newton wrote in a letter to Robert Hooke, "If I have seen further, it is because I have stood on the shoulders of Giants." However, looking back over the last years, I am inclined to paraphrase Newton by saying that if I have been successful, it is only because I have stood on the toes of Giants and strained to see further. I have been extremely fortunate to boast a large network of mentors and friends, willing and able to prop me up and give me guidance throughout my academic and personal journeys. I am sincerely indebted to a host of individuals, without whom I could not have accomplished this work.

Thesis committee

First and foremost, I cannot thank enough Dr. Thierry Magin who has been a wonderful adviser, mentor, and friend throughout these last years at VKI. Beyond the obvious technical wizardry, which he graciously imparted unto me (at least as much as I could understand), he was always available to discuss and provide guidance on all aspects of the Ph.D. Since we first met at NASA Ames Research Center to discuss the "von Carbon" institute, he has pushed me to tackle problems that I would never have considered on my own, which greatly expanded both my expertise and the available career options moving forward. He provided me with endless opportunities to collaborate with others and travel to many conferences to discuss with experts in the field. In addition, he was always careful to strike a balance between letting me chart my own scientific path and preventing me from wasting time on the more hopeless or unimportant avenues of research. It is for all of these reasons and more that I have him to thank for making this thesis a success and I am really looking forward to continuing our shared research interests in the future.

I would like to sincerely thank Dr. Anouar Soufiani and Dr. Philippe Rivière for being truly excellent advisers at CentraleSupélec (previously at Ecole Centrale Paris). I'm not sure they would have agreed had they realized how much I needed to learn about radiation! However, regardless of the learning curve I had ahead of me at the start, they were very patient and helpful along the way and I am very grateful to all of their hard work and generous efforts, without which I can safely say this thesis would have been impossible. I have learned a great deal from both of them, not only because of their expertise in the field, but also from their attention to detail and scientific rigor, qualities which I think will be invaluable to me as I begin the rest of my career. I would also like to thank Dr. Soufiani for all that he did to guide me through the bureaucratic web of a French university, which was quite daunting for a boy from North Carolina, struggling to speak the language.

I would like to wholeheartedly express my gratitude to Dr. Nagi Mansour for not only traveling all the way from San Francisco to Paris for my defense, or for his remarks which followed, but for all of the guidance, encouragement, mentoring, and support he gave me over the last several years that we have worked together. What started as a summer internship at NASA Ames Research Center quickly turned into a very productive and satisfying collaboration, which I hope to continue in the future.

Finally, I want to sincerely thank the other thesis committee members for their honest and helpful feedback, which served to elevate the quality of this thesis beyond what I was capable of on my own. Dr. Sergey Surzhikov and Dr. Yann Cressault have my utmost gratitude for agreeing to review the manuscript and for providing their extremely detailed comments and insights. I would also like to thank Dr. Marc Massot for agreeing to chair the committee and for his helpful questions and comments during the defense.

North Carolina State University

Stories are often best told from the beginning and I would be remiss if I did not mention my time at NCSU where I received my B.Sc. and M.Sc. degrees in Aerospace Engineering and where

the groundwork for this thesis was actually laid. During my time at NCSU, I was fortunate to learn from some exceptional professors. In particular I want to thank Dr. Hall, Dr. Luo, and Dr. Edwards for their enlightening courses and guidance throughout my senior and graduate years at NCSU. I would also like to especially acknowledge Dr. Hassan Hassan for plucking me up as a senior and convincing me to begin a graduate research project with him on the modeling of thermal protection systems for atmospheric entry vehicles. This was the real start of my journey towards completing a Ph.D. and I am very grateful for the trust he put in me and for his tutorship during the early years of my graduate education.

At N.C. State, I found a real home on the NCSU Aerial Robotics Team, which undoubtedly shaped my career and personal life for the better. In particular, I want to thank Dan, Dave, Cheng, and Jonathan for being excellent mentors and friends during my early days on the team. It wasn't until I was a senior myself, with the massive workload, which that entails, before I realized how incredibly generous they were with their time and patience for the "newbs" like me. I also want to thank Matt, Alan, Trent, Tim, Lars, Michael, and the rest of the ARC members for all the great times we had, for being roommates and friends, and for being there when I needed you most.

I also want to thank my other NCSU family, which suffered with me through the late nights, project deadlines, and homework assignments of grad school while being the source of endless laughs and good times. In particular, thanks to Evan, Judy, Jeff, Ilya, Amar, Ghosh, and Jesse.

NASA Ames Research Center

I was extremely lucky to spend several summers at NASA Ames Research Center during the first years of grad school. NASA was pivotal during my Masters and Ph.D., providing funding through a N.C. Space Grant and a Graduate Student Research Program fellowship. Above all, I want to thank NASA Ames for allowing me to get to know some incredible scientists and mentors. For example, it was there I met Dr. Jean Lachaud who taught me a great deal about thermal protection system modeling and fostered the idea to create the Mutation++ library, a key element of this thesis. Since our first encounter, I have enjoyed a fantastic collaboration with Jean, which I hope to continue in the future. I would also like to thank Dr. David Hash for all of his hard work over the years to provide outstanding internship experiences at Ames. I also want to thank all of the other members of the Aerothermodynamics branch who helped make my internships extremely rewarding through enlightening discussions and advice. In particular, thanks to Drs. Aaron Brandis, Brett Cruden, Grant Palmer, Richard Jaffe, Dinesh Prahbu, and Mike Wright. And finally, thanks to all the other interns that shared the summers with me at Ames. Thanks for all the pool parties, BBQ's, and late night antics!

von Karman Institute for Fluid Dynamics

When I first moved to Belgium to start a Ph.D. at VKI, I was pretty nervous that I might have made a mistake. After all, I was moving to a country that was quite different from my own. I didn't know anybody and I didn't speak French (or Dutch, or "VKI English"). I wasn't sure how it would affect my career to move from a university in the U.S. to a small research institute in Brussels. However, looking back on those early fears, I couldn't be happier with the result. I would like to thank all of the people at VKI who have made my time here so rewarding. I have truly made lifelong friends and learned a great deal from others.

I want to start by thanking the members of our research group: Bernd, Alessandro M., Alessandro T., Erik, Pierre, Aurélie, George, Bruno, Federico, Laurent, and Vincent. There is a little bit (and a lot for some) of each of you in this thesis. Thank you for all the discussions, advice, and data, which you gave me over the last five years. In particular, I want to thank the core ablation group - Bernd, Alessandro, and Pierre - for all the collaborations, which helped me so much during the Ph.D. Laurent, you were absolutely crucial to the success of this thesis. I really enjoyed working with you during your postdoc and I owe a significant amount of the results in this thesis to you. Vincent, thanks for showing me "proper" coding and version control techniques and for how to kill scores of zombies. Thank you to Andrea Lani for all the helpful discussions about the design of Mutation++, especially early on in the Ph.D. I also had the pleasure to mentor several students

along the way. Brad, Bruno, George, Benjamin Barros Fernandez, Gabriele, Dinesh, Alexandre, Claudio, Michele, and Benjamin Terschanski - I hope you have learned as much from me as I learned from you.

Apart from the excellent working relationships I have built at VKI, I am extremely grateful to all the other amazing friends I have made along the way, who made this experience so enjoyable. Alejandro, Marina, Chiara, Sophia, Bariş, Işıl, Clara, Jorge, Fabrizio, Alessia, Laura, Francesco, and everyone else, it is a pleasure to know you. Thanks for all the great times we've had and for all that are left to come!

Lastly, I want to thank the hardworking and dedicated staff in the VKI computer center and library who keep VKI running and made my own experience here possible. In particular, thank you Raimondo, Nathalie, Christelle, and Evelyne.

Family

I want to thank my family for supporting me and being a constant source of love and encouragement throughout my life. To my brothers, aunts and uncles, cousins, and grand parents, thank you for believing in me. I owe everything to my parents, James and Susan, who sacrificed more than I'm sure I'll ever really know to allow me to follow my passion. I have never been torn between doing what I love and getting a "real job" because you were always there, backing me up and giving me the freedom to choose. I recognize this was a huge privilege, and will forever be grateful to you for that.

And finally, to my best friend and companion, Anabel - looking back, I have no idea how I was supposed to get through these last years without you. Thank you for all the words of encouragement, the endless trips back and forth to test the Belgian health care system, the amazing experiences we've had traveling the world, for picking me up every time I was down, and for being my biggest fan. Through everything, you kept me laughing and you kept me inspired. Thanks for being you.

J.B. Scoggins
Brussels, 2017

Contents

List of Publications

The following publications have contributed directly or indirectly to this thesis. The author would also like to gratefully acknowledge the opportunities to present unpublished work at various international meetings, including the Ablation Workshops, IPPW, and the ESA TPS and Hot Structures Workshops. These meetings have significantly contributed to this thesis through collaboration and discussion with experts in the field.

Journal articles

1. J. B. Scoggins, J. Rabinovitch, B. Barros-Fernandez, A. Martin, J. Lachaud, R. L. Jaffe, N. N. Mansour, G. Blanquart, T. E. Magin. Thermodynamic properties of equilibrium carbon-phenolic gas mixtures. *Aerospace Science and Technology, 66:177-192, 2017.*

2. J. Lachaud, J. B. Scoggins, T. E. Magin, M. G. Meyer, N. N. Mansour. A generic local thermal equilibrium model for porous reactive materials submitted to high temperatures. *International Journal of Heat and Mass Transfer, 108:1406-1417, 2017.*

3. B. Helber, A. Turchi, J. B. Scoggins, A. Hubin, T. E. Magin. Experimental investigation of ablation and pyrolysis processes of carbon-phenolic ablators in atmospheric entry plasmas. *International Journal of Heat and Mass Transfer, 100:810-824, 2016.*

4. L. Soucasse, J. B. Scoggins, P. Rivière, T. E. Magin, A. Soufiani. Flow-radiation coupling for atmospheric entries using a Hybrid Statistical Narrow Band model. *Journal of Quantitative Spectroscopy and Radiative Transfer, 180:55-56, 2016.*

5. J. B. Scoggins, T. E. Magin. Gibbs function continuation for linearly constrained multiphase equilibria. *Combustion and Flame, 162(12):4514-4522, 2015.*

6. J. Lachaud, T. van Eekelen, J. B. Scoggins, T. E. Magin, N. N. Mansour. Detailed equilibrium model for porous ablative materials. *International Journal of Heat and Mass Transfer, 90:1034-1045, 2015.*

Conference proceedings

Publications after the start of the thesis:

1. J. B. Scoggins, A. Lani, P. Rivière, A. Soufiani, T. E. Magin. 3D Radiative Heat Transfer Calculations using Monte Carlo Ray Tracing and the Hybrid Statistical Narrow Band Model for Hypersonic Vehicles. AIAA Paper 2017-4536. *47^{th} AIAA Thermophysics Conference, Denver, CO, June 2017.*

2. J. B. Scoggins, P. Knisely, T. E. Magin. Crossed contributions to electron and heavy-particle transport fluxes for magnetized plasmas in the continuum regime. *AIP Conference Proceedings, 1786(130002), 2016.*

3. J. B. Scoggins, L. Soucasse, P. Rivière, A. Soufiani, T. E. Magin. Coupled flow, radiation, and ablation simulations of atmospheric entry vehicles using the Hybrid Statistical Narrow Band model. AIAA Paper 2015-3112. *45^{th} AIAA Thermophysics Conference, Dallas, TX, June 2015.*

4. J. B. Scoggins, L. Soucasse, P. Rivière, A. Soufiani, T. E. Magin. An adaptive Hybrid Statistical Narrow Band model for coupled radiative transfer in atmospheric entry flows. *Proc. of the 8^{th} European Symposium on Aerothermodynamics for Space Vehicles, Lisbon, Portugal, March 2015.*

5. L. Soucasse, J. B. Scoggins, T. E. Magin, P. Rivière, A. Soufiani. Radiation calculations along the stagnation line of atmospheric entry flows using a Hybrid Statistical Narrow Band model. *Proc. of the 6th International Workshop on Radiation of High Temperature Gases in Atmospheric Entry, St. Andrews, United Kingdom, November 2014.*

6. J. B. Scoggins, T. E. Magin. Development of Mutation++: multicomponent thermodynamic and transport properties for ionized plasmas written in C++. AIAA Paper 2014-2966. *11th AIAA/ASME Joint Thermophysics and Heat Transfer Conference, Atlanta, GA, June 2014.*

7. J. B. Scoggins, T. E. Magin, A. A. Wray, N. N. Mansour. Multi-group reductions of LTE air plasma radiative transfer in cylindrical geometries. AIAA Paper 2013-3142. *44th AIAA Thermophysics Conference, San Diego, CA, June 2013.*

Publications before the start of the thesis:

8. J. B. Scoggins, N. N. Mansour, H. A. Hassan. Development of a reduced kinetic mechanism for PICA pyrolysis products. AIAA Paper 2011-3126. *42nd AIAA Thermophysics Conference, Honolulu, HI, June 2011.*

9. J. B. Scoggins, H. A. Hassan. Pyrolysis mechanism of PICA. AIAA Paper 2010-4655. *10th AIAA/ASME Joint Thermophysics and Heat Transfer Conference, Chicago, IL, June 2010.*

VKI PhD Symposium reports

1. J. B. Scoggins, A. Soufiani, T. E. Magin. Fast Hybrid Statistical Narrow Band model for radiative transfer in atmospheric entry flows. *Proc. of the 6th VKI PhD Symposium, Sint-Genesius Rode, Belgium, March 2015.*

2. J. B. Scoggins, A. Soufiani, T. E. Magin. An extension of the Gibbs function continuation method for linearly constrained multiphase equilibria. *Proc. of the 5th VKI PhD Symposium, Sint-Genesius Rode, Belgium, March 2014.*

3. J. B. Scoggins, A. Soufiani, T. E. Magin. Development of Mutation++: multicomponent thermodynamics and transport properties in ionized gases library in C++. *Proc. of the 4th VKI PhD Symposium, Sint-Genesius Rode, Belgium, March 2013.*

List of Figures

List of Tables

Nomenclature

Symbols with multiple definitions should be clear from the context in which they are used.

Constants

c	Speed of light
h	Planck's constant
k_B	Boltzmann constant
N_A	Avogadro number
R_u	universal gas constant, $R_u = k_B N_A$
R_y	Rydberg constant
σ	Stefan-Boltzmann constant

Roman Symbols

a	speed of sound
a	degeneracy of a particular energy state
A_{ul}	spontaneous emission Einstein coefficient of bound-bound transition ul
B_{lu}	absorption Einstein coefficient of bound-bound transition ul
B_{ul}	induced emission Einstein coefficient of bound-bound transition ul
B^{e}	Elemental stoichiometry coefficient matrix
$\boldsymbol{B}$	magnetic field
c_p	specific heat at constant pressure
c_v	specific heat at constant volume
$\mathscr{D}$	binary diffusion coefficient
e	energy
E	energy of a particle or energy level
$\boldsymbol{E}$	electric field
$\boldsymbol{E}'$	electric field in hydrodynamic velocity frame
f^{ab}	absorption spectral line profile

f^{ie}	induced emission spectral line profile
f^{se}	spontaneous emission spectral line profile
f	oscillator strength
g	relative velocity between two particles
g	species pure Gibbs function
$\tilde{g}$	species non-dimensionalized pure Gibbs function
G	mixture Gibbs function
$\tilde{G}$	mixture normalized Gibbs function
h	enthalpy
$\mathcal{H}$	set of heavy species
$\bar{\boldsymbol{I}}$	identity matrix
I	radiant intensity
I^b	Planck function
$\boldsymbol{J}$	diffusive mass flux
$\boldsymbol{j}$	conduction current
$\overline{k}$	mean absorption coefficient per partial pressure of absorbing species
$\mathcal{L}$	set of energy levels
M	molecular weight
m	particle mass
n	number density
$n^{\mathcal{H}}$	number of heavy species
$n^{\mathcal{P}}$	number of phases
$n^{\mathcal{S}}$	number of species
N	species moles
$\boldsymbol{N}$	species mole vector
$\bar{N}$	phase moles
$\bar{\boldsymbol{N}}$	phase moles vector
p	pressure
$\mathcal{P}$	radiative power
$\mathcal{P}$	set of phases indices
P	phase summation function
$\mathbf{P}$	phase summation matrix

q	charge
$\boldsymbol{q}$	convective heat flux
$\boldsymbol{q}^{\boldsymbol{r}}$	radiative heat flux
Q	partition function
$\bar{Q}$	reduced collision integral
R	specific gas constant, $R_j = R_u/M_j$
$\mathfrak{R}$	reaction rate of progress
$\mathcal{R}$	set of reaction indices
s	entropy
$\mathfrak{S}^{\mathrm{se}}$	spontaneous emission cross-section for bound-free process
$\mathfrak{S}^{\mathrm{ie}}$	induced emission cross-section for bound-free process
$\mathfrak{S}^{\mathrm{abs}}$	absorption cross-section for bound-free process
$\mathcal{S}$	set of species indices
T	temperature
T_e	free electron translational temperature
T_{el}	electronic temperature
T_h	heavy particle translational temperature
T_r	rotational temperature of molecules
T_v	vibrational temperature of molecules
$\boldsymbol{u}$	hydrodynamic velocity
$\boldsymbol{V}$	diffusion velocity
$\mathcal{V}$	set of vibrating molecules
$\overline{W}$	mean black equivalent line width
x	mole fraction
y	mass fraction

Greek Symbols

α	absorptivity or absorptance
$\overline{\beta}$	line overlap parameter for narrow band
χ^e	free electron thermal diffusion ratio
χ^h	heavy particle thermal diffusion ratio
χ^{neq}	non-equilibrium coefficient used for bound-free processes
ϵ	emittance or emissivity
η	emission coefficient

η	shear viscosity
κ	absorption coefficient
κ	bulk viscosity
λ	thermal conductivity
λ_e	free-electron thermal conductivity
λ_h	heavy particle thermal conductivity
μ	reduced mass of two particles
$\bar{\mathbf{\Pi}}$	viscous stress tensor
$\dot{\omega}$	mass production rate due to chemical reactions
Ω	collision integral
Ω^{CV}	chemical-vibrational energy coupling term
Ω^{ET}	heavy-electron translational energy relaxation rate
Ω^{EV}	electron-vibrational energy relaxation rate
Ω^{I}	thermal energy lost provided by electrons during electron impact reactions
Ω^{VT}	vibrational-translational energy relaxation rate
Ω^{VV}	vibrational-vibrational energy relaxation rate
$\dot{\phi}$	mass production rate due to photochemical reactions
ρ	mass density
$\hat{\rho}$	molar density
ρ	reflectivity or reflectance
σ	wavenumber
τ	transmissivity
τ^{ET}	heavy-electron translational energy relaxation time
τ^{VT}	vibrational-translational energy relaxation time
θ^B	non-Boltzmann equilibrium parameter
$\nu^{'}$	forward stoichiometry coefficient
$\nu^{''}$	backard stoichiometry coefficient

Acronyms

ANL	Argonne National Laboratory
ATcT	Active Thermochemical Tables
BRVC	Boltzmann rovibrational collisional
CEA	Chemical Equilibrium with Applications

CFD	Computational Fluid Dynamics
CFL	Courant-Friedrichs-Lewy
CG	Conjugate-Gradient
CR	Collisional-Radiative
DNRS	Dimensionally Reduced Navier Stokes
EDC	Eddy Dissipation Concept
EDL	Entry, Descent, and Landing
EPE	Element Potential Equations
ESA	European Space Agency
FV	Finite Volume
GFC	Gibbs function continuation
GMRES	Generalized minimum residual
GSI	gas-surface interactions
HSNB	Hybrid Statistical Narrow Band
HTGR	High Temperature Gas Radiation
HWHM	half-width at half-maximum
LBL	line-by-line
LHTS	Local Heat Transfer Simulation
LTE	local thermodynamic equilibrium
MPGFC	multiphase Gibbs function continuation
MT	multi-temperature
MUSCL	Monotone Upstream Centered Schemes for Conservation Laws
NASA	National Aeronautics and Space Administration
NIST	National Institute for Standards and Technology
OOP	Object-Oriented Programming
ODE	Ordinary Differential Equation
PAH	Polycyclic Aromatic Hydrocarbons
PES	potential energy surface
QCT	quasi-classical trajectory
RCCE	Rate-Controlled Chemical Equilibrium
RCCE-GALI	RCCE using greedy algorithm with local improvement
RRHO	Rigid-Rotor Harmonic-Oscillator
RRM	Relaxa tion-Redistribution method

RTE	Radiative Transport Equation
RVC	rovibrational collisional
SNB	Statistical Narrow-Band
SRE	Specified Reaction Efficiency
STANJAN	Stanford-JANAF
STS	State-to-State
TN	Thermochemical Network
TOPBASE	The Opacity Project atomic database
TPS	Thermal Protection System
TRC	Thermochemical Research Center
UML	Unified Modeling Language
VC	vibronic-specific collisional
XML	eXtensible Markup Language

CHAPTER 1

Introduction

"At first they thought the steam was escaping somewhere, but, looking upwards, they saw that the strange noise proceeded from a ball of dazzling brightness, directly over their heads, and evidently falling towards them with tremendous velocity. Too frightened to say a word, they could only see that in its light the whole ship blazed like fireworks and the whole sea glittered like a silver lake. Quicker than tongue can utter, or mind can conceive, it flashed before their eyes for a second, an enormous [meteor] set on fire by friction with the atmosphere, and gleaming in its white heat like a stream of molten iron gushing straight from the furnace."

— Jules Verne, (translated from *Autour de la lune*)

1.1. Historical Perspective on Space Exploration

In his 1870 novel, *Autour de la lune* (*Around the moon*), the prolific French writer Jules Verne describes the reentry of his fictitious spacecraft, a Columbiad projectile, from the viewpoint of the sailors aboard the recovery ship. Apart from a few physical inaccuracies – for instance, you can't hear an object moving towards you faster than the speed of sound – Verne had no way of knowing that he had imagined the scene that would take place nearly one hundred years later as the sailors aboard the USS *Hornet* (and indeed the rest of the world) awaited the return of the world's first lunar explorers: Neil Armstrong, Buzz Aldrin, and Michael Collins, aboard the Apollo 11 Command Module, *Columbia*. The space race, which began as a cold war struggle between the United States and the Soviet Union in the late 1950's, had culminated in the successful completion of the most daunting technological challenge in human history. Human exploration of the lunar surface returned a wealth of scientific knowledge concerning the geological formation of the Moon as well as clues regarding the early history of our own planet. Beyond the scientific and technological advancements, the lunar program served to fuel our collective curiosity about our place in the universe through images like the ones broadcast aboard Apollo 8 on Christmas Eve, 1968, of the lunar Earthrise.

Unlike those early days of space exploration, the bulk of the space missions in the proceeding decades have been largely robotic in nature, with the notable exception of the more than 16 years of continuous human presence in space aboard the international space station. However, the technological and scientific achievements of these missions are no less important or awe inspiring. Notable scientific advancements from these missions include the discovery of liquid hydrocarbon lakes on the surface of Saturn's moon Titan by the joint NASA/ESA Cassini-Huygens mission and the recent discoveries of organic matter on the surface of Mars and in the coma of the *Wild 2* comet by the NASA Mars Science Laboratory and Stardust missions, respectively.

1.2. Entry, Descent, and Landing

A common feature of most planetary exploration or sample return missions, is the need to enter into the atmosphere of a celestial body at high velocity. Atmospheric entry is the first phase of a

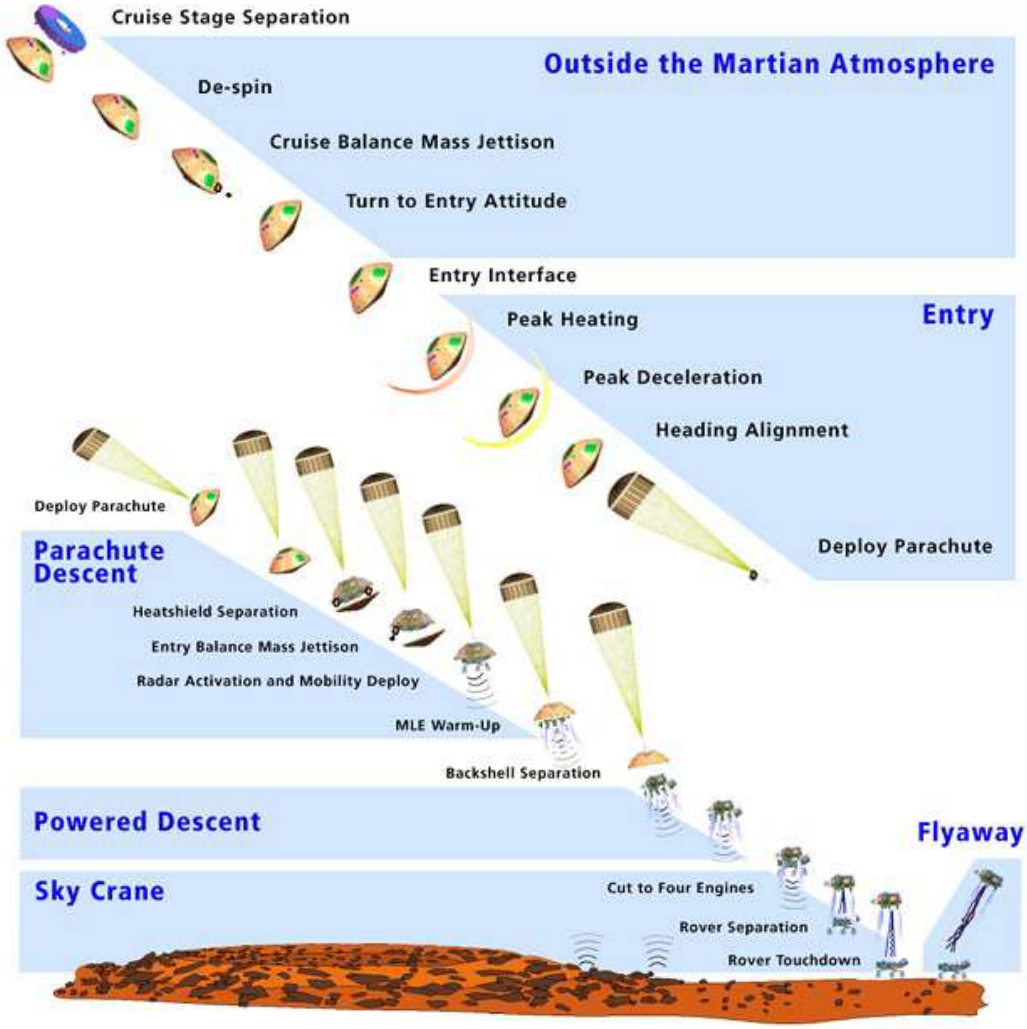

Figure 1.1.: *Entry, Descent, and Landing sequence for the Mars Science Laboratory (source: NASA/JPL).*

mission's Entry, Descent, and Landing (EDL) sequence. As the name suggests, the purpose of the EDL sequence is to bring the spacecraft safely to the surface of the planet from its initial cruise velocity. One of the most technologically advanced EDL sequences to date is that of the NASA Mars Science Laboratory's (MSL) Curiosity rover, which was successfully deployed on the Martian surface on the 6^{th} of August, 2012. A diagram of this sequence is shown in Fig. (1.1). Among the many achievements of the MSL landing were the first ever controlled entry phase which is responsible for the most accurate Martian landing in history, targeting a landing ellipse of just 7 km by 20 km, and an innovative sky crane which lowered the Curiosity rover to the surface, preventing damage to the rover from the the dust and rocks blown around by conventional landing jets.

From the standpoint of energy, an EDL sequence is responsible for reducing the kinetic and potential energy of the spacecraft, measured relative to the planet's surface, to zero. The bulk of this energy is dissipated during the entry phase by converting the kinetic energy of the vehicle into thermal energy in the surrounding atmosphere through the formation of a strong bow-shock ahead of the vehicle. In general, about 90 % of the energy dissipated to the atmosphere is carried away from the vehicle through convection and radiation, leaving about 10 % to be absorbed back into the vehicle as thermal energy. A Thermal Protection System (TPS) is used to mitigate this

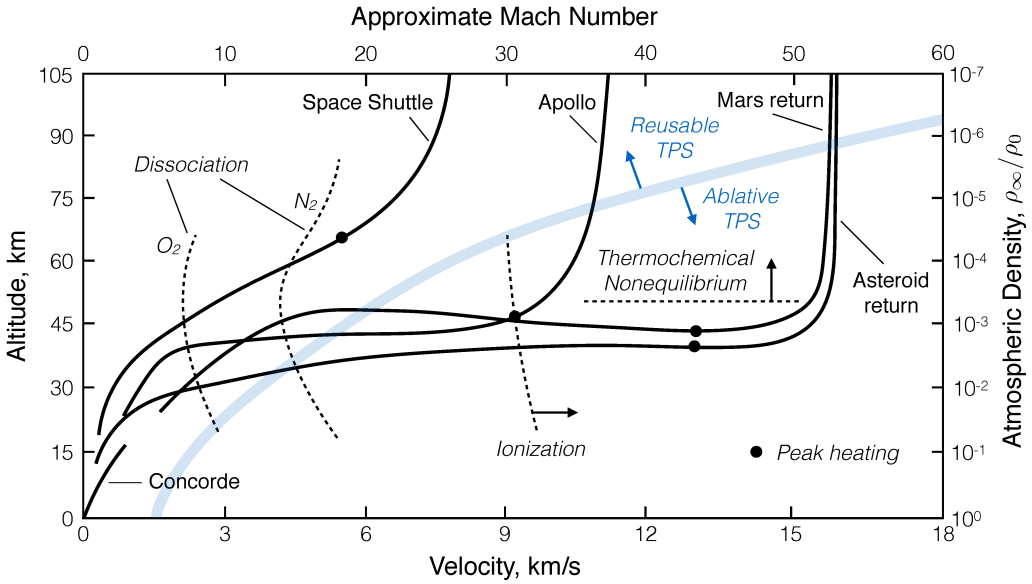

Figure 1.2.: *Flight regimes in Earth's atmosphere. Trajectories of various vehicles are shown in solid lines. Dashed lines represent the onset of real gas effects. Bullets indicate the trajectory point of maximum heating. Adapted from Howe [1] and Rivell [2].*

heat load and ensure that the temperature limits of critical components on board are not exceeded during the entry phase.

In general, two categories of TPS have been used for atmospheric entry, depending on the entry velocity and expected heat load. A velocity / altitude map for Earth entry is given in Fig. (1.2) which shows the flight profiles of several vehicles. For moderate entry velocities, reusable heat shields, like the one used on NASA's Space Shuttle vehicle, can be used to dissipate heat by re-radiating the energy back into the free stream. Reusable heat shields are designed to withstand multiple uses without need for replacement or repair. They are typically constructed from carbon or silicon carbide materials which have high emissivities at high temperatures in order to promote re-radiation. In practice, the use of reusable heat shields is limited to relatively slow entry velocities on the order of about 7 - 8 km/s, corresponding to Earth orbital velocities. For the space exploration missions of interest, such as Apollo or sample return from Mars or distant asteroids, entry velocities are greater 10 km/s and ablative thermal protection systems must be used. Like reusable materials, ablators dissipate a significant amount of heat through radiation. However, unlike reusables, ablators are designed for single use, dissipating the remaining heat by converting thermal energy into decomposition and degradation of the material itself, causing the surface of the ablator to recess over time. Ablative TPS are generally constructed from rigid carbon fiber or silicon composites, impregnated with an organic resin matrix which serves as a pyrolyzing binder and provides strength to the overall TPS structure.

As will be shown in the following section, the aerothermal environment surrounding a vehicle during atmospheric entry is extremely complex. As such, prediction of the heating rate which is experienced by the thermal protection system remains an imperfect art. For example, prediction uncertainty for Martian entry remains as high as 60 % for laminar convective heating [3]. In addition, the accurate characterization of the thermal protection system response to the imposed heat load adds further uncertainties due to the complexity of the decomposition and recession processes. Together, these uncertainties make selecting the right TPS type and thickness a challenging task, as mission designers have to balance minimizing the TPS mass while minimizing the risk of failure. A classic example is the NASA Galileo probe. Launched on October 18, 1989, Galileo spent over 8 years studying Jupiter and its moons. On September 21, 2003, after 14 years in space, Galileo ended its mission by entering the Jovian atmosphere with a relative velocity of 47.5 km/s, representing the most severe atmospheric entry environment ever attempted. The reentry probe,

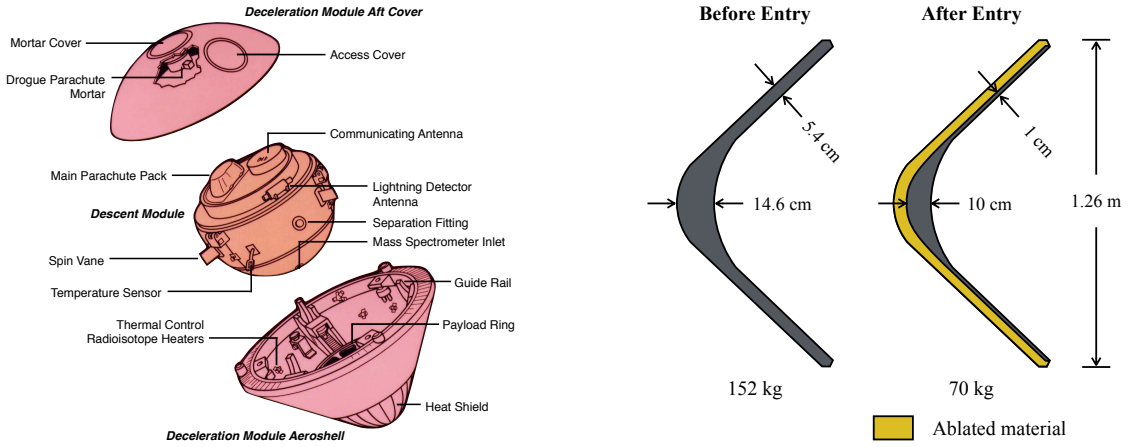

Figure 1.3.: *Diagram of the Galileo atmospheric entry probe (left) and the estimated TPS thickness before and after entry (right). Recession diagram is modified from the work of Laub and Venkatapathy [4].*

depicted on the left of Fig. (1.3) employed a fully dense carbon phenolic forebody TPS, designed to withstand the extreme heating environment so that on board sensors could collect valuable data about the atmosphere of Jupiter. Meanwhile, recession sensors embedded in the TPS itself, allowed direct measurement of the TPS performance during entry. The estimated recession profile of the Galileo TPS is shown on the right of Fig. (1.3). The data shows that the stagnation point recession was far less than predicted, while the recession at the shoulder was greater and nearly lead to a complete burn through which would have prematurely destroyed the probe. Fortunately, Galileo was a huge success for the American space exploration program, however, the recession data serves to underline the importance of being able to accurately characterize the aerothermal heating environment during atmospheric entry.

Failure to accurately predict the heat loads and associated material response of the TPS during the design phase can lead to catastrophic mission failure. In order to mitigate these failures, large safety factors are typically applied to the thickness of ablative TPSs during the design of atmospheric entry vehicles. Fig. (1.4) shows the percentage of total vehicle mass devoted to the thermal protection system versus the total expected heat load imposed for several vehicles. As can be seen in the figure, the TPS mass fraction scales proportionally to the total heat load, and reaches as high as 50 % in the case of Galileo. High TPS mass fractions mean that less mass is available for fuel or scientific payloads. Reducing the uncertainties associated with atmospheric entry heating, could allow for a reduction in the added TPS mass by excessive safety factor margins.

1.3. Atmospheric Entry Phenomena

The environment surrounding an atmospheric entry vehicle during entry represents a highly complex, coupled, multiphysics problem. Broadly speaking, the various phenomena which affect the resulting heat flux to the vehicle can be split into three domains: the aerothermal flow field, thermal protection material response, and thermal radiation. A diagram depicting some of these phenomena is shown in Fig. (1.5).

1.3.1. Shock Layer Physics

As the entry vehicle collides with the previously undisturbed atmospheric gases, a bow shock is formed upstream of the vehicle, compressing and energizing the translational energy modes of the gas particles. The temperature downstream of the shock can reach tens of thousands of degrees, depending on the atmospheric entry conditions. Collisions between these energized molecules

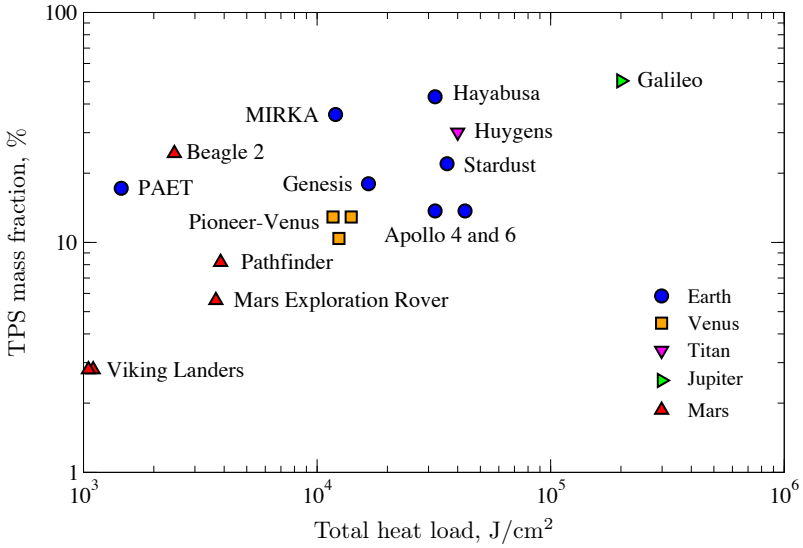

Figure 1.4.: *Percentage of vehicle mass used for thermal protection for several atmospheric vehicles. Data compiled from [5].*

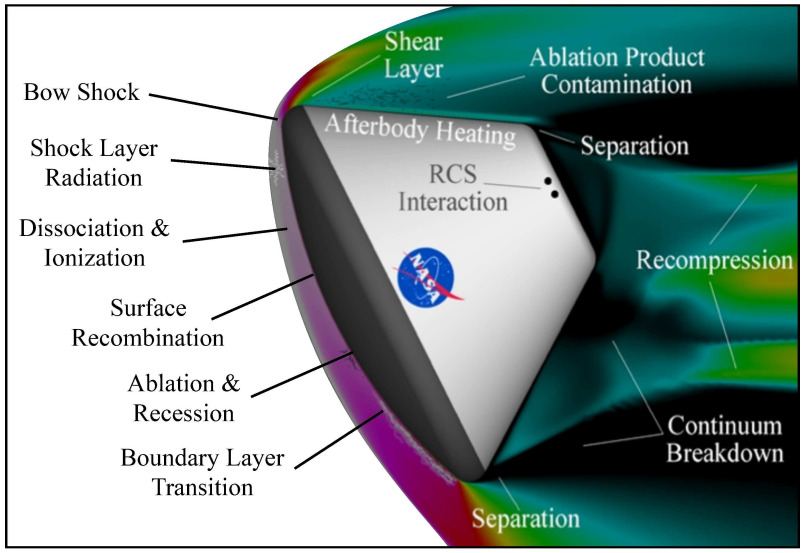

Figure 1.5.: *Diagram of various physicochemical phenomena occurring in the environment surrounding an atmospheric entry vehicle. Adapted from* `http://class.tamu.edu/projects/pecos`.

transfer some of the translational energy into the internal energy modes of the gas causing the translational energy to relax. In general, rotational and vibrational mode excitation is induced before excitation of the electronic modes.

Once the vibrational modes of the molecules become sufficiently energetic, additional collisions provide the energy necessary to break their inter-nuclear bonds, leading to dissociation. In air, for example, dissociation leads to the formation of atomic nitrogen and oxygen from N_2 and O_2. At the same time, Zelodvich exchange reactions between atoms and molecules form NO which can then dissociate as well. In the Martian atmosphere, on the other hand, dissociation of CO_2 creates CO and O_2 molecules and finally O atoms. Further collisional excitation of the atoms and molecules excites the bound electrons to higher electronic states. If the electrons become sufficiently excited, they may be stripped from their parent species, forming a plasma. In air, this process begins with the associative ionization of the NO molecule ($N + O \rightleftharpoons NO^+ + e^-$), producing a singly ionized NO^+ and a free electron. The positive molecule is then typically neutralized through a charge exchange reaction with N or O, stripping an electron from one of those atoms to form ionized N^+ or O^+. Over time, the associative ionization reactions build up the concentration of free electrons until a critical mass is formed. At this point, electron impact ionization reactions, create a chain reaction and the level of ionization increases dramatically. This process is called the electron avalanche. A similar process is also found during Martian entries, starting from the associative ionization of CO. However, Martian entries typically occur at a slower velocities than those on Earth, leading to far less ionization in general.

In addition to dissociation and ionization, collisional excitation may lead to thermal radiation as excited atoms and molecules spontaneously emit a photon and drop to a lower energy state. The radiant energy can then be absorbed by other atoms and molecules in the flow field, causing particles to jump to higher energy levels, or directly absorbed by the surface of the vehicle. Emission and absorption from bound levels to other bound levels is referred to as bound-bound radiation. The emission and absorption spectra of bound-bound processes is highly oscillatory in nature due to the many transitions between discrete internal energy levels of atoms and molecules. For sufficiently energetic atoms and molecules, absorption of a photon may lead to dissociation or ionization. In particular, the photo-dissociation of O_2 and photo-ionization of N and O are common in air. These processes are called bound-free since the particles in question begin the process bound to one another and are separate or "free" at the end. The reverse processes are likewise termed free-bound. Finally, free electrons may also contribute to radiation. As an electron passes through the electric field of another charged particle, it may undergo a deceleration and emit a photon with energy equal to the difference between the kinetic energy of the electron before and after the collision. This process is known as Bremsstrahlung from the german words *bremsen* for "to brake" and *strahlung* for "radiation". Bremsstrahlung is also called free-free radiation, since transitions occur between two unbound electrons. Bound-free and free-free processes exhibit a continuous spectrum, since the energy transitions are not limited to discrete jumps.

A significant portion of the energy emitted is radiated out of the shock layer into the free stream, reducing the temperature of the shock layer gas. This process is referred to as radiative cooling. For cases in which radiation is a significant source of heat transfer, radiative cooling may introduce a strong coupling mechanism between the flow and radiation fields and must be taken into account in order to accurately predict the heat flux reaching the surface of the vehicle. Assessing the importance of this coupling mechanism for a given entry is typically done by considering the so-called Goulard number Γ [6],

$$\Gamma = \frac{2q^r_{\mathrm{ad}}}{0.5\rho_\infty \boldsymbol{u}^3_\infty}, \tag{1.1}$$

which is the ratio of the adiabatic (uncoupled) radiative flux, approximated as twice the surface flux, to the total energy flux. As a general rule of thumb radiation coupling can be neglected for conditions in which $\Gamma < 0.01$. For higher values of the Goulard number, radiation coupling should be considered. In addition, for strongly radiating shock layers, the internal energy modes of the free stream ahead of the shock may be sufficiently excited by absorption processes to cause photo-ionization leading to the generation of free electrons. The effect of this precursor ionization on the shock structure and the ensuing thermochemical relaxtion processes downstream of the

shock remains an open research problem.

The collisional and radiative processes described above act to alter the thermodynamic state of the gas as the various energy modes transition from the equilibrium state of the undisturbed free stream to a different equilibrium state downstream of the shock. During this transition period, the gas may go through a series of thermochemical nonequilibrium states until sufficient collisions have occurred. The length of the nonequilibrium zone behind a shock is dependent on a number of factors, including the free stream density and composition as well as the vehicle size and velocity. The accurate prediction of the nonequilibrium states in this zone is crucial for the correct description of the radiative and convective heat flux on the surface of the vehicle. For example, in the case of the Huygens probe which entered the atmosphere of the Saturnian moon Titan on January 14, 2005, the radiative heat flux was found to be reduced between 2 to 15 times of that computed using an equilibrium assumption when nonequilibrium electronic populations of the CN molecule were considered [7].

1.3.2. Material Response

As the flow progresses towards the surface of the vehicle, a boundary layer develops due to viscous interactions between the plasma and the surface. Thermal and species gradients near the surface generate a convective heat flux into the vehicle via conduction and diffusion. In addition, irradiation of the surface by the radiant emission from the shock layer further increases the heat flux experienced by the vehicle. As the temperature of the surface rises, the bulk of the energy is re-radiated back into the free stream by the thermal protection material while the rest of the energy is conducted inside. For the carbon-phenolic thermal protection systems of interest in this work, the heat flux is mitigated through two main processes, called pyrolysis and ablation. Fig. (1.6) describes the phenomenology of the material response associated with carbon-phenolic thermal protection systems. Before atmospheric entry, the thermal protection material is in its virgin state, comprised of a carbon fibers impregnated with a phenolic resin matrix. As the the surface heats up during entry, a wave of heat is conducted into the virgin material. Once the temperature in the material rises above a certain level, the phenolic resin undergoes an endothermic thermal decomposition in which the chains of the polymer matrix begin to break, known as pyrolysis.

The pyrolysis gases formed during the thermal decomposition of a phenolic resin are strongly dependent on the molecular structure of the original polymer and the local temperature at which decomposition occurs. Phenolic resins are generally formed through a polycondensation reaction which occurs when a combination of phenol (C_6H_5OH) and formaldehyde (CH_2O) are heated in the presence of a catalyst. When excess formaldehyde is present in the mixture, a basic (alkaline) catalyst is used to promote cross-linking of the polymer through ethylene bridges, forming a novolac resin. When there is an excess of phenol, a resole type resin is produced in the presence of an acidic catalyst. Depending on the formaldehyde to phenol ratio, reaction temperature, catalyst, reaction time, and distillation amount, a wide variety of phenolic resin structures may be obtained, with various degrees of cross-linking and impurities. Linear polymers have a minimal amount of cross-linking and a repeated stoichiometry of C_7H_6O, while fully cross-linked polymers can be characterized by a stoichiometry of $C_{15}H_{12}O_2$. Typical polymer structures fall somewhere in between these idealized cases due to incomplete cross-linking and the presence of impurities embedded in the resin, such as nitrogen [10].

A significant number of experimental studies have been performed to characterize the thermal decomposition of various types of carbon-phenolic resins and TPS. In particular, several important studies have measured the composition of the pyrolysis gases produced versus temperature for various materials, including novolac [11] and resol [12] resins, carbon-phenolic [13], and PICA [14, 15]. While some variability exists, the thermal decomposition of a phenolic resin can generally be described in three temperature regimes. Between 300 °C to 600 °C, small molecules which are not linked to the bulk polymer (left over from resin formation) are allowed to escape. In addition, ether and nitrogen linkages begin to break, forming a mixture of aldehydes, cresols, and azomethines. The most significant pyrolysis gas formed in this stage is typically water. From 600 °C to 900 °C, the bulk of the pyrolysis gases are formed. A significant shrinkage of the polymer occurs due to

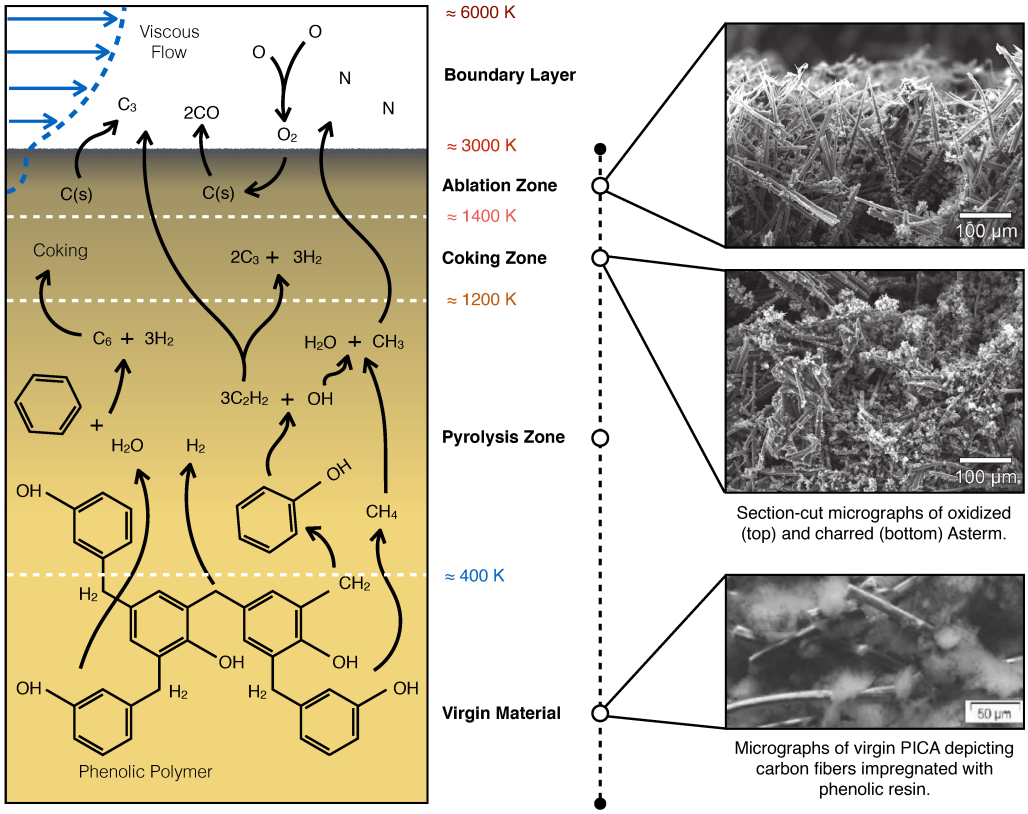

Figure 1.6.: *Phenomenology of thermal protection material response. Top two micrographs are taken from [8] while the bottom is taken from [9].*

the creation of carbon-carbon bonds between aromatic rings, forming a polyaromatic char. Several gases may be formed in this range, such as H_2, CH_4, H_2O, CO, CO_2, and volatile aromatics such as phenol (C_6H_5OH) and benzene (C_6H_6). Finally, above about 900 °C, dehydrogenation further shrinks the polymer forming mostly H_2 and other small noncarbonacious molecules.

Once formed, the pyrolysis gases are convected and diffused through the porous material, driven by a pressure gradient originating in the pyrolysis zone. As the gases flow towards the surface they may react with one another to form new compounds or dissociate further. Closer to the surface, the gas passes through a char layer, leftover from the completion of the pyrolysis processes. In some cases, the presence of carbonaceous pyrolysis gases leads to coking, in which some of the carbon in the gas is redeposited onto the polyaromatic char. At the surface of the thermal protection system, the pyrolysis gases generated inside are convected into the boundary layer. Atmospheric gases, diffusing to the surface, interact with the carbon fibers and carbonaceous char. In air, for example, nitrogen and oxygen atoms may undergo a catalytic recombination at the surface to form N_2 and O_2. In addition, oxidation and nitridation reactions may remove carbon from the surface, causing the surface to recess and generating CO, CO_2, and CN. At temperatures above about 3000 K, the carbon surface begins to sublimate, generating carbonaceous species such as C, C_2, and C_3, and increasing the surface recession rate. In extreme cases, surface spallation can also occur, in which large particles are ejected from the surface due to mechanical and thermal loads. Spallation is highly undesirable since it can dramatically increase the recession rate with little thermodynamic benefit. When combined, the processes which remove material from the surface are collectively known as ablation.

1.3.3. Flow, Material, Radiation Coupling

The gaseous products of ablation and pyrolysis are blown into the boundary layer where they may react with the atmospheric gases coming from the shock layer. For strong mass blowing rates, the boundary layer can be blown off of the surface, significantly reducing the thermal gradients at the surface and decreasing the convective heat flux. Depending on their type and concentration, ablation and pyrolysis gases may block a significant amount of the incoming radiation as well, through absorption. This process, known as radiation blockage, is still not fully characterized, due to the complexity of the phenomena leading to the creation of the ablation and pyrolsyis gases. To further complicate matters, certain ablation products such as CO, CN, and C_3 are known to be strong radiators, leading to the possibility that ablation may actually increase the radiative flux to the vehicle through spontaneous emission of these species as they are heated in the boundary layer. For example, Johnston *et al.* [16] have shown for a simplified boundary layer in air, contamination with ablation products may block radiation in the vacuum ultraviolet through increased absorption, while increasing it in the infrared and visible regions of the spectrum due to emission from CO, C_2, and CN.

Finally, as the flow moves across the surface of the ablator, the boundary layer thickness tends to grow. For larger vehicles, the laminar boundary layer flow can transition to turbulent, which may significantly increase the convective heating rate to the surface. As the flow wraps around the leading corner of the vehicle, a significant decompression and separation occurs, generating a large, turbulent wake. As the wake cools, previously dissociated atmospheric gases and ablation products may recombine. For Martian entries, a significant radiative heat flux can occur on the backshell of the vehicle due recombination of CO_2 which is a strong emitter in the infrared region. This phenomena may become increasingly important for future missions aiming to send increasingly large vehicles to Mars.

1.4. State-of-the-Art Flow-Radiation Tools

In this section, the current state-of-the-art of numerical prediction and modeling of atmospheric entry flows is briefly reviewed with a focus on topics relevant to this thesis. A more detailed review of the relevant literature is made throughout the thesis, as necessary. For a review of experimental

studies of ablation phenomena, the reader is referred to the recent work of Helber [17]. In general, state-of-the-art TPS design tools typically split the solution of the aerothermal environment surrounding atmospheric entry vehicles into three computational domains: the flow field, material response of the TPS, and the radiation field. Each computational domain is then solved in a loosely coupled fashion. This approach proved successful for a number of atmospheric entry cases when coupling phenomena are secondary to other features of the flow. Recently, a unified approach for flow / material coupling has been developed by Schrooyen [18] which computes the solution of an ablating, porous medium in the same computational domain as the flow.

On the other hand, past numerical investigations have shown several major radiation coupling effects, including (i) radiative cooling of the shock layer due to the strong emission of the plasma [19–21], (ii) the production of precursor chemical compounds ahead of the shock [22], and (iii) the promotion of ablation products released by the heat shield which may in turn contribute to increased radiation blockage in the boundary layer [16]. At high altitudes corresponding to low densities, the need to consider detailed nonequilibrium radiation appeared since the middle of the 1980s [23] and thermodynamic and chemical nonequilibrium flowfield solvers, coupled to radiative transfer, became common in the 1990s [24, 25].

A review of the thermochemical nonequilibrium models and governing equations used for hypersonic flows is detailed in the next chapter. In general, these models rely on the multicomponent, reacting Navier-Stokes equations [26] and are typically solved using finite-volume shock capturing methods [27, 28]. Thermochemical nonequilibrium is accounted for using simple multitemperature models [26, 29, 30] which split the internal energy of atoms and molecules into different modes assumed to be at equilibrium at different temperatures.

The numerical simulation of radiative transfer is a challenging problem because of the spatial, angular, and spectral dependence of the radiation field. The reference approach for treating the spectral dependence is the Line-By-Line (LBL) method which consists in finely discretizing the radiative properties over the relevant spectral range. These radiative properties depend on level populations and on fundamental spectroscopic data gathered in spectral databases such as NEQAIR [31, 32], SPRADIAN [33], MONSTER [34], SPECAIR [35]. The High Temperature Gas Radiation (HTGR) spectral database, previously developed at the EM2C laboratory at CentraleSupélec for O_2-N_2 and CO_2-N_2 plasma applications [36–40], will be used in this work. HTGR gathers up-to-date atomic spectroscopic data from various sources (such as NIST [41] and TOPbase [42]) together with exhaustive and accurate calculations of diatomic molecular spectra and atomic line shapes. It includes bound-bound atomic and molecular transitions, bound-free transitions resulting from various mechanisms, and free-free transitions. The covered spectral range is [1000 - 200,000 cm^{-1}] and the targeted maximum temperature is 50,000 K. The HTGR database has been used in several studies for LBL radiative transfer calculations in hypersonic entries. In particular, Lamet *et al.* [43] performed uncoupled radiation simulations of the Fire II flight experiment using a two-temperature approach to model the thermal nonequilibrium. More recently, Lopez *et al.* [44] carried out coupled flow-radiation simulations of the relaxation behind a shock wave in air with a consistent state-to-state modeling of the atomic electronic levels.

A full LBL closely coupled flowfield-radiation model has been developed by Feldick *et al.* [45] for Earth hypersonic reentries. They used the tangent slab approximation and introduced optimized variable wavelength steps to decrease the computational costs. The full LBL simulations were successfully compared to a hybrid line-by-line-gray model where molecular radiation in optically thin systems was assumed to be gray inside narrow bands. However, although the LBL method is very accurate, the large number of radiative transitions that have to be taken into account makes it very computationally expensive and impractical for coupled simulations in complex geometries. The Smeared-Rotational-Band (SRB) model is a common way to simplify the calculation of molecular radiation but its accuracy is restricted to small optical thicknesses. It has been used for instance in Ref. [46], together with a LBL treatment of atomic radiation.

More sophisticated approaches for radiative property modeling include the k-distribution methods which are based on the distribution functions of the absorption coefficient over the whole spectrum (for example, [47]) or over spectral narrow bands [48]. They have been widely used for modeling IR radiation in the field of atmospheric physics or for combustion applications, but

also for modeling visible, UV and VUV radiation of astrophysical (Opacity Distribution Function model of Ref. [49]) or thermal [50] plasmas. Recently, such models have been developed in the framework of hypersonic nonequilibrium flows for air mixtures [51, 52] and also in carbonaceous atmospheres [53]. They are based on the Full-Spectrum Correlated-k approach (FSCK) previously developed for IR applications [54] and use efficient tabulations and rescaling of the various required distribution functions against temperatures, molecular electronic state populations, and a typical Stark width of the atoms. The accuracy of these approaches was demonstrated by successful comparisons with LBL results. In the case of carbonaceous atmospheres [53], where only three non-overlapping molecular band systems are considered, such an approach is very efficient and easy to implement. Moreover, it retains a description of radiative properties in terms of absorption coefficients and is therefore applicable to any radiation solver. For more arbitrary gas mixtures such as ablation contaminated boundary layers, a large number of overlapping, non-weak molecular electronic systems, absorbing in the Voigt regime, and whose induced emission contribution may not be negligible, have to be accounted for. In this case, the multi-scale MS-FSCK approach can become tedious to implement. Moreover, the spectral information is completely lost when using such full-spectrum approaches. This is not an intrinsic limitation if one is only interested in heat transfer with gray walls, but such models do not enable comparisons with experiments done in limited spectral ranges.

Recently, Lamet *et al.* [55] have developed the Hybrid Statistical Narrow Band (HSNB) model, combining a Statistical Narrow-Band (SNB) model for optically thick molecular systems with a box model for optically thin molecular systems and continua, and a LBL description of atomic lines. Band parameters have been computed using the HTGR database and tabulated against translational-rotational and vibrational temperatures. The HSNB model can easily include new radiating species and electronic systems, and arbitrary electronic populations may be specified. In addition, it can be applied to predict the radiative flux in the case of non-gray walls. However, the accuracy of the HSNB model has not yet been assessed in the case of ablation contaminated boundary layers. Moreover, no study to date has demonstrated the efficiency of the HSNB model necessary for coupled flow, radiation, ablation calculations.

1.5. Objectives and Outline of the Thesis

The goal of this work is to develop physicochemical models and numerical methods for the study of the complex, coupled, multiphysics phenomena associated with atmospheric entry plasmas. In particular, the thesis is focused on the coupling between the flow, ablation, and radiation phenomena encountered in the stagnation region of the flow surrounding atmospheric entry vehicles with carbon-phenolic thermal protection systems. Three broad objectives have been identified:

1. Many models associated with the complex thermochemical nonequilibrium phenomena summarized in Section 1.3 require substantial amounts of basic data and specialized algorithms to evaluate properties of the flow field during the course of a Computational Fluid Dynamics (CFD) calculation. For example, the solution of accurate transport properties for partially ionized plasmas requires the evaluation of many collision integrals, proportional to the square of the number of binary interactions in the species mixture. These data can be tedious to implement or difficult to find and are often "hard coded" in many modern hypersonic CFD tools in use today. The first objective of this work is therefore to develop a new software library capable of providing a centralized repository for the basic physico-chemical models, algorithms, and data relevant to nonequilibrium plasma flows.

2. The accuracy of the HSNB model has been successfully demonstrated against reference LBL solutions in previous work for uncoupled radiative heat transfer in nonequilibrium atmospheric entry flows. However, as discussed in the previous section, the accuracy and efficiency of the model has not yet been assessed using a coupled approach with ablation contaminated boundary layers. A second objective of this thesis is to develop a numerical approach for calculating coupled flow, radiation, and ablation solutions along the stagnation line of at-

mospheric entry vehicles and to assess the accuracy and efficiency of HSNB model using the new approach.

3. Lastly, a third objective is to study the effects of flow, radiation, and ablation coupling on the predicted heat fluxes at the stagnation point of real atmospheric entry vehicles, using the tools developed in the previous objectives.

The thesis is divided into a total of eight chapters, including this introduction.

Chapter 2 presents a review of the thermochemical nonequilibrium models and governing equations applicable to hypersonic flows and atmospheric entry. In addition, the necessary closure models for thermodynamics, transport fluxes, chemical reaction rates, and energy transfer mechanisms are reviewed. The main goals of this review is to lay the groundwork for the numerical tools described in later chapters and to develop a generalized system of governing equations, capable of encompassing all relevant thermochemical nonequilibrium models in use today.

Chapter 3 details the calculation of the radiative source terms which enter into the governing equations presented in Chapter 2. A review of important radiative mechanisms is outlined, followed by a description of the HTGR database, used to compute high resolution emission and absorption spectra for the flow fields studied in this work. The HSNB model is also presented as a method for reducing the computational time required for calculating the radiative source terms. Several new contributions to both the HTGR and HSNB databases for modeling radiation in ablation contaminated boundary layers are detailed.

Chapter 4 presents the development of a new software library called "MUlticomponent Thermodynamic And Transport properties for IONized gases, written in C++" (MUTATION^{++}). Building on the results of Chapter 2, the library provides thermodynamic, transport, chemistry, and energy transfer models, data, and algorithms, relevant to nonequilibrium flows. It has been written in C++ using modern, object oriented designed techniques in an effort to maximize its efficiency and extensibility.

Chapter 5 describes a novel algorithm for the solution of linearly constrained, multiphase equilibria. Multiphase equilibrium calculations are a crucial component of many material response codes. The new algorithm developed in this work, called Multiphase Gibbs Function Continuation (MPGFC), is shown to be provably robust for all well posed problems. The merits and efficiency of the algorithm are discussed in detail.

Chapter 6 presents the remaining numerical tools developed in this work. The steady-state flow along the stagnation line of an atmospheric entry vehicle is computed using a one-dimensional, finite-volume tool, based on the dimensionally reduced Navier-Stokes equations for stagnation line flows. In an effort to limit the scope of this thesis, coupling with ablation is achieved through a steady-state ablation boundary condition, in place of a full material response solution methodology. The boundary condition accounts for finite-rate heterogeneous reactions at the surface and imposed equilibrium compositions of pyrolysis out-gassing based on the steady-state ablation assumption. Computation of the radiative source terms is performed using the Tangent Slab approximation.

Chapter 7 applies the numerical tools and algorithms described in the previous chapters to real flight conditions, in particular, key trajectory points along the entries of the Fire II, Apollo 4, and Huygens vehicles. The relative accuracy and computational efficiency of the HSNB method is assessed, compared to LBL calculations for stagnation point radiative heating calculations. In addition, the effects of coupled flow, radiation, and ablation phenomena on the predicted heating rates are discussed.

Chapter 8 summarizes the main contributions of the thesis and provides perspective for possible future work.

CHAPTER 2

Governing Equations for Hypersonic Flows

2.1. Introduction

Atmospheric entry vehicles operate in the hypersonic flow regime due to their extreme velocities relative to the atmosphere in which they enter. Hypersonic flight is characterized by velocity timescales on the same order of magnitude as the chemical and kinetic timescales of the shocked gas. Under such conditions, thermal and chemical nonequilibrium may dominate the aerothermal environment surrounding the entry vehicle. In addition, radiative heating becomes important as atoms and molecules are excited to higher internal energy levels. These phenomena have substantial effects on vehicle heating and aerodynamic forces affecting its trajectory and must be accurately characterized during the design phase.

This chapter reviews the approaches typically used to model thermochemical nonequilibrium and radiative heat transfer in hypersonic flow fields for atmospheric entry. In particular, the various species internal energy partitioning models are discussed as well as the closure models employed to compute the necessary thermodynamic, transport, and chemistry properties required to close the governing equations. One contribution of this chapter is to formulate the governing equations using a generalized notation, valid for most thermochemical models of interest in the literature. As will be shown, this framework represents a powerful tool for abstracting away the physico-chemical models from the governing equations for hypersonic flows and forms the basis of the MUTATION^{++} library presented in Chapter 4.

2.2. Review of Energy Partitioning Models

Quantum mechanics dictates that atoms and molecules are permitted only discrete energy levels [56]. For atoms, this energy is contained within translational and electronic energy modes. Molecules have two additional energy storage modes via rotation and vibration of the molecule. In general, all energy modes are coupled. For weakly interacting particles (dilute gases), however, translational energy may be considered decoupled from the internal energy. Note that this use of "internal energy" should not be confused with the typical fluid dynamic description of the internal energy of a gas, which includes translational energy. Here, internal energy is meant to differentiate between energy associated with the translation of the center of mass of a particle and the energy associated with the relative motion of its constituents (nuclei and electrons). While translational energy levels are discrete, the spacing between levels is extremely small. For all practical purposes, this permits a semi-classical approach in which translational energy is assumed continuous while internal energy is left discrete. Furthermore, it is assumed that the populations of internal energy levels satisfy Maxwell-Boltzmann statistics, such that the quantum effects differentiating bosons (Bose-Einstein statistics) and fermions (Fermi-Dirac statistics) are negligible [56].

Fig. (2.1) provides potential energy curves of N_2 for selected electronic energy states of the molecule. Energy levels are measured from the zero point energy of the molecule (energy of the ground state at 0 K). Vibrational energy levels are denoted with tick marks for each electronic state. Rotational levels are spaced even closer together between vibrational levels. Individual particles may jump from one state to another through collisional or radiative (de)excitation processes or react with other particles to form an entirely different species.

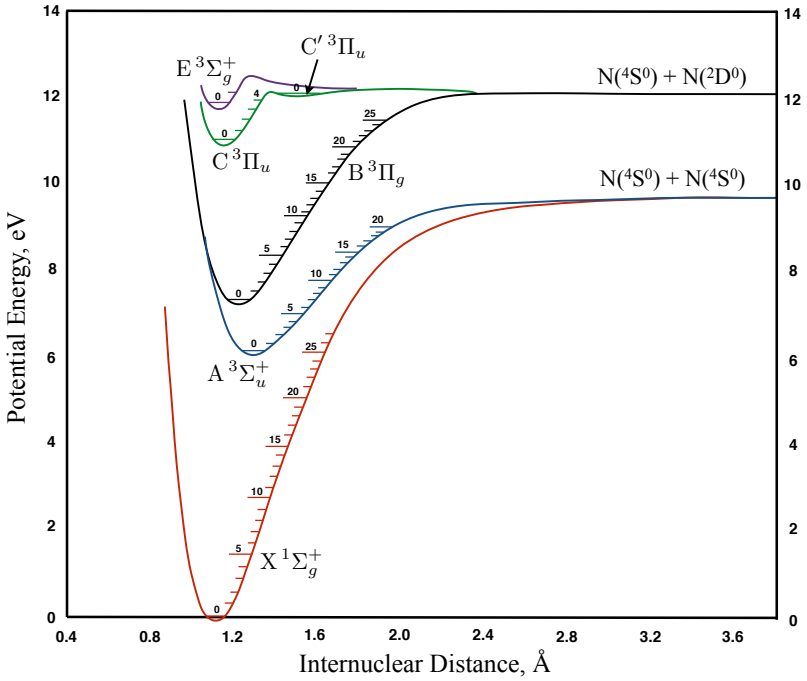

Figure 2.1.: *Potential energy curves for selected electronic states of N_2, measured from the ground state. Lowest vibrational energy levels are indicated by tick marks. Curves reproduced from [57].*

A complete description of any flow field requires knowledge of the energy state of all particles in the flow and their positions, versus time. In principle, each and every particle could be tracked individually, however this represents an insurmountable computational problem. A less costly approach is instead to track the population of particles in each internal energy state as the number of energy states is vastly smaller than the number of particles in continuum flows. This approach, known as the State-to-State approach, can also represent a daunting computational challenge as the number of populated rovibronic energy states for simple diatomic molecules can be on the order of tens of thousands. Because of this, many different approaches have been adopted in the literature for treating nonequilibrium energy distributions. Such models are known as "energy partitioning" models as they generally describe the way energy is distributed or partitioned among the allowable energy states of a given atom or molecule. In this section, various energy partitioning models are reviewed. The discussion of each model is ordered loosely by their departure from equilibrium and more generally, in chronological order of when each model was successfully employed in modern CFD computations for hypersonic flow fields. This review is not intended to represent a comprehensive list of all energy partitioning models (indeed, many of these models are routinely mixed to form hybrid models) however, it serves to discuss the major features and assumptions of each.

2.2.1. Thermal Equilibrium

When the excitation/deexcitation processes are in equilibrium (flow timescale much larger than kinetic timescale), the mixture is in local thermal equilibrium. Under these conditions, the distribution of energy levels for a given species follows a Boltzmann distribution, for non-degenerate gases. Denoting the set of all species indices in a gas mixture as $\mathcal{S}$ and the set of all electronic levels of atom j or rovibronic levels of molecule j as $\mathcal{L}_j$, then the Boltzmann distribution is given as

$$n_j^l = \frac{n_j}{Q_j^{\text{int}}(T)} a_j^l \exp\left(-\frac{E_j^l}{k_B T}\right), \quad j \in \mathcal{S}, \quad l \in \mathcal{L}_j, \tag{2.1}$$

where n_j^l is the number density of species j with energy level l, $n_j = \sum_l n_j^l$ is the total number density of species j, E_j^l is the internal energy of level (j,l) relative to the zero point energy of species j, and a_j^l is the degeneracy of the level. The quantity Q_j^{int} is called the internal partition function for species j and is given by

$$Q_j^{\text{int}}(T) = \sum_{l \in \mathcal{L}_j} a_j^l \exp\left(-\frac{E_j^l}{k_B T}\right), \quad j \in \mathcal{S}. \tag{2.2}$$

Note that the only unknowns present in Eq. (2.1) are the number density of species j, n_j, and the mixture temperature T. These quantities must be determined through suitable governing equations which are discussed in the next section.

When thermal equilibrium is no longer valid, a suitable energy partitioning model must be used to provide the distribution of energy levels for each species. The following subsections review the most common models found in the literature.

2.2.2. Multitemperature Models

The thermal nonequilibrium models which are still used today for aerospace engineering applications can be attributed to the works of Park [58–60] and Lee [29, 61] in the mid to late 1980's who developed so-called multi-temperature models. The main idea behind multi-temperature (MT) models is that the energy associated with any internal level can be separated into various energy modes. When the fine structure is neglected, all internal energy levels of a diatomic molecule may be enumerated by the electronic, rotational, and vibrational quantum numbers, n, J, ν, respectively. Electronic states may be characterized by the label ${}^{2S+1}\Lambda$ where $2S+1$ is the spin multiplicity and Λ is the absolute value of the electronic orbital momentum on the internuclear axis. Under this notation, the electronic degeneracy is then given as $a_j^{\text{el}} = (2-\delta_{0,\Lambda})(2S+1)$, where δ is the Kronecker delta. The rotational degeneracy is simply $a_j^{\text{r}} = 2J+1$. Vibrational states are not degenerate ($a_j^{\text{v}} = 1$).

Assuming that each energy mode is decoupled from the others, a rovibronic energy level $l = (n, J, \nu)$ of a diatomic molecule j, could be split according to [61], such that

$$E_j^l \equiv E_j(n, J, \nu) = E_j^{\text{el}}(n) + E_j^{\text{r}}(J) + E_j^{\text{v}}(\nu), \tag{2.3}$$

where E_j^{el}, E_j^{r}, and E_j^{v} are the electronic, rotational, and vibrational contributions to energy level l. Each energy mode is then assumed to represent a thermal bath in equilibrium at a separate temperature, yielding

$$n_j^l = \frac{n_j}{Q_j^{\text{int}}(T_{el}, T_r, T_v)} a_j^l \exp\left(-\frac{E_j^{\text{el}}(n)}{k_B T_{el}} - \frac{E_j^{\text{r}}(J)}{k_B T_r} - \frac{E_j^{\text{v}}(\nu)}{k_B T_v}\right), \tag{2.4}$$

where $a_j^l = a_j^{\text{el}} a_j^{\text{r}} a_j^{\text{v}}$ and $Q_j^{\text{int}}(T_{el}, T_r, T_v)$ is the multitemperature internal partition function of species j,

$$\begin{aligned} Q_j^{\text{int}}(T_{el}, T_r, T_v) &= \sum_{l \in \mathcal{L}_j} a_j^l \exp\left(-\frac{E_j^{\text{el}}(n)}{k_B T_{el}} - \frac{E_j^{\text{r}}(J)}{k_B T_r} - \frac{E_j^{\text{v}}(\nu)}{k_B T_v}\right) \\ &= Q_j^{\text{el}}(T_{el}) Q_j^{\text{r}}(T_r) Q_j^{\text{v}}(T_v). \end{aligned} \tag{2.5}$$

The assumption of perfect separability of the energy modes allows the internal partition function to be split into a product of partition functions for each mode as is shown on the second line of Eq. (2.5), where the partition function for mode m can be written generically as

$$Q_j^m(T_m) = \sum_{k \in \mathcal{L}_j^m} a_j^m(k) \exp\left(-\frac{E_j^m(k)}{k_B T_m}\right), \tag{2.6}$$

where $\mathcal{L}_j^m$ is the set of pure energy levels for mode m.

Eqs. (2.4) and (2.5) drastically reduce the number of unknowns required to model thermal nonequilibrium as compared to those required for State-to-State (STS) models. However, decoupling of the internal degrees of freedom as in Eq. (2.3) is a strong assumption and may introduce significant errors in the thermodynamic properties of the gas. Based on the Born-Oppenheimer approximation, electronic motion may be decoupled from the nuclear motion above relatively low temperatures, below the range of interest for atmospheric entry simulations [62]. Unfortunately, this is not the case for rotation and vibration due to a strong coupling caused by centrifugal forces created by rotation and the dependence of the moment of inertia of a vibrating molecule on the internuclear distances between its constituent nuclei. In addition, since the rotational and vibrational spectroscopic constants depend on the electronic states, the rovibrational energy may exhibit a strong coupling with the electronic energy of a molecule, even when the Born-Oppenheimer approximation is appropriate.

Jaffe [63] first introduced a "general" MT model which takes into account rovibrational energy coupling in a consistent way for diatomic molecules by introducing the following energy splitting,

$$E_j^l \equiv E_j(n,J,\nu) = E_j^{\mathrm{el}}(n) + E_j^{\mathrm{r}\prime}(n,J,\nu) + E_j^{\mathrm{v}\prime}(n,J,\nu), \tag{2.7}$$

where $E_j^{\mathrm{el}}(n)$ is the pure electronic energy for electronic state n and

$$E_j^{\mathrm{r}\prime}(n,J,\nu) = E_j^{\mathrm{r}}(n,J) + E_j^{\mathrm{rv}}(n,J,\nu)\,(1-\alpha), \tag{2.8}$$

$$E_j^{\mathrm{v}\prime}(n,J,\nu) = E_j^{\mathrm{v}}(n,\nu) + E_j^{\mathrm{rv}}(n,J,\nu)\,\alpha, \tag{2.9}$$

where $E_j^{\mathrm{r}}(n,J)$ and $E_j^{\mathrm{v}}(n,\nu)$ are the pure rotational and vibrational energies for electronic level n and $E_j^{\mathrm{rv}}(n,J,\nu)$ is the rotation-vibration interaction energy. The parameter $0 \leq \alpha \leq 1$ in Jaffe's model is used to distribute the rovibrational interaction energy into rotational and vibrational modes. There is no physical basis for this distribution, however it has been shown that this parameter has little effect on thermodynamic properties for diatomic air species [43, 63].

When all of the interaction energy is added to the vibrational mode ($\alpha = 1$), the following generic MT distribution is obtained for diatomic molecules,

$$n_j^l = \frac{n_j a_j^l}{Q_j^{\mathrm{int}}} \exp\left(-\frac{E_j^{\mathrm{el}}(n)}{k_B T_{el}} - \frac{E_j^{\mathrm{r}}(n,J)}{k_B T_r} - \frac{E_j^{\mathrm{v}}(n,\nu) + E_j^{\mathrm{rv}}(n,J,\nu)}{k_B T_v} \right), \tag{2.10}$$

where the internal partition function may be written as

$$\begin{aligned} Q_j^{\mathrm{int}} = &\sum_n (2 - \delta_{0,\Lambda(n)})(2S(n)+1) \exp\left(-\frac{E_j^{\mathrm{el}}(n)}{k_B T_{el}} \right) \times \\ &\sum_J (2J+1) \exp\left(-\frac{E_j^{\mathrm{r}}(n,J)}{k_B T_r} \right) \times \\ &\sum_\nu \exp\left(-\frac{E_j^{\mathrm{v}}(n,\nu) + E_j^{\mathrm{rv}}(n,J,\nu)}{k_B T_v} \right) \end{aligned} \tag{2.11}$$

Eqs. (2.10) and (2.11) provide a consistent, general MT model for describing nonequilibrium state distributions. Like the Park and Lee models in Eqs. (2.4) and (2.5), the general model significantly reduces the number of parameters required to describe nonequilibrium flows. However, it is important to note that the partition function in Eq. (2.11) cannot be split into separable modes as in Eq. (2.5) due to the coupled summation over the level quantum numbers.

The MT models presented in this section may be easily adapted to polyatomic species with more degrees of freedom [64, 65]. In general, any polyatomic species j with n_j^a nuclei have $3n_j^a - (\mathfrak{L}_j + 3)$ normal vibrational modes, where $\mathfrak{L}_j = 2$ for linear molecules and $\mathfrak{L}_j = 3$ for nonlinear molecules. Each new vibrational mode can be enumerated with an additional vibrational quantum number and the corresponding energy partitioning updated. It should also be noted that the models shown

here all assumed a single temperature for each energy mode, however it is common for example to have separate vibrational temperatures for each vibrational mode in each molecule. The separable and nonseparable MT models presented above can be easily generalized by appending a species subscript to the temperatures (e.g., T_{vj} for a vibrational mode of species j).

MT models have been used with great success since the late 1980's for a variety of CFD applications [26, 27, 29, 43, 58–61, 66–71]. However, because they are based on Boltzmann distributions, these models are valid for only small departures from equilibrium [72]. With recent advancements in computational efficiency and multiprocessor computer architectures, collisional models have become more feasible. In particular, state-specific and energy binning models are discussed in the next sections.

2.2.3. State-Specific Models

State-specific models attempt to increase the validity range of MT models beyond small departures from equilibrium by modeling some states as pseudo-species [7, 73, 74]. In general, the energy of a particular molecular state is split into two categories: 1) modes assumed to be in full nonequilibrium and must be treated as pseudo-species, and 2) those which follow a Boltzmann distribution with all the modeling possibilities presented in Section 2.2.2.

Cambier [73] introduced an electronic-specific Collisional-Radiative (CR) model for molecular plasmas, in which each electronic mode of a given molecule is treated as a separate pseudo-species. We will denote this species with the subscript $j(n)$ for the n^{th} electronic state of species j. The number of particles of species j at the electronic state n is given by

$$n_{j(n)} = \sum_{\nu J} n_j^{nJ\nu}. \tag{2.12}$$

The rovibrational levels in each electronic state are then populated according to a Boltzmann distribution at the species rotation and vibration temperature, such that for diatomic molecules,

$$n_j^l \equiv n_j^{nJ\nu} = \frac{n_{j(n)} a_j^{nJ\nu}}{Q_{j(n)}^{\text{int}}} \exp\left(- \frac{E_j^{\text{el}}(n)}{k_B T_{el}} - \frac{E_j^{\text{r}}(n,J)}{k_B T_{rj}} - \frac{E_j^{\text{v}\prime}(n,J,\nu)}{k_B T_{vj}} \right), \tag{2.13}$$

where the rovibrational partition function for electronic state n is given by

$$Q_{j(n)}^{\text{int}} = \exp\left(- \frac{E_j^{\text{el}}(n)}{k_B T_{el}} \right) \sum_{\nu J} a_j^{nJ\nu} \exp\left(- \frac{E_j^{\text{r}}(n,J)}{k_B T_{rj}} - \frac{E_j^{\text{v}\prime}(n,J,\nu)}{k_B T_{vj}} \right), \tag{2.14}$$

and $E_j^{\text{v}\prime}(n, J, \nu)$ represents the energy partitioned into the vibrational mode as was done in Eq. (2.9). Notice that the term $a_j^n \exp(-E_j^{\text{el}}(n)/k_B T_{el})$ (with arbitrary T_{el}) in Eq. (2.13) is canceled out when the rovibrational partition function is substituted into the equation, however we have opted to include this term in the definition of the partition function in order to obtain a general relation for thermodynamic properties later on (see Section 2.4).

When applied to atoms, electronic-specific models, like the one above, represent the most rigorous nonequilibrium model possible. In this case, the approach is typically referred to as a full STS model which is discussed in Section 2.2.4. Under some conditions, a large number of atomic and molecular electronic states may be populated, requiring many pseudo-species to be retained in the energy partitioning model. To reduce the system size, some researchers propose to group close electronic states [73] into a single pseudo-species. Relations similar to Eqs. (2.13) and (2.14) can then be obtained by summing over all electronic levels in each group. Care should be taken when grouping electronic levels to take into account the distribution of energy accross the levels, major radiative transitions, and chemistry coupling [73, 75]. As an example, consider the electronic states of N_2 shown in Fig. (2.1). The low lying states in the figure will dissociate to two $N(^4S^0)$ atoms while the upper states will dissociate to $N(^4S^0)$ and $N(^2D^0)$. Based on this observation, grouping lower electronic states of N_2 with higher states will introduce errors in the dissociation of N_2 and should be avoided if possible.

Vibronic-specific collisional (VC) models have also been widely used in the literature [74]. Here, all vibrational-electronic (vibronic) states are treated as a pseudo-species by summing over all rotational levels,

$$n_{j(n\nu)} = \sum_J n_j^{nJ\nu}, \tag{2.15}$$

and appropriate relationships are derived for the number densities and state-specific internal partition functions as was done for the electronic-specific case. VC models are important for studying preferential dissociation rates of high-lying vibrational levels [74], among other things. In general however, the large number of vibronic states of a given molecule, make VC models impractical in multidimensional CFD simulations.

2.2.4. State-to-State Models

The most rigorous energy partitioning models are the so-called STS or collisional models which treat all internal energy levels as pseudo-species [76–78]. When all collisional processes are taken into account and assuming that the corresponding rate coefficients are correct, collisional models accurately capture all nonequilibrium phenomena occuring in the flow field.

The STS approach makes no assumption on the distribution of energy states and thus no temperature has been introduced into the expression for the number densities of individual levels. However, it is still useful to define a partition function for the internal energy of a single energy state in order to correctly evaluate the thermodynamics associated with each level. This will become more clear when the thermodynamics associated with such models are developed in Section 2.4.1. The partition function for a single energy state l for species j is thus given by,

$$Q_j^l(T) = a_j^l \exp\left(-\frac{E_j^l}{k_B T}\right), \tag{2.16}$$

where the choice of T is arbitrary.

With the advancement of computational resources, accurate STS collision cross sections and reaction rates can now be computed with quasi-classical trajectory (QCT) methods using potential energy surfaces (PESs) obtained from detailed ab initio quantum chemistry calculations [79]. For example, Panesi *et al.* [78] have recently developed a rovibrational collisional (RVC) model for the $N_2(^1\Sigma_g^+)$–$N(^4S_u)$ system based on STS rate coefficients developed at NASA Ames Research Center [80–83]. The NASA Ames database provides consistent thermodynamic and kinetic data for 9390 rovibrational levels of the N_2 ground electronic state. Such models allow us to study nonequilbrium chemistry and energy exchange processes with an unprecedented level of detail and remove much of the empiricism involved in the energy partitioning methods previously discussed. However, because of the large number of unknowns, molecular STS models are currently relegated to 0D reactors or simple 1D flows [76–78, 84–95]. In addition, when radiative heat transfer is considered, the electronically excited states of molecules like N_2 must also be accounted for, significantly increasing the size and complexity of STS models.

2.2.5. Coarse-Grain and Energy Binning Models

The reduced nonequilibrium models presented thus far have all made use of the concept of separable internal energy modes (e.g., Eq. (2.3)). However, these approaches do not have a physical basis because energy modes are in fact coupled. Coarse-grained models [72, 75, 96, 97] provide an alternative approach which attempts to decrease the resolution of STS models by grouping close energy levels into bins. For a species j with energy levels $l \in \mathcal{L}_j$, the levels are ordered and grouped into bins labeled with index $b \in \mathcal{B}_j$. We will denote the set of level indices belonging to bin b for species j as $\mathcal{I}_{bj}$. Each bin is then treated as a pseudo-species, requiring a mass conservation equation to be solved for the population of the bin.

Various strategies have been proposed for which parameter to conserve [96], including the total number density of all levels in each bin or the number density of the lowest level in the bin. The

levels in each bin can then be populated according to a particular distribution function. In the case of a uniform distribution, levels are populated according to

$$n_j^l = \frac{a_j^l}{\tilde{a}_b}\tilde{n}_b, \tag{2.17}$$

where $\tilde{a}_b = \sum_{l\in\mathcal{I}_{bj}} a_j^l$ and $\tilde{n}_b$ are the bin degeneracy and number density, respectively. Levels may also be populated using a Boltzmann distribution at the translational temperature of the heavy particles. In that case,

$$n_j^l = \frac{a_j^l}{\tilde{Q}_b^{\text{int}}}\exp\left(-\frac{\Delta E_{bj}^l}{k_B T_h}\right), \tag{2.18}$$

where $\Delta E_{bj}^l \equiv E_j^l - \tilde{E}_b$, $\tilde{E}_b$ is the energy of the lowest level in bin b, and the bin partition function is

$$\tilde{Q}_b^{\text{int}} = \sum_{l\in\mathcal{I}_{bj}} a_j^l \exp\left(-\frac{\Delta E_{bj}^l}{k_B T_h}\right). \tag{2.19}$$

The uniform distribution above does not retrieve equilibrium and thus a Boltzmann distribution is typically preferred [72].

While still relatively young, coarse-grained models show a great deal of promise for the efficient computation of nonequilibrium phenomena. For example, Munafò *et al.* [72, 97] have performed a bin convergence study for the relaxation of shock-heated nitrogen using a Boltzmann rovibrational collisional (BRVC) model based on the NASA Ames nitrogen STS database [80–83] and have shown that accurate relaxation times and post-shock conditions are obtained with just 20 bins. In that work, bins were formed using uniform energy discretizations of 9390 rovibrational levels of the N_2 ground electronic state. The resulting size of the system of conservation equations is on par with the number of equations typically solved in the state-specific models. However, coarse-grain models make no assumptions on the nature of the nonequilibrium phenomena, except for the intrabin distribution, and can be generated to any level of resolution from detailed ab initio STS data obtained from accurate quantum chemistry calculations.

2.3. Governing Equations

The nonequilibrium models presented in the previous sections provide relationships for individual level populations as functions of independent mass and energy variables. Additional conservation equations are required to relate these parameters to the flow field. Before proceeding with the description of these equations, a few preliminary assumptions and notations are introduced, defining the framework around which general governing equations are written, valid for any energy partitioning model. Following this setup, the necessary equations to model both thermochemical equilibrium and nonequilibrium, hypersonic, plasma flows are presented.

2.3.1. Preliminaries

We begin by considering a partially ionized gas phase mixture composed of $n^{\mathcal{S}}$ distinct chemical species, including neutral and ionized atoms and molecules, and free electrons. The set of species indices which enumerate each species in the mixture is denoted as $\mathcal{S} = \{e\} \cup \mathcal{H} = \{1, \ldots, n^{\mathcal{S}}\}$, where the set of heavy species $\mathcal{H}$ has been defined for convenience and e represents the index of free electrons. In addition, the set of chemical elements which combine to form the species set $\mathcal{S}$ is denoted as $\mathcal{E} = \{1, \ldots, n^{\mathcal{E}}\}$, where $n^{\mathcal{E}} \leq n^{\mathcal{S}}$ is the number of elements considered. Following convention [65], $\mathcal{E}$ contains the electron as well, in order to track the electric charge of each species. An elemental stoichiometry matrix B_{ji}^{e} defines the number of atoms (or electrons) $i \in \mathcal{E}$ used to form the species $j \in \mathcal{S}$. From purely stoichiometric arguments, the species masses and charges are

then written as

$$m_j = \sum_{i \in \mathcal{E}} m_i^e B_{ji}^{\mathrm{e}}, \quad \forall\, j \in \mathcal{S}, \tag{2.20}$$

$$q_j = -q_e B_{je}^{\mathrm{e}}, \quad \forall\, j \in \mathcal{S}, \tag{2.21}$$

where m_j and m_i^e are the particle masses of species j and element i, while q_j and q_e are the elemental charge of species j and free electrons, respectively.

Following the discussion of Section 2.2, each species is assigned an energy partitioning model, requiring the definition of at least one pseudo-species per species in the mixture. The set of pseudo-species indices which belong to a species $j \in \mathcal{S}$ is denoted $\mathcal{S}_j^*$ such that the set of all pseudo-species in the mixture is given as $\mathcal{S}^* = \{e\} \cup \mathcal{H}^* = \cup_{j \in \mathcal{S}} \mathcal{S}_j^* = \{1, \ldots, n^{\mathcal{S}^*}\}$, where $n^{\mathcal{S}^*} \geq n^{\mathcal{S}}$ is the total number of pseudo-species defined by the species energy partitioning models. Pseudo-species, by definition, share the same mass and charge as the physical species which they model. Thus, the density of a species $j \in \mathcal{S}$ is given as

$$\rho_j = \sum_{k \in \mathcal{S}_j^*} \rho_k = m_j \sum_{k \in \mathcal{S}_j^*} n_k, \tag{2.22}$$

where ρ_k and n_k are the mass and number densities, respectively, of pseudo-species $k \in \mathcal{S}_j^*$. Apart from the pseudo-species themselves, species energy partitioning models also define the separation of energy modes belonging to each pseudo-species. It is now assumed that each energy mode δ, in the set of $n_k^{\mathcal{M}}$ separable modes $\mathcal{M}_k$ belonging to each pseudo-species $k \in \mathcal{S}^*$, represents an energy bath with average specific energy $e_{k\delta} = e_{k\delta}(T_{k\delta})$, characterized by suitable thermodynamic relations in terms of a partition function $Q_k^\delta = Q_k^\delta(T_{k\delta})$ and temperature $T_{k\delta}$. Upon careful review, it can be seen that this assumption encompasses all of the partitioning models described in Section 2.2, except the generalized MT model of Jaffe which defines a multitemperature partition function. The generalized MT model is convenient for approximating nonequilibrium molecular energy level populations, necessary for the calculation of molecular radiative spectra [55]. However, to the author's knowledge, no rigorous theory for the conservation of energy in a multitemperature thermal bath has yet been developed. Therefore, no penalty has been paid by this restriction in terms of developing the necessary governing equations. Furthermore, from the separability of the energy modes, the total energy of a pseudo-species $k \in \mathcal{S}^*$ can be written as

$$e_k = \sum_{\delta \in \mathcal{M}_k} e_{k\delta}(T_{k\delta}) + e_{k0}, \tag{2.23}$$

where e_{k0} is the zero-point energy of the species.

Finally, a set of global energy modes are now defined which represent collections of thermal baths, in equilibrium with one another and characterized by a single temperature. The set of all $n^{\mathcal{M}}$ global energy modes is denoted $\mathcal{M} = \{1, \ldots, n^{\mathcal{M}}\}$. The set of separate energy modes belonging to a pseudo-species $k \in \mathcal{S}^*$ which are assigned to a global mode $m \in \mathcal{M}$ is then defined as $\mathcal{M}_k^m$, such that $\mathcal{M}_k = \cup_{m \in \mathcal{M}} \mathcal{M}_k^m$. In addition, for each global mode $m \in \mathcal{M}$, a temperature T_m is also defined, such that

$$T_{k\delta} = T_m, \forall\, \delta \in \mathcal{M}_k^m, m \in \mathcal{M}, k \in \mathcal{S}^*. \tag{2.24}$$

Following these definitions, the total specific energy of the global mode $m \in \mathcal{M}$ is given by

$$e^m = \frac{1}{\rho} \sum_{k \in \mathcal{S}^*} \rho_k e_k^m(T_m), \tag{2.25}$$

where $\rho = \sum_{k \in \mathcal{S}^*} \rho_k$ is the total density of the mixture and the specific energy of pseudo-species $k \in \mathcal{S}^*$ associated with global mode $m \in \mathcal{M}$ is

$$e_k^m(T_m) = \sum_{\delta \in \mathcal{M}_k^m} e_{k\delta}(T_m). \tag{2.26}$$

Note that the specific energy e_k^m is defined per mass of pseudo-species k, while e^m is per mass of the mixture. Furthermore, when the energy e^m for $m \in \mathcal{M}$ and the mixture composition are known, Eq. (2.25) represents an implicit relation for the solution of the temperature T_m.

In summary, a full thermochemical model is described by the list of species considered (characterized by B_{ji}^{e} for $j \in \mathcal{S}$ and $i \in \mathcal{E}$), the species energy partitioning models (characterized by $e_{k\delta}(T_{k\delta})$ for $\delta \in \mathcal{M}_k$, $k \in \mathcal{S}_j^*$, and $j \in \mathcal{S}$), and the global thermal nonequilibrium model (characterized by $T_{k\delta} = T_m$ for $\delta \in \mathcal{M}_k^m$, $k \in \mathcal{S}^*$, and $m \in \mathcal{M}$). When $n^{\mathcal{M}} = 1$, thermal equilibrium is enforced. Conversely, when $n^{\mathcal{M}} > 1$, thermal nonequilibrium is envisaged in the thermochemical model. With this framework in place, a generic set of governing equations may be written, valid for all thermochemical models expressible with this notation. Two particular cases are considered: 1) multicomponent, partially ionized, plasma flows in thermochemical nonequilibrium ($n^{\mathcal{M}} \geq 1$), and 2) flows in local thermodynamic equilibrium (LTE) ($n^{\mathcal{M}} = 1$). In both cases, the effects of an electromagnetic field and thermal radiation are taken into account.

In principle, the governing equations should be derived from a suitable kinetic theory based on a generalized Chapmann-Enskog perturbative solution of the Boltzmann equation [56, 98, 99] accounting for 1) thermal nonequilibrium of translational energy, 2) the influence of the electromagnetic field, 3) excitation of internal energy modes through inelastic collisions and radiative processes, 4) reactive collisions, and 5) photochemical processes. However, no such uniform theory, incorporating all of these phenomena, currently exists. While significant progress has been made in this direction [100–102], current state-of-the-art models rely instead on the principle of generalized balancing to describe the evolution of extensive flow field quantities, namely the conservation of total or partial mass, momentum, and energy [65]. The resulting governing equations derived in this way for the two cases considered here are presented in the next sections. Closure of the governing equations in terms of thermodynamic, transport, and chemical properties, are then presented.

2.3.2. Thermochemical Nonequilibrium

This section presents the necessary equations to model flows in thermochemical nonequilibrium using the general thermochemical model introduced in the previous section. In general, these consist of $n^{\mathcal{S}^*}$ mass, 1 momentum, and $n^{\mathcal{M}}$ energy conservation equations. Chemical nonequilibrium is described by a set of elementary chemical reactions involving the $n^{\mathcal{S}^*}$ pseudo-species in $\mathcal{S}^*$. For convenience, it is assumed that heavy species translation thermalizes to the same temperature T_h and electrons thermalize to T_e, which may be different than T_h. In addition, the semi-classical approach in which translational energy is treated as continuous while internal energy is discrete according to quantum mechanics, is recalled from Section 2.2.

Pseudo-species mass conservation

Conservation of mass for each pseudo-species k is written as

$$\frac{\partial}{\partial t}(\rho_k) + \boldsymbol{\nabla} \cdot (\rho_k \boldsymbol{u}) + \boldsymbol{\nabla} \cdot (\rho_k \boldsymbol{V}_k) = \dot{\omega}_k + \dot{\phi}_k, \quad \forall\, k \in \mathcal{S}^* \tag{2.27}$$

where $\boldsymbol{u}$ is the mass-averaged mixture velocity,

$$\rho \boldsymbol{u} = \sum_{k \in \mathcal{S}^*} \rho_k \boldsymbol{u}_k, \tag{2.28}$$

and $\boldsymbol{u}_k$ is the average velocity for the pseudo-species k. Diffusion velocities are defined as $\boldsymbol{V}_k \equiv \boldsymbol{u}_k - \boldsymbol{u}$ and are linearly dependent, such that

$$\sum_{k \in \mathcal{S}^*} \rho_k \boldsymbol{V}_k = 0. \tag{2.29}$$

The source terms on the right-hand-side of Eq. (2.27) account for the mass production of species k due to elementary homogeneous chemical reactions, $\dot{\omega}_k$, and radiative processes, $\dot{\phi}_k$, respectively.

Note that the species mass production due to ablation and pyrolysis has been entirely neglected in Eq. (2.27), as only the flow and radiative fields are considered here, sufficiently far from the thermal protection system. When modeling the flow near and inside a charring, porous ablator, these terms must be taken into account. All chemical and photochemical processes satisfy element and charge conservation, leading to

$$\sum_{k\in\mathcal{S}^*} \dot{\omega}_k = 0, \quad \text{and} \tag{2.30}$$

$$\sum_{k\in\mathcal{S}^*} \dot{\phi}_k = 0. \tag{2.31}$$

The evaluation of chemical production rates are detailed in Section 2.6.1, while photochemical processes are discussed in Chapter 3.

Total mass continuity

Summing Eq. (2.27) over all species and energy levels and substituting in Eqs. (2.28 - 2.31) yields the total mass conservation, or continuity, equation,

$$\frac{\partial}{\partial t}(\rho) + \boldsymbol{\nabla}\cdot(\rho\boldsymbol{u}) = 0. \tag{2.32}$$

Note that Eq. (2.32) remains valid regardless of the thermochemical model employed and is a direct consequence of conservation of mass. In practice two options are possible for the solution of the $n^{\mathcal{S}^*}$ pseudo-species densities: 1) solution of $n^{\mathcal{S}^*}$ pseudo-species mass balance equations, or 2) the solution of $n^{\mathcal{S}^*}-1$ pseudo-species mass balance equations supplied with the total continuity equation. In the first option, the total density can be found from the sum of the pseudo-species densities, while in the second, the missing pseudo-species density is found from the total density minus the known species densities. In practice, this choice is generally a matter of preference.

Momentum conservation

Conservation of total momentum yields

$$\frac{\partial}{\partial t}(\rho\boldsymbol{u}) + \boldsymbol{\nabla}\cdot(\rho\boldsymbol{u}\otimes\boldsymbol{u}) = -\boldsymbol{\nabla}p + \boldsymbol{\nabla}\cdot\bar{\boldsymbol{\Pi}} + nq\boldsymbol{E}' + \boldsymbol{j}\times\boldsymbol{B}, \tag{2.33}$$

where $n=\sum_{k\in\mathcal{S}^*} n_k$ is the mixture number density, $q=\sum_{k\in\mathcal{S}^*} x_k q_k$ is the mixture charge, $x_k = n_k/n$ the mole fraction of pseudo-species k, $\boldsymbol{j}=\sum_{k\in\mathcal{S}^*}\boldsymbol{j}_k$ is the mixture conduction current, $\boldsymbol{j}_k = n_k q_k \boldsymbol{V}_k$ is the conduction current for species k, $\boldsymbol{E}' = \boldsymbol{E} + \boldsymbol{u}\times\boldsymbol{B}$ is the electric field in the hydrodynamic velocity frame, $\boldsymbol{E}$ is the electric field, and $\boldsymbol{B}$ is the magnetic field. The terms on the right-hand-side of Eq. (2.33) account for pressure, viscous, and electric forces, respectively. For electrically neutral gas mixtures, the term $nq\boldsymbol{E}'$ vanishes. The radiation pressure is neglected and the static pressure is given by the combination of the perfect gas and Dalton's laws,

$$p = \sum_{k\in\mathcal{H}^*} \rho_k R_k T_h + \rho_e R_e T_e, \tag{2.34}$$

where $R_k = k_B/m_k$ is the specific gas constant for species k. The exact form of the viscous stress tensor $\bar{\boldsymbol{\Pi}}$ is determined by the type of energy partitioning model used and is discussed in Section 2.5.1.

Total energy conservation

The total energy of the system is also conserved. Total energy conservation is written as

$$\frac{\partial}{\partial t}(\rho E) + \boldsymbol{\nabla}\cdot(\rho H\boldsymbol{u}) = \boldsymbol{\nabla}\cdot(\bar{\boldsymbol{\Pi}}\boldsymbol{u}) - \boldsymbol{\nabla}\cdot\boldsymbol{q} + \mathcal{P} + \boldsymbol{j}\cdot\boldsymbol{E}', \tag{2.35}$$

where the specific total energy of the gas E is the sum of mixture "internal" and kinetic energies,

$$E = e + \frac{1}{2}\boldsymbol{u}\cdot\boldsymbol{u}, \tag{2.36}$$

with the specific "internal" energy written as

$$e = \frac{1}{\rho}\sum_{k\in\mathcal{S}^*}\rho_k e_k = \sum_{m\in\mathcal{M}} e^m(T_m). \tag{2.37}$$

The word "internal" is written in quotes here to indicate the conventional thermodynamic definition of internal energy, including the translational modes. Likewise, the total specific enthalpy is given as

$$H = E + \frac{p}{\rho}. \tag{2.38}$$

The four terms on the right-hand-side of Eq. (2.35) account for work done on the fluid due to viscous forces, heating due to conduction and diffusion, energy emitted or absorbed through thermal radiation, and the total Joule heating, respectively. The total heat flux vector $\boldsymbol{q}$ is described in Section 2.5.3 while the calculation of the radiative power $\mathcal{P}$ is detailed in Chapter 3.

Free-electron energy conservation

Conservation of free electron energy is expressed as,

$$\frac{\partial}{\partial t}(\rho_e e_e) + \boldsymbol{\nabla}\cdot(\rho_e e_e\boldsymbol{u} + p_e\boldsymbol{u}) = \boldsymbol{u}\cdot\boldsymbol{\nabla}p_e - \boldsymbol{\nabla}\cdot\boldsymbol{q}_e + \Omega^e + \boldsymbol{j}_e\cdot\boldsymbol{E}' + \mathcal{P}_e. \tag{2.39}$$

The second term in Eq. (2.39) accounts for the convection of the enthalpy of free electrons, while the third term represents the work done on electrons by an electric field induced from an electron pressure gradient. Typically, these two terms are combined, resulting in

$$\frac{\partial}{\partial t}(\rho_e e_e) + \boldsymbol{\nabla}\cdot(\rho_e e_e\boldsymbol{u}) = -p_e\boldsymbol{\nabla}\cdot\boldsymbol{u} - \boldsymbol{\nabla}\cdot\boldsymbol{q}_e + \Omega_e + \boldsymbol{j}_e\cdot\boldsymbol{E}' + \mathcal{P}_e. \tag{2.40}$$

Eq. (2.40) is usually preferred over Eq. (2.39) as it simplifies the resulting Eigen system for the convective flux, necessary in various upwind schemes [26], when the non conservative term $-p_e\boldsymbol{\nabla}\cdot\boldsymbol{u}$ is discretized as a source term. This pragmatic choice remains questionable at best, however the correct treatment of the electron energy equation is beyond the scope of this thesis and will not be addressed here. The last four terms in Eq. (2.40) account for conduction and diffusion of electron energy, electron energy exchanged from other energy modes, Joule heating, and electron energy absorbed or emitted through radiative processes. Note that electrons do not contribute to the viscous shear stress due to their small mass compared to heavy particles, thus there is no work done on electrons by viscous forces. The electron heat flux vector $\boldsymbol{q}_e$ is detailed in Section 2.5.3.

The electron energy transfer source Ω_e is split into several components,

$$\Omega_e = \sum_{n\in\mathcal{M}}\Omega^{en} + \Omega^{Ce}, \tag{2.41}$$

where Ω^{en} accounts for exchange between electrons and heavy particles due to elastic and inelastic collisions while Ω^{Ce} accounts for energy provided to the free electron thermal bath through chemical reactions. These terms are detailed in Section 2.7. Lastly, the radiative source term is discussed in Chapter 3.

Internal energy conservation

Finally, conservation of any purely internal energy mode m may be written as

$$\frac{\partial}{\partial t}(\rho e^m) + \boldsymbol{\nabla} \cdot (\rho e^m \boldsymbol{u}) = -\boldsymbol{\nabla} \cdot \boldsymbol{q}^m + \Omega^m + \mathcal{P}_m. \tag{2.42}$$

The expression of the heat flux vector for an internal energy mode $\boldsymbol{q}^m$ is given in Section 2.5.3. The remaining two source terms in Eq. (2.42) account for energy exchanged from another mode to mode m through collisional and radiative processes, respectively. The collisional source term Ω^m is generally written as

$$\Omega^m = \sum_{\substack{n \in \mathcal{M} \\ n \neq m}} \Omega^{mn} + \Omega^{Cm}, \tag{2.43}$$

where the first term accounts for relaxation with translation and internal energy modes through elastic and inelastic collisions and Ω^{Cm} accounts for energy gained (or lost) through reactive collisions.

Conservation of mass and energy leads to the following constraints on the energy transfer terms,

$$\sum_{m \in \mathcal{M}} \Omega^{Cm} = 0, \tag{2.44}$$

$$\Omega^{nm} + \Omega^{mn} = 0, \quad m, n \in \mathcal{M}. \tag{2.45}$$

Two popular energy MT models are the so called two temperature (2T) and three temperature (3T) models [26, 92]. The 3T model splits the energy into three groups, namely heavy translational-rotational energy, vibrational energy, and electronic-electron energy. The 2T model combines the vibrational energy and electronic-electron energy into a single thermal bath. In both cases, the total energy conservation equation is solved in conjunction with two or one additional energy equations. The corresponding energy equations for the 3T model are given as

$$\frac{\partial}{\partial t}(\rho e^v) + \boldsymbol{\nabla} \cdot (\rho e^v \boldsymbol{u}) = -\boldsymbol{\nabla} \cdot \boldsymbol{q}^v + \Omega^{\mathrm{VT}} - \Omega^{\mathrm{EV}} + \Omega^{\mathrm{CV}} + \mathcal{P}_v, \tag{2.46}$$

$$\frac{\partial}{\partial t}(\rho e^e) + \boldsymbol{\nabla} \cdot (\rho e^e \boldsymbol{u}) = -p_e \boldsymbol{\nabla} \cdot \boldsymbol{u} - \boldsymbol{\nabla} \cdot \boldsymbol{q}^e + \Omega^{\mathrm{ET}} + \Omega^{\mathrm{EV}} - \Omega^{\mathrm{I}} + \mathcal{P}_e, \tag{2.47}$$

where Ω^{VT} accounts for vibration-translation energy exchange, Ω^{EV} accounts for energy exchange between electronic-electron and vibrational modes, Ω^{CV} accounts for vibrational energy gained through chemical processes, Ω^{ET} is the energy transferred from heavy particle to electron translational modes through elastic collisions, and Ω^{I} is the energy lost by the electron thermal bath due to electron impact reactions (ionization, excitation, dissociation, etc.). Summing the two equations above yields the 2T model internal energy equation,

$$\frac{\partial}{\partial t}(\rho e^{ve}) + \boldsymbol{\nabla} \cdot (\rho e^{ve} \boldsymbol{u}) = -p_e \boldsymbol{\nabla} \cdot \boldsymbol{u} - \boldsymbol{\nabla} \cdot \boldsymbol{q}^{ev} + \Omega^{\mathrm{VT}} + \Omega^{\mathrm{ET}} + \Omega^{\mathrm{CV}} - \Omega^{\mathrm{I}} + \mathcal{P}_{ve}. \tag{2.48}$$

The treatment of the radiative source terms in the 3T and 2T models remains unclear. In practice, for the 2T model, a practical choice is to neglect radiative energy transfer to the rotational mode such that all radiant power is converted to vibration and electronic energy. See Chapter 3 for a in-depth discussion of this topic.

2.3.3. Local Thermodynamic Equilibrium

So far, the main emphasis of this chapter was to establish the thermochemical nonequilibrium models and conservation equations used to simulate hypersonic flows. Such models are necessary when characteristic time scales of the flow match or fall below the kinetic time scales, causing significant departures from equilibrium. However, it is often necessary to simulate flows relevant to hypersonics which fall in the LTE regime, such that the thermochemical equilibrium can be

assumed. Examples include flow field rebuilding of plasma torch test facilities [103] and Mars return vehicle entry simulations [16].

Under LTE conditions, all energy states of every species are assumed to be in equilibrium at a single mixture temperature T ($n^{\mathcal{M}} = 1$). Species densities ρ_j are an implicit function of elemental densities ρ_i^e and the mixture energy,

$$\rho_j = f(\rho_i^e \; \forall \; i \in \mathcal{E};\; \rho e(T)), \tag{2.49}$$

where the mass density of element i is given by

$$\rho_i^e = \sum_{j \in \mathcal{S}} B_{ji}^e \frac{m_i^e}{m_j} \rho_j, \quad \forall \; i \in \mathcal{E}. \tag{2.50}$$

The unspecified function f in Eq. (2.49) may represent the minimization of the system-wide Gibbs free energy or equivalently, the simultaneous solution of $n^{\mathcal{S}}$ formation reaction equations. The reader is referred to Chapter 5 for an in-depth discussion on this topic.

Eqs. (2.49) and (2.50) may be used to significantly reduce the number of conservation equations required to simulate flows in LTE. The following subsections describe the conservation of mass, momentum, and energy for LTE flows.

Elemental mass conservation

Summing Eq. (2.27) over all species and weighting by $B_{ji}^e m_i^e / m_j$, $n^{\mathcal{E}}$ elemental mass conservation equations are obtained, yielding

$$\frac{\partial}{\partial t}(\rho_i^e) + \boldsymbol{\nabla} \cdot (\rho_i^e \boldsymbol{u}) + \boldsymbol{\nabla} \cdot \boldsymbol{J}_i^e = 0 \quad \forall \; i \in \mathcal{E}, \tag{2.51}$$

where element mass diffusion fluxes are,

$$\boldsymbol{J}_i^e = \rho_i^e \boldsymbol{V}_i^e = \sum_{j \in \mathcal{S}} B_{ji}^e \frac{m_i^e}{m_j} \rho_j \boldsymbol{V}_j, \quad \forall \; i \in \mathcal{E}. \tag{2.52}$$

Element diffusion velocities are readily obtained from Eqs. (2.50) and (2.52) and can be expressed as

$$\boldsymbol{V}_i^e = \frac{\boldsymbol{J}_i^e}{\rho_i^e} = \frac{1}{x_i^e} \sum_{j \in \mathcal{S}} x_j B_{ji}^e \boldsymbol{V}_j, \quad \sum_{i \in \mathcal{E}} \rho_i^e \boldsymbol{V}_i^e = 0, \tag{2.53}$$

where x_i^e is the elemental mole fraction for element i. The linear dependence of the element diffusion velocities makes use of the relation $m_j = \sum_i B_{ji}^e m_i^e$.

Momentum and total energy conservation

Momentum and total energy conservation for equilibrium flows remains identical to Eq. (2.33) and Eq. (2.35) shown for nonequilibrium flows.

2.4. Thermodynamics

The governing equations described in the previous section require the evaluation of mixture and species thermodynamic properties. In particular, energy and enthalpy are explicitly necessitated by the conservation of energy. As will be shown in the proceeding sections, other thermodynamic properties are also required for the evaluation of the transport, chemistry, and energy transfer terms. This section provides general descriptions of the necessary thermodynamic properties in terms of the species partition functions detailed in Section 2.2.

2.4.1. Thermodynamics of Pure Gases

Relations for the thermodynamic properties of pure gases are derived from statistical mechanics [56]. Recall from Eq. (2.23) that the energy of a given species or pseudo-species $k \in \mathcal{S}^*$ is the sum of the energy attributed from each separable energy mode (or thermal bath) $\delta \in \mathcal{M}_k$, where the energy of each mode is a function of a separate temperature $T_{k\delta}$. Following the semi-classical approach described in Section 2.2, it is convenient to organize these modes into translational and internal energy, such that

$$e_k = e_{kt}(T_{kt}) + \sum_{\delta \in \mathcal{M}_k^{\text{int}}} e_{k\delta}(T_{k\delta}) + e_{k0} \tag{2.54}$$

where e_{kt} is the translational energy of pseudo-species k and $\mathcal{M}_k^{\text{int}}$ denotes the set of all other energy modes which contribute to the internal energy, such that $\mathcal{M}_k = \{t\} \cup \mathcal{M}_k^{\text{int}}$. Furthermore, the energy in each internal mode $\delta \in \mathcal{M}_k^{\text{int}}$ is split into a set of discrete energy levels $l \in \mathcal{L}_k^\delta$ according to quantum mechanics and the temperature describes the distribution of these level in the Boltzmann limit,

$$\frac{n_{k\delta}^l}{n_k} = \frac{a_{k\delta}^l}{Q_{k\delta}(T_{k\delta})} \exp\left(- \frac{E_{k\delta}^l}{k_B T_{k\delta}} \right), \tag{2.55}$$

$$Q_{k\delta} = \sum_{l \in \mathcal{L}_k^\delta} a_{k\delta}^l \exp\left(- \frac{E_{k\delta}^l}{k_B T_{k\delta}} \right), \tag{2.56}$$

where $a_{k\delta}^l$ and $E_{k\delta}^l$ are the degeneracy and energy of level $l \in \mathcal{L}_k^\delta$, respectively, and $Q_{k\delta}$ is the partition function for pseudo-species $k \in \mathcal{S}^*$ and internal mode $\delta \in \mathcal{M}_k^{\text{int}}$. Note that all of the energy partitioning models discussed in Section 2.2, except for the MT model of Jaffe, can be described by Eqs. (2.55) and (2.56). Recall that, in the case of the STS model, the partition function is written for a single energy level only. It this case, Eq. (2.55) reduces to $n_{k\delta}^l = n_k$ as expected. From these assumptions, the translational and internal energies are now readily given as

$$e_{kt} = \frac{3}{2} R_k T_{kt}, \tag{2.57}$$

$$e_{k\delta} = \frac{1}{\rho_k} \sum_{l \in \mathcal{L}_k^\delta} n_{k\delta}^l E_{k\delta}^l = R_k T_{k\delta}^2 \frac{\partial}{\partial T_{k\delta}} \big(\ln Q_{k\delta} \big), \quad \forall\, \delta \in \mathcal{M}_k^{\text{int}} \tag{2.58}$$

where $T_{kt} = T_h, k \in \mathcal{H}^*$ and $T_{kt} = T_e, k = e$, according to the assumptions made in Section 2.3.2. The first expression given in Eq. (2.58) is simply the definition of the average energy of a distribution of energy states. The second expression is easily derived by substitution of Eqs. (2.55) and (2.56). The benefit of defining a STS partition function in Eq. (2.16) is now clear, since it allows the inclusion of the STS model under the general notation of Eq. (2.58).

Pseudo-species enthalpies h_k and entropies s_k for $k \in \mathcal{S}^*$ are likewise split into translational and internal modes, such that

$$h_k = h_{kt} + \sum_{\delta \in \mathcal{M}_k^{\text{int}}} h_{k\delta} + e_{k0}, \tag{2.59}$$

$$s_k = s_{kt} + \sum_{\delta \in \mathcal{M}_k^{\text{int}}} s_{k\delta}, \tag{2.60}$$

where $h_{k\delta} \equiv e_{k\delta} + p_{k\delta}/\rho_k$, $p_{k\delta}$, and $s_{k\delta}$ are the enthalpy, pressure, and entropy associated with each thermal bath $\delta \in \mathcal{M}_k$. The thermodynamic pressure is zero for all but the translational

modes, permitting the enthalpies to be written as

$$h_{kt} = e_{kt} + R_k T_{kt}, \tag{2.61}$$

$$h_{k\delta} = e_{k\delta}, \quad \forall\, \delta \in \mathcal{M}_k^{\text{int}}. \tag{2.62}$$

The translational and internal entropies for pseudo-species $k \in \mathcal{S}^*$ are found to be

$$s_{kt} = R_k \left[\frac{5}{2} + \ln Q_{kt} - \ln n_k \right], \tag{2.63}$$

$$s_{k\delta} = R_k \left[T_{k\delta} \frac{\partial}{\partial T_{k\delta}} \left(\ln Q_{k\delta} \right) + \ln Q_{k\delta} \right], \quad \forall\, \delta \in \mathcal{M}_k^{\text{int}}, \tag{2.64}$$

where the volumetric translational partition function is evaluated as

$$Q_{kt} = \left(\frac{2\pi m_k k_B T_{kt}}{h^2} \right)^{3/2}. \tag{2.65}$$

When computing the entropy of free electrons, it is important to take into account their spin. The electron spin yields a degeneracy of 2 in the "internal" partition function such that $Q_e^{\text{int}} = 2$ (zero energy of electron "ground state" measured from zero point energy).

Species Gibbs free energies are necessary for the computation of equilibrium constants, as will be shown in Section 2.6. The Gibbs energy for a pseudo-species $k \in \mathcal{S}^*$ is defined as

$$g_k = \sum_{\delta \in \mathcal{M}_k} g_{k\delta}, \tag{2.66}$$

$$g_{k\delta} \equiv h_{k\delta} - T_{k\delta} s_{k\delta}. \tag{2.67}$$

In Section 2.3.1, a generic set of global energy modes, representing collections of thermal baths in thermal equilibrium with one another, was also defined. It is necessary to derive the thermodynamic properties of these global modes as well for the solution of the governing equations which necessitates the formulation of the contribution of each species or pseudo-species to these properties. Since each of the modes $\delta \in \mathcal{M}_k$ are assumed to be separable for a pseudo-species $k \in \mathcal{S}^*$, the contribution of species k to any extensive thermodynamic property of the mixture α^m for the global mode $m \in \mathcal{M}$ is readily given by

$$\alpha_k^m = \sum_{\delta \in \mathcal{M}_k^m} \alpha_{k\delta}(T_m). \tag{2.68}$$

Eq. (2.68) is a generalization of Eq. (2.26) to any extensive thermodynamic property of interest.

Finally, species specific heats are required for the evaluation of transport properties as well as in the solution of temperatures from given energies. Using Eq. (2.68), pseudo-species specific heats are defined per constant pressure and volume for each global energy mode $m \in \mathcal{M}$ and species $k \in \mathcal{S}^*$ as

$$c_{p_k}^{\,m} = \left(\frac{\partial h_k}{\partial T_m} \right)_p = \sum_{\delta \in \mathcal{M}_k^m} \frac{d\, h_{k\delta}}{d\, T_m}, \tag{2.69}$$

$$c_{v_k}^{\,m} = \left(\frac{\partial e_k}{\partial T_m} \right)_V = \sum_{\delta \in \mathcal{M}_k^m} \frac{d\, e_{k\delta}}{d\, T_m}, \tag{2.70}$$

where $h_{k\delta}$ and $e_{k\delta}$ are evaluated at the global temperature T_m corresponding to $\delta \in \mathcal{M}_k^m$.

2.4.2. Formation Enthalpies

In general, it is not possible to calculate or measure species zero-point energies. Fortunately, they are not necessary since only the change in enthalpy is important for modeling thermochemical processes. In particular, the governing equations require the enthalpy gradient to be known and chemical equilibrium constants are based on enthalpy changes across a reaction (see Section 2.6). The *heat of formation* or *formation enthalpy* $\Delta h_{f,i}(T)$ of any substance i is the energy required to create one mole of that substance from its elements in their standard conditions. The standard condition of an element is the form in which it naturally exists at the standard state temperature and pressure (298.15 K and 1 atm). For example, the formation enthalpy of carbon dioxide is the change in enthalpy across the formation reaction

$$\mathrm{C(graphite)} + \mathrm{O_2} \longrightarrow \mathrm{CO_2},$$

where C(graphite) and $\mathrm{O_2}$ are the natural forms of carbon and oxygen atoms at the standard state conditions.

It is trivial to show that the change in formation enthalpies across any reaction is equal to the change in zero-point energies across the same reaction [104]. Therefore, in practice, the zero-point energies e_{k0} in Eqs. (2.54) and (2.59) are replaced with species formation enthalpies at standard state conditions computed relative to reference species with defined formation enthalpies of zero. Reference species are chosen based on the elements in their natural state at standard conditions (i.e.,: $\mathrm{N_2}$, $\mathrm{O_2}$, C(graphite), $\mathrm{H_2}$, Ar, etc.). Note that this is a practical convention used in much of the literature, however using a different convention would not change the underlying equations governing the transport of mass, momentum, and energy.

2.4.3. Mixture Thermodynamic Properties

Mixture thermodynamic quantities are derived from pure species quantities through mixing rules. For a perfect gas, mixture thermodynamic properties are simply the sum of pure species properties weighted by the composition of the mixture. Thus, mixture energies, enthalpy, entropy, and specific heats are given as

$$e = \frac{1}{\rho} \sum_{k \in \mathcal{S}^*} \rho_k e_k, \tag{2.71}$$

$$e^m = \frac{1}{\rho} \sum_{k \in \mathcal{S}^*} \rho_k e_k^m, \quad \forall\, m \in \mathcal{M}, \tag{2.72}$$

$$h = \frac{1}{\rho} \sum_{k \in \mathcal{S}^*} \rho_k h_k, \tag{2.73}$$

$$s = \frac{1}{\rho} \sum_{k \in \mathcal{S}^*} \rho_k (s_k - R_k \ln x_k), \tag{2.74}$$

$$g = \frac{1}{\rho} \sum_{k \in \mathcal{S}^*} \rho_k (g_k - R_k \ln x_k), \tag{2.75}$$

$$c_p^m = \frac{1}{\rho} \sum_{k \in \mathcal{S}^*} \rho_k c_{pk}^m, \quad \forall\, m \in \mathcal{M}, \tag{2.76}$$

$$c_v^m = \frac{1}{\rho} \sum_{k \in \mathcal{S}^*} \rho_k c_{vk}^m, \quad \forall\, m \in \mathcal{M}, \tag{2.77}$$

where the $-R_k \ln x_k$ term in Eqs. (2.74) and (2.75) accounts for the entropy of mixing.

For flows in LTE, the mixture composition is a function of a single temperature T, pressure p, and elemental mole fractions. Under these conditions, the composition's dependence on temperature must be taken into account in the formulation of specific heats. The equilibrium specific heat at

constant pressure is thus

$$c_{p,\mathrm{eq}} \equiv \left(\frac{\partial h}{\partial T}\right)_p = \sum_{k\in\mathcal{S}^*}\left[y_k c_{pk} + h_k\left(\frac{\partial y_k}{\partial T}\right)_p\right], \tag{2.78}$$

where $y_k = \rho_k/\rho$ is the mass fraction of species k, evaluated at equilibrium. The first term in the sum of Eq. (2.78) is call the "frozen" specific heat since it matches the specific heat of a non-LTE mixture in which the composition is taken as constant or frozen. The second term is called the "reactive" specific heat as it accounts for chemical reactions in equilibrium. The equilibrium specific heat at constant volume is similarly written as

$$\begin{aligned} c_{v,\mathrm{eq}} &\equiv \left(\frac{\partial e}{\partial T}\right)_V = \sum_{k\in\mathcal{S}^*}\left[y_k c_{vk} + e_k\left(\frac{\partial y_k}{\partial T}\right)_V\right] \\ &= c_{p,\mathrm{eq}} + \left[\frac{p}{\rho^2} - \left(\frac{\partial e}{\partial p}\right)_T\left(\frac{\partial p}{\partial \rho}\right)_T\right]\left(\frac{\partial \rho}{\partial T}\right)_p, \end{aligned} \tag{2.79}$$

where the second relation in terms of $c_{p,\mathrm{eq}}$ is provided for convenience. Note that for an ideal gas, $\rho = pM_{\mathrm{mix}}/(R_u T)$, and thus at equilibrium

$$\frac{\partial \rho}{\partial p} = \frac{\rho}{M_{\mathrm{mix}}}\sum_{i\in\mathcal{S}^*} M_i \frac{\partial x_i}{\partial p} + \frac{\rho}{p}. \tag{2.80}$$

The equilibrium mole and mass fraction derivatives in Eqs. (2.78) and (2.80) may be easily obtained from the solution of the equilibrium mole fractions. See Chapter 5 for more details.

2.5. Transport

Closure of the transport fluxes is achieved through a multiscale Chapman-Enskog perturbative solution of the Boltzmann equation [98, 105]. Graille *et al.* [100] have derived a rigorous kinetic model for multicomponent plasmas accounting for the influence of the electromagnetic field and thermal nonequilibrium between free electrons and heavy particles. They showed through a dimensional analysis that the correct scaling of the Boltzmann equation is obtained by using a scaling parameter equal to the square-root of the ratio between the electron mass and a characteristic heavy-particle mass. Magin *et al.* [106] have provided explicit expressions for the transport coefficients in terms of binary collision integrals based on the approach in [107] for weakly ionized and unmagnetized plasmas. These works have neglected the treatment of internal energy in the transport systems. Treatment of internal energy is presented in the book of Giovangigli [99]. In addition, Nagnibeda and Kustova [101] have proposed a transport theory accounting for internal energy and thermal nonequilibrium effects. In this work, the transport of internal energy is treated simply by neglecting inelastic collisions.

2.5.1. Stress Tensor

The viscous stress tensor in Eq. (2.33) is defined as

$$\bar{\boldsymbol{\Pi}} = \eta\left[\boldsymbol{\nabla u} + (\boldsymbol{\nabla u})^T - \frac{2}{3}\boldsymbol{\nabla}\cdot\boldsymbol{u}\bar{\boldsymbol{I}}\right] + \kappa\boldsymbol{\nabla}\cdot\boldsymbol{u}\bar{\boldsymbol{I}} - p^{\mathrm{reac}}\bar{\boldsymbol{I}}. \tag{2.81}$$

where η and κ are the dynamic (shear) and bulk (volume) mixture viscosities and p^{reac} is called the chemical pressure. For STS models, the bulk viscosity is zero. Bruno and Giovangigli [108] provide an important discussion of the various effects contributing to the bulk viscosity in nonequilibrium plasmas. This term is nearly always neglected in hypersonic flow calculations under the assumption that $\kappa/\eta \ll 1$. However, Giovangigli *et al.* [109] have shown that this assumption is not always

valid for larger polyatomic gases. The chemical pressure is given by

$$p^{\text{reac}} = \sum_{r \in \mathcal{R}} \mathfrak{y}_r \mathfrak{R}_r, \tag{2.82}$$

where $\mathfrak{y}_r$ and $\mathfrak{R}_r$ are the chemical pressure coefficient and the net rate of progress for reaction r, respectively. For gases in the Maxwellian regime, the chemical pressure term vanishes in the viscous stress tensor and is generally thought to be small in comparison to the other terms. In this work, both bulk viscosity and chemical pressure effects are neglected.

The dynamic viscosity η is obtained from the first Laguerre-Sonine polynomial approximation of the Chapman-Enskog expansion. The resulting expression requires the solution of the linear system

$$\begin{aligned} \eta &= \sum_{i \in \mathcal{H}^*} \alpha_i^\eta x_i, \\ \sum_{j \in \mathcal{H}^*} G_{ij}^\eta \alpha_j^\eta &= x_i \quad \forall\, i \in \mathcal{H}^*, \end{aligned} \tag{2.83}$$

where G_{ij}^η is the viscosity transport matrix depending on the species mole fractions and binary collision integrals, detailed in Appendix A. Notice that electrons do not contribute to mixture viscosity due to the mass disparity with heavy particles.

2.5.2. Diffusion Fluxes

Species diffusion velocities can be obtained from the multicomponent diffusion coefficient matrix D_{ij} by

$$\boldsymbol{V}_i = -\sum_{j \in \mathcal{S}^*} D_{ij} \left(\boldsymbol{d}_j + \chi_j^h \boldsymbol{\nabla} \ln T_h + \chi_j^e \boldsymbol{\nabla} \ln T_e \right), \tag{2.84}$$

where $\boldsymbol{d}_j$ are the species specific driving forces defined as

$$\boldsymbol{d}_j = \frac{\boldsymbol{\nabla} p_j}{n k_B T_h} - \frac{y_j p}{n k_B T_h} \boldsymbol{\nabla} \ln p - \kappa_j \boldsymbol{E} \tag{2.85}$$

with $\kappa_j \equiv x_j q_j / (k_B T_h) - y_j q / (k_B T_h)$, $q = \sum_{i \in \mathcal{S}} x_i q_i$ is the mixture charge, and $\boldsymbol{E}$ is the electric field. The species diffusion fluxes, $J_i = \rho_i \boldsymbol{V}_i$, satisfy the mass conservation constraint, such that $\sum_{i \in \mathcal{S}^*} J_i = 0$. Furthermore, the driving forces and κ_i values are linearly dependent, namely $\sum_{i \in \mathcal{S}^*} \boldsymbol{d}_i = 0$ and $\sum_{i \in \mathcal{S}^*} \kappa_i = 0$.

An equivalent formulation of the species diffusion velocities are found from the solution of the generalized Stefan-Maxwell equations [110],

$$\sum_{j \in \mathcal{S}^*} G_{ij}^V \boldsymbol{V}_j = -\boldsymbol{d}_i' + \kappa_i \boldsymbol{E}, \quad \forall\, i \in \mathcal{H}^*, \tag{2.86}$$

$$\sum_{j \in \mathcal{S}^*} G_{ej}^V \boldsymbol{V}_j = -\left(\boldsymbol{d}_e' + \kappa_e \boldsymbol{E} \right) \frac{T_h}{T_e}, \tag{2.87}$$

where the modified driving forces are

$$\boldsymbol{d}_j' = \frac{\boldsymbol{\nabla} p_j}{n k_B T_h} - \frac{y_j p}{n k_B T_h} \boldsymbol{\nabla} \ln p + \chi_j^h \boldsymbol{\nabla} \ln T_h + \chi_j^e \boldsymbol{\nabla} \ln T_e. \tag{2.88}$$

The multicomponent diffusion coefficient matrix D_{ij} and the diffusion transport system matrix G_{ij}^V are functions of the species binary collision integrals and compositions. The exact expressions for these matrices are given in Appendix A.

2.5.3. Heat Flux

The heat flux vector in Eq. (2.35) accounts for the energy transferred through diffusion, thermal diffusion, and conduction, such that

$$\boldsymbol{q} = \sum_{k\in\mathcal{S}^*} \rho_k h_k \boldsymbol{V}_k + nk_B T_h \sum_{k\in\mathcal{S}^*} \left(\chi_k^h + \chi_k^e\right)\boldsymbol{V}_k - \sum_{m\in\mathcal{M}} \lambda_m \boldsymbol{\nabla} T_m, \tag{2.89}$$

where χ_k^h and χ_k^e are heavy particle thermal diffusion ratios for pseudo-species $k \in \mathcal{S}^*$ and $\lambda_m = \lambda_m^t + \lambda_m^{\text{int}}$ is the effective thermal conductivity of the global energy mode $m \in \mathcal{M}$ which can be split into translational λ_m^t and internal λ_m^{int} components. From the assumption in Section 2.3.2 that heavy particles thermalize at temperature T_h and electrons at T_e, the translational thermal conductivities can be written as

$$\lambda_m^t = \alpha_m^h \lambda_h + \alpha_m^e \lambda_e, \tag{2.90}$$

where λ_h and λ_e are the thermal conductivities associated with translation of heavy particles and electrons, respectively, and the constants α_m^h and α_m^e indicate whether or not the global mode $m \in \mathcal{M}$ includes translational energy of heavy particles and electrons, respectively. Thus, $\alpha_m^h = 1$ when heavy particle translational energy is included in the thermal bath m, and $\alpha_m^h = 0$ otherwise. Likewise, $\alpha_m^e = 1$ when free-electron translational energy is included in the thermal bath m, and $\alpha_m^e = 0$ otherwise.

The electron heat flux from Eqs. (2.39) and (2.40) and internal energy heat flux from Eq. (2.42) are given as,

$$\boldsymbol{q}_e = \rho_e h_e \boldsymbol{V}_e + nk_B T_h \sum_{k\in\mathcal{S}^*} \chi_k^e \boldsymbol{V}_k - \lambda_e \boldsymbol{\nabla} T_e, \tag{2.91}$$

$$\boldsymbol{q}_m = \sum_{k\in\mathcal{S}^*} \rho_k h_k^m \boldsymbol{V}_k - \lambda_m \boldsymbol{\nabla} T_m, \tag{2.92}$$

where the flux $\boldsymbol{q}_m$ in Eq. (2.92) is valid only for purely internal energy modes ($\alpha_m^h = \alpha_m^e = 0$).

The heavy particle translational thermal conductivity is obtained from the second order Laguerre-Sonine polynomial approximation of the Chapman-Enskog expansion. The resulting expression requires the solution of the linear system similar to that of the dynamic viscosity,

$$\begin{aligned} \lambda_h &= \sum_{i\in\mathcal{H}^*} \alpha_i^{\lambda_h} x_i, \\ \sum_{j\in\mathcal{H}^*} G_{ij}^{\lambda_h} \alpha_j^{\lambda_h} &= x_i \quad \forall\, i \in \mathcal{H}^*. \end{aligned} \tag{2.93}$$

The transport matrix $G_{ij}^{\lambda_h}$ is given in Appendix A and is a function of species mole fractions and binary collision integrals.

Heavy particle thermal diffusion ratios may then be computed via

$$\chi_i^h = \frac{5}{2} \sum_{j\in\mathcal{H}^*} \Lambda_{ij}^{01} \alpha_j^{\lambda_h}, \quad \forall i \in \mathcal{H}^* \tag{2.94}$$

$$\chi_e^h = 0, \tag{2.95}$$

where Λ_{ij}^{01} is another transport matrix based on binary collision integrals and α^{λ_h} is obtained from the solution of the linear system in Eq. (2.93). Heavy particle thermal diffusion ratios satisfy the expression $\sum_{i\in\mathcal{H}^*} \chi_i^h = 0$. Note that free electrons do not contribute to the mixture viscosity, heavy particle thermal conductivity, or the heavy particle thermal diffusion ratios.

Expressions for the electron thermal conductivity, λ_e, and thermal diffusion ratios, χ_i^e, may be obtained from second or third order Laguerre-Sonine approximations (denoted by (2) or (3)) and

are given by

$$\lambda_e(2) = \frac{x_e^2}{\Lambda_{ee}^{11}}, \tag{2.96}$$

$$\lambda_e(3) = \frac{x_e^2 \Lambda_{ee}^{22}}{\Lambda_{ee}^{11}\Lambda_{ee}^{22} - \left(\Lambda_{ee}^{12}\right)^2}, \tag{2.97}$$

and

$$\chi_i^e(2) = \frac{5}{2}\frac{T_e}{T_h} x_e \frac{\Lambda_{ie}^{01}}{\Lambda_{ee}^{11}} \quad \forall\, i \in \mathcal{S}^*, \tag{2.98}$$

$$\chi_i^e(3) = \frac{5}{2}\frac{T_e}{T_h} x_e \frac{\Lambda_{ie}^{01}\Lambda_{ee}^{22} - \Lambda_{ie}^{02}\Lambda_{ee}^{12}}{\Lambda_{ee}^{11}\Lambda_{ee}^{22} - (\Lambda_{ee}^{12})^2} \quad \forall\, i \in \mathcal{S}^*. \tag{2.99}$$

The Λ_{ie}^{lk} and Λ_{ee}^{lk} matrices are complex functions of the binary collision integrals for heavy-electron and electron-electron interactions. The electron thermal diffusion ratios satisfy the relation $\sum_{i\in\mathcal{H}^*} \chi_i^e + \chi_e^e T_e/T_h = 0$. Magin *et al.* [106] have studied the convergence of the λ_e and χ_i^e due to the Laguerre-Sonine order and found that differences can exist in the levels of approximation even in plasmas with relatively low degrees of ionization. Therefore, the third order expressions should be used in practice.

Finally, the thermal conductivity associated with the internal energy of mode $m \in \mathcal{M}$, is given by the so called Euken corrections, such that

$$\lambda_m^{\text{int}} = \sum_{k\in\mathcal{H}^*} \frac{\rho_i c_{pk}^{m,\text{int}}}{\sum_{j\in\mathcal{H}^*} x_j/\mathscr{D}_{kj}}, \tag{2.100}$$

where $\mathscr{D}_{kj}$ is the binary diffusion coefficient for pseudo-species k and j, defined in Appendix A, and the internal specific heat for mode m has been defined as

$$c_{pk}^{m,\text{int}} = \sum_{\delta\in\mathcal{M}_k^{m,\text{int}}} \left(\frac{\partial h_{k\delta}}{\partial T_{k\delta}}\right)_p, \tag{2.101}$$

where $\mathcal{M}_k^{m,\text{int}} = \mathcal{M}_k^m \cap \mathcal{M}_k^{\text{int}}$ indicates the intersection of sets $\mathcal{M}_k$ and $\mathcal{M}_k^{\text{int}}$. It can be shown that the Euken corrections are exact when the internal energy modes are separable and inelastic collisions are neglected [107].

2.6. Chemical Kinetics

Chemistry plays a major role in the accurate description of hypersonic flows. This section details the important chemical kinetic models relevant to hypersonics and how they fit into the governing equations described in Section 2.3. In the first subsection, a description of the species production rates for flows in thermal equilibrium is presented. The effects of thermal nonequilibrium are then discussed. Finally, the relevant models used to simulate heterogeneous chemistry at the surface of an ablating heat shield are briefly introduced.

2.6.1. Homogeneous Chemistry (Gas Phase)

The chemical production source term found in Eq. (2.27) accounts for the production and destruction of individual species through elementary chemical reactions. Every elementary (single-step) chemical reaction r, in the set of reactions $\mathcal{R}$, can be described through the general formula,

$$\sum_{k\in\mathcal{S}^*} \nu_{kr}^{'} \mathrm{A}_k \rightleftharpoons \sum_{k\in\mathcal{S}^*} \nu_{kr}^{''} \mathrm{A}_k,$$

where $\nu_{kr}^{'}$ and $\nu_{kr}^{''}$ are the forward and reverse stoichiometric coefficients for species A_k in reaction r. As an example, for the water-gas shift reaction,

$$CO + H_2O \longrightarrow CO_2 + H_2,$$

the forward stoichiometric coefficients of CO and H_2O and the reverse stoichiometric coefficients of CO_2 and H_2 are all equal to unity, while all other stoichiometric coefficients are zero. For elementary reactions, the overall order of a reaction is the sum of the reactant stoichiometric coefficients.

A rigorous derivation of the chemical production rate from kinetic theory yields an expression of the form,

$$\dot{\omega}_k = \dot{\omega}_k^0 + \dot{\omega}_k^1, \tag{2.102}$$

where $\dot{\omega}_k^0$ is the zero-order Maxwellian production rate and $\dot{\omega}_k^1$ is a first-order perturbation [111]. The structure of the first-order term has been studied by Giovangigli [99] for general reacting mixtures in the strong reaction regime and is found to be a sum of quadratics in the forward and backward rates of progress for each reaction plus a linear term in the rates of progress multiplied by the velocity divergence. Estimates for several simplified cases has shown $\dot{\omega}_k^1$ to be small compared to the zero-order term [112–116] and it is typically neglected in CFD calculations. In the Maxwellian regime, $\dot{\omega}_k^1$ is exactly zero.

Law of Mass Action

Zero-order production rates are compatible with the *Law of Mass Action* which states that the rate of production of a reaction product is proportional to the product of the reactant densities raised to their stoichiometric coefficients [117]. For example, the rate of change of the number density of carbon dioxide in the water-gas shift reaction, may be written as

$$\frac{\partial}{\partial t}(n_{CO_2}) = k_f \; n_{CO} \; n_{H_2O},$$

where the proportionality constant k_f is called the reaction rate coefficient and is not a function of the reactant densities. The subscript f denotes that the rate coefficient is for the "forward" process.

In general, reactions are reversible and the reverse process must be taken into account. The molar rate-of-progress for any homogeneous reaction r is given as

$$\mathfrak{R}_r = k_{f,r} \prod_{j \in \mathcal{S}^*} \hat{\rho}_j{}^{\nu_{jr}^{'}} - k_{b,r} \prod_{j \in \mathcal{S}^*} \hat{\rho}_j{}^{\nu_{jr}^{''}}, \tag{2.103}$$

which represents the net rate of moles of reactants which are destroyed to form products with units of mol/m^3s. $\hat{\rho}_j = \rho_j / M_j$ is the molar density or concentration of species j and $k_{b,r}$ represents the backward reaction rate coefficient for reaction r. At equilibrium, the rate-of-progress of all reactions is zero, which yields the following relationship between the forward and backward rate coefficients,

$$\frac{k_{f,r}}{k_{b,r}} \equiv K_{eq,r} = \prod_{j \in \mathcal{S}^*} (\hat{\rho}_j^*)^{(\nu_{jr}^{''} - \nu_{jr}^{'})}, \tag{2.104}$$

where $K_{eq,r}$ is called the equilibrium constant for reaction r and the superscript $*$ on the species concentrations is used to denote equilibrium quantities. The equilibrium constant is related to the change in Gibbs free energy across a reaction ΔG_r° by

$$K_{eq,r} = \left(\frac{p^\circ}{R_u T} \right)^{\Delta \nu_r} \exp\left(- \frac{\Delta G_r^\circ}{R_u T} \right), \tag{2.105}$$

where $\Delta \nu_r = \sum_{j \in \mathcal{S}^*} (\nu_{jr}^{''} - \nu_{jr}^{'})$ is the difference in reaction orders in the forward and reverse

directions and $\Delta G_r^\circ = \sum_{j\in\mathcal{S}^*}(\nu_{jr}^{''} - \nu_{jr}^{'})G_j^\circ$ is the change in Gibbs energy across the reaction, where G_j° is the standard state molar Gibbs energy of species j, and R_u is the universal gas constant. The left-hand-side of Eq. (2.104) is only a function of temperature while the right-hand-side is only a function species concentrations. Therefore, Eq. (2.104) remains valid under all conditions, not just at chemical equilibrium.

Using Eq. (2.103), the total mass production rate for a species k due to all reactions considered is readily given by

$$\dot{\omega}_k = M_k \sum_{r\in\mathcal{R}} (\nu_{kr}^{''} - \nu_{kr}^{'})\, \mathfrak{R}_r, \quad k \in \mathcal{S}^*. \tag{2.106}$$

The difference in backward and forward stoichiometry coefficients in Eq. (2.106) relates the number of moles of species k created or destroyed by the reaction r to the molar rate-of-progress for that reaction.

Rate coefficients

For second- and third-order reactions, the rate coefficient depends on

1. the frequency of collisions between reactants,
2. the fraction of such collisions with sufficient energy for the reaction, and
3. the fraction of those collisions which actually react.

First-order reactions, such as predissociation (for example $N_2 \longrightarrow 2\,N$), do not depend on the collision rate as these reactions occur spontaneously. Instead, the rate coefficients depend on the energy of the reactant above some threshold energy. For example, predissociation occurs when a molecule in a quasi-bound vibrational energy state, above the dissociation energy level, spontaneously dissociates.

For the majority of reactions of interest in hypersonics, the reaction rate coefficients may be expressed as

$$k_f(T) = AT^\beta \exp\left(-\frac{E_a}{R_u T}\right), \tag{2.107}$$

where the pre-exponential term represents the temperature dependence of the collision frequency and the exponential term, called the Boltzmann factor, specifies the fraction of collisions with energy greater than the activation energy of the reaction, E_a. Eq. (2.107) is called the (modified) *Arrhenius rate law* after the Swedish physicist Svante Arrhenius who originally proposed the dependence of the reaction rate on the activation energy of the reaction. While the formula has some theoretical basis, the rate constants A, β, and E_a are usually determined experimentally as their theoretical values often do not provide sufficient accuracy. This is largely due to the difficulty in describing the third dependency of the rate coefficient listed above, namely the fraction of collisions with sufficient energy that actually cause a reaction (embedded in the constant A). This fraction is called the steric factor and depends on the collision dynamics and relative orientation of the reacting species.

A promising alternative to the experimentally determined rate coefficients are those integrated from effective reaction cross sections, based on QCT calculations using accurate PESs from quantum mechanics. For example, statistical mechanics provides the following expression for the state-to-state rate coefficient k_f for a reaction going from initial state i to final state j [79],

$$k_f(T_h) = \frac{1}{3}(2R_u T_h)^{\frac{3}{2}}(\mu\pi)^{-\frac{1}{2}} \int_0^\infty \sigma_{ij}(E_i) E_i \exp\left(-\frac{E_i}{R_u T_h}\right) dE_i, \tag{2.108}$$

where σ_{ij} is the effective cross section of reaction as a function of the translational energy of the initial state E_i. Rate coefficients computed in this way could be tabulated versus temperature or fitted to an Arrhenius form for efficient use in hypersonic CFD codes.

Third-body reactions

Some reactions require an additional species to provide or remove energy from the reactants, though the species remains inert. Consider, for example, the heavy-particle impact dissociation of the nitrogen molecule by collisions with N and O atoms,

$$\begin{aligned} \mathrm{N_2 + N} &\rightleftharpoons \mathrm{N + N + N}, \\ \mathrm{N_2 + O} &\rightleftharpoons \mathrm{N + N + O}. \end{aligned}$$

In this case, N and O are called third bodies and provide the necessary energy for N_2 to overcome its dissociation energy and dissociate. Likewise, in the reverse direction, the third-body species remove sufficient energy from the two N atoms and allow them to recombine. It is common to denote a generic third-body species in a chemical reaction with the letter M, such that

$$\mathrm{N_2 + M} \rightleftharpoons \mathrm{N + N + M}$$

represents all heavy-particle impact nitrogen dissociation reactions.

Each third body considered in a third-body reaction represents a unique elementary chemical pathway. However, the activation energy required in a given third-body reaction is the same, regardless of which third-body provides that energy. It is therefore common to assume that the rate coefficients associated with the reactions of different third bodies differ only by a constant factor. Upon simple review of Eqs. (2.103) and (2.104), this allows the net rate-of-progress for a third-body reaction, considering all third bodies, to be written as

$$\mathfrak{R}_r = \left[k_{f,r} \prod_{j \in \mathcal{S}^*} \hat{\rho}_j{}^{\nu'_{jr}} - k_{b,r} \prod_{j \in \mathcal{S}^*} \hat{\rho}_j{}^{\nu''_{jr}} \right] \sum_{j \in \mathcal{S}^*} \alpha_{jr} \hat{\rho}_j, \tag{2.109}$$

where the stoichiometric coefficients are only assigned to non third-body species. The constant α_{jr} parameters are called third-body efficiency factors and represent the ratio of the forward reaction rate coefficient associated with the third body j to the reference rate coefficient $k_{f,r}$. Evaluating the rates-of-progress for third-body reactions in this way can significantly decrease the size of a given reaction mechanism as well as the time necessary to compute the species chemical production rates.

2.6.2. Effect of thermal nonequilibrium on reaction rates

For strong nonequilibrium flows, the distribution of internal energy states can play an important role in the description of kinetic rates. The most accurate method for treating nonequilibrium rates is with a full STS model, like those described in Section 2.2.4. However, since such models remain prohibitively expensive from a computational standpoint, most hypersonic CFD codes rely on MT models. For this reason, an extensive literature exists on the study of nonequilibrium reaction kinetics and many models have been proposed, in particular for the dissociation of oxygen and nitrogen molecules (i.e., [58, 60, 90, 91, 118–127]).

In general, nonequilibrium models multiply the equilibrium rate coefficient by a nonequilibrium factor Φ,

$$k_f(T_f, T_{\mathrm{int}}) = k_f^{\mathrm{eq}}(T_f)\ \Phi(T_f, T_{\mathrm{int}}), \tag{2.110}$$

where $k_f^{\mathrm{eq}}(T_f)$ represents the forward rate coefficient in thermal equilibrium as discussed in the previous section, evaluated at the heat-bath temperature T_f, and Φ is a function of T_f and an internal temperature T_{int}. At thermal equilibrium, $\Phi = 1$. Classically, the temperature T_f represents the temperature of the thermal bath which provides the energy for the reaction to proceed. For third-body reactions, the translational energy of the inert particle is typically chosen as the thermal bath. Thus, for heavy-particle impact reactions, generally $T_f = T_h$, while for electron-impact reactions the convention is $T_f = T_e$. For some reactions, the choice of T_f remains an active area of research. The dependence of Eq. (2.110) on an internal temperature T_{int} relies on the type of reaction considered and in some cases, T_{int} may represent more than one temperature.

Table 2.1.: *Summary of important homogeneous chemical processes occurring in hypersonics. Reaction formulas represent general processes. State-specific reactions include indices in parentheses to indicate electronic/rovibronic states. The associated forward and backward temperatures used to evaluate reaction rates for each general process are also given.*

Reaction	T_f	T_b
Associative ionization and dissociative recombination		
$\mathrm{A} + \mathrm{B} \rightleftharpoons \mathrm{AB}^+ + \mathrm{e}^-$	T_h	T_e
Charge exchange		
$\mathrm{A}^+ + \mathrm{B} \rightleftharpoons \mathrm{A} + \mathrm{B}^+$	T_h	T_h
Electron impact dissociation and recombination		
$\mathrm{AB} + \mathrm{e}^- \rightleftharpoons \mathrm{A} + \mathrm{B} + \mathrm{e}^-$	T_e	T_e
Electron impact excitation and de-excitation		
$\mathrm{A(i)} + \mathrm{e}^- \rightleftharpoons \mathrm{A(j)} + \mathrm{e}^-,\ \mathrm{j} > \mathrm{i}$	T_e	T_e
Electron impact ionization and ion recombination		
$\mathrm{A} + \mathrm{e}^- \rightleftharpoons \mathrm{A}^+ + \mathrm{e}^- + \mathrm{e}^-$	T_e	T_e
Electronic attachment and detachment		
$\mathrm{A} + \mathrm{e}^- + \mathrm{M} \rightleftharpoons \mathrm{A}^- + \mathrm{M}$	T_e	T_h
Exchange		
$\mathrm{AB} + \mathrm{CD} \rightleftharpoons \mathrm{AC} + \mathrm{BD}$	T_h	T_h
Heavy particle impact dissociation and recombination		
$\mathrm{AB} + \mathrm{M} \rightleftharpoons \mathrm{A} + \mathrm{B} + \mathrm{M}$	$T_h^q T_v^{1-q}$	T_h
Heavy particle impact excitation and de-excitation		
$\mathrm{A(i)} + \mathrm{M} \rightleftharpoons \mathrm{A(j)} + \mathrm{M},\ \mathrm{j} > \mathrm{i}$	T_h	T_h
Heavy particle impact ionization and ion recombination		
$\mathrm{A} + \mathrm{M} \rightleftharpoons \mathrm{A}^+ + \mathrm{e}^- + \mathrm{M}$	T_h	T_h

The nonequilibrium backward rate coefficient is typically evaluated using the equilibrium constant from Eq. (2.104), such that

$$k_b(T_b) = \frac{k_f^{\mathrm{eq}}(T_b)}{K_{\mathrm{eq}}(T_b)}, \tag{2.111}$$

where T_b is the temperature describing the thermal bath for the reverse process. A summary of important reaction types and the choice of temperatures used in this work for T_f and T_b are shown in Table 2.1. Some of the commonly used models for the nonequilibrium factor for several reactions are presented in the following subsections.

Dissociation and recombination

Molecules with a higher vibrational state require less translational energy to dissociate than those at lower lying vibrational energy levels. Thus, the distribution of vibrational energy states of a molecule can have a large impact on the average rate at which the molecule dissociates. Dissociation models are typically split into two groups: preferential and non-preferential dissociation. Preferential dissociation assumes that molecules at high vibrational states are more likely to dissociate than those at lower states. Thus, molecules at low lying vibrational states must "ladder-climb" to higher vibrational states through excitation processes before being allowed to dissociate. Preferential dissociation models result in an incubation period behind strong shock waves in which the vibrational energy builds up before molecules can dissociate. In effect, this serves to lengthen the nonequilibrium zone and shock stand-off distances. Conversely, non-preferential models impose

the same likelihood that a molecule will dissociate from all vibrational levels. Three important nonequilibrium models for dissociation and recombination are presented here.

Marrone and Treanor [119], building on the work on Hammerling *et al.* [118] for non-preferential dissociation, derived an expression for the nonequilibrium factor assuming that higher vibrational energy levels were more likely to dissociate. The resulting expression may be written as

$$\Phi(T_h, T_v) = \frac{Q_j^v(T_h)\, Q_j^v(T_F)}{Q_j^v(T_v)\, Q_j^v(-U)}, \tag{2.112}$$

$$\frac{1}{T_F} = \frac{1}{T_v} - \frac{1}{T_h} - \frac{1}{U}, \tag{2.113}$$

where U is a fictitious temperature used to adjust the probability of dissociation from a given vibrational energy level and is usually taken to be $U = D/3k_B$ and D is the dissociation energy of the molecule. Under thermal equilibrium, $T_v = T_h$ and $T_F = -U$ such that $\Phi(T_h, T_v) = 1$ as expected. When $U = \infty$, the non-preferential model of Hammerling is obtained. Q_j^v represents the partition function for a truncated harmonic-oscillator. According to Marrone and Treanor, the negative value $-U$ represents the "vibrational temperature" at which molecules are formed by recombination.

Park [58, 60] developed a simple phenomenological model to describe the nonequilibrium dissociation of nitrogen which remains widely used today. When applied to the Arrhenius rate law, Eq. (2.107), Park's model is given as

$$\Phi(T_h, T_v) = T_a^{\beta} {T_h}^{-\beta} \exp\left(\frac{E_a}{R_u T_h} - \frac{E_a}{R_u T_a}\right), \tag{2.114}$$

where $T_a = {T_h}^q {T_v}^{1-q}$, for $0 \leq q \leq 1$, is an "average" temperature. Park originally suggested to use a geometric mean such that $q = 0.5$, though this was later improved by Sharma [120] to $q = 0.7$ in order to better match experimental data. Typically, this model is implemented by treating $\Phi = 1$ and simply evaluating the equilibrium rate coefficient with $T_f = T_a$. It is well known that Park's model substantially under predicts dissociation rates when $T_v \ll T_h$, however it remains a popular choice in hypersonic CFD codes because of its simplicity.

Finally, Macheret [123, 124, 127] derived a model based on the assumption of impulsive collisions and rigid-rotor harmonic oscillators. The resulting expression for the nonequilibrium factor may be written as

$$\Phi(T_h, T_r, T_v) = \frac{1}{k_f^{\text{eq}}(T_h)}\Big[k_l(T_h, T_r, T_v) + k_h(T_v)\Big], \tag{2.115}$$

$$k_l(T_h, T_r, T_v) \propto \exp\left[-\frac{D}{T_a} + 6\alpha^2 D\left(\frac{1}{T_a} - \frac{1}{T_h}\right)\right], \tag{2.116}$$

$$k_h(T_v) \propto \exp\left(-\frac{D}{T_v}\right), \tag{2.117}$$

where k_l and k_h represent the contribution of low and high vibrational energy levels of the dissociating molecule to the dissociation rate coefficient, $T_a = \alpha T_v + (1-\alpha)T_k$ is an "average" temperature, $T_k = (T_h + \sqrt{\alpha}T_r)/(1 + \sqrt{\alpha})$ is the "kinetic" temperature, and α is a simple factor related to the masses of the colliding species. The proportionality factors which complete the expressions for the low and high rate coefficients depend on the type of collision partners involved (diatom-diatom or diatom-atom) and are described in detail in [124]. Macheret's model has been shown to accurately describe nitrogen dissociation rates under nonequilibrium conditions as compared to those obtained to detailed STS rates [128]. Furthermore, the model does not require any tuned or empirically derived parameters, which represents a major advantage to the models of Park and Treanor and Marrone.

Other reactions

The effect of internal energy on nonequilibrium reaction rates is typically modeled for dissociation reactions only due to the important role they play behind strong shock waves. However, models also exist for other types of reactions as well. For example, Knab *et al.* [122, 125] have developed expressions similar to those described above for dissociation reactions which model the nonequilibrium factor for exchange, associative ionization, and electron impact ionization and dissociation reactions. These expressions are not given here for the sake of brevity.

2.6.3. Heterogeneous Chemistry (Gas-Surface Interaction)

As with homogeneous chemistry mechanisms, heterogeneous chemistry plays an important role in the description of the thermochemical environment surrounding hypersonic vehicles. In particular, an accurate prediction of the heat flux to the surface of a vehicle may depend strongly on the correct solution of catalysis and ablation processes occurring at the gas-surface interface, known in general as gas-surface interactions (GSI). These processes may strongly affect the composition of the boundary layer, which in turn may alter the convective or radiative heating at or near the vehicle surface. For Martian entries, these effects have also been shown to be important down stream as ablated species radiate and increase the radiative flux to the back-shell of the vehicle. Typically, GSI models are implemented as boundary conditions along the vehicle surface. In this section, the relevant heterogeneous chemical processes and the corresponding models used to simulate them are reviewed.

For non-ablating thermal protection systems, catalysis may play an important role in the heating to the surface of the TPS. In particular, for Earth entries, catalytic recombination of the N_2, O_2, and NO at the surface,

$$\begin{aligned} \mathrm{N} + \mathrm{N} &\rightleftharpoons \mathrm{N_2}, \\ \mathrm{O} + \mathrm{O} &\rightleftharpoons \mathrm{O_2}, \\ \mathrm{N} + \mathrm{O} &\rightleftharpoons \mathrm{NO}, \end{aligned}$$

are well known. Catalytic reactions do not participate in the surface mass balance but can promote substantial heat transfer. As an example, the reactions shown above release approximately 950, 500, and 630 kJ per mole of product, respectively [129].

Surface participating reactions involve both heat and mass transfer between the surface and surrounding gas. As such, these reactions always include reactants originating from the TPS material. Examples include the nitridation or oxidation of solid carbon C(s),

$$\begin{aligned} \mathrm{C(s)} + \mathrm{N} &\rightleftharpoons \mathrm{CN}, \\ \mathrm{C(s)} + \mathrm{O} &\rightleftharpoons \mathrm{CO}, \\ \mathrm{C(s)} + \mathrm{O_2} &\rightleftharpoons \mathrm{CO_2}, \end{aligned}$$

the passive and active oxidation of silicon carbide,

$$\begin{aligned} \mathrm{SiC(s)} + 2\,\mathrm{O_2} &\rightleftharpoons \mathrm{SiO_2(s)} + \mathrm{CO_2}, \\ \mathrm{SiC(s)} + 3\,\mathrm{O} &\rightleftharpoons \mathrm{SiO_2(s)} + \mathrm{CO}, \\ \mathrm{SiC(s)} + \mathrm{O_2} &\rightleftharpoons \mathrm{SiO} + \mathrm{CO}, \\ \mathrm{SiC(s)} + 2\,\mathrm{O} &\rightleftharpoons \mathrm{SiO} + \mathrm{CO}, \end{aligned}$$

and the sublimation of solid carbon to form C, C_2, or C_3. In general, there are two types of models which are used to describe surface chemistry and these are discussed below.

Specified reaction efficiency models

Perhaps the most widely used GSI model in hypersonics is the Specified Reaction Efficiency (SRE) model. These models describe the mass production rate of a species at the surface as the product of the mass flux of the reactant impinging on the surface Γ_i and a reaction efficiency γ_r which takes a value between 0 and 1. For example, the surface mass production rate of O and O_2 (in kg/ms) as a result of the catalytic recombination reaction $O + O \longrightarrow O_2$ is given as

$$\dot{\omega}_O = -\gamma_O \Gamma_O = -\gamma_O \frac{\rho_O}{4}\sqrt{\frac{8k_B T_h}{\pi m_O}}, \tag{2.118}$$

$$\dot{\omega}_{O_2} = -\frac{\dot{\omega}_O}{2}. \tag{2.119}$$

Note that the production rate of O_2 is half the destruction rate of O since two O atoms are required to form a single O_2 molecule. SRE models are often called "gamma" models because the symbol γ is the typical choice for the reaction efficiency. The surface heat flux associated with the oxygen recombination reaction above is then computed as

$$q_{O_2} = \dot{\omega}_{O_2} E^{\text{diss}}_{O_2}, \tag{2.120}$$

where $E^{\text{diss}}_{O_2}$ is the dissociation energy O_2 in J/kg.

For sublimation, there is no reactant which impinges on the surface. Therefore, the reverse process must be taken into account leading to the following expression for the production rate of C_3 due to the sublimation reaction $C_3(s) \rightleftharpoons C_3$,

$$\dot{\omega}_{C_3} = (\rho^*_{C_3} - \rho_{C_3})\frac{\gamma_{C_3}}{4}\sqrt{\frac{8k_B T_h}{\pi m_{C_3}}}, \tag{2.121}$$

where $\rho^*_{C_3}$ is the equilibrium surface density of C_3. Park *et al.* [69] provide the following expression for the equilibrium C_3 density,

$$\rho^*_{C_3} = M_{C_3} 1.9 \times 10^7 T_w^{-1} \exp\left(-\frac{59410}{T_w}\right), \tag{2.122}$$

where T_w is the wall temperature.

SRE models are widely used in the hypersonics community because of their ease of use and small data requirements. However there are a number of significant drawbacks to such models. For starters, the laws of thermodynamics are not satisfied because most reactions are assumed to be irreversible. With no alternative, these models assume that all of the heat produced (or consumed) by a reaction at the surface is entirely absorbed or provided by the surface itself. In addition, SRE models remain simple to implement for a single reaction, however when multiple reactions are considered which contain the same reactants, care must be taken to ensure that the reaction efficiencies associated with a single reactant do not sum to a value greater than 1. Finally, SRE models do not accurately describe the underlying physics occurring during gas-surface interactions which is discussed in following section. In spite of these issues, the SRE model has been used in this work due to its simplicity (see Chapter 6). To provide contrast to the SRE model however, a higher fidelity class of GSI models is briefly described in the next section.

Finite-rate models

The SRE model presented above assumes that gas-surface reactions occur in a single step, however in reality these reactions are the result of multiple processes which occur at finite rates. In general, surface reactions are only allowed at a finite number of "active sites" on the surface. These active sites are highly dependent on the topology and chemical structure of the surface and are reaction dependent. Fig. (2.2) describes some important GSI elementary processes that may occur. When gaseous species collide with the surface, they may be adsorbed by an available active site. Con-

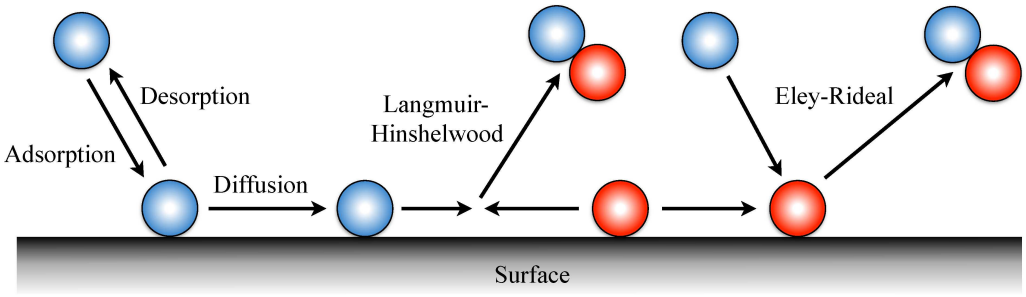

Figure 2.2.: *Idealized gas-surface interactions.*

versely, atoms may desorb from occupied sites to form gaseous species. Adsorbed species may also diffuse along the surface between active sites. A Langmuir-Hinshelwood reaction occurs between two adsorbed species or atoms in the bulk phase which combine and are released as a gaseous molecule. Recombination may also occur through an Eley-Rideal mechanism in which a gaseous species reacts with an adsorbed or bulk species, which is then released from the surface.

Finite-rate surface chemistry models describe the net surface reactions as a series of the elementary processes shown in Fig. (2.2). For example, Marschall *et al.* [129] describe the catalytic recombination of oxygen atoms on a silica surface through the following elementary processes,

$$
\begin{aligned}
&\mathrm{O} + (\mathrm{s}) \rightleftharpoons \mathrm{O}(\mathrm{s}),\\
&\mathrm{O}_2 + (\mathrm{s}) \rightleftharpoons \mathrm{O}_2(\mathrm{s}),\\
&\mathrm{O} + \mathrm{O}(\mathrm{s}) \rightleftharpoons \mathrm{O}_2(\mathrm{s}),\\
&\mathrm{O} + \mathrm{O}(\mathrm{s}) \rightleftharpoons \mathrm{O}_2 + (\mathrm{s}),\\
&\mathrm{O} + \mathrm{O}_2(\mathrm{s}) \rightleftharpoons \mathrm{O}_2 + \mathrm{O}(\mathrm{s}),
\end{aligned}
$$

where (s), O(s), and O_2(s) represent active sites in the bulk phase and absorbed oxygen atom and molecule, respectively. The first two reactions account for the adsorption of oxygen atoms and molecules onto the bulk surface. Each reaction converts an active site in the bulk phase to active sites on adsorbed oxygen atoms. The third reaction represents adsorption of an oxygen atom onto an active O site to form an O_2 site. Finally, the last two reactions represent the Eley-Rideal recombination of oxygen. Each of these processes may occur at different temperature dependent rates. Furthermore, the reverse processes are related to the forward reaction through an equilibrium constant. The heat flux to the surface of a material is then related to the rate of change in the density of active sites. Thus, a finite-rate surface chemistry model ensures the conservation of mass and energy at the surface. However, as can be seen by this simple example, finite-rate models require significantly more data than that required in the SRE models. In addition, the initial distribution of active sites on a surface remains a difficult parameter to determine for most applications. Some finite-rate models assume that the active site density follows a steady-state solution, allowing for this parameter to be determined analytically. A detailed analysis of finite-rate surface chemistry models is beyond the scope of this thesis and thus only this simple discussion is provided.

2.7. Energy Transfer Mechanisms

As previously discussed, nonequilibrium kinetics are most accurately described by full STS models. However, as these models are extremely costly, most CFD codes resort to the use of MT models instead. For such models, the energy transferred between different energy modes is not explicitly determined through the reaction mechanism and must therefore be modeled by the various energy transfer source terms presented in Section 2.3.2. In general, energy transfer mechanisms fall into two categories: energy relaxation processes and chemical energy exchange processes. Both are

described in detail in the following subsections.

2.7.1. Energy relaxation processes

Energy relaxation is the process in which two distributions of energy states exchange energy through elastic and inelastic collisions and "relax" to a final equilibrium distribution. For the MT models, relaxation processes describe the exchange of energy between different energy modes with Boltzmann distributions described by separate temperatures. In general, we are interested in how the average or total energy of one mode equilibrates with another.

Vibration-translation energy exchange

Vibration-translation energy exchange plays a major role in the relaxation behind strong shock waves. We first consider a harmonic-oscillator interacting with a single heat bath of translational energy. The rate of change for this harmonic-oscillator's vibrational energy, measured from the ground state, is written

$$\frac{\partial}{\partial t}(\rho_j e_j^v) = h\nu_j \sum_{i=1}^{\infty} i \frac{\partial}{\partial t}(n_j^i), \tag{2.123}$$

where ν_j represents the characteristic frequency of vibration for species j and $\partial n_j^i/\partial t$ is the rate of change of the number density of vibrational level i due to (de)excitation processes.

For weak binary interactions [56], transitions may be assumed to occur only between neighboring vibrational states. Under these conditions, the following rate equation is then easily derived,

$$\frac{\partial}{\partial t}(n_j^i) = -k_j^{i,i+1}\, n_j^i + k_j^{i+1,i}\, n_j^{i+1} - k_j^{i,i-1}\, n_j^i + k_j^{i-1,i}\, n_j^{i-1}, \tag{2.124}$$

where $k_j^{a,b}$ represents the rate coefficient for the transition from vibrational state a to b for species j. The rate coefficients depend primarily on a) the number of collisions between oscillators and molecules of the heat bath with sufficient energy to cause transition and b) the probability that such a collision results in a transition. For harmonic-oscillators, the rate coefficients are proportional to the vibrational quantum number, $k_j^{i,i-1} = ik_j^{1,0}$ [30]. Thus, using detailed balancing to relate the excitation and deexcitation rate coefficients, Eq. (2.124) may be rewritten as

$$\frac{\partial}{\partial t}(n_j^i) = k_j^{1,0}\left\{ -in_j^i + (i+1)n_j^{i+1} + \exp\left(\frac{\theta_j^v}{T_h}\right)\left[-(i+1)n_j^i + in_j^{i-1}\right]\right\}, \tag{2.125}$$

where $\theta_j^v = h\nu_j/k_B$ is the characteristic vibrational temperature for species j.

Substituting Eq. (2.125) in Eq. (2.123) and simplifying the summation over states yields the Landau-Teller form [130] for vibrational energy relaxation,

$$\frac{\partial}{\partial t}(\rho_j e_j^v) = \rho_j \frac{e_j^{v*}(T_h) - e_j^v}{\tau_j^{\mathrm{VT}}}, \tag{2.126}$$

where $e_j^{v*}(T_h)$ denotes the vibrational energy for a Boltzmann distribution at temperature T_h and $\tau_j^{\mathrm{VT}} = [k_j^{1,0}(1 - \exp(-\theta_j^v/T_h)]^{-1}$ is the relaxation time. Physically, the relaxation time represents the time in seconds required for the difference $(e_j^{v*}(T_h) - e_j^v)$ to fall to $1/e$ of its original magnitude in a constant heat bath. Eq. (2.126) shows that the vibrational energy tends to equilibrate with the translational heat bath at a linear rate which is proportional to the degree of nonequilibrium. It is important to note that no assumptions were made on the distribution of vibrational states in the derivation of Eq. (2.126) or the degree of nonequilibrium. However, the assumption of harmonic-oscillators is only valid for low vibrational states, limiting the validity of the formulation to small departures from equilibrium and relatively low vibrational temperatures.

The theoretical treatment of the relaxation time present in Eq. (2.126) is very difficult. Millikan and White [131] have shown that many diatomic collision systems can be described by the simple

phenomenological formula at low temperatures ($< 8000K$),

$$(1 - x_e)\, p\, \tau_j^{\mathrm{MW}}[\mathrm{atm\,s}] = \sum_{s \in \mathcal{H}} x_s \exp\left[a_{js}(T^{-\frac{1}{3}} - b_{js}) - 18.42\right] \tag{2.127}$$

where $a_{js} = 1.16 \times 10^{-3}\, \mu_{js}^{\frac{1}{2}}\, \theta_j^{v\,\frac{4}{3}}$, $b_{js} = 0.015\, \mu_{js}^{\frac{1}{4}}$, and μ_{js} is the reduced molecular weight of the vibrator j and heat bath species s. At high temperatures, the Millikan and White model underpredicts the relaxation time because it does not take into account the limiting of excitation rates due to the finiteness of elastic collision cross-sections. Park [67] proposed the simple formula for the relaxation time at high temperatures,

$$\tau_j^{\mathrm{P}} = \left(n_j \sqrt{\frac{8 k_B T_h}{\pi m_j}} \sigma_j^v\right)^{-1}, \tag{2.128}$$

where σ_j^v is an effective cross-section for vibrational relaxation. In addition, at high temperatures, the kinetic energy of the gas becomes much greater than the vibrational energy gap between excited vibrational levels. In this regime, vibrational excitation and deexcitation behave classically and the vibrational energy may be treated as continuously distributed, leading to a diffusion-like equation for the rate of change in the density of a vibrational state [30]. In order to combine the diffusion and Landau-Teller models, Park [60] has suggested a correction to the relaxation time for shock heated flows, such that

$$\tau_j^{\mathrm{VT}} = \left(\tau_j^{\mathrm{MW}} + \tau_j^{\mathrm{P}}\right) \left| \frac{T_s - T_{vs}}{T_s - T_{vj}} \right|^{s-1}, \tag{2.129}$$

where T_s and T_{vs} are the heavy-particle translational and vibrational temperatures immediately behind the normal shock wave. The parameter $s = 3.5 \exp(-5000/T_s)$ acts as a bridging function between the high and low temperature regimes. For one-dimensional problems, the high temperature correction is straight forward to implement. For two- and three-dimensional flows, the shock wave location should be based on a streamwise trace from the local point to the shock front, though in practice the average post shock temperature is typically used instead [26].

When separate vibrational temperatures are used to describe the vibrational energy distributions of each vibrating molecule, the resulting energy transfer terms for each vibrator j are easily derived from Eq. (2.126), such that

$$\Omega_j^{\mathrm{VT}} = \rho_j \frac{e_j^v(T_h) - e_j^v(T_{vj})}{\tau_j^{\mathrm{VT}}}, \tag{2.130}$$

where the superscript $*$ has been dropped because the vibrational energy is assumed to follow a Boltzmann distribution. If all vibrators have the same vibrational temperature, then the source term is simply the net energy transfer due to each molecule,

$$\Omega^{\mathrm{VT}} = \sum_{j \in \mathcal{V}} \Omega_j^{\mathrm{VT}} = \sum_{j \in \mathcal{V}} \rho_j \frac{e_j^v(T_h) - e_j^v(T_v)}{\tau_j^{\mathrm{VT}}}. \tag{2.131}$$

The Landau-Teller form for vibration-translation energy exchange has several limitations, which may severely limit its accuracy. For example, anharmonicity, rovibration coupling effects, and real collision dynamics are not taken into account. Nikitin and Troe [132] provide a historical review of energy transfer models developed since the landmark paper of Landau and Teller in 1936 [130]. In general, these models build on the original Landau-Teller formulation by incorporating a more detailed Master equation than Eq. (2.124) and using higher fidelity collision dynamics such as those obtained through QCT calculations. Despite the many advances, Eqs. (2.127 - 2.131) remain widely used in the field of hypersonics due to their ease of implementation and small data requirements.

Free electron-vibration energy exchange

Electron-impact vibrational (de)excitation processes play an important role in the energy exchange between electrons and molecules. In particular, the resonant electron impact nitrogen excitation reaction

$$\mathrm{N_2(X^1\Sigma_g{}^+;}\ v) + \mathrm{e^-} \longrightarrow \mathrm{N_2{}^-(^2\Pi_g)} \longrightarrow \mathrm{N_2(X^1\Sigma_g{}^+;}\ w) + \mathrm{e^-}, \quad w > v$$

is known to be very efficient. Electron impact excitation reactions for other air molecules are negligible [27]. Studies of electron-vibration energy exchange for nitrogen plasmas suggest that this process may be modeled with a Landau-Teller rate equation [133–135], where

$$\Omega_j^{\mathrm{EV}} = \rho_j \frac{e_j^v(T_e) - e_j^v(T_{vj})}{\tau_j^{\mathrm{EV}}}. \tag{2.132}$$

Laporta and Bruno [135] have developed analytical expressions for the relaxation time τ_j^{EV} based on STS calculations using accurate theoretical cross sections.

Vibration-vibration energy exchange

When separate vibrational energy equations are attributed to each vibrating molecule, the vibrational energy exchanged between each of these vibrators should be taken into account. Knab *et al.* [122] have proposed the following consistent model for vibrational energy exchange,

$$\Omega_j^{\mathrm{VV}} = N_A \sqrt{\frac{8R_uT_h}{\pi}} \sum_{s\in\mathcal{V}} \sigma_{js} P_{js} \frac{\rho_s}{M_s} \rho_j \left[\frac{e_j^v(T_h)}{e_s^v(T_h)} e_s^v(T_{vs}) - e_j^v(T_{vj}) \right], \tag{2.133}$$

where P_{js} is the exchange probability, taken to be 0.01 [122]. Panesi [128] has shown vibration-vibration energy exchange to be of secondary importance for nonequilibrium air flows.

Elastic energy exchange between free electrons and heavy particles

Elastic energy exchange between free electrons and heavy particles has been studied in-depth for partially ionized nonequilibrium plasmas based on kinetic theory [100, 107]. This energy exchange follows the Landau-Teller form, such that

$$\Omega^{\mathrm{ET}} = \rho_e \frac{e_e(T_h) - e_e(T_e)}{\tau^{\mathrm{ET}}} = \frac{3}{2}\rho_e R_e \frac{T_h - T_e}{\tau^{\mathrm{ET}}}. \tag{2.134}$$

The average relaxation time is derived directly from kinetic theory as

$$\frac{1}{\tau^{\mathrm{ET}}} = \sum_{i\in\mathcal{H}} \frac{8}{3} \frac{m_e}{m_i} n_i \sqrt{\frac{8k_BT_e}{\pi m_e}} \bar{Q}_{ei}^{(1,1)}, \tag{2.135}$$

where $\bar{Q}_{ei}^{(1,1)}$ is the reduced collision integral for the electron-heavy interaction.

2.7.2. Chemical energy exchange processes

Chemical energy exchange processes result from reactive collisions between particles in which energy is transferred in order to promote the reaction. Important coupling mechanisms are described below.

Electron-impact ionization

Electron-impact ionization reactions result in a lowering of the overall electron translational energy since the free-electrons provide the energy necessary to ionize the heavy particle. It is important

to take this energy transfer mechanism into account, in particular to accurately describe electron avalanche. The amount of energy lost from the electron bath is modeled as

$$\Omega^{\mathrm{I}} = \sum_{r \in \mathcal{I}} \Delta h_r \mathfrak{R}_r, \tag{2.136}$$

where $\mathcal{I}$ is the set of electron impact ionization reactions and Δh_r and $\mathfrak{R}_r$ are the molar reaction enthalpy and rate of progress for the ionization reaction r. The reaction enthalpy represents the average energy required to ionize the heavy particle in reaction r and the rate of progress is equal to the rate of electron impact ionization reactions. Note that this model assumes that all the energy required to ionize a given species comes from the free-electrons which may overestimate the rate of electron energy loss.

Vibration-chemistry-vibration coupling

When molecules are created or destroyed through chemical reactions, vibrational energy is added or removed from the gas. This creates an important coupling mechanism between the vibrational energy distribution of a given molecule and the rate of creation or destruction of that molecule, which in turn effects the net vibrational energy exchange of the gas. Vibration-chemistry-vibration coupling is strongly related to the vibrational chemical nonequilibrium model in use. As such, the models are split again into preferential and non-preferential dissociation categories.

Preferential dissociation leads to the following general expression for the vibration-chemistry energy transfer source term,

$$\Omega_m^{\mathrm{CV}} = M_m \sum_{r \in \mathcal{R}} \mathfrak{R}_r \left[\nu_m^{''} G_{rm}^{''} - \nu_m^{'} G_{rm}^{'} \right], \tag{2.137}$$

where $G_{rm}^{'}$ and $G_{rm}^{''}$ are the average vibrational energy gained or lost per mass of molecule m associated with the forward and reverse process of reaction r. The actual form of these parameters must be consistent with the vibration-chemistry model being employed. For example, in the case of the Treanor and Marrone model [119] discussed in Section 2.6.2, these average energies become

$$G_{rm}^{'} = \frac{R_m \theta_m^v}{\exp(-\theta_m^v/U) - 1} - \frac{R_m \theta_m^D}{\exp(-\theta_m^D/U) - 1}, \tag{2.138}$$

$$G_{rm}^{''} = \frac{R_m \theta_m^v}{\exp(-\theta_m^v/T_F) - 1} - \frac{R_m \theta_m^D}{\exp(-\theta_m^D/T_F) - 1}, \tag{2.139}$$

where θ_m^D is the dissociation energy of molecule m (associated with the dissociation reaction r) and T_F and U were defined in Eq. (2.113).

Non-preferential models assign equal probability to a molecule dissociating from any vibrational energy state. Therefore, the average vibrational energy lost or gained by a molecule which dissociates or recombines is equal to the average vibrational energy of the molecule itself, e_m^v (regardless of energy distribution). Therefore, for non-preferential dissociation Eq. (2.137) readily assumes the form proposed by Candler and MacCormack [27],

$$\Omega_m^{\mathrm{CV}} = c_1 e_m^v \dot{\omega}_m, \tag{2.140}$$

where the factor c_1 is introduced as a preferential dissociation factor. For $c_1 = 1$, Eq. (2.140) represents a non-preferential dissociation model while for $c_1 > 1$, a simple preferential model is obtained.

2.8. Concluding Remarks

The goal of this chapter was to present the general governing equations for hypersonic, atmospheric entry flows. Hypersonic flows are characterized by flow time scales on the order of chemical and relaxation time scales which result in significant thermal and chemical nonequilibrium phenomena. Thermal nonequilibrium is treated through the use of so-called energy partitioning models in which assumptions are made on the relative distribution of populated energy states for each component of the flow. Various energy partitioning models have been reviewed in this chapter and their role in the governing fluid equations has been detailed. In particular, both thermochemical nonequilibrium and LTE flows have been considered.

Closure models for the thermodynamic, transport, and chemistry properties, whose evaluation is required to solve the governing equations, have also been presented. In general, all properties have been shown to be functions of the local state of the fluid. General relations for thermodynamic properties were provided, based on the a statistical mechanics description of individual species energy partitioning models and associated partition functions. Transport properties were presented based on a perturbative Chapmann-Enskog solution of the scaled Boltzmann equation, which results in linear transport systems defined in terms of temperature dependent collision integrals and species concentrations. Chemical production rates were formulated in terms of the Law of Mass Action. The effect of thermal nonequilibrium was also considered and several common models for nonequilibrium rate coefficients were presented. In addition, several important energy transfer models were discussed in the context of a MT approach.

Radiation was largely ignored in this chapter, except in the presentation of the governing equations. The computation of radiative source terms represents a significant numerical and theoretical effort. In addition, the treatment of radiation in the governing equations alters the general nature of the equations from differential to integro-differential. For these reasons, the discussion of radiation has been postponed until Chapter 3. Finally, it is worth noting that this chapter presented the governing equations in a general manner. The specific models and data used in this work are presented in Chapter 4.

CHAPTER 3

Radiative Transfer for Atmospheric Entry

3.1. Introduction

The radiative heat flux, energy source, and photochemical source terms required to couple radiative transfer to the fluid dynamic conservation equations, were presented in Chapter 2. As will be evident from the following sections, the accurate calculation of these quantities involves a significant modeling and numerical effort. This chapter is broken into three distinct sections. Section 3.2 provides an introduction to radiation for atmospheric entry applications. Section 3.3 details the HTGR database, used in this work to compute high resolution emission and absorption spectra. Finally, Section 3.4 derives the so-called hybrid statistical narrow band model, used in this work to significantly improve the performance of radiative transfer calculations.

3.2. Radiative Transfer in Participating Media

This section provides a short introduction to the basics of modeling radiative transfer in participating media, in particular, gases. The various radiative processes which occur in gases are first outlined, followed by a description of the governing equations for radiation transport including the radiative boundary conditions typically used for atmospheric entry applications. Finally, the radiative surface heat flux, energy source, and species mass production rates due to photochemical processes are detailed.

3.2.1. Radiative Processes in Gases

Radiative processes in gaseous media can be grouped into three categories, namely bound-bound, bound-free or free-bound, and free-free processes. Each one is discussed below.

Bound-bound

Bound-bound processes are radiative transitions between bound electronic states of atoms or rovibronic states of molecules. Bound-bound transitions can occur through absorption,

$$\mathrm{A(l)} + \mathrm{hc}\sigma \longrightarrow \mathrm{A(u)},$$

spontaneous emission,

$$\mathrm{A(u)} \longrightarrow \mathrm{A(l)} + \mathrm{hc}\sigma,$$

and induced emission,

$$\mathrm{A(u)} + \mathrm{hc}\sigma \longrightarrow \mathrm{A(l)} + 2\,\mathrm{hc}\sigma.$$

Each process is depicted graphically in Fig. (3.1). Spontaneous emission occurs when an atom or molecule at an upper energy state u with energy E_u spontaneously emits a photon with energy $hc\sigma$ and falls to a lower energy state l with energy $E_l = E_u - hc\sigma$. Absorption is the opposite process, in which a photon with energy $hc\sigma$ is absorbed to raise the energy from E_l to E_u. Apart

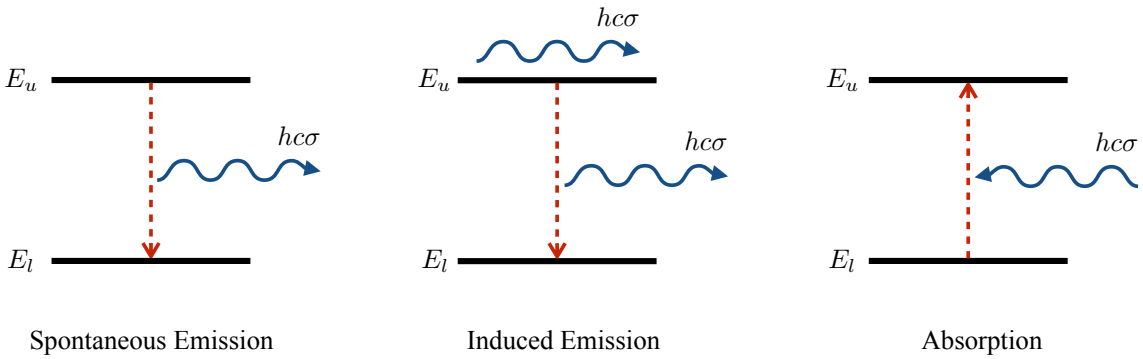

Figure 3.1.: *Types of atomic bound-bound transitions between arbitrary upper and lower energy states.*

from spontaneous emission, atoms and molecules may also emit a photon in the presence of another passing photon. This process is called induced or stimulated emission. Induced emission is sometimes referred to as negative absorption.

As electronic and rovibronic levels are quantized, bound-bound transitions result in discrete spectral lines corresponding to emission and absorption of specific photon energies, centered around the wavelength of the transition energy. Several factors contribute to the broadening of these spectral lines. These details are discussed in Section 3.3.1.

Bound-free and free-bound

Bound-free processes are radiative transitions between a bound and unbound energy states. Bound-free processes included photoionization

$$\mathrm{A} + \mathrm{hc}\sigma \longrightarrow \mathrm{A}^+ + \mathrm{e}^-,$$

photodissociation

$$\mathrm{AB} + \mathrm{hc}\sigma \longrightarrow \mathrm{A} + \mathrm{B},$$

dissociative photoionization

$$\mathrm{AB} + \mathrm{hc}\sigma \longrightarrow \mathrm{A} + \mathrm{B}^+ + \mathrm{e}^-,$$

and photodetachment processes

$$\mathrm{A}^- + \mathrm{hc}\sigma \longrightarrow \mathrm{A} + \mathrm{e}^-.$$

Each bound-free process absorbs a photon at a high enough energy to fully dissociate or ionize the absorbing species into two or three separate particles. Free-bound processes represent the opposite transitions, in which two or three particles recombine, emitting the excess energy as a photon. The energy of the dissociation products are essentially not quantized, thanks to the translational energy of the particles. Therefore, bound-free processes result in a near continuous emission and absorption spectrum above the ionization or dissociation energy of the bound state.

Free-Free

A free electron may interact with the electric field of an atom or molecule, causing the electron to decelerate and the resulting energy lost by deceleration is emitted as a photon

$$\mathrm{A} + \mathrm{e}^- \longrightarrow \mathrm{A} + \mathrm{e}^- + \mathrm{hc}\sigma.$$

This mechanism is called Bremsstrahlung radiation after the German word for *brake radiation* because the free electron is slowed in the process. The reverse process is known as inverse Bremsstrahlung radiation. Because the translational energy of the free electron is essentially continuous, the resulting Bremmstrahlung spectrum is also continuous.

3.2.2. The Radiative Transport Equation

Each radiative mechanism discussed in the previous section contributes to the net emission and absorption of photons. The energy carried by a photon at wavenumber σ is given $hc\sigma$. Therefore, emission and absorption of photons results in a net energy transfer between points in the flow field, or from the flow field to the vehicle surface.

The radiant intensity $I_\sigma(\boldsymbol{x}, \hat{\boldsymbol{s}})$ is defined as the photon energy flux per unit area, per elementary solid angle, per wavenumber, in the direction $\hat{\boldsymbol{s}}$ at wavenumber σ and position $\boldsymbol{x}$. In the absence of scattering, the steady Radiative Transport Equation (RTE) describes the variation of spectral intensity I_σ along a ray with length parameter s as

$$\frac{dI_\sigma}{ds} = \hat{\boldsymbol{s}} \cdot \boldsymbol{\nabla} I_\sigma(\hat{\boldsymbol{s}}) = \eta_\sigma - \kappa_\sigma I_\sigma(\hat{\boldsymbol{s}}), \tag{3.1}$$

where η_σ and κ_σ are the local emission and absorption coefficients at point s along the ray.

Photons may be emitted in any direction. Therefore, the spectral emission coefficient is independent of direction and represents the total photon energy emitted per volume, per time, per wavenumber, and per elementary solid angle. The absorption coefficient represents the fraction of photon energy absorbed by the gas over a unit distance, and is independent of direction as well. In general, these coefficients are functions of the local energy level populations of the participating gaseous species. They will be described in more detail in Section 3.3.

Under radiative equilibrium conditions, the intensity follows Planck's law such that

$$I_\sigma = I_\sigma^b \equiv 2hc^2\sigma^3 \Big[\exp\Big(\frac{hc\sigma}{k_B T}\Big) - 1 \Big]^{-1}, \tag{3.2}$$

and the emission and absorption coefficients are related through Kirchhoff's law by $\eta_\sigma = I_\sigma^b \kappa_\sigma$. This relation is also satisfied for flows in thermo-chemical equilibrium.

The formal solution of Eq. (3.1) may be written as

$$I_\sigma(s) = I_\sigma(0)\tau_\sigma(0, s) + \int_0^s \eta_\sigma(s')\tau_\sigma(s', s) ds', \tag{3.3}$$

where the spectral transmissivity τ_σ between points s' and s is given by Beer's law,

$$\tau_\sigma(s', s) = \exp\Big(- \int_{s'}^{s} \kappa_\sigma(s'')\, ds'' \Big). \tag{3.4}$$

The integral inside the exponential is called the optical thickness of the gas. When the optical thickness is large, the transmissivity approaches zero, indicating that no radiation is transmitted through the gas. Conversely, for optically thin media, the transmissivity approaches unity and all radiation is transmitted.

3.2.3. Boundary Conditions

Eq. (3.3) represents an integral equation for the solution of the radiant intensity at a given point in space, in the direction defined by the ray. This equation may be solved by integrating along the ray from a known boundary condition, $I_\sigma(0)$. Two types of boundaries will be considered in this work.

Diffuse surfaces

Vehicle surfaces are assumed to be diffuse, and opaque, such that

$$I_\sigma(\boldsymbol{x}_\mathrm{w}, \hat{\boldsymbol{s}}) = \epsilon_\sigma I_\sigma^b(T_\mathrm{w}) + \frac{\rho_\sigma}{\pi} \int_{\hat{\boldsymbol{n}} \cdot \hat{\boldsymbol{s}}' < 0} I_\sigma(\boldsymbol{x}_\mathrm{w}, \hat{\boldsymbol{s}}')\, |\hat{\boldsymbol{n}} \cdot \hat{\boldsymbol{s}}'|\, d\Omega', \quad \hat{\boldsymbol{n}} \cdot \hat{\boldsymbol{s}} > 0, \tag{3.5}$$

where ϵ_σ and ρ_σ are the local spectral emittance and reflectance of the surface and $\hat{\boldsymbol{n}}$ is the outward facing surface normal. Emittance represents the fraction of black body radiation emitted by the surface, while reflectance represents the fraction of incoming intensity that is reflected away from the wall. For an opaque surface, the reflectance is related to the absorptance α_σ of the surface by

$$\rho_\sigma = 1 - \alpha_\sigma, \tag{3.6}$$

where the absorptance represents the fraction of incoming energy absorbed by the material at the surface. Also, for a diffuse surface, the emittance and absorptance are independent of direction, leading to $\epsilon_\sigma = \alpha_\sigma$.

The integral in Eq. (3.5) represents the spectral irradiation, or incoming spectral flux, onto the surface. For partially reflecting boundaries ($\epsilon < 1$), the reflective term in Eq. (3.5) imposes a coupling between the incoming and outgoing intensities at the boundaries.

Free-stream boundaries

It is assumed that free-stream boundaries are sufficiently far from the shock layer to ensure that all temperatures associated with the flow field are equal and relatively low. Under these assumptions, the domain boundaries may be treated as black walls at the local temperature, such that

$$I_\sigma(\boldsymbol{x}_\infty, \hat{\boldsymbol{s}}) = I^b_\sigma(T_\infty), \tag{3.7}$$

where the subscript ∞ represents the free-stream quantity.

3.2.4. Coupling to Fluid Dynamics

Once the intensity field is known, the solution must be coupled back to the mass and energy transport equations derived in Chapter 2 via the radiative surface heat flux, power, and species mass production rates due to photochemical processes.

Heat flux and its divergence

The total radiative flux at any location in the flow field is given by the integral of intensity over all wavenumbers and directions,

$$\boldsymbol{q^r} = \int_0^\infty \int_{4\pi} I_\sigma(\hat{\boldsymbol{s}})\ \hat{\boldsymbol{s}}\ d\Omega\ d\sigma. \tag{3.8}$$

We may also construct the total radiative energy fluxes going into and out of a wall with surface normal $\hat{\boldsymbol{n}}$, respectively as

$$q^r_{\text{in}} = \int_0^\infty \int_{\hat{\boldsymbol{n}}\cdot\hat{\boldsymbol{s}}<0} I_\sigma(\boldsymbol{x}_\text{w}, \hat{\boldsymbol{s}})\ |\hat{\boldsymbol{n}}\cdot\hat{\boldsymbol{s}}|\ d\Omega\ d\sigma, \tag{3.9}$$

$$q^r_{\text{out}} = \int_0^\infty \int_{\hat{\boldsymbol{n}}\cdot\hat{\boldsymbol{s}}>0} I_\sigma(\boldsymbol{x}_\text{w}, \hat{\boldsymbol{s}})\ |\hat{\boldsymbol{n}}\cdot\hat{\boldsymbol{s}}|\ d\Omega\ d\sigma. \tag{3.10}$$

Using Eq. (3.5), the total radiative heat flux on a gray, diffuse, and opaque surface is then given as

$$q^r_\text{w} = q^r_{\text{out}} - q^r_{\text{in}} = \epsilon(\sigma T^4_\text{w} - q^r_{\text{in}}). \tag{3.11}$$

Finally, the heat flux itself is not a particularly useful parameter within the flow field. Instead, the radiative power, defined by the negative divergence of the heat flux is required to determine the amount of radiant energy being deposited or emitted at any given point. Using Eqs. (3.1) and

(3.8), the radiative power may be written as

$$\begin{aligned} -\boldsymbol{\nabla}\cdot\boldsymbol{q}^{\boldsymbol{r}} &= -\boldsymbol{\nabla}\cdot\int_0^\infty\int_{4\pi} I_\sigma(\hat{\boldsymbol{s}})\;\hat{\boldsymbol{s}}\;d\Omega\;d\sigma \\ &= \int_0^\infty \kappa_\sigma G_\sigma - 4\pi\eta_\sigma\;d\sigma, \end{aligned} \tag{3.12}$$

where G_σ is called the spectral incident radiation,

$$G_\sigma \equiv \int_{4\pi} I_\sigma(\hat{\boldsymbol{s}})\;d\Omega. \tag{3.13}$$

Photochemical source terms

The bound-bound and bound-free processes described in Section 3.2.1 alter the chemical composition of the gas through emission or absorption of photons and are known collectively as photochemical processes. The net rate of production of photons at wavenumber σ from a reversible photochemical process is equal to the net photon energy emitted by that process, divided by the energy of a single photon, $hc\sigma$. Using the definition of the emission and absorption coefficients for a single photochemical process, it is then plain to see that the net production rate of a species (or pseudo-species) j is given as

$$\begin{aligned} \dot{\phi}_j &= \frac{m_j}{hc}\sum_p \nu_{pj}\int_0^\infty \frac{1}{\sigma}\int_{4\pi}\left(\kappa_\sigma^p I_\sigma - \eta_\sigma^p\right)\;d\Omega\;d\sigma \\ &= \frac{m_j}{hc}\sum_p \nu_{pj}\int_0^\infty \frac{\kappa_\sigma^p G_\sigma - 4\pi\eta_\sigma^p}{\sigma}\;d\sigma, \end{aligned} \tag{3.14}$$

where the sum over p represents the sum over all photochemical processes and ν_{pj} is the stoichiometry difference of species j across process p.

3.3. High Temperature Gas Radiation Database

The emission and absorption coefficients required in the solution of the RTE presented in the previous section are taken from the HTGR spectroscopic database [36, 37, 39, 40]. An overview of the database is presented in this section. In addition, new mechanisms which have been added in this work are highlighted. Contributions to the emission and absorption coefficients are split into bound-bound transitions and bound-free and free-free continua. Total emission and absorption coefficients are obtained by summing each contribution. All radiative mechanisms included in the database are summarized in Table 3.1.

3.3.1. Bound-Bound Transitions

Radiative transitions between bound energy levels of an arbitrary species A follow the general form,

$$\mathrm{A(l)} + \mathrm{hc\sigma} \rightleftharpoons \mathrm{A(u)}, \quad E_l < E_u. \tag{3.15}$$

The emission and absorption coefficients for all such transitions are given by

$$\eta_\sigma = \sum_{ul} n_u \frac{A_{ul}}{4\pi} hc\sigma f_{ul}^{\mathrm{se}}(\sigma - \sigma_{ul}) \tag{3.16}$$

$$\kappa_\sigma = \sum_{ul}\left[n_l B_{lu} f_{ul}^{\mathrm{ab}}(\sigma - \sigma_{ul}) - n_u B_{ul} f_{ul}^{\mathrm{ie}}(\sigma - \sigma_{ul})\right] h\sigma \tag{3.17}$$

Table 3.1.: *A summary of the radiative mechanisms included in the HTGR database and used in this work. The first reference corresponds to the spectroscopic data while the second reference corresponds to the SNB parameters (when applicable).*

Species	Process / Band System	Upper - Lower Electronic States	Spectral Range [1000 cm^{-1}]	Ref.
C	Lines			[39]
	Bremsstrahlung		1 - 200	[39], [137]
	Photoionization		1 - 200	[39], [137]
C^+	Lines			[39]
	Bremsstrahlung		1 - 200	[39], [137]
	Photoionization		1 - 200	[39]
C^-	Photodetachment		1 - 200	[39], [137]
C_2	Balik-Ramsay	$b^3\Sigma_g^- - a^3\Pi_u$	1 - 48	[39], [137]
	Deslandres-d'Azambuja	$C^1\Sigma_g - A^1\Pi_u$	1 - 42	[39], [137]
	Fox-Herzberg	$e^3\Sigma_g - a^3\Pi_u$	5 - 51	[39], [137]
	Mulliken	$D^1\Sigma_u^+ - X^1\Sigma_g^+$	28 - 77	[39], [137]
	Phillips	$A^1\Sigma_g - X^1\Sigma_g^+$	1 - 49	[39], [137]
	Swan	$d^3\Sigma_g - a^3\Pi_u$	1 - 43	[39], [137]
	Photoionization		1 - 200	[39], [137]
C_3	Swings	$A^1\Pi_u - X^1\Sigma_g^+$	20 - 35	[138], here
	UV	${}^1\Sigma_u^+ - X^1\Sigma_g^+$	30 - 74	[139], here
CH	AX	$A^2\Delta - X^2\Pi$	1 - 37	[40], [40]
	BX	$B^2\Sigma^- - X^2\Pi$	1 - 27	[40], [40]
	CX	$C^2\Sigma^+ - X^2\Pi$	1 - 40	[40], [40]
	Infrared	$X^2\Pi - X^2\Pi$	1 - 27	[40], [40]
	Photoionization		85 - 193	[140], here
CN	LeBlanc	$B^2\Sigma^+ - A^2\Pi_i$	1 - 54	[39], [137]
	Red	$A^2\Pi_i - X^2\Sigma^+$	1 - 58	[39], [137]
	Violet	$B^2\Sigma^+ - X^2\Sigma^+$	4 - 62	[39], [137]
	Photoionization		1 - 200	[39], [137]
CO	Third positive	$b^3\Sigma_g^+ - a^3\Pi$	13 - 43	[39], [137]
	Fourth positive	$A^1\Pi - X^1\Sigma^+$	11 - 90	[39], [137]
	Hopfield-Birge	$B^1\Sigma^+ - X^1\Sigma^+$	14 - 91	[39], [137]
	Infrared	$X^1\Sigma^+ - X^1\Sigma^+$	1 - 77	[39], [137]
	Photoionization		1 - 200	[39], [137]
CO^+	Baldet-Johnson	$B^2\Sigma^+ - A^2\Pi_i$		[39], [137]
	Comet-tail	$A^2\Pi_i - X^2\Sigma^+$		[39], [137]
	First negative	$B^2\Sigma^+ - X^2\Sigma^+$		[39], [137]
CO_2	Infrared	$X^1\Sigma_g^+ - X^1\Sigma_g^+$	0.25 - 8.3	[141], [142]
H	Lines			here
	Photoionization			here
H_2	Lyman	$B^1\Sigma - X^1\Sigma$	60 - 120	[143], here
	Werner	$C^1\Pi - X^1\Sigma$	60 - 120	[143], here
	Photoionization			[144], here
N	Lines		1 - 200	[37]
	Photoionization		1 - 200	[37], [55]
	Bremsstrahlung		1 - 200	[37], [55]
N^+	Lines		1 - 200	[37]
	Bremsstrahlung		1 - 200	[37], [55]
N^-	Photodetachment		1 - 200	[37], [55]
N_2	First positive	$B^3\Pi_g - A^3\Sigma_u^+$	1 - 42	[36], [55]
	Second positive	$C^3\Pi_u - B^3\Pi_g$	1 - 40	[36], [55]
	Birge-Hopfield 1	$b^1\Pi_u - X^1\Sigma_g^+$	55 - 117	[36], [55]
	Birge-Hopfield 2	$b'^1\Sigma_u^+ - X^1\Sigma_g^+$	36 - 124	[36], [55]
	Caroll-Yoshino	$c_4'^1\Sigma_u^+ - X^1\Sigma_g^+$	54 - 123	[36], [55]
	Worley	$o_3^1\Pi_u - X^1\Sigma_g^+$	71 - 121	[36], [55]

Continued on next page

Table 3.1 – *Continued from previous page*

Species	Process / Band System	Upper - Lower Electronic States	Spectral Range [1000 cm^{-1}]	Ref.
	Worley-Jenkins	$c_3^1\Pi_u - X^1\Sigma_g^+$	67 - 116	[36], [55]
	Photoionization		1 - 200	[37], [55]
	Bremsstrahlung		1 - 200	[37], [55]
N_2^+	First negative	$B^2\Sigma_u^+ - X^2\Sigma_g^+$	1 - 42	[36], [55]
	Second negative	$C^2\Sigma_u^+ - X^2\Sigma_g^+$	26 - 77	[36], [55]
	Meinel	$A^2\Pi_u - X^2\Sigma_g^+$	1 - 49	[36], [55]
NO	11 000 Å	$D^2\Sigma^+ - A^2\Sigma^+$	1 - 22	[36], [55]
	β	$B^2\Pi_r - X^2\Pi_r$	7 - 74	[36], [55]
	β'	$B'^2\Delta - X^2\Pi_r$	22 - 69	[36], [55]
	δ	$C^2\Pi_r - X^2\Pi_r$	15 - 75	[36], [55]
	ϵ	$D^2\Sigma^+ - X^2\Pi_r$	16 - 68	[36], [55]
	$\gamma_{'}$	$A^2\Sigma^+ - X^2\Pi_r$	7 - 66	[36], [55]
	γ	$E^2\Sigma^+ - X^2\Pi_r$	23 - 73	[36], [55]
	Infrared	$X^2\Pi_r - X^2\Pi_r$	1 - 37	[36], [55]
	Photoionization		1 - 200	[37], [55]
O	Lines		1 - 200	[37]
	Photoionization		1 - 200	[37], [55]
	Bremsstrahlung		1 - 200	[37], [55]
O^+	Lines		1 - 200	[37]
	Bremsstrahlung		1 - 200	[37], [55]
O^-	Photodetachment		1 - 200	[37], [55]
O_2	Schumann-Runge	$B^3\Sigma_u^- - X^3\Sigma_g^-$	14 - 60	[36], [55]
	Photoionization		1 - 200	[37], [55]
	Photodissociation (Schumann-Runge)		1 - 200	[37], [55]
	Bremsstrahlung		1 - 200	[37], [55]

where the summation over ul denotes summation over all bound-bound transitions from an upper energy level u to a lower energy level l and A_{ul} , B_{lu}, B_{ul}, and f_{ul}^{se}, f_{ul}^{ab}, and f_{ul}^{ie} correspond to Einstein coefficients and spectral line profiles for spontaneous emission, absorption, and induced emission, respectively [136]. Line centers are given by $hc\sigma_{ul} = E_u - E_l$, for each transition $u \to l$. Detailed balancing under thermal equilibrium yields the following relationships for the Einstein coefficients and line shapes [136],

$$B_{ul} f_{ul}^{\mathrm{ie}}(\sigma - \sigma_{ul}) = \frac{1}{8\pi hc\sigma^3} A_{ul} f_{ul}^{\mathrm{se}}(\sigma - \sigma_{ul}), \tag{3.18}$$

$$B_{lu} f_{ul}^{\mathrm{ab}}(\sigma - \sigma_{ul}) = \frac{1}{8\pi hc\sigma^3} A_{ul} f_{ul}^{\mathrm{se}}(\sigma - \sigma_{ul}) \frac{a_u}{a_l} \exp\Big[\frac{hc(\sigma - \sigma_{ul})}{k_B T}\Big]. \tag{3.19}$$

In addition, the spontaneous emission Einstein coefficient is related to the oscillator strength of a particular line via

$$A_{ul} = \frac{2\pi\sigma_{ul}^2 q_e^2}{\epsilon_0 m_e c} \frac{a_l}{a_u} f_{lu}. \tag{3.20}$$

Line shapes

Various line broadening mechanisms contribute to the line shape of an individual line. Doppler broadening results from the relative motion of a radiating particle to the observer. A pure Doppler profile can be derived from kinetic theory assuming a Maxwellian velocity distribution [145], such that

$$f_{ul}^D(\sigma - \sigma_{ul}) = \frac{1}{\gamma_{ul}^D}\sqrt{\frac{\ln 2}{\pi}} \exp\Big[-\ln 2 \frac{(\sigma - \sigma_{ul})^2}{(\gamma_{ul}^D)^2}\Big], \tag{3.21}$$

where γ_{ul}^D is the half-width at half-maximum (HWHM) of the Doppler line shape, given by

$$\gamma_{ul}^D = \sigma_{ul}\sqrt{\frac{2\ln 2\, k_B T_h}{m\, c^2}}, \tag{3.22}$$

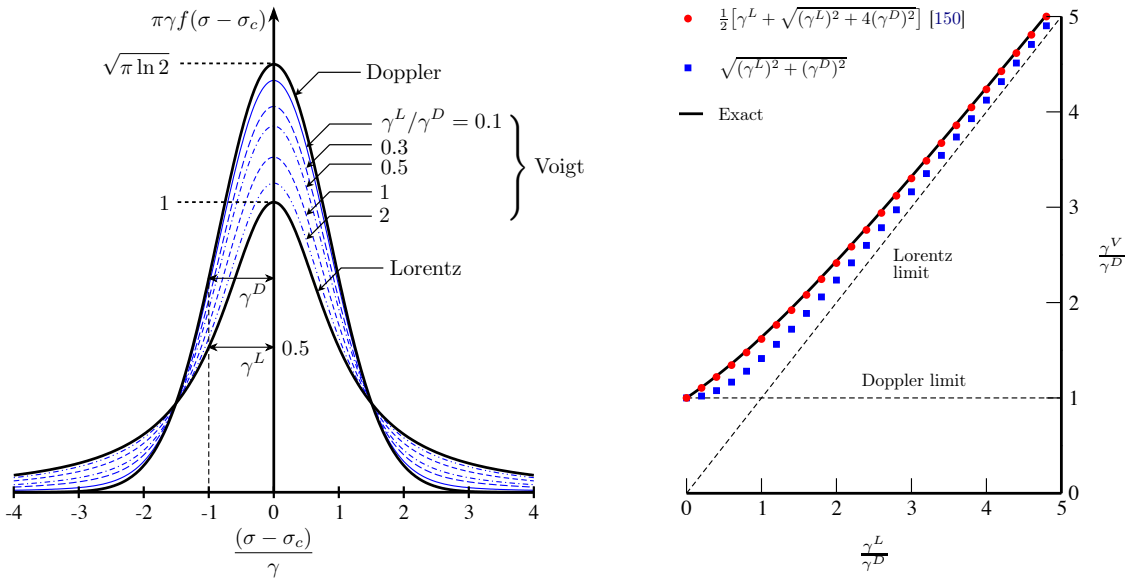

(a) *Normalized Doppler, Lorentz, and Voigt profiles, reproduced from [145].*

(b) *Voigt half-width at half-maximum.*

Figure 3.2.: *Description of the Voigt line profile and comparison with Doppler and Lorentz shapes.*

with m, the mass of the radiating particle. As can be seen from the equation, Doppler broadening is proportional to $\sigma\sqrt{T_h}$.

Pressure broadening occurs when a radiating particle interacts with a charged (Stark) or neutral (Resonance, van der Waals, etc.) particle through collisions. The resulting line shape under the impact approximation is Lorentzian. A pure Lorentz profile is given by

$$f^L_{ul}(\sigma-\sigma_{ul}) = \frac{1}{\pi}\frac{(\gamma^L_{ul})^2}{(\gamma^L_{ul})^2+(\sigma-\sigma_{ul})^2}, \tag{3.23}$$

where γ^L_{ul} is the Lorentz HWHM. Lorentz half-widths are proportional to the average collision frequency of the gas (e.g., for hard-spheres, $\gamma^L_{ul} \propto p/\sqrt{T_h}$).

When both Doppler and Lorentz broadening are important, the combined line shape follows from a convolution of the two profiles, yielding the so-called Voigt profile,

$$\begin{aligned} f^V_{ul}(\sigma-\sigma_{ul}) &= \frac{1}{\gamma^D_{ul}}\sqrt{\frac{\ln 2}{\pi}}K\left(\sqrt{\ln 2}\,\frac{(\sigma-\sigma_{ul})}{\gamma^D_{ul}}, \sqrt{\ln 2}\,\frac{\gamma^L_{ul}}{\gamma^D_{ul}}\right), \\ K(x,y) &= \frac{y}{\pi}\int_{-\infty}^{\infty}\frac{e^{-\xi^2}}{(x-\xi)^2+y^2}d\xi. \end{aligned} \tag{3.24}$$

Unfortunately, no analytical expression exists for the Voigt profile. Several numerical approaches have been developed to compute the Voigt profile accurately and quickly, typically relying on rational function approximations [146–149]. In this work, the method of Drayson [146] has been used, modified by moving the outer loop over wavenumbers into the function evaluation as suggested by Schreier [149].

Fig. (3.2) shows a comparison of the Doppler, Lorentz, and Voigt profiles, normalized by their respective HWHM. The "exact" value of the Voigt HWHM, γ^V, has been computed through a simple Newton procedure using the Drayson Voigt approximation [146]. Two common approximations to the Voigt half-width are also shown. The first approximation in Fig. (3.2b) was originally developed by Whiting [150] and is found to be accurate to about 1 %.

Atomic lines

It is convenient to express electronic energy level populations of atoms in terms of Boltzmann populations at an electronic temperature T_{el}. Introducing a non-Boltzmann parameter $\theta_k^B \equiv n_k/n_k^B$ for an arbitrary electronic level k of atom A, the number density of level k can be expressed as

$$n_k = \theta_k^B \frac{n_{\mathrm{A}}}{Q_{\mathrm{A}}^{\mathrm{int}}(T_{el})} a_k \exp\Big(-\frac{E_k^{\mathrm{A}}}{k_B T_{el}}\Big), \tag{3.25}$$

where n_k^B represents the Boltzmann number density of level k and n_{A} is the total number density for the atom. $Q_{\mathrm{A}}^{\mathrm{int}}(T_{el})$ is the atomic internal (electronic) partition function evaluated at T_{el}.

Inserting Eq. (3.25) along with Eqs. (3.18 - 3.20) into Eqs. (3.16) and (3.17), the emission and absorption coefficients associated with a single transition $u \to l$ for an atom A are given as

$$\eta_{\sigma,ul}^{\mathrm{A}} = \frac{h\sigma q_e^2}{2\epsilon_0 m_e} \theta_u^B \frac{n_{\mathrm{A}}}{Q_{\mathrm{A}}^{\mathrm{int}}} \exp\Big(\frac{-E_u^{\mathrm{A}}}{k_B T_{el}}\Big) a_l f_{lu}\, \sigma_{ul}^2\, f_{ul}^{\mathrm{se}}(\sigma - \sigma_{ul}), \tag{3.26}$$

$$\kappa_{\sigma,ul}^{\mathrm{A}} = \frac{1}{2hc^2\sigma^3}\Big[\frac{\theta_l^B}{\theta_u^B} \exp\Big(\frac{hc\sigma}{k_B T_{el}}\Big) - 1\Big] \eta_{\sigma,ul}^{\mathrm{A}}. \tag{3.27}$$

The total emission and absorption coefficients associated with atomic lines are obtained by summing Eqs. (3.26) and (3.27) over all considered atoms and transitions. Note that in equilibrium, the non-Boltzmann parameters are equal to unity and Eq. (3.27) is simply a statement of Kirchhoff's law.

Previous compilations of the necessary line data ($a_l f_{lu}$, E_u^{A}, and σ_{ul}) for N, O, N^+, O^+ [37] as well as C and C^+ [39] have been made using the NIST atomic line database [41]. Line shapes associated with spontaneous emission are assumed to be Voigt to account for Doppler and neutral collisional broadening at a temperature T_h and Stark broadening at temperature T_e. Stark broadening parameters for these lines are computed based on a semi-classical approach using line oscillator strengths of The Opacity Project atomic database (TOPBASE) [42] and compiled in [37, 39, 151].

H transitions have also been added in this work using the NIST database for line positions and strengths. The simple approximation of Zoby *et al.* [152] is retained for Stark broadening, based on [153], expressing the Lorentz half-width of hydrogen lines as

$$\gamma_{ul}^L\ [\mathrm{eV}] = 1.05 \times 10^{-15}\,(n^2 - m^2)\, n_{\mathrm{e}^-}^{2/3} \begin{cases} 0.642 & n = m+1 \\ 1 & \text{otherwise} \end{cases}, \tag{3.28}$$

where n and m are the principle quantum numbers of the upper and lower electronic states and $m = n+1$ indicates the first line in each series. The hydrogen electronic partition function is given simply as

$$Q_{\mathrm{H}}^{\mathrm{int}}(T_{el}) = \sum_{k=1}^{40} 2k^2 \exp\Big[\frac{R_y}{k_B T_{el}}\Big(\frac{1}{k^2} - 1\Big)\Big], \tag{3.29}$$

where the level cutoff of 40 has been used in order to match the maximum level retained in the NIST line database. R_y is the Rydberg constant, defined as the ionization energy of the hydrogen ground state.

Molecular electronic systems

The HTGR database contains the necessary line information for several air and carbonaceous molecules. Chauveau *et al.* [36] have included 19 electronic systems of N_2, N_2^+, NO, and O_2 for high temperature air radiation calculations for atmospheric reentry and electric arc applications. Babou *et al.* [39] extended the database to include 16 electronic systems of C_2, CN, CO, and CO^+. In addition, 4 electronic systems of CH have been presented by Soufiani *et al.* [40]. CO_2 infrared transitions have been included based on the CDSD-4000 spectroscopic database [141]. Prasanna *et al.* [143] have recently compiled line data for the H_2 Lyman and Werner bands based on the work of Abgrall *et al.* [154] and Dabrowski *et al.* [155].

Finally, averaged C_3 absorption cross-sections for the Swings ($A^1\Pi_u - X^1\Sigma_g^+$) [138] and UV ($^1\Sigma_u^+ - X^1\Sigma_g^+$) [139] systems have been added in this work for the calculation of SNB parameters presented in Section 3.4, however high-resolution line data has not been included due to lack of data in the literature.

3.3.2. Bound-Free Processes

Bound-free processes, such as photoionization (e.g., $\mathrm{N} + hc\sigma \rightleftharpoons \mathrm{N}^+ + \mathrm{e}^-$) or photodissociation (e.g., $\mathrm{O}_2 + hc\sigma \rightleftharpoons \mathrm{O} + \mathrm{O}$), follow the general formula

$$\mathrm{AB\,(i)} + \mathrm{hc\sigma} \rightleftharpoons \mathrm{A\,(j)} + \mathrm{B\,(k)}, \tag{3.30}$$

where A (j) and B (k) represent dissociation products at energy levels j and k respectively from the dissociation of an arbitrary species AB (i) at level i through absorption of a photon with energy $hc\sigma$. Lamet *et al.* [43] have presented a formal approach to calculate absorption and emission coefficients for all such mechanisms, which is summarized here.

The relative velocity g of the dissociation products is obtained from conservation of energy as

$$\frac{1}{2}\mu g^2 = hc\sigma + E_i^{\mathrm{AB}} - E_j^{\mathrm{A}} - E_k^{\mathrm{B}}, \tag{3.31}$$

where μ is the reduced mass of species A and B and E_i^{X} represents the energy of species X at level i, with all energies relative to a common reference energy. Introducing effective cross-sections relative to spontaneous emission $\mathfrak{S}_{jk,i}^{\mathrm{se}}$, induced emission $\mathfrak{S}_{jk,i}^{\mathrm{ie}}$, and absorption $\mathfrak{S}_{i,jk}^{\mathrm{abs}}$, for bound-free processes which are analogous to the Einstein coefficients for bound-bound transitions, the emission and absorption coefficients are given by

$$\eta_\sigma^{bf} = \sum_{ijk} n_j^{\mathrm{A}} n_k^{\mathrm{B}}\, hc\sigma\, g\, \mathfrak{S}_{jk,i}^{\mathrm{se}}(\sigma)\, 4\pi g^2\, f^0(g) \frac{dg}{d\sigma}, \tag{3.32}$$

$$\kappa_\sigma^{bf} = \sum_{ijk} \left[n_i^{\mathrm{AB}}\, \mathfrak{S}_{i,jk}^{\mathrm{abs}}(\sigma) - n_j^{\mathrm{A}} n_k^{\mathrm{B}}\, g\, \mathfrak{S}_{jk,i}^{\mathrm{ie}}(\sigma)\, 4\pi g^2\, f^0(g) \frac{dg}{d\sigma} \right] h\sigma, \tag{3.33}$$

where $f^0(g)$ represents the distribution function of the relative velocity between the dissociation products A and B. The summation over ijk represents the summation over all transitions corresponding to Eq. (3.30). At equilibrium, the intensity satisfies Planck's law. Therefore, substituting Eqs. (3.32) and (3.33) into Eq. (3.1) yields the following relationships for bound-free cross-sections [43],

$$\mathfrak{S}_{jk,i}^{\mathrm{se}}(\sigma) = 2hc\sigma^3\, \mathfrak{S}_{jk,i}^{\mathrm{ie}}(\sigma), \tag{3.34}$$

$$\mathfrak{S}_{jk,i}^{\mathrm{ie}}(\sigma) = \frac{h^2}{4\pi\mu^2 g^2 c} \frac{a_i}{a_j a_k} \mathfrak{S}_{i,jk}^{\mathrm{abs}}(\sigma). \tag{3.35}$$

Assuming the relative velocity distribution function is Maxwellian at a temperature T_{rel} and substituting the above relations into Eqs. (3.32) and (3.33), the following expressions are obtained for the bound-free emission and absorption coefficients,

$$\eta_\sigma^{bf} = 2h^2c^2\sigma^4 \sum_{ijk} \frac{n_j^{\mathrm{A}} n_k^{\mathrm{B}}}{\xi_\mu(T_{\mathrm{rel}})} \frac{a_i}{a_j a_k} \mathfrak{S}_{i,jk}^{\mathrm{abs}} \exp\left(\frac{E_j^{\mathrm{A}} + E_k^{\mathrm{B}} - E_i^{\mathrm{AB}} - hc\sigma}{k_B T_{\mathrm{rel}}} \right), \tag{3.36}$$

$$\kappa_\sigma^{bf} = h\sigma \sum_{ijk} \mathfrak{S}_{i,jk}^{\mathrm{abs}} \left[n_i^{\mathrm{AB}} - \frac{n_j^{\mathrm{A}} n_k^{\mathrm{B}}}{\xi_\mu(T_{\mathrm{rel}})} \frac{a_i}{a_j a_k} \exp\left(\frac{E_j^{\mathrm{A}} + E_k^{\mathrm{B}} - E_i^{\mathrm{AB}} - hc\sigma}{k_B T_{\mathrm{rel}}} \right) \right], \tag{3.37}$$

where the volumetric translational partition function is given as

$$\xi_\mu(T_{\rm rel}) = \Big(\frac{2\pi\mu k_B T_{\rm rel}}{h^2}\Big)^{3/2}. \tag{3.38}$$

Atomic photoionization

Atomic photoionization absorption cross-sections $\mathfrak{S}_i^{\rm abs}$ have been taken from TOPBASE [42] for N, N^+, O, and O^+ [37] as well as C and C^+ [39]. Additional cross-sections for H have been added to the database in this work. These cross-sections are related to the effective cross-sections in Eqs. (3.36) and (3.37) by

$$\mathfrak{S}_i^{\rm abs}(\sigma) = h\sigma \sum_{jk} \mathfrak{S}_{i,jk}^{\rm abs}(\sigma), \tag{3.39}$$

where the summation over jk represents the sum over all electronic levels of the ion and the unique electron energy level with a degeneracy of 2. Fig. (3.3) shows the computed equilibrium absorption cross-sections at various temperatures for H as obtained from TOPBASE. Equilibrium cross-sections are obtained by averaging the level cross-sections, weighted by the Boltzmann distribution at the given temperature. Starting with the general formulation in Eqs. (3.36) and (3.37) and assuming the electronic energy levels of the ion are populated according to a Boltzmann distribution at T_{el} and that $T_{\rm rel} = T_{el}$, the emission and absorption coefficients associated with the photoionization of an atom A at level i are given by

$$\eta_{\sigma,i}^{{\rm A},bf} = 2hc^2\sigma^3 \exp\Big(-\frac{hc\sigma}{k_B T_{el}}\Big)\frac{n_{\rm A}}{Q_{\rm A}}\chi^{\rm neq} a_i \exp\Big(-\frac{E_i^{\rm A}}{k_B T_{el}}\Big)\mathfrak{S}_i^{\rm abs}(\sigma), \tag{3.40}$$

$$\kappa_{\sigma,i}^{{\rm A},bf} = \frac{1}{2hc^2\sigma^3}\Big[\frac{\theta_i^B}{\chi^{\rm neq}}\exp\Big(\frac{hc\sigma}{k_B T_{el}}\Big) - 1\Big]\eta_{\sigma,i}^{{\rm A},bf}, \tag{3.41}$$

where the non-equilibrium factor is given by

$$\chi^{\rm neq} = \frac{n_{\rm A^+} n_{\rm e}}{n_{\rm A}}\frac{Q_{\rm A}}{2\xi_{m_e}(T_e)Q_{\rm A^+}}\exp\Big(\frac{E_{\rm ion}^{\rm A}}{k_B T_{el}}\Big). \tag{3.42}$$

In the above expressions we have used the non-Boltzmann parameter of Eq. (3.25) to account for possible nonequilibrium in the neutral atom electronic energy levels. $E_{\rm ion}^{\rm A}$ is the ionization energy of the atom corrected by the Debye ionization lowering, $Q_{\rm A}$ and $Q_{\rm A^+}$ are the atom and ion partition functions, and $n_{\rm A}$, $n_{\rm A^+}$, and $n_{\rm e}$ are the total number densities of the atom, ion, and free electrons respectively. Summing Eqs. (3.40) and (3.41) over all electronic levels for each atom yields the total emission and absorption coefficients associated with atomic photoionization. Note that in LTE, θ_i^B and $\chi^{\rm neq}$ are both unity, and Kirchhoff's law is recovered in Eq. (3.41) as for the bound-bound case.

Molecular photoionization

Photoionization absorption cross-sections for molecules are typically only provided at room temperature. Therefore, the following pragmatic approach is used to compute emission and absorption coefficients [55],

$$\eta_\sigma = 2hc^2\sigma^3 \exp\Big(-\frac{hc\sigma}{k_B T_e}\Big) n_{\rm mol}\chi^{\rm neq}\mathfrak{S}^{\rm abs}(\sigma), \tag{3.43}$$

$$\kappa_\sigma = \frac{1}{2hc^2\sigma^3}\Big[\frac{1}{\chi^{\rm neq}}\exp\Big(\frac{hc\sigma}{k_B T_e}\Big) - 1\Big]\eta_\sigma, \tag{3.44}$$

where

$$\chi^{\rm neq} = \frac{n_{\rm ion} n_{\rm e}}{n_{\rm mol}}\frac{Q_{\rm mol}(T_e, T_e, T_e)}{2\xi_{m_e}(T_e)Q_{\rm ion}(T_e)}\exp\Big(\frac{E_{\rm ion}^{\rm mol}}{k_B T_e}\Big). \tag{3.45}$$

The database includes appropriate molecular photoionization absorption cross-sections for C_2, CN, CO, N_2, NO, and O_2 [37, 39]. The cross-sections for N_2, NO, and O_2 actually correspond to global absorption cross-sections, including dissociative photoionization, however these contributions are at least an order of magnitude less than photoionization [37] and are therefore treated as pure photoionization in this work. In addition, photoionization of CH and H_2 have been added in this work using absorption cross-sections taken from [140] and [144, 156], respectively, and are plotted in Fig. (3.3). The sharp drop-offs in the CH and H_2 cross-sections correspond to the ionization energy of those molecules. For example, the ionization energy of H_2 is approximately 15.6 eV or about 126 000 cm^{-1}. Therefore, only photons with at least that much energy can ionize H_2.

An example hydrogen absorption spectrum is shown in Fig. (3.4) for a pure hydrogen plasma in LTE, at a temperature and pressure of 6000 K and 0.3 bar respectively. Under these conditions, H_2 accounts for just 0.1 % of the mixture by volume, however the Lyman and Werner bands dominate the absorption spectrum. Photoionization of H_2 is the dominate contribution to the absorption spectrum for wavenumbers above the ionization energy.

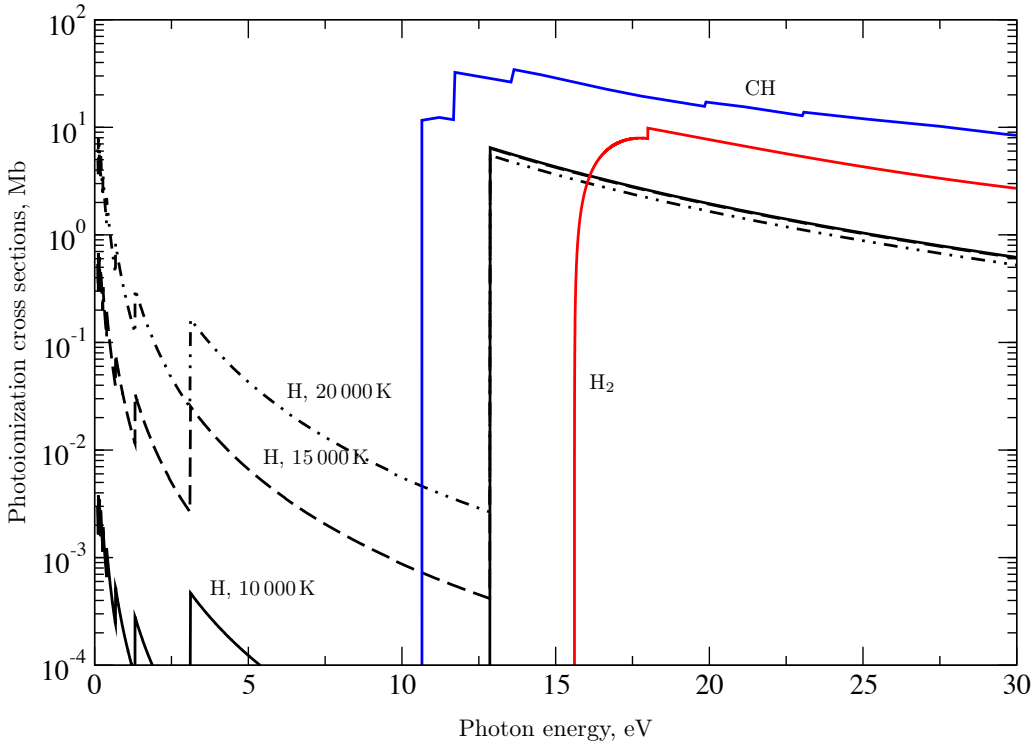

Figure 3.3.: *Equilibrium photoionization absorption cross-sections of CH, H, and H_2, used in this work. Data for each species has been taken from [140], [42], and [144, 156], respectively.*

Other bound-free mechanisms

The HTGR databse includes photodetachment of the C^-, N^-, and O^- anions [37, 39]. In general, these processes are not well understood. The database relies on simple absorption cross-sections related to the most dominate contributions to the photodetachment of each species. Typically, these species are not included in CFD calculations for atmospheric entry flows. In this case, the populations of the negative ions are computed assuming a Saha equilibrium at T_e.

Schumann-Runge photodissociation of O_2 is also considered, using LTE absorption cross-sections compiled in [37]. The extension to a MT approach is presented by Lamet *et al.* [43].

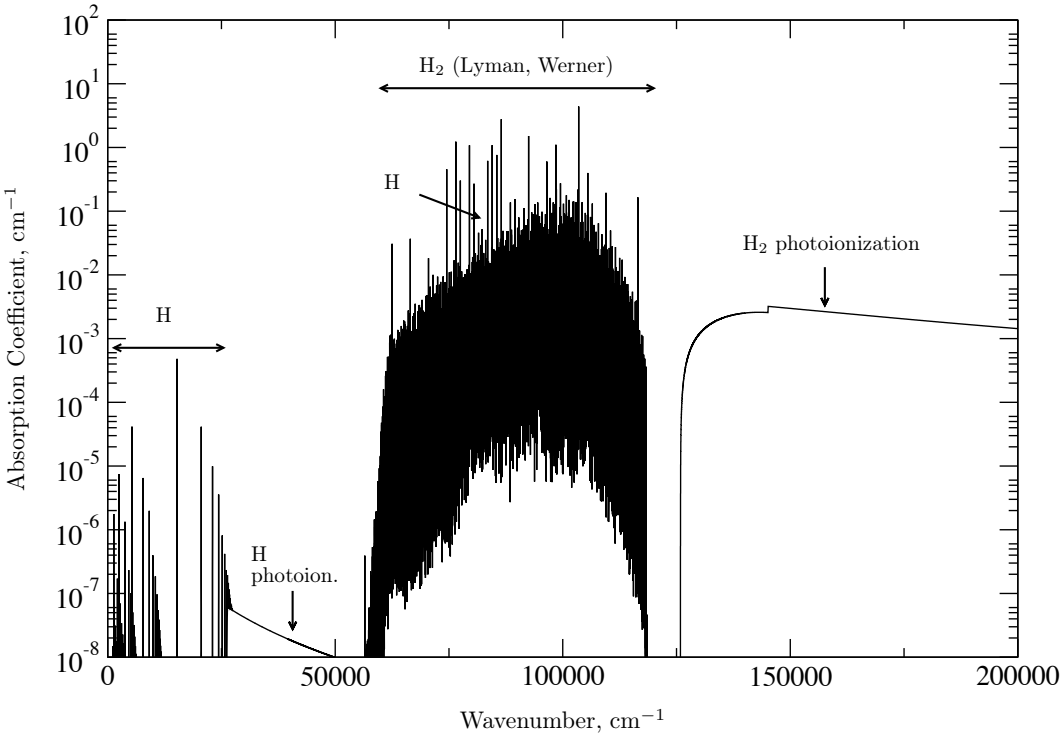

Figure 3.4.: *LTE hydrogen absorption spectrum at* $T = 6000\,\mathrm{K}$ *and* $p = 0.3\,\mathrm{bar}$.

3.3.3. Free-Free Processes

Free-free transitions, known as Bremsstrahlung radiation, occur when an electron emits a photon after passing through the electric field of a neutral or ionic species. Bremsstrahlung radiation of the atomic ions C^+, N^+, and O^+ is considered using Kramers' formula [157] corrected by a Gaunt factor [37, 39]. Inverse Bremsstrahlung radiation of C [39], and N, O, N_2, and O_2 [37] is also included through estimated absorption cross-sections obtained from the literature.

3.4. The Hybrid Statistical Narrow Band Model

It is evident from the previous sections that the accurate solution of the radiant intensity field requires a massive computational undertaking. To solidify this fact, recall that the RTE must be integrated along lines of sight passing through each point in the flow field, in every direction, and at every wavenumber. The emission and absorption coefficients, required to solve the RTE, are dependent on the local energy level populations of each species which may change rapidly throughout the flow field, thanks to the strong thermochemical nonequilibrium that is characteristic of hypersonic flows. In addition, because of the quantized nature of bound-bound transitions, the emission and absorption coefficients have strong spectral variations, requiring millions of spectral points to accurately resolve the spectral intensity for typical atmospheric entry problems. The computational complexity is further increased when coupled solutions are needed, as a new intensity field is required for each update of the radiative source terms.

In this section, the HSNB model is described which significantly reduces the computational complexity of computing the radiative intensity by decreasing spectral detail of the resulting solution. To begin, we recall that contributions of each radiative mechanism to the spectral emission and absorption coefficients are additive, allowing Eq. (3.3) to be rewritten as

$$I_\sigma(s) = I_\sigma(0) \prod_{k\in\mathcal{R}} \tau_\sigma^k(0,s) + \sum_{k\in\mathcal{R}} \int_0^s \eta_\sigma^k(s') \prod_{k'\in\mathcal{R}} \tau_\sigma^{k'}(s',s)\, ds', \tag{3.46}$$

where $\mathcal{R}$ is the set of all considered radiative mechanisms (atomic lines, molecular systems, and continuum processes) and the superscripts k and k' represent contributions to the emission coefficient and transmissivities of an individual radiative mechanism.

Using $\overline{X}^{\Delta\sigma}$ to denote the band-averaged quantity

$$\overline{X}^{\Delta\sigma} \equiv \frac{1}{\Delta\sigma}\int_{\sigma_1}^{\sigma_2} X\, d\sigma, \tag{3.47}$$

for a spectral narrow-band $\Delta\sigma$, ranging from σ_1 to σ_2, integration of Eq. (3.46) over a narrow-band yields

$$\overline{I_\sigma(s)}^{\Delta\sigma} = \overline{I_\sigma(0)}^{\Delta\sigma}\prod_{k\in\mathcal{R}}\overline{\tau_\sigma^k(0,s)}^{\Delta\sigma} + \sum_{k\in\mathcal{R}}\overline{I_\sigma^k(s)}^{\Delta\sigma}, \tag{3.48}$$

where the band-averaged intensity associated with contribution k is given as

$$\overline{I_\sigma^k(s)}^{\Delta\sigma} = \int_0^s \overline{\eta_\sigma^k(s')\tau_\sigma^k(s',s)}^{\Delta\sigma}\prod_{\substack{k'\in\mathcal{R}\\ k'\neq k}}\overline{\tau_\sigma^{k'}(s',s)}^{\Delta\sigma}\, ds'. \tag{3.49}$$

The following assumptions have been made to arrive at Eqs. (3.48) and (3.49):

1. absorption is statistically uncorrelated from the band-averaged boundary intensity over a narrow-band, and
2. only self absorption is correlated with emission for a narrow-band.

The first assumption is generally valid because only highly emissive boundaries are considered in this work, and thus

$$\overline{I_\sigma(0)}^{\Delta\sigma} \approx \bar{\epsilon}^{\Delta\sigma}\,\overline{I_\sigma^b(T_{\text{wall}})}^{\Delta\sigma}. \tag{3.50}$$

The second assumption is more subtle, but is likely valid as there are no physical reasons for the absorption of one mechanism to be significantly correlated to the emission of another.

Lamet *et al.* [55] have proposed to separate the set of radiative mechanisms into three groups: 1) optically thick molecular systems, 2) optically thin molecular systems and continua, and 3) atomic lines. The band-averaged quantities required in Eq. (3.48) can then be computed using a specific model, depending on which of the three groups the contribution belongs. This allows the total intensity to be split according to

$$\overline{I_\sigma}^{\Delta\sigma} = \overline{I_\sigma^{\text{bound}}}^{\Delta\sigma} + \overline{I_\sigma^{\text{thick}}}^{\Delta\sigma} + \overline{I_\sigma^{\text{box}}}^{\Delta\sigma} + \overline{I_\sigma^{\text{at}}}^{\Delta\sigma}, \tag{3.51}$$

where $\overline{I_\sigma^{\text{bound}}}^{\Delta\sigma}$, $\overline{I_\sigma^{\text{thick}}}^{\Delta\sigma}$, $\overline{I_\sigma^{\text{box}}}^{\Delta\sigma}$, and $\overline{I_\sigma^{\text{at}}}^{\Delta\sigma}$ correspond to the band-averaged intensities from the boundaries and the three groups listed above, respectively. Optically thick systems are treated using a statistical narrow band approach, detailed in Section 3.4.1, while thin systems and continua are treated with a simple box model presented in Section 3.4.2. Due to the relatively small number of lines associated with electronic transitions of atoms, atomic lines are treated using a full line-by-line (LBL) approach, discussed in Section 3.4.3. When the groups are coupled together, the resulting method is called the Hybrid Statistical Narrow Band model [55].

3.4.1. Optically Thick Molecular Systems

The molecular systems presented in Section 3.3 are considered thick if the optical depth of the system $\max_\sigma(\kappa_\sigma^k l)$ is greater than 0.1 for a homogeneous slab of pure gas in thermal equilibrium at $T = 8000\,\text{K}$, $p = 2\,\text{atm}$, and $l = 10\,\text{cm}$. This criterion represents a conservative estimate for typical atmospheric entry conditions.

For optically thick systems, the self absorption term in Eq. (3.49) is approximated as

$$\overline{\eta_\sigma^k(s')\tau_\sigma^k(s',s)}^{\Delta\sigma} = \overline{\frac{\eta_\sigma^k(s')}{\kappa_\sigma^k(s')}\frac{\partial}{\partial s'}\tau_\sigma^k(s',s)}^{\Delta\sigma} \approx \overline{\frac{\eta_\sigma^k(s')}{\kappa_\sigma^k(s')}}^{\Delta\sigma}\frac{\partial}{\partial s'}\overline{\tau_\sigma^k}^{\Delta\sigma}(s',s). \tag{3.52}$$

Under thermal equilibrium conditions, this approximation is valid because the emission and absorption coefficients satisfy Kirchhoff's law, and thus the ratio is equal to the Planck function, Eq. (3.2), and is uncorrelated over a narrow band to the transmissivity of the system. Lamet *et al.* [55] have shown that Eq. (3.52) also remains valid in thermal nonequilibrium for the range of conditions representative of atmospheric entry flows. For example, it was shown that for an extreme temperature ratio of $T_r/T_v = 2$, the maximum error introduced by the splitting in Eq. (3.52) for the N_2 Birge-Hopfield 2 system was less than 10 % and in general, far less than 1 %.

We now consider the intensity along a discretized ray with constant thermochemical properties between points s_i such that $\phi_\sigma(s) = \phi_\sigma(s_i)$ for $s_i \leq s < s_{i+1}$, where ϕ_σ represents any spectral radiative property. Inserting Eq. (3.52) into Eq. (3.49), the band-averaged intensity associated with a thick molecular system k at point s_j along such a ray may be expressed as

$$\overline{I_\sigma^k(s_j)}^{\Delta\sigma} = \sum_{i=1}^{j-1}\left[\overline{\tau_\sigma^k(s_{i+1},s_j)}^{\Delta\sigma} - \overline{\tau_\sigma^k(s_i,s_j)}^{\Delta\sigma}\right]\overline{\frac{\eta_\sigma^k}{\kappa_\sigma^k}(s_i)}^{\Delta\sigma}\prod_{\substack{k'\in\mathcal{R}\\k'\neq k}}\overline{\tau_\sigma^{k'}(s_i^*,s_j)}^{\Delta\sigma}, \tag{3.53}$$

where the mean equivalent point s_i^* has been introduced, such that

$$\overline{\tau_\sigma^k(s_i^*,s_j)}^{\Delta\sigma} \equiv \sqrt{\overline{\tau_\sigma^k(s_i,s_j)}^{\Delta\sigma}\,\overline{\tau_\sigma^k(s_{i+1},s_j)}^{\Delta\sigma}}, \tag{3.54}$$

in order to simplify the spatial integration in Eq. (3.49). The introduction of s_i^* is a pragmatic choice with little impact on the solution (e.g., see [71]).

The band-averaged emission to absorption coefficient ratio is only a function of the local state of the gas, and thus can be easily tabulated. What remains is to define how to compute the mean transmissivity which depends on integration along the ray.

Uniform path

The SNB model assumes that individual lines are randomly located within a narrow band and that the strengths of the lines follow a given probability distribution. We first consider a homogeneous path of length l. Meyer and Goody [136] have shown that the mean transmissivity of a narrow band along this path will be

$$\overline{\tau_\sigma(l)}^{\Delta\sigma} = \exp\left(-\frac{\overline{W}}{\delta}\right), \tag{3.55}$$

where $\delta = \Delta\sigma/N$ is the average line spacing for the N lines in the spectral band and $\overline{W}$ is the mean black equivalent line width of the band, defined as

$$\overline{W} = \frac{1}{N}\sum_{i=1}^{N}\int_{-\infty}^{+\infty}\left[1-\exp(-\kappa_\sigma^i\, l)\right]d\sigma, \tag{3.56}$$

with κ_σ^i representing the contribution of the i^{th} line to the spectral absorption coefficient.

Table 3.2 provides a summary of analytical expressions for the mean black equivalent line width, assuming Lorentz or Doppler line shapes with unique half widths γ_0^L and γ_0^D in the band, for three common line strength probability distribution functions. It is clear from the table that $\overline{W}_L/\delta$ and $\overline{W}_D/\delta$ depend on only three parameters, $\overline{k}$, $\overline{\beta}_L$, and $\overline{\beta}_D$, regardless of the line intensity distribution function. $\overline{k}$ is the mean absorption coefficient per partial pressure of the absorbing species, while $\overline{\beta}$ characterizes the degree of line overlap for Lorentz or Doppler line shapes.

Unfortunately, there is no analytical expression for the mean black equivalent line width in the Voigt regime. The approximate expression of Ludwig *et al.* [158] has been retained in this work

Table 3.2.: *Summary of analytical relationships for mean black equivalent line widths for a uniform path of length l, corresponding to different probability distribution functions $P(S)$ of line strength S. $\overline{k}$ is the mean absorption coefficient per partial pressure p_a of species a.*

$P(S)$	$\overline{k}$	Lorentz profile		Doppler profile	
		$\overline{\beta}_L$	$\overline{W}_L/\delta$	$\overline{\beta}_D$	$\overline{W}_D/\delta$
Uniform $\delta(S-S_0)$	$\frac{S_0}{\delta}$	$\frac{\gamma_0^L}{\delta}$	$2\pi\overline{\beta}_L L\Big(\frac{p_a l\overline{k}}{2\pi\overline{\beta}_L}\Big)^a$	$\frac{\gamma_0^D}{\delta}\sqrt{\frac{\pi}{\ln 2}}$	$\overline{\beta}_D D\Big(\frac{p_a l\overline{k}}{\overline{\beta}_D}\Big)^b$
Goody exponential $\frac{1}{S_0}\exp\Big(-\frac{S}{S_0}\Big)$	$\frac{S_0}{\delta}$	$\frac{\gamma_0^L}{\delta}$	$\frac{p_a l\overline{k}}{\sqrt{1+\frac{p_a l\overline{k}}{4\overline{\beta}_L}}}$	$\frac{\gamma_0^D}{\delta}\sqrt{\frac{\pi}{\ln 2}}$	$\overline{\beta}_D E\Big(\frac{p_a l\overline{k}}{\overline{\beta}_D}\Big)^c$
Malkmus tail inverse-exponential $\frac{\exp\big(-\frac{S}{S_m}\big)-\exp\big(-\frac{RS}{S_m}\big)}{S\ln R}$	$\frac{S_m}{\delta\ln R}$	$\frac{\pi\gamma_0^L}{\delta\ln R}$	$2\overline{\beta}_L\Big(\sqrt{1+\frac{p_a l\overline{k}}{\overline{\beta}_L}}-1\Big)$	$\frac{\gamma_0^D}{\delta\ln R}\sqrt{\frac{\pi}{\ln 2}}$	$\overline{\beta}_D H\Big(\frac{p_a l\overline{k}}{\overline{\beta}_D}\Big)^d$

[a] $L(x) = xe^{-x}[I_0(x)+I_1(x)]$
[b] $D(x) = \frac{1}{\sqrt{\pi}}\int_{-\infty}^{\infty}[1-\exp(-xe^{-\xi^2})]d\xi$
[c] $E(x) = \frac{1}{\sqrt{\pi}}\int_{-\infty}^{\infty}\frac{xe^{-\xi^2}}{1+xe^{-\xi^2}}d\xi$
[d] $H(x) = \frac{1}{\sqrt{\pi}}\int_{-\infty}^{\infty}\ln(1+xe^{-\xi^2})d\xi$

for computing the Voigt width as

$$\begin{aligned}\frac{\overline{W}_V}{\delta} &= p_a l\overline{k}\sqrt{1-\Omega^{-1/2}},\\ \Omega &= \left[1-\left(\frac{1}{p_a l\overline{k}}\frac{\overline{W}_D}{\delta}\right)^2\right]^{-2}+\left[1-\left(\frac{1}{p_a l\overline{k}}\frac{\overline{W}_L}{\delta}\right)^2\right]^{-2}-1.\end{aligned} \tag{3.57}$$

The Ludwig formula has the advantage that the correct solution is obtained in a pure Lorentzian or Doppler regime.

Non-uniform path

Both the classical Curtis-Godson and Lindquist-Simmons approaches [159] are considered for computing $\overline{W}/\delta$ along a non-uniform path. The Curtis-Godson method assumes that non-uniform paths may be treated the same as a uniform path, using path-averaged properties. The pressure path length u, mean absorption coefficient $\overline{k}^*$ per partial pressure p_a of the absorbing species, and mean overlap parameter $\overline{\beta}^*$ are defined as

$$u = \int_{s'}^{s} p_a(s'')ds'', \tag{3.58}$$

$$\overline{k}^* = \frac{1}{u}\int_{s'}^{s} p_a(s'')\overline{k}(s'')ds'', \tag{3.59}$$

$$\overline{\beta}^* = \frac{1}{u\overline{k}^*}\int_{s'}^{s} p_a(s'')\overline{k}(s'')\overline{\beta}(s'')ds''. \tag{3.60}$$

The expressions given in Table 3.2 and Eq. (3.57) can then be reused along a non-homogeneous path by replacing $p_a l$ with u, $\overline{k}$ with $\overline{k}^*$, and $\overline{\beta}_{L,D}$ with $\overline{\beta}^*_{L,D}$. The resulting expressions for the Lorentz and Doppler mean black equivalent line widths are given in Table 3.3 for the line strength distributions of interest in this work and Eq. (3.57) is updated accordingly,

$$\begin{aligned}\frac{\overline{W}_V}{\delta} &= u\overline{k}^*\sqrt{1-\Omega^{-1/2}},\\ \Omega &= \left[1-\left(\frac{1}{u\overline{k}^*}\frac{\overline{W}_D}{\delta}\right)^2\right]^{-2}+\left[1-\left(\frac{1}{u\overline{k}^*}\frac{\overline{W}_L}{\delta}\right)^2\right]^{-2}-1.\end{aligned} \tag{3.61}$$

The Lindquist-Simmons approach consists in finding a suitable expression for the local spatial derivative of the mean black equivalent width in the Lorentz and Doppler regimes and then computing $\overline{W}/\delta$ through numerical integration,

$$\frac{\overline{W}}{\delta}(s',s) = -\int_{s'}^{s}\frac{1}{\delta}\frac{\partial}{\partial s''}\overline{W}(s'',s)ds'', \tag{3.62}$$

where the derivative $\partial\overline{W}/\partial s''$ is a function of both local and averaged parameters. Table 3.3 provides the expressions necessary to compute the mean black equivalent width derivatives for both Lorentz and Doppler regimes [160]. The Voigt mean black equivalent widths are then obtained using Eq. (3.61) as in the Curtis-Godson approximation.

3.4.2. Optically Thin Molecular Systems and Continua

The band-averaged intensity associated with optically thin systems and continua may be expressed as

$$\overline{I^k_\sigma(s_j)}^{\Delta\sigma} = \sum_{i=1}^{j-1}\overline{\eta^k_\sigma(s_i)}^{\Delta\sigma}\prod_{k'\in\mathcal{R}}\overline{\tau^{k'}_\sigma(s^*_i,s_j)}^{\Delta\sigma}, \tag{3.63}$$

Table 3.3.: *Summary of analytical relationships for mean black equivalent line widths for a non-uniform path using the Curtis-Godson and Lindquist-Simmons approximations.*

Line shape	Curtis-Godson	Lindquist-Simmons
$P(S)$	$\frac{\overline{W}}{\delta}(s',s)$	$-\frac{1}{\delta}\frac{\partial}{\partial s''}\overline{W}(s'',s)\Big[p_a(s'')\overline{k}(s'')\Big]^{-1}$
Lorentz: $x = u\overline{k}^*/2\overline{\beta_L}^*$, $\rho = \overline{\beta_L}(s'')/\overline{\beta_L}^*$		
Malkmus	$2\overline{\beta_L}^*(\sqrt{1+2x}-1)$	$\frac{2x\rho+(1-\rho^2)\sqrt{1+2x}}{(1-\rho^2+2x)\sqrt{1+2x}}$
Doppler: $x = u\overline{k}^*/\overline{\beta_D}^*$, $\rho = \overline{\beta_D}(s'')/\overline{\beta_D}^*$		
Goody	$\overline{\beta_D}^* E(x)^a$	$\frac{1}{\sqrt{\pi}}\int_{-\infty}^{+\infty}\frac{\exp(-\xi^2)}{[1+x\exp(-\rho^2\xi^2)]^2}d\xi$
Malkmus	$\overline{\beta_D}^* H(x)^a$	$\frac{1}{\sqrt{\pi}}\int_{-\infty}^{+\infty}\frac{\exp(-\xi^2)}{1+x\exp(-\rho^2\xi^2)}d\xi$

[a] $E(x)$ and $H(x)$are defined in Table 3.2.

where self absorption is assumed to be uncorrelated to the emission of the mechanism k. This is valid for optically thin systems because the spectral transmissivity is nearly unity over the entire band. In the case of continuum contributions, Eq. (3.63) is also valid due to the low spectral variability of continuum absorption and emission coefficients. For example, the photoionization absorption cross-sections shown in Fig. (3.3) may be assumed to be constant over a narrow spectral band.

The band averaged transmissivity for optically thin systems and continua are computed using the simple Box model [145], such that

$$\overline{\tau_\sigma^k(s',s)}^{\Delta\sigma} = \exp\Big(-\int_{s'}^{s}\overline{\kappa_\sigma^k(s'')}^{\Delta\sigma}\,ds''\Big). \tag{3.64}$$

In practice, the use of the Box model allows us to reduce all optically thin systems and continua into a single pseudo mechanism which we denote with super script "box" notation. Denoting the set of optically thin and continua contributions as $\mathcal{R}_{\text{box}}$, Eq. (3.49) may be summed over all such contributions to yield

$$\begin{aligned}\overline{I_\sigma^{\text{box}}(s_j)}^{\Delta\sigma} &= \sum_{k\in\mathcal{R}_{\text{box}}}\overline{I_\sigma^k(s_j)}^{\Delta\sigma}\\ &= \sum_{i=1}^{j-1}\overline{\eta_\sigma^{\text{box}}(s_i)}^{\Delta\sigma}\,\overline{\tau_\sigma^{\text{box}}(s_i^*,s_j)}^{\Delta\sigma}\prod_{k'\in\mathcal{R}'_{\text{box}}}\overline{\tau_\sigma^{k'}(s_i^*,s_j)}^{\Delta\sigma},\end{aligned} \tag{3.65}$$

where $\mathcal{R}'_{\text{box}}$ denotes all contributions not belonging to $\mathcal{R}_{\text{box}}$, and the pseudo mean transmissivity for all Box model contributions simplifies to,

$$\overline{\tau_\sigma^{\text{box}}(s_i^*,s_j)}^{\Delta\sigma} = \exp\Bigg[-\frac{(s_{i+1}-s_i)}{2}\overline{\kappa_\sigma^{\text{box}}(s_i)}^{\Delta\sigma} - \sum_{k=i+1}^{j-1}(s_{k+1}-s_k)\,\overline{\kappa_\sigma^{\text{box}}(s_k)}^{\Delta\sigma}\Bigg]. \tag{3.66}$$

based on Eqs. (3.54) and (3.64) for the discretized ray discussed in Section 3.4.1. The pseudo mean

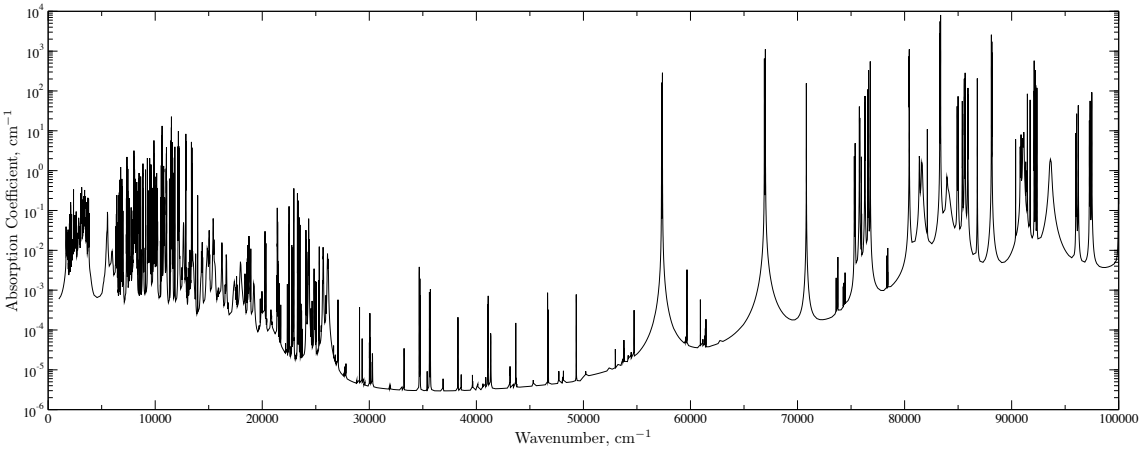

Figure 3.5.: *Absorption coefficient spectrum of N, O, N^+, and O^+ lines for the wavenumber range* $1000\,\mathrm{cm}^{-1}$ *to* $100\,000\,\mathrm{cm}^{-1}$ *at* 1 bar *and* 15 000 K. *Mole fractions for N, O, N^+, O^+ are 0.67, 0.13, 0.08, and 0.02 respectively.*

absorption and emission coefficients are given simply by the sum over all contributions in $\mathcal{R}_{\mathrm{box}}$,

$$\overline{\kappa_\sigma^{\mathrm{box}}(s)}^{\Delta\sigma} = \sum_{k\in\mathcal{R}_{\mathrm{box}}} \overline{\kappa_\sigma^{k}(s)}^{\Delta\sigma}, \text{and} \tag{3.67}$$

$$\overline{\eta_\sigma^{\mathrm{box}}(s)}^{\Delta\sigma} = \sum_{k\in\mathcal{R}_{\mathrm{box}}} \overline{\eta_\sigma^{k}(s)}^{\Delta\sigma}. \tag{3.68}$$

The use of Eq. (3.66) can greatly reduce the number of exponential and square-root evaluations required to compute the transmissivity of all thin and continua contributions, especially when a large number of spatial points or radiative mechanisms are required for accurate radiative heat transfer calculations.

3.4.3. Atomic Lines

Unfortunately, the SNB and Box models are not suitable for atomic spectra due to the weak spectral density of atomic lines [55]. Therefore, the contribution of atomic lines to the band-averaged intensity is taken to be

$$\overline{I_\sigma^{\mathrm{at}}(s_j)}^{\Delta\sigma} = \sum_{i=1}^{j-1} \overline{\left[\tau_\sigma^{\mathrm{at}}(s_{i+1},s_j) - \tau_\sigma^{\mathrm{at}}(s_i,s_j)\right]\frac{\eta_\sigma^{\mathrm{at}}}{\kappa_\sigma^{\mathrm{at}}}(s_i)}^{\Delta\sigma} \prod_{\substack{k\in\mathcal{R}\\ k\neq\mathrm{at}}} \overline{\tau_\sigma^{k}(s_i^*,s_j)}^{\Delta\sigma}, \tag{3.69}$$

where $\overline{[\tau_\sigma^{\mathrm{at}}(s_{i+1},s_j) - \tau_\sigma^{\mathrm{at}}(s_i,s_j)]\eta_\sigma^{\mathrm{at}}/\kappa_\sigma^{\mathrm{at}}(s_i)}^{\Delta\sigma}$ is obtained exactly from a LBL calculation. Handling atomic spectra in this way is not too penalizing because the typical number of atomic lines is relatively minimal (on the order of one thousand) compared to that of molecular systems which may contain millions of individual lines. A notable example is the CO_2 infrared spectrum which contains over 600 million lines [141].

In addition to the significantly smaller line count, the spacing between atomic lines allows for a highly reduced spectral mesh size when only atoms are considered. Fig. (3.5) shows an example atomic absorption spectrum obtained with the HTGR database, relevant to atmospheric reentry, in which significant spacing is present between many of the lines. A notable contribution of this work, first presented in [161], was to develop a spectral mesh adaptation algorithm which minimizes the number of spectral points required to compute the band-averaged product in Eq. (3.69).

Fixed point adaptive mesh

Da Silva [162] has developed fixed, 5, 7, 9, and 11 point stencils for approximating the Voigt line shape based on the estimated line center, line wing, and far wing regions of each line. For a given line, the estimated distance from the line center, to the line wing, $\Delta\sigma_W$, and far wing, $\Delta\sigma_{FW}$, boundaries are computed by

$$\Delta\sigma = \frac{2}{\pi}\left(1+\zeta\right)\gamma_L + \beta\gamma_D. \tag{3.70}$$

For $\Delta\sigma_W$, the values of the $\{\zeta,\beta\}$ constants are taken to be $\{1, 1.8\}$, while for $\Delta\sigma_{WF}$, they are chosen as $\{2.6, 5.8\}$ based on an analysis of Lorentz and Doppler line profiles by Lino da Silva. The 11 point line stencil, which will be used in this work, is then taken to be $\sigma_{ul}, \sigma_{ul} \pm \Delta$ where Δ is the 5 point half-stencil

$$\Delta = \left\{\tfrac{1}{8}\gamma_V, \tfrac{1}{2}\gamma_V, \Delta\sigma_W, \Delta\sigma_{FW}, \tfrac{25}{2}\gamma_V\right\}.$$

$\gamma_V = \sqrt{\gamma_D^2 + \gamma_L^2}$ is the estimated Voigt half-width. For each atomic line, the 11 points above are added to the overall spectral mesh. It was shown that such a mesh provides a reasonably accurate resolution of line intensities for low pressure atmospheric entry conditions due to the low degree of line broadening in that regime [162]. This method will therefore be used as a benchmark for a slightly more detailed algorithm presented in the next section.

Augmenting with bisection

The fixed point method above is likely to work well in spectral regions with a high number of electronic transitions and with a large degree of line overlap because the majority of the points are distributed around the line centers. For areas in which there are large distances between neighboring line centers, the method is likely to provide poor estimates of spectral quantities due to the large error in interpolating the spectral values in the far line wing regions.

For this reason, the 11 point stencil in the previous section has been modified to ensure the far line wing regions are correctly handled. To begin, the complete line list for all atoms considered is first ordered by ascending line center values. Then, each region between two consecutive lines is considered. It is assumed that consecutive lines have little overlap, and thus the regions around each line center can be assumed to be well approximated by the line shape corresponding to that line alone, and not by other lines in the same vicinity. For each consecutive line pair, an adaptive mesh is then created based on the two corresponding line shapes. We will denote the left line shape properties with the superscript L, and the right properties with an R. First, the approximate "center" point between each line is defined simply as $\sigma_{LR} = (\sigma_{ul}^L + \sigma_{ul}^R)/2$. Next the following set of points are added to the mesh based on the 11 point stencil above, but ensuring that points added for each line do not overlap one another.

$$\sigma_{ul}^L + \Delta^L, \quad \forall\, \Delta^L < \sigma_{LR} - \sigma_{ul}^L$$

$$\sigma_{ul}^R - \Delta^R, \quad \forall\, \Delta^R < \sigma_{ul}^R - \sigma_{LR}$$

For lines which are sufficiently close, the above procedure will prevent unnecessary points from being added to the spectral grid. Note that it may easily be adapted to any other fixed point stencil based on line shape widths.

For lines which are very far apart in comparison to their line widths, the region around σ_{LR} will likely be poorly resolved. Therefore, the above set of points are augmented by adding points recursively to the center region by successively bisecting the two intervals closest to the last points added by the stencil above until the spacing between the outermost two stencil points for each line is at least half the size of the spacing between the outermost stencil point and the next point. In other words, two bisection fronts are propagated towards the line centers until the spacing between points matches that of the two outermost stencil points of each line.

Fig. (3.6) and Fig. (3.7) show both the absorption spectra and band averaged curves of growth for two spectral regions from Fig. (3.5) as obtained using the adaptive meshes compared to high resolution spectra. In the small wavenumber range $10\,000\,\mathrm{cm}^{-1}$ to $12\,000\,\mathrm{cm}^{-1}$ shown in Fig. (3.6),

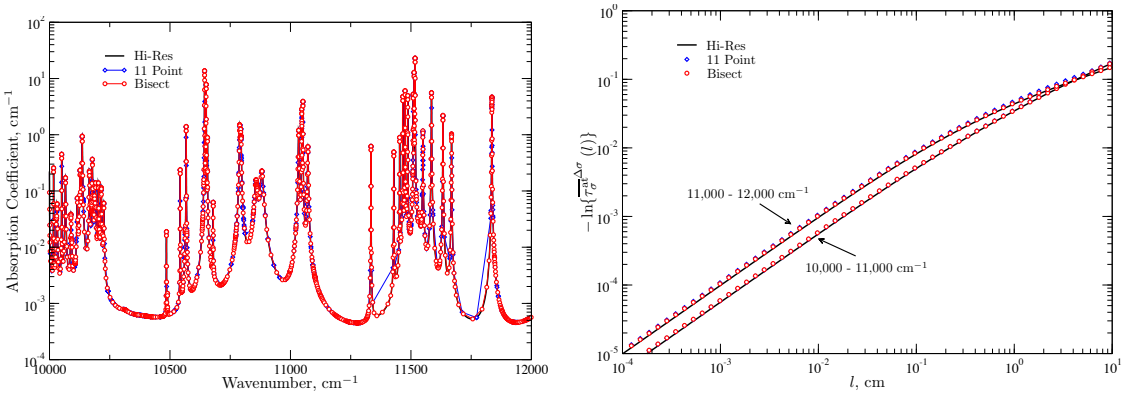

(a) *Absorption coefficients.* **(b)** *Curves of growth.*

Figure 3.6.: *Atomic absorption coefficients and curves of growth using adaptive spectral grids, compared to a high-resolution mesh, for the spectral range* $10\,000\,\mathrm{cm}^{-1}$ *to* $12\,000\,\mathrm{cm}^{-1}$. *Same conditions as in Fig. (3.5).*

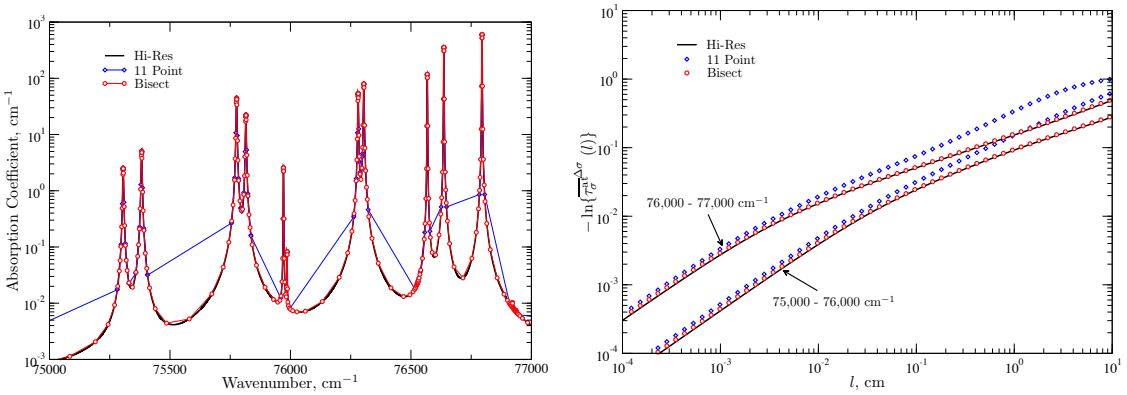

(a) *Absorption coefficients.* **(b)** *Curves of growth.*

Figure 3.7.: *Atomic absorption coefficients and curves of growth using adaptive spectral grids, compared to a high-resolution mesh, for the spectral range* $75\,000\,\mathrm{cm}^{-1}$ *to* $77\,000\,\mathrm{cm}^{-1}$. *Same conditions as in Fig. (3.5).*

both adaptive methods work well. This is largely due to the fact that there are many spectral lines close to one another, and while some of them are very weak, they still contribute grid points in the wing regions of stronger lines. The differences become much more apparent in the larger wavenumber range $75\,000\,\mathrm{cm}^{-1}$ to $77\,000\,\mathrm{cm}^{-1}$ as in Fig. (3.7). Here, the atomic lines are far enough apart such that the 11 point stencil is not wide enough to encompass the far wing regions of some lines. Therefore, large interpolation errors are clearly visible in the absorption spectrum using only these points, while the points augmented with the bisection algorithm represent the true spectrum well. The affect this interpolation error has on the computed curves of growth is also clearly visible, with a significant error shown even at a column length of 1 mm for both band regions.

Conditions for line width calculations

A careful reader will note that the conditions for calculating the line widths in the previous subsections were not specified. In general, the spectral mesh should remain constant for all points in the flow field in order to integrate along each ray. However, the above mesh adaptation scheme

would generate different spectral meshes for each spatial location thanks to the variation in mixture temperatures and pressure.

In practice, the spectral mesh is computed using a "representative" spatial point from the flow field calculation. Using the temperatures and species number densities at this point, line widths are computed for each atomic line and the adaptive mesh is generated according to the procedure detailed in the previous subsections. The choice of this point is somewhat arbitrary. A pragmatic choice was made in this work to use the point with the maximum translational temperature as the representative point when generating the atomic spectral mesh. In order to investigate the utility of this choice, the adaptive spectral mesh size and error in the wall radiative heat flux relative to a high resolution mesh, associated with all locations in a typical flow field, are given in Fig. (3.8). From the figure, it is clear that the mesh size is loosely correlated with the combination of pressure and temperature, following the scaling of the line half widths discussed in Section 3.3.1. However, it is important to note that atomic line radiation is only one component of the total radiative heat flux and the errors shown in Fig. (3.8) are not indicative of the error on the total heat flux, when all contributions are included. A more thorough investigation of the impact the choice of representative flow field point has on the overall accuracy and efficiency of the HSNB method could be made in the future.

3.4.4. Putting It All Together: The HSNB Database

SNB parameters have been generated using the spectroscopic data from the HTGR database described in Section 3.3. SNB parameters for air systems were computed by Lamet *et al.* [55] while the majority of the parameters for contributions from carbonaceous species have been computed by Depraz *et al.* [137]. An SNB model for carbon dioxide was recently developed by Rivière *et al.* [142, 160] based on the extensive CDSD-4000 spectroscopic database [141]. Lastly, SNB parameters for the C_3 Swings and UV band systems, H_2 Lyman and Werner bands, as well as CH, H, and H_2 photoionization have been computed in this work based on the data presented in Section 3.3. Table 3.4 summarizes the parameters stored in the SNB database for the different types of radiative contributions.

Optically thick molecular systems

The SNB model is used to treat optically thick molecular systems. The SNB parameters, $\overline{k}$, $\overline{\eta}$, $\overline{\eta/\kappa}$, $\overline{\beta}_D$, and $\overline{\beta}_L$, have been tabulated for narrow bands of $1000\,\mathrm{cm}^{-1}$ ranging from $1000\,\mathrm{cm}^{-1}$ to $200\,000\,\mathrm{cm}^{-1}$ assuming a two-temperature model (ie: $T_h = T_r$, $T_v = T_{el} = T_e$). Air systems are treated with a temperature grid of $500 \leq T_r \leq 50\,000\,\mathrm{K}$ and $500 \leq T_v \leq 25\,000\,\mathrm{K}$ [55] while carbonaceous systems use a grid of $500 < T_r < 26\,000\,\mathrm{K}$ and $500 < T_v < 16\,000\,\mathrm{K}$ [137]. Extensions

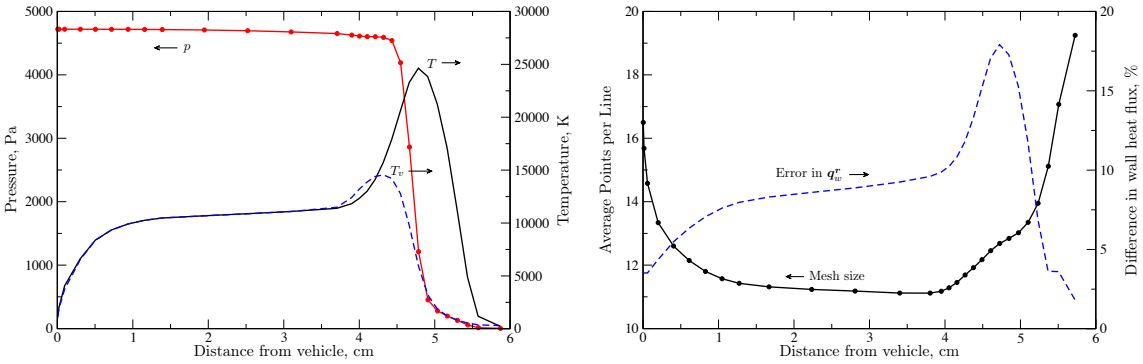

Figure 3.8.: *Example Fire II flow field (left) and adaptive spectral mesh characteristics obtained using each point in the flow field as the reference condition for line half widths (right) for lines of N, N^+, O, and O^+. Errors in wall heat flux are relative to that obtained using a high resolution spectral mesh.*

Table 3.4.: *Relationship between stored database quantities and SNB parameters required for each radiative contribution. Barred symbols in the table body represent stored quantities. p, p_a, and p_e are the mixture static pressure, partial pressure of the species on the absorption side of each process, and free-electron pressure, respectively, in* Pa.

Type / Model	# of Params.	$\overline{\kappa_\sigma}^{\Delta\sigma}$	$\overline{\eta_\sigma}^{\Delta\sigma}$	$\overline{\eta_\sigma/\kappa_\sigma}^{\Delta\sigma}$	$\overline{\beta}_D$	$\overline{\beta}_L$
Optically thick molecular systems (non-predissociative)						
SNB	5	$p_a\overline{k}(T_r,T_v)$	$p_a\overline{\eta}(T_r,T_v)$	$\overline{\eta/\kappa}(T_r,T_v)$	$\overline{\beta}_D(T_r,T_v)$	$p\overline{\beta}_L(T_r,T_v,10^5\,\text{Pa})10^{-5}$
Optically thick molecular systems (predissociative)						
SNB	6	$p_a\overline{k}(T_r,T_v)$	$p_a\overline{\eta}(T_r,T_v)$	$\overline{\eta/\kappa}(T_r,T_v)$	$\overline{\beta}_D(T_r,T_v)$	$\overline{a}(T_r,T_v)p+\overline{b}(T_r,T_v)$
Optically thin molecular systems						
Box	2	$p_a\overline{\kappa}(T_r,T_v)$	$p_a\overline{\eta}(T_r,T_v)$			
Atomic photoionization continua						
Box	3	$\frac{p_a}{Q_a(T_e)}\frac{T_e}{T_h}\left[\overline{\kappa^{\text{abs}}}(T_e)-\chi^{\text{neq}}\overline{\kappa^{\text{ie}}}(T_e)\right]$	$\frac{p_a}{Q_a(T_e)}\frac{T_e}{T_h}\chi^{\text{neq}}\overline{\eta^{\text{se}}}(T_e)$			
Molecular photoionization continua						
Box	3	$p_a\frac{T_e}{T_h}\left[\overline{\kappa^{\text{abs}}}(T_e)-\chi^{\text{neq}}\overline{\kappa^{\text{ie}}}(T_e)\right]$	$p_a\frac{T_e}{T_h}\chi^{\text{neq}}\overline{\eta^{\text{se}}}(T_e)$			
Photodissociation continua						
Box	3	$p_a\left[\frac{T_v}{T_h}\overline{\kappa^{\text{abs}}}(T_v)-\chi^{\text{neq}}\overline{\kappa^{\text{ie}}}(T_h)\right]$	$p_a\chi^{\text{neq}}\overline{\eta^{\text{se}}}(T_h)$			
Photodetachment continua						
Box	2	$p_a\frac{T_e}{T_h}\overline{\kappa}(T_e)$	$p_a\frac{T_e}{T_h}\overline{\eta}(T_e)$			
Free-free continua						
Box	2	$p_ap_e\frac{T_e}{T_h}\overline{\kappa}(T_e)$	$p_ap_e\frac{T_e}{T_h}\overline{\eta}(T_e)$			

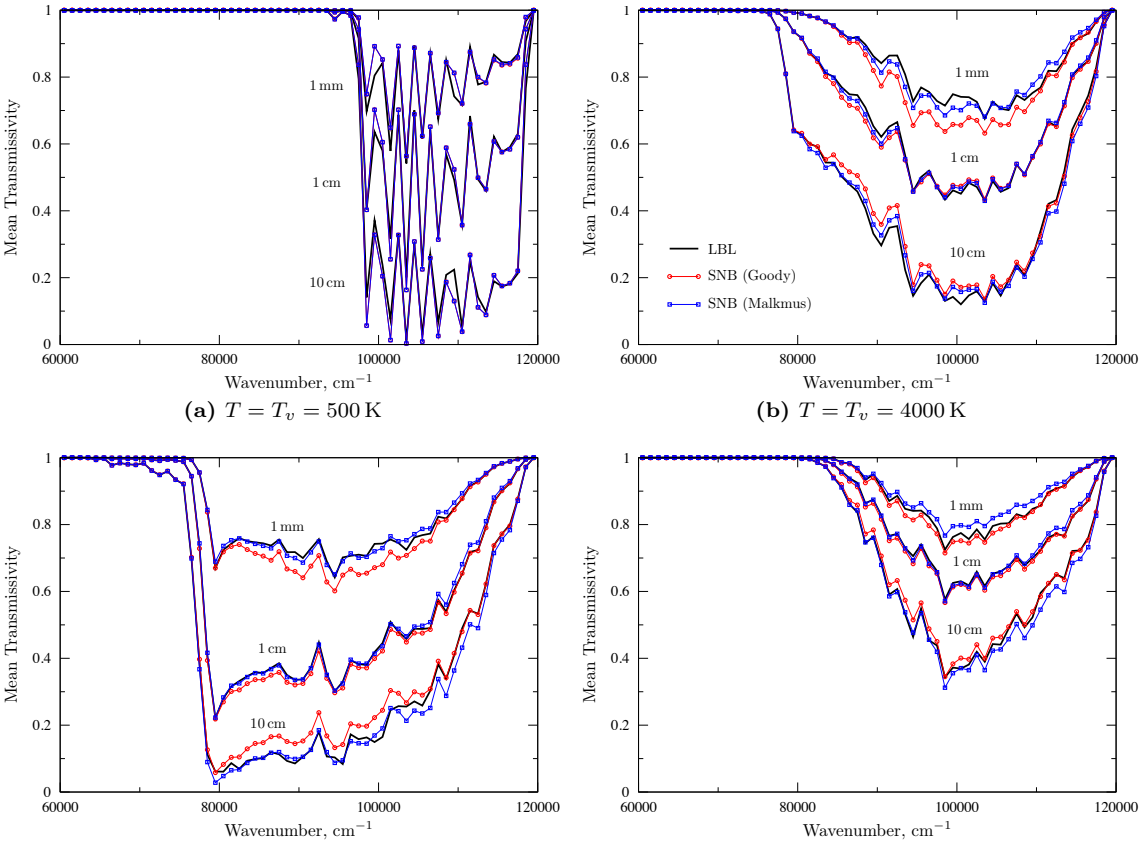

(a) $T = T_v = 500\,\mathrm{K}$ **(b)** $T = T_v = 4000\,\mathrm{K}$

(c) $T = T_v = 10\,000\,\mathrm{K}$ **(d)** $T = 10\,000\,\mathrm{K}$, $T_v = 1000\,\mathrm{K}$

Figure 3.9.: *Comparison of band-averaged transmissivities between full LBL and SNB models for the H_2 Werner system at* 1 atm.

of the expressions in Table 3.4 to account for cases when the electronic levels are not populated according to a Boltzmann distribution at T_v (ie: electronic specific CR or Boltzmann at $T_{el} \neq T_v$) have been previously reported by Lamet *et al.* [55].

The parameters $\overline{k}$, $\overline{\eta}$, and $\overline{\eta/\kappa}$ have been computed by averaging LBL spectra for each temperature condition and are stored per partial pressure of the absorbing species.

The mean overlap parameters, $\overline{\beta}_D$, and $\overline{\beta}_L$, have been adjusted using a non-linear least squares procedure to best match band-averaged curves of growth computed using LBL calculations in pure Doppler and Lorentz regimes (resp.). It was found that a Malkmus distribution best matched LBL results for the Lorentz overlapping parameter for all systems [55, 137]. Since Lorentz broadening is proportional to pressure, $\overline{\beta}_L$ is tabulated at a total pressure of 1 bar and the actual value is retrieved by multiplying by p in bar. When predissociative broadening is taken into account, two parameters, a and b, are tabulated to account for the constant offset, as shown in Table 3.4. Which group each species belongs to is shown graphically in Fig. (3.10).

For the Doppler overlap parameter, it was found that the Goody distribution gave the best results for air systems, while the Malkmus worked best for carbonaceous systems. A similar study was conducted in this work during the development of SNB parameters for the H_2 Lyman and Werner systems. Mean transmissivities for both systems using adjusted values of $\overline{\beta}_D$ assuming both Goody and Malkmus distributions have been systematically compared to LBL results for various temperature and pressure combinations. Example mean transmissivities for the H_2 Werner system at 1 atm are shown in Fig. (3.9). Based on this analysis, it was determined the Malkmus distribution was best suited for computing $\overline{\beta}_D$, in agreement with other non-air systems.

Optically thin molecular systems

Optically thin molecular systems are treated using the Box model as shown in Section 3.4.2. The required averaged quantities, $\overline{\kappa}$ and $\overline{\eta}$, have been tabulated using the same procedure as for the thick systems. Which systems are considered thick or thin is shown in Fig. (3.10).

Continua

Continua are also treated using the Box model. However, for each continuum process detailed in Sections. (3.3.2) and (3.3.3), the band-averaged parameters are only functions of a single temperature. Therefore, parameters for all continuum processes are tabulated using a single temperature. Nonequilibrium values can then be retrieved using the expressions in Table 3.4.

3.5. Concluding Remarks

In this chapter, the necessary ingredients for coupling radiation with the fluid conservation equations have been detailed. In particular the radiative heat flux, power, and photochemical mass production terms were given as integral functions of the radiant intensity field. The solution of the RTE for the intensity was also given, including appropriate boundary conditions typical of atmospheric entry problems.

The various bound-bound, bound-free, and free-free radiative mechanisms which contribute to the spectral emission and absorption coefficients of the gas have been summarized. These coefficients are computed with the HTGR database which has also been summarized in this chapter. In particular, a focus was placed on the implementation of nonequilibrium spectral emission and absorption coefficients for each type of radiative mechanism. The data required and their sources for each mechanism have been carefully enumerated, including mechanisms added to the database in this work. The new contributions include hydrogen lines, C_3 Swings and UV systems, as well as the photoionization of H, H_2, and CH.

The HSNB model has been described in detail, which combines the statistical narrow band, box, and adaptive line-by-line models as an efficient and accurate alternative to the full line-by-line solution of the intensity field. The narrow band parameters required for the model implementation have been thoroughly presented for each radiative mechanism. SNB parameters have been computed in this work for the H_2 Lyman and Werner systems, by adjusting the Doppler and Lorentz overlap parameters to fit curves of growth for each narrow band. Comparisons with band-averaged transmissivities computed with the line-by-line approach show excellent agreement with the resulting SNB parameters for these systems.

Lastly, a new adaptive mesh algorithm tailored to the spectra of atomic lines has also been presented in this work. The algorithm combines a simple fixed point stencil designed to accurately capture line centers with an adaptive bisection algorithm for the placement of spectral points in the far line wing regions of atomic lines. The computational benefits of this method as compared to conventional line-by-line approaches will be demonstrated in Chapter 7.

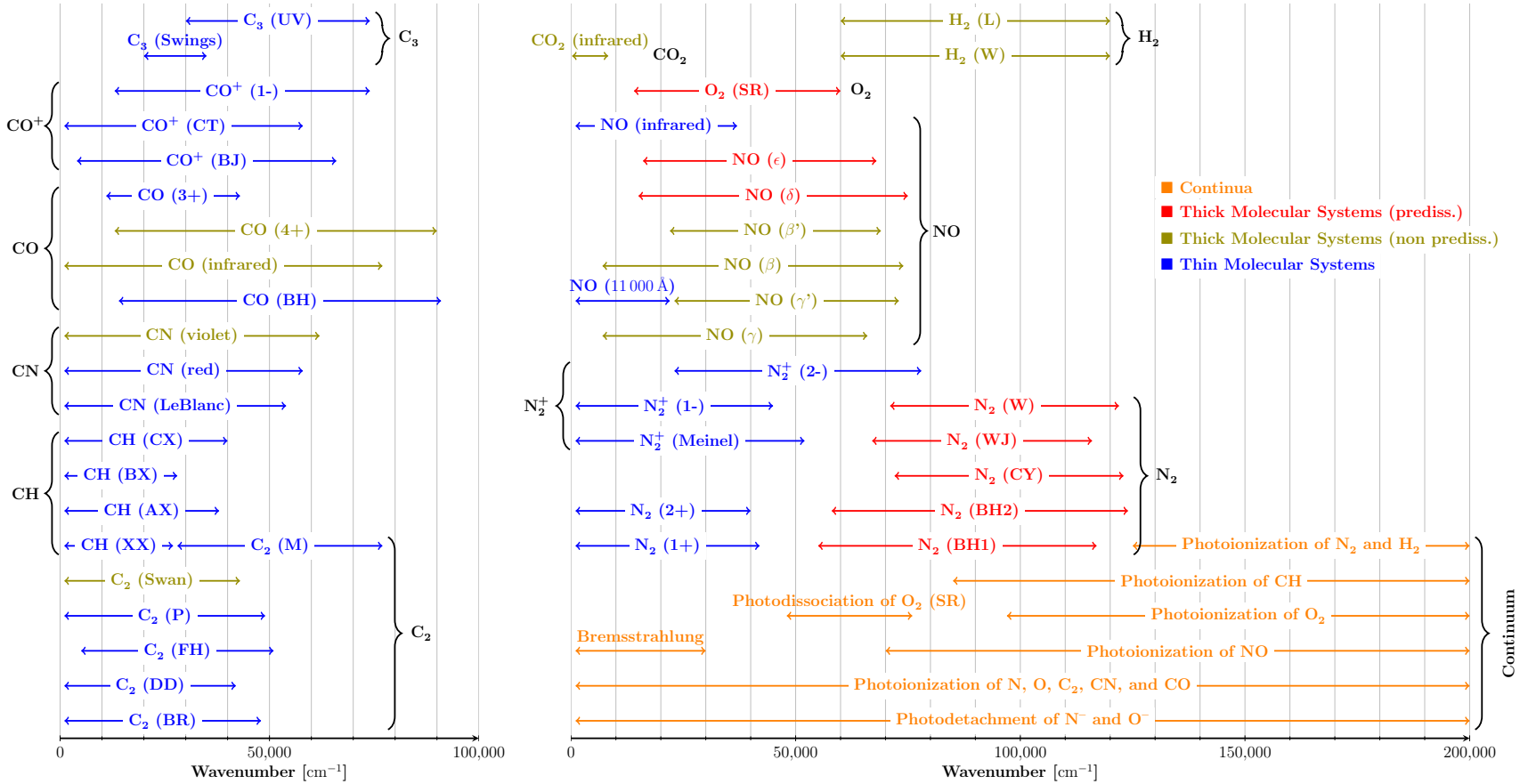

Figure 3.10.: *Graphical summary of the molecular systems and continuum processes included in the SNB database.*

CHAPTER 4

Development of MUTATION^{++}

"The best computer is a man, and it's the only one that can be mass-produced by unskilled labor."

— Wernher von Braun

4.1. Introduction

As was shown in Chapter 2, several different thermochemical models can be used for hypersonic flows depending on the problem of interest and the level of fidelity required in the solution. The thermochemical model used has a direct effect on the evaluation of physicochemical properties necessary to solve the governing equations. These include thermodynamic and transport properties, chemical production rates, and energy transfer rates. The evaluation of each of these properties further depends on the selection of a variety of specialized algorithms and physicochemical data including species partition functions, transport collision integrals, and reaction rate coefficients. The implementation, testing, and maintenance of all of the physicochemical models, algorithms, and data required to simulate hypersonic flows represent a significant cost in terms of human resources and time necessary to develop a hypersonic CFD tool. Furthermore, as newer models, algorithms, or data become available, a significant amount of work is typically needed to update existing CFD codes when the thermochemical model is embedded directly in the code.

These observations have led to the desire to reduce the work necessary to implement new models and algorithms and centralize their development into a single software library which may be used by multiple CFD codes to maximize code reuse and testing. As a result, one outcome of this thesis was the development of a new software library called "MUlticomponent Thermodynamic And Transport properties for IONized gases, written in C++" (MUTATION^{++}). The library was designed with several goals in mind, including

1. provide accurate thermodynamic, transport, and chemical kinetic properties for multicomponent, partially ionized gases,
2. ensure the efficient evaluation of these properties using state-of-the-art algorithms and data structures,
3. be easily extendable to incorporate new data or algorithms as they become available,
4. interface to any CFD tool through a consistent and logical interface,
5. use self-documenting database formats to decrease data transcription errors and increase readability, and
6. be open source to promote code and data sharing among different research groups.

Solutions to the first three goals have been previously developed by Bottin *et al.* [103] in the PEGASE library and more recently by Magin [163] in the MUTATION library. These predecessors were developed in the procedural Fortran programming language and were primarily aimed at the

accurate and efficient evaluation of thermodynamic and transport properties for a few mixtures relevant to atmospheric entry. MUTATION++ builds on these works, using the C++ language and advanced Object-Oriented Programming (OOP) programming techniques. In particular, starting from about 50 species in MUTATION, this work extends the reach of the thermodynamic data to over 1200 species through the incorporation of new databases. An advanced equilibrium solver has also been developed as part of the library for computing linearly constrained, multiphase equilibria. This algorithm is presented in Chapter 5. A new collision integral database has also been developed which accepts user-defined collision integral formats and provides an extensible way to manage the default behavior for missing data. In addition, the library successfully provides a level of abstraction between any generic CFD tool and the thermochemical models employed by exploiting the structure of generalized governing equations for hypersonic flows, combined with modern OOP techniques.

It is worth noting that some of the features in MUTATION++ already exist in other libraries, such as Cantera [164], Chemkin [165], CEA [166], and EGlib [167]. However, these libraries tend to focus either on combustion related problems in thermal equilibrium or are specialized in providing only certain types of properties. The MUTATION++ library is designed from the ground up with hypersonic plasma flows and nonequilibrium effects in mind.

In the context of this thesis, the library has been coupled with the numerical tools described in Chapter 6 to provide the solutions obtained in Chapter 7. This chapter presents the object-oriented design and validation of MUTATION++. In the next section, a short introduction to OOP concepts in C++ is presented in order to define the vocabulary used throughout the rest of the chapter. Section 4.3 gives a brief overview of the design of the library including how it interfaces with a generic CFD code. The next three sections provide a more detailed discussion of the thermodynamic, transport, and chemical kinetics data and algorithms used. Finally, some concluding remarks are presented in Section 4.7.

4.2. Object Oriented Software Design in C++

C++ is a general-purpose programming language, supporting (among others) procedural, objected-oriented, and generic programming paradigms [168]. Procedural languages such as C or Fortran rely on blocks of code, known as procedures (also known as functions or subroutines), which are run in serial to complete a task. In contrast, OOP languages break the description of a task into a collection of *objects* which each have specific attributes and functionality. The task is then solved through the interaction of different objects. In C++, the definition of a type of object is called a *class*. Classes represent the prototypes from which objects are created and describe the attributes a type of object has and what *methods* the objects can perform to modify those attributes (known as *member variables* in C++). For example, a class could be used to describe a person. The person class will be denoted as **`Person`**. A **`Person`** has attributes such as their name and gender and can perform actions such as walking or talking. Several **`Person`** objects can then be created to model a collection of people.

A brief review of a few important C++ concepts used in the design and implementation of MUTATION++ is presented below. This is by no means a complete or thorough review of the topic. For more detailed information, the reader is referred to dedicated works on the C++ language such as [168–170].

Data encapsulation

Data encapsulation is a central feature of OOP in which data about specific objects are encapsulated in those objects. From a design standpoint, data encapsulation allows users of a class to ignore the implementation of the class and instead focus on how it should be used.

Polymorphism and abstraction

Polymorphism allows classes to *inherit* or *extend* the attributes and functionality of another class or classes. A class which extends another class is called the *child* class or *subclass* and the class which is extended is called the *parent* or *base* class. Base classes can also be *abstract*, meaning that they do not fully implement all of their methods, instead forcing child classes to provide the appropriate implementation. Polymorphism and abstraction are very important components in OOP. They provide the ability to have a collection of objects which share the same interface but may have different behaviors.

Templates and metaprogramming

C++ supports generic programming through *templates*. A *templated* class or method is a generic program unit which acts on a general type. A simple example would be an **`Array`** type which consists of an ordered collection of numbers. In C++, a "number" can be represented by a variety of different types such as integers or floating point decimal numbers. Instead of creating multiple classes which provide exactly the same behavior for each numeric type, such as **`IntegerArray`** and **`FloatArray`**, a templated class could be used to write a generic array type. The templated version is written as **`Array<T>`**, where **`<T>`** denotes the **`Array`** class excepts a generic *template parameter* **`T`**. Then, in order to create an array of integers, one simply writes **`Array<int>`**.

Templates are evaluated at compile-time, meaning that all generic template classes in C++ become specific classes when compiled. For example, the compiler will actually create two separate array classes when it sees **`Array<int>`** and **`Array<float>`**. Compile-time template evaluation provides an extremely powerful programming technique to be used in C++, known as *metaprogramming*. Template metaprogramming allows certain methods or algorithms to be evaluated at compile-time, which can provide significant performance improvements over conventional programming techniques.

Self registration

Self registration is a programming pattern in which concrete child classes can be instantiated as a base class using a given name represented as a string. In short, self registration allows a user to select a particular implementation of a base class, without needing to know how to create that specific type of object. As will be shown in this chapter, self registration has been used in MUTATION^{++} to enable a variety of interchangeable models and algorithms to be selected by a user through a string loaded from an input file. For a more detailed discussion of the self registration pattern, see the work of Lani [171].

Class diagrams

Finally, the remainder of the chapter makes use of a diagram style, known as a *class diagram*, in order to convey certain aspects of the design of the MUTATION^{++} library. Class diagrams are part of the Unified Modeling Language (UML) which provides structural and behavior diagram formats for representing object-oriented software designs. In particular, they represent the static relationship between individual classes which form a software solution. Fig. (4.1) provides a generic example of a UML class diagram, depicting the format used here for representing class attributes and methods, composition, aggregation, abstract classes, inheritance, templated classes, and the self registration pattern.

4.3. Overview of the Library

This section provides a general overview of the MUTATION^{++} library. To begin, a general set of governing equations is presented, encompassing all of the energy partitioning and thermochemical nonequilibrium models discussed in Chapter 2. A separation between the solution of the governing

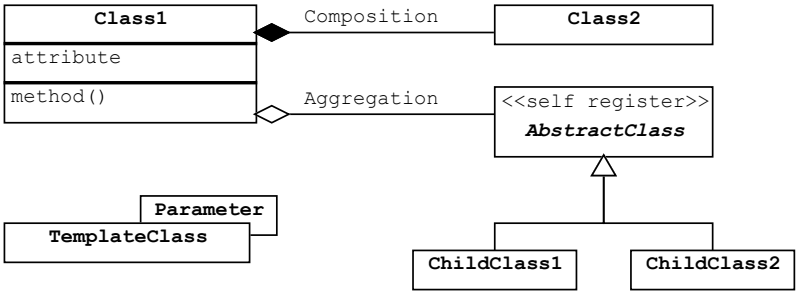

Figure 4.1.: *Example UML class diagram.*

equations and the evaluation of the physicochemical properties is then illustrated and used to define the high-level design of MUTATION++.

4.3.1. Generalized System of Governing Equations

The governing equations presented in Chapter 2 for hypersonic flows can be described generally by the equation,

$$\frac{\partial}{\partial t}\boldsymbol{U} + \boldsymbol{\nabla}\cdot\boldsymbol{F}^c + \boldsymbol{\nabla}\cdot\boldsymbol{F}^d = \boldsymbol{S}^k + \boldsymbol{S}^r, \tag{4.1}$$

where the conservative variable and convective and diffusive flux vectors are

$$\boldsymbol{U} = \begin{bmatrix} \tilde{\rho}_j \\ \rho\boldsymbol{u} \\ \rho E \\ \rho\tilde{e}^m \end{bmatrix}, \quad \boldsymbol{F}^c = \begin{bmatrix} \tilde{\rho}_j\boldsymbol{u}^T \\ \rho\boldsymbol{u}\otimes\boldsymbol{u} + p\bar{\boldsymbol{I}} \\ \rho H\boldsymbol{u}^T \\ \rho\tilde{e}^m\boldsymbol{u}^T \end{bmatrix}, \quad \text{and} \quad \boldsymbol{F}^d = \begin{bmatrix} \tilde{\boldsymbol{J}}_j \\ -\bar{\boldsymbol{\Pi}} \\ \boldsymbol{q} - \bar{\boldsymbol{\Pi}} \\ \tilde{\boldsymbol{q}}_m \end{bmatrix}, \tag{4.2}$$

and the kinetic and radiative source term vectors are written as

$$\boldsymbol{S}^k = \begin{bmatrix} \tilde{\omega}_j \\ 0 \\ 0 \\ \tilde{\Omega}^m - \tilde{\psi}_m p_e \boldsymbol{\nabla}\cdot\boldsymbol{u} \end{bmatrix}, \quad \text{and} \quad \boldsymbol{S}^r = \begin{bmatrix} \tilde{\phi}_j \\ 0 \\ \mathcal{P}^r \\ \tilde{\mathcal{P}}^r_m \end{bmatrix}, \tag{4.3}$$

where the tilde on top of the mass and internal energy variables indicates that these parameters expand to fit the size of the energy partitioning model being used. For example, when a thermochemical nonequilibrium model is used, $\tilde{\rho}_j = \rho_j,\ \forall\ j \in \mathcal{S}^*$. If instead, chemical equilibrium with elemental demixing is assumed, then $\tilde{\rho}_j = \rho^e_j,\ \forall\ j \in \mathcal{E}$. If the mixture is frozen or in equilibrium without elemental demixing, then only the total continuity equation is needed and $\tilde{\rho}_j = \rho$. The diffusive fluxes, internal energies, and source terms scale in the same way. The $\tilde{\psi}_m$ in the kinetic source term vector is unity if the internal energy mode m contains the electron energy and zero otherwise.

Regardless of which model is used, the total density, energy, and enthalpy are given as

$$\rho = \sum_{j\in\mathcal{S}^*} \rho_j(\tilde{\boldsymbol{U}}), \tag{4.4}$$

$$\rho E = \sum_{j\in\mathcal{S}^*} (\rho e)_j(\tilde{\boldsymbol{U}}) + \frac{1}{2}\rho\boldsymbol{u}\cdot\boldsymbol{u}, \quad \text{and} \tag{4.5}$$

$$\rho H = \rho E + p(\tilde{\boldsymbol{U}}), \tag{4.6}$$

where $\tilde{\boldsymbol{U}} = [\tilde{\rho}_j,\ \rho e,\ \rho\tilde{e}^m]^T$ is the thermochemical state-vector. The exact functional dependence each thermochemical property has on the state vector depends on the model being used.

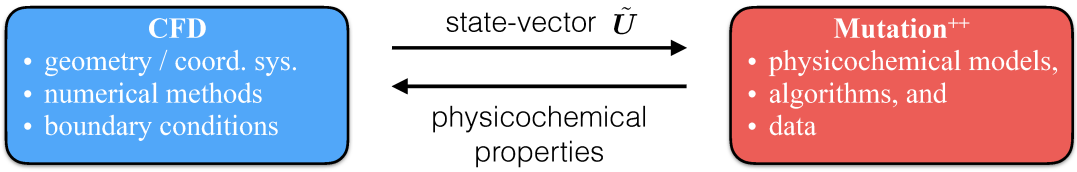

Figure 4.2.: *Relational dependence between* MUTATION^{++} *and a CFD solver.*

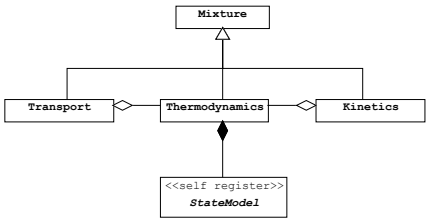

Figure 4.3.: *Overview of the* MUTATION^{++} *library.*

4.3.2. The State Model

The mapping $\boldsymbol{U} \mapsto \tilde{\boldsymbol{U}}$ which converts the conservative variable vector to the thermochemical state vector, introduced in the previous section, is independent on the thermochemical model employed, since the static energy density can always be constructed from conserved quantities. Therefore, from the point-of-view of a CFD code, the numerical method used to solve Eq. (4.1) is independent of the thermochemical model, since the form of the governing equations does not change. This observation leads to a clear separation between the CFD solver and the physicochemical modeling used for a given problem and provides the foundation of the MUTATION^{++} library.

The relational dependence between a CFD solver and MUTATION^{++} is given in Fig. (4.2). The CFD code is responsible for the solution of the governing equations. This includes the selection of the geometry, coordinate system, numerical solution methods, and boundary conditions. Conversely, MUTATION^{++} handles the evaluation of thermodynamic and transport properties, chemical production and energy transfer rates, depending on the desired physicochemical model and given a generic state vector from the CFD code. The link between CFD and MUTATION^{++} has been called a state model in this work. A state model represents a specific thermochemical model, interprets the state vector given by the CFD tool, and provides state-dependent properties back. For example, an equilibrium state model would interpret the state vector as element densities and total static energy and know that the thermal conductivity is a combination of heavy, electron, internal, and reactive terms. Using this state model concept allows different physicochemical models to be interchanged in a single CFD code and maximizes the reuse of data and algorithms necessary for computing thermochemical properties.

4.3.3. High-level Design

Fig. (4.3) provides an overview of the design of the MUTATION^{++} library. The library is split into three main modules - thermodynamics, transport, and kinetics - which are implemented as classes. A **`Mixture`** class inherits the methods of each module in order to provide all of the functionality in a single class. Organizing the library in this way promotes data encapsulation and extendability. The **`Thermodynamics`** class owns a **`StateModel`** which implements the state model concept described in the previous subsection. The **`StateModel`** is self registering, allowing a user to change the model being used at any time using a simple string. In the following sections, each of the modules presented in Fig. (4.3) are discussed in further detail.

4.4. Thermodynamics

This section details the design of the thermodynamics module in MUTATION++. Two thermodynamic database formats have been considered: a simple Rigid-Rotor Harmonic-Oscillator (RRHO) model, and a database of polynomial curve-fits developed at NASA Glenn Research Center. Both models are described in the following sections, followed by an overview of the object-oriented design of the thermodynamics module.

4.4.1. The Rigid-Rotor and Harmonic Oscillator Model

Under the RRHO approximation, the internal energy of a molecule i is partitioned into separate rotation, vibration, and electronic contributions, allowing the internal partition function to be written as

$$Q_i^{\text{int}} = Q_i^{\text{r}}(T_r)\, Q_i^{\text{v}}(T_v)\, Q_i^{\text{el}}(T_{el}), \tag{4.7}$$

according to the discussion presented in Section 2.2.2. In order to compute the rotational contribution, the molecule is treated as a rigid-rotor and characterized by a constant moment of inertia I_i. The vibrational contribution is determined by assuming that each vibrational mode k of the molecule may be treated as a harmonic-oscillator with frequency ν_{ki}. Under these assumptions, the rotational, vibrational, and electronic partition functions may be expressed as [172]

$$Q_i^{\text{r}}(T_r) = \frac{1}{\sigma_i}\left(\frac{T_r}{\theta_i^{\text{r}}}\right)^{\frac{L_i}{2}}, \tag{4.8}$$

$$Q_i^{\text{v}}(T_v) = \prod_k \left[1 - \exp\left(-\frac{\theta_{ki}^{\text{v}}}{T_v}\right)\right]^{-1}, \tag{4.9}$$

$$Q_i^{\text{el}}(T_{el}) = \sum_k a_{ki}^{\text{el}} \exp\left(-\frac{\theta_{ki}^{\text{el}}}{T_{el}}\right), \tag{4.10}$$

where $\theta_i^{\text{r}} = h^2/(8\pi^2 I_i k_B)$ is a characteristic temperature for rotation, $\theta_{ki}^{\text{v}} = h\nu_{ki}/k_B$ are characteristic temperatures for each vibrational mode k, and $\theta_{ki}^{\text{el}} = E_{ki}^{\text{el}}/k_B$ are the characteristic temperatures associated with the electronic level k, having energy E_{ki}^{el} and degeneracy a_{ki}^{el}. Constants σ_i and L_i describe the symmetry and linearity of the molecule. For linear molecules, the steric (or symmetry) factor, σ_i, is defined as 1 for unsymmetric molecules (CO, NO, etc.) and 2 for symmetric ones (N_2, O_2, CO_2, etc.). For nonlinear polyatomic molecules, the value of σ_i depends on the molecule geometry. Finally, L_i is 2 for linear molecules and 3 for nonlinear molecules. These basic data are typically determined through quantum mechanics calculations requiring accurate force potentials between each interacting particle in a molecule. Data for many species relevant to atmospheric entry, have been collected in the works of Gurvich *et al.* [172–177].

Substitution of Eqs. (4.7 - 4.10) into Eqs. (2.58 - 2.66) yields relations for the pure species thermodynamic properties obtained with the RRHO model (translation is treated classically). Expressions for species energy, enthalpy, and entropy are summarized in Table 4.1 and the resulting contributions to the enthalpies of N_2 and CO_2 are shown in Fig. (4.4) as example.

4.4.2. NASA Thermodynamic Polynomials

One of the more commonly used data sources are the National Aeronautics and Space Administration (NASA)thermodynamic polynomial databases of Gordon and McBride [178–181] provided with the NASA Chemical Equilibrium with Applications (CEA) program [166, 182]. The data for the majority of the species are provided by calculations made at NASA Glenn Research Center by Gordon and McBride. The remainder of the species data is taken from several other sources, namely the thermodynamic tables of Gurvich *et al.* [183], the National Institute for Standards and Technology (NIST) Thermochemical Research Center (TRC) tables [184], and the NIST-JANAF thermochemical tables [185, 186]. The NASA polynomials come in either 7- or 9-coefficient forms.

Table 4.1.: *Rotational, vibrational, and electronic contributions to pure species thermodynamic properties based on the RRHO model.*

Mode	$\frac{e_i^m}{R_i}$	$\frac{h_i^m}{R_i}$	$\frac{s_i^m}{R_i} - \frac{h_i^m}{R_i T}, -\frac{g_i^m}{R_i T}$
Rotation	$\frac{L_i}{2}T$	e_i^{r}	$\frac{L_i}{2}\ln\left(\frac{T}{\theta_i^{\mathrm{r}}}\right) - \ln\sigma_i$
Vibration	$\sum_k \theta_{ki}^{\mathrm{v}}\left[\exp\left(\frac{\theta_{ki}^{\mathrm{v}}}{T}\right)-1\right]^{-1}$	$\tilde{e}_i^{\mathrm{v}}$	$-\sum_k \ln\left[1-\exp\left(\frac{-\theta_{ik}^{\mathrm{v}}}{T}\right)\right]$
Electronic	$Q_i^{\mathrm{el}\,-1}\sum_k a_{ki}^{\mathrm{el}}\theta_{ki}^{\mathrm{el}}\exp\left(-\frac{\theta_{ki}^{\mathrm{el}}}{T}\right)$	e_i^{el}	$\ln Q_i^{\mathrm{el}}$

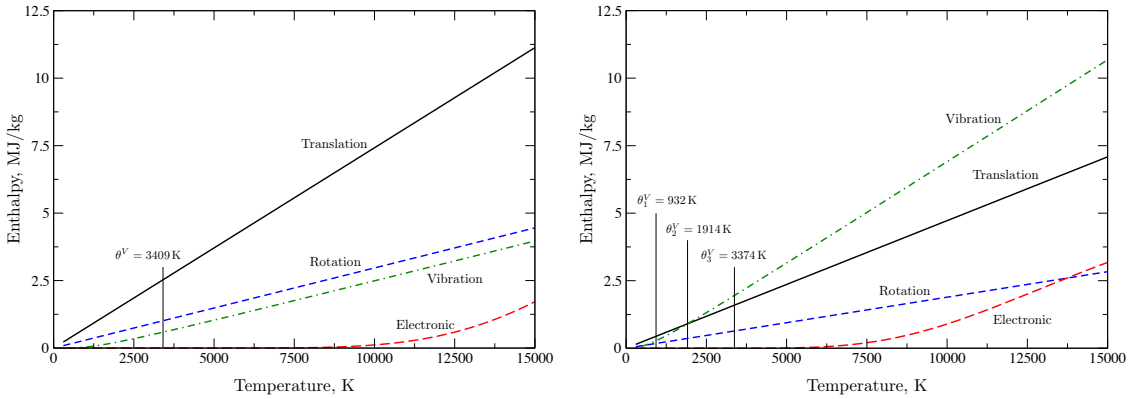

(a) N_2. **(b)** CO_2.

Figure 4.4.: *Contributions to species enthalpies using the rigid-rotor and harmonic-oscillator model.*

Species thermodynamic properties are computed as

$$c_{pi} = R_i \sum_{j=0}^{4+q} a_{ij} T^{j-q}, \quad h_i = \int c_{pi} dT + b_{i1} R_i T, \quad s_i = \int \frac{c_{pi}}{T} dT + b_{i2} R_i, \tag{4.11}$$

where $q = 0$ for the 7-coefficient format or $q = 2$ for the 9-coefficient format and the a and b parameters are provided by the database, typically for multiple temperature ranges.

While the CEA database is used extensively, several drawbacks may decrease the overall accuracy of computations made using its dataset. For example, the database has been constructed using a range of computational methods and experimental results, without regard to the consistency of species enthalpies of formation. Ruscic *et al.* [187, 188] introduced the concept of the Thermochemical Network (TN) which relates the species enthalpy of formation to one another through thermochemically relevant data from literature. A TN can be used to develop a statistically correlated set of formation enthalpies across all of the species in the database. This ensures consistency in the formation enthalpy for each species and improves the estimated accuracy of each value. Furthermore, a TN allows new data to be processed easily and provides insight into which experimental or numerical investigations can most readily impact and expand the currently available set of thermochemical information. The Argonne National Laboratory (ANL) maintains an updated TN published in the Active Thermochemical Tables (ATcT) [189] which is considered the most accurate and self consistent source for species formation enthalpies.

While the ATcT provides a set of consistent formation enthalpies for many species, it does not provide the additional thermodynamic data required to build a useful database. However, Burcat *et al.* [190] currently maintain a vast thermodynamic database which is linked to the formation

enthalpies provided by the ATcT. In total, it consists of 1031 species with the desired elements, of which, 249 have been linked to the ATcT. The majority of the species thermodynamic data in Burcat's database were selected from a range of sources including CEA and journal articles. A significant number of species have been updated based on quantum mechanical calculations using the so called G3B3 methodology [190].

Blanquart *et al.* [191–194] have computed thermodynamic properties for large Polycyclic Aromatic Hydrocarbons (PAH) for the study of soot formation. The database currently includes 64 PAH species ranging from benzene (C_6H_6) to coronenen ($C_{24}H_{12}$). Optimized geometric structures of each molecule were obtained using the B3LYP/6-31++G(d,p) method. Enthalpies of formation were determined using the G3MP2//B3 method with group corrections to account for systematic inaccuracies and are consistent with ATcT.

Finally, Goldsmith *et al.* [195] have recently computed highly accurate thermochemical data for 219 small hydrocarbon species using the RQCISD(T)/cc-PV∞QZ//B3LYP/6-331++G(d,bp) method to compute electronic energies. Consistency with the ATcT was also ensured by using a bond additivity correction method which removed systematic errors in the enthalpy of formation of each species.

In a parallel work to this thesis, a composite database valid for carbon-phenolic mixtures relevant to ablation has been developed based on a critical review of the above data sources. Special care was taken to identify like-species, shared between multiple sources, and to maximize the consistency of formation enthalpies with the ATcT. The resulting database includes more than 1200 neutral and ionized species containing C, H, O, and N and is included in the MUTATION++ library in the NASA 9-coefficient format. The details of this database have been published in [196].

A comparison of mixture thermodynamic properties computed for equilibrium air is provided in Fig. (4.5) using both the RRHO model presented above and the NASA 9-coefficient polynomial database. Where possible, comparisons with the equilibrium air curve-fits of D'Angola *et al.* [197] are also shown. In general, agreement is excellent between all three databases. The largest differences occur in the values of the frozen specific heat ratios at 1 atm between the RRHO model and the NASA polynomials above 12 500 K. However, this translates into negligible differences in the computed speeds of sound as is shown in Fig. (4.5d).

4.4.3. Object-Oriented Design

A simplified class diagram, describing the structure of the thermodynamics module in MUTATION++, is given in Fig. (4.6). The **`Thermodynamics`** class is responsible for providing pure species and mixture thermodynamic functions to the **`Mixture`** class. **`Thermodynamics`** contains the **`StateModel`**, **`ThermoDB`**, and **`MultiPhaseEquilSolver`** objects. The equilibrium solver is responsible for computing equilibrium compositions at fixed temperature, pressure, and element fractions. A robust equilibrium solution algorithm has been developed in this work for linearly constrained, multiphase equilibria, and is presented in Chapter 5.

A **`StateModel`** is a self registering object representing which state model is being used to describe the state of the mixture as discussed in Section 4.3.2. Three concrete **`StateModel`** types have been implemented in this work. The **`EquilStateModel`** represents a mixture in thermochemical equilibrium including the effect of elemental demixing. The **`ChemNonEqStateModel`** and **`ChemNonEqTTvStateModel`** represent mixtures in chemical and thermochemical nonequilibrium, respectively.

`ThermoDB` provides an interface for computing pure species (or pseudo-species) thermodynamic properties. It is also responsible for managing the loaded **`Species`** and **`Element`**s in the mixture. The type of thermodynamic database being used is selected by the user through the self registration of the **`ThermoDB`** type. A special eXtensible Markup Language (XML) format has been created in the development of the library for representing the RRHO model and can be loaded with the **`RrhoDB`** type. The format is human readable, extensible, and self-documenting. In addition, both the NASA-7 and -9 thermodynamic polynomial formats have been implemented.

The simple architecture shown in Fig. (4.6) provides an extensible framework for introducing new state models or thermodynamic database types in MUTATION++, without the need for extensive

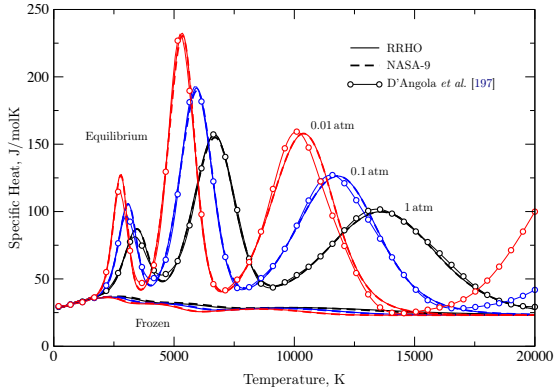

(a) *Specific heats at constant pressure.*

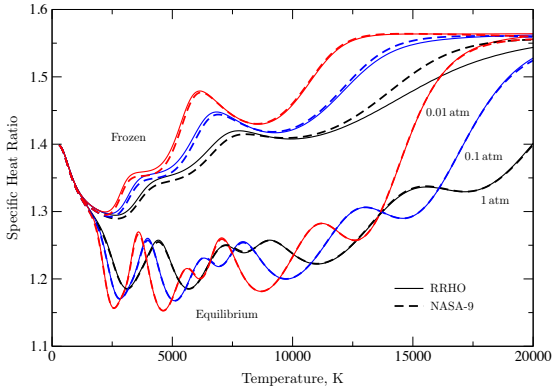

(b) *Specific heat ratios.*

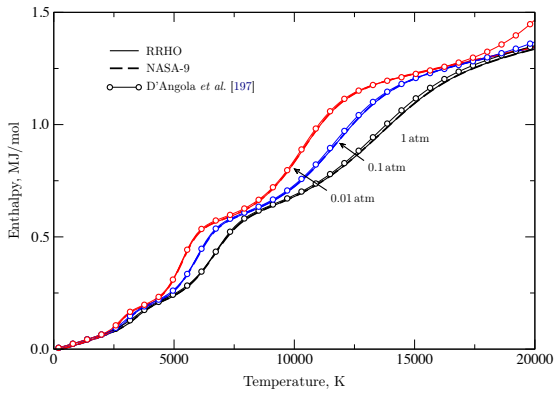

(c) *Enthalpy.*

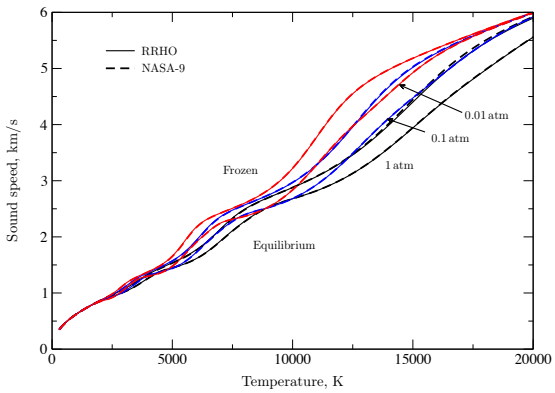

(d) *Sound speed.*

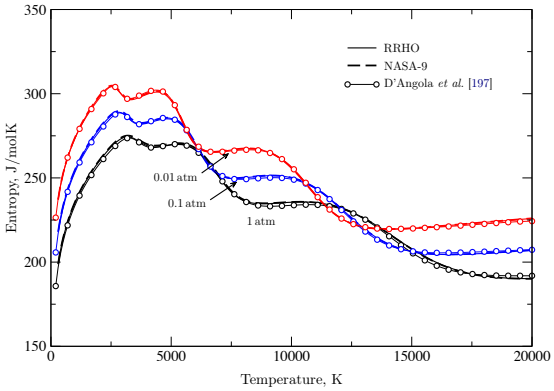

(e) *Entropy.*

Figure 4.5.: *Mixture thermodynamic properties of equilibrium air at various pressures.*

coding or redesign. In addition, users can easily change state models at runtime, which may be beneficial in some applications. Lastly, by hiding the thermodynamic database and state model selections from the rest of the library, the approach forces the other modules to be written in a more general and extensible way.

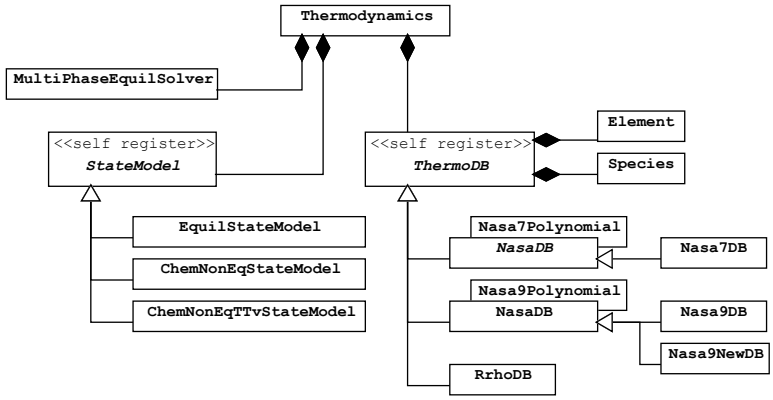

Figure 4.6.: *UML diagram of* MUTATION^{++} *thermodynamics module.*

4.5. Transport Fluxes

This section describes the transport module in MUTATION^{++}. In particular, the constraints on and design of the collision integral database, necessary for computing transport coefficients, is described. Transport algorithms are reviewed, and a selection of transport properties are also compared with literature results for several mixtures.

4.5.1. Collision Integrals

The solution of transport coefficients is based on the evaluation of the collision integrals which are weighted averages over the Maxwellian distribution of collision cross-sections for each pair of species considered in a given mixture [98, 198]. The weighting depends on the Sonine polynomial order (l, s) used in the spectral method to solve the integro-differential kinetic equation resulting from the Chapman-Enskog solution procedure [199]. For mixtures in thermal nonequilbrium, collision integrals of order (l, s) for the interaction of two colliding species (i, j) may be written compactly as,

$$\Omega_{ij}^{(l,s)}(T_{ij}) = \left(\frac{k_B T_{ij}}{2\pi\tilde{\mu}_{ij}}\right)^{\frac{1}{2}} \int_0^\infty \exp(-\gamma^2)\, \gamma^{2s+3}\, Q_{ij}^{(l)}\, d\gamma, \tag{4.12}$$

where T_{ij} is the temperature associated with the interaction (i, j), $\tilde{\mu}_{ij}$ is a modified reduced mass of the colliding system, γ is the ratio of kinetic and thermal energy, $\gamma^2 = \tilde{\mu}_{ij} g^2/(2k_B T_{ij})$, g is the relative collision velocity, and $Q_{ij}^{(l)}$ is the generalized collision cross-section. For neutral or neutral-ion interactions between heavy species, $T_{ij} = T_h$, while $T_{ij} = T_e$ for collisions between a free electron and another species. As will be shown, charged interactions have an additional temperature dependence from the introduction of the Debye length in the screened Coulomb interaction potential. The modified reduced mass is evaluated as $\tilde{\mu}_{ij} = \mu_{ij}$, $\tilde{\mu}_{ij} = m_e$, and $\tilde{\mu}_{ij} = m_e/2$ for heavy-heavy, electron-heavy, and electron-electron interactions, respectively. Collision cross-sections are defined as

$$Q_{ij}^{(l)} = 2\pi \int_0^\infty \left(1 - \cos^l \chi_{ij}\right) b\, db, \tag{4.13}$$

where χ and b are the deflection angle and impact parameter describing a binary collision (see for example [98]). The deflection angle is given from classical mechanics as

$$\chi_{ij} = \pi - 2b \int_{r_m}^\infty \frac{dr/r^2}{\sqrt{1 - b^2/r^2 - \phi_{ij}(r)/\left(\frac{1}{2}\mu_{ij} g^2\right)}}, \tag{4.14}$$

where r is the distance between particles, r_m the distance of closest approach, and $\phi_{ij}(r)$ is the spherical interaction potential.

It is convenient to express collision integrals in terms of dimensional, reduced collision integrals $\bar{Q}_{ij}^{(l,s)}$ [200], defined as

$$\begin{aligned}\bar{Q}_{ij}^{(l,s)} &= \pi\sigma_{\mathrm{HS}}^2\Omega_{ij}^{(l,s)*} \\ &= \frac{4(l+1)}{(s+1)![2l+1-(-1)^l]}\int_0^\infty \exp(-\gamma^2)\,\gamma^{2s+3}\,Q_{ij}^{(l)}\,d\gamma,\end{aligned} \tag{4.15}$$

where $\Omega_{ij}^{(l,s)*}$ are the standard reduced collision integrals normalized by the corresponding hard-sphere values [198] and $\pi\sigma_{\mathrm{HS}}^2$ is the hard-sphere cross-section. Reduced collision integrals represent the deviation from the rigid-sphere values and are often used since they have a weaker dependence on temperature than Eq. (4.12), making them easier to represent with curve-fits. Notice that the hard-sphere cross-section is not actually needed to evaluate the reduced collision integrals. The following ratios also occur frequently enough in the calculation of transport properties, that they are explicitly defined as

$$A_{ij}^* = \bar{Q}_{ij}^{(2,2)}/\bar{Q}_{ij}^{(1,1)}, \tag{4.16}$$

$$B_{ij}^* = \left(5\bar{Q}_{ij}^{(1,2)} - 4\bar{Q}_{ij}^{(1,3)}\right)/\bar{Q}_{ij}^{(1,1)}, \tag{4.17}$$

$$C_{ij}^* = \bar{Q}_{ij}^{(1,2)}/\bar{Q}_{ij}^{(1,1)}, \tag{4.18}$$

$$E_{ij}^* = \bar{Q}_{ij}^{(2,3)}/\bar{Q}_{ij}^{(2,2)}, \tag{4.19}$$

$$F_{ij}^* = \bar{Q}_{ij}^{(3,3)}/\bar{Q}_{ij}^{(1,1)}, \tag{4.20}$$

$$G_{ij}^* = \bar{Q}_{ij}^{(4,4)}/\bar{Q}_{ij}^{(2,2)}. \tag{4.21}$$

Tables A.1 and A.2 provide practical expressions for the linear transport systems in terms of reduced collision integrals and ratios based on the derivation of Magin and Degrez [107] for partially ionized and unmagnetized plasmas. The derivation is based on a modified Chapman-Enskog perturbative solution of the scaled Boltzmann equation, using the electron to heavy particle mass ratio as the scaling parameter. The effects of chemistry and internal energy on the transport systems are neglected. Instead, the Euken corrections for internal energy have been used. Only one non-vanishing Sonine polynomial order is retained for heavy-heavy interactions. Two non-vanishing orders are retained for interactions involving electrons. A summary of the required collision integral data necessary to compute each transport coefficient based the expressions of Magin and Degrez is provided in Table 4.2. As is shown by last row in the table, the total number of collision integrals required to compute all of the transport coefficients scales with the number of species squared, since all collision pairs must be taken into account. As an example, the 11-species air mixture, consisting of 5 neutrals (N, O, N_2, O_2, and NO) and their first ions and free electrons, has 66 unique collision pairs and requires the evaluation of 273 collision integrals, based on Table 4.2. Thus, the data requirements for transport properties grows significantly faster than for thermodynamics, which grows linearly with the number of species.

The preferred method to computed collision integrals is to numerically integrate from accurate *ab initio* potential energy surfaces. Such data is available for several important collision systems. Recent reviews of available collision integral data for neutral-neutral interactions are provided by Wright *et al.* [201, 202] for air, Mars, and Venus mixtures and collision integrals have been tabulated versus temperature up to 20 000 K. The review of Bruno *et al.* [203] has been used for Jupiter mixtures and provides accurate curve-fits suitable for collision integral calculations up to 50 000 K. When potential energy surfaces are not available, collision integrals are typically integrated from model interaction potentials. The evaluation of these potentials is typically split into four groups: neutral-neutral, ion-neutral, electron-neutral, and charged interactions. The following subsections review commonly used potentials for each type of interaction and present the data sources for collision integrals required in this work.

Table 4.2.: *Summary of required collision integral data for each transport coefficient $\mu(\xi)$ with Sonine polynomial order ξ, including number of unique collision integrals which must be evaluated for each coefficient. Note that some integrals are required by several coefficients.*

$\mu(\xi)$	Collision Integrals	Number*
$\eta(1)$	$\bar{Q}_{ij}^{(1,1)}, \bar{Q}_{ij}^{(2,2)}$	$n^{\mathcal{H}}(n^{\mathcal{H}}+1)$
$\lambda_h(2)$	$\bar{Q}_{ij}^{(1,1-3)}, \bar{Q}_{ij}^{(2,2)}$	$2n^{\mathcal{H}}(n^{\mathcal{H}}+1)$
λ_{int}	$\bar{Q}_{ij}^{(1,1)}$	$n^{\mathcal{H}}(n^{\mathcal{H}}+1)/2$
$\lambda_e(2)$	$\bar{Q}_{ie}^{(1,1-3)}, \bar{Q}_{ee}^{(2,2)}$	$a^e(3n^{\mathcal{H}}+1)$
$\lambda_e(3)$	$\bar{Q}_{ie}^{(1,1-5)}, \bar{Q}_{ee}^{(2,2-4)}$	$a^e(5n^{\mathcal{H}}+3)$
$\chi_i^h(2)$	$\bar{Q}_{ij}^{(1,1-2)}$	$n^{\mathcal{H}}(n^{\mathcal{H}}+1)$
$\chi_i^e(2)$	$\bar{Q}_{ie}^{(1,1-3)}, \bar{Q}_{ee}^{(2,2)}$	$a^e(3n^{\mathcal{H}}+1)$
$\chi_i^e(3)$	$\bar{Q}_{ie}^{(1,1-5)}, \bar{Q}_{ee}^{(2,2-4)}$	$a^e(5n^{\mathcal{H}}+3)$
$\boldsymbol{V}_k(1)$	$\bar{Q}_{ij}^{(1,1)}, \bar{Q}_{ie}^{(1,1)}$	$n^{\mathcal{H}}(n^{\mathcal{H}}+1)/2 + a^e n^{\mathcal{H}}$
$\boldsymbol{V}_k(2)$	$\bar{Q}_{ij}^{(1,1-3)}, \bar{Q}_{ie}^{(1,1-3)}, \bar{Q}_{ij}^{(2,2)}, \bar{Q}_{ee}^{(2,2)}$	$2n^{\mathcal{H}}(n^{\mathcal{H}}+1) + a^e(3n^{\mathcal{H}}+1)$
$\sigma_e(1)$	$\bar{Q}_{ie}^{(1,1)}$	$a^e n^{\mathcal{H}}$
$\sigma_e(2)$	$\bar{Q}_{ie}^{(1,1-3)}, \bar{Q}_{ee}^{(2,2)}$	$a^e(3n^{\mathcal{H}}+1)$
All	$\bar{Q}_{ij}^{(1,1-3)}, \bar{Q}_{ij}^{(2,2)}, \bar{Q}_{ie}^{(1,1-5)}, \bar{Q}_{ee}^{(2,2-4)}$	$2n^{\mathcal{H}}(n^{\mathcal{H}}+1) + a^e(5n^{\mathcal{H}}+3)$

* a^e is 1 if free electrons are present in the mixture, 0 if not

Neutral-neutral interactions

A wide range of potential functions have been developed in the literature to model neutral-neutral interactions [198]. The Lennard-Jones (12-6) and Stockmayer potentials have been used extensively to model non-polar and polar gases. The Stockmayer potential superimposes the Lennard-Jones potential and a dipole-dipole interaction, such that [204]

$$\phi(r) = 4\,\phi_{ij}^0 \left[\left(\frac{\sigma_{ij}}{r}\right)^{12} - \left(\frac{\sigma_{ij}}{r}\right)^{6} + \delta\left(\frac{\sigma_{ij}}{r}\right)^{3} \right], \tag{4.22}$$

where δ is function of the dipole moments and angular dependence of the dipole-dipole interaction, ϕ_{ij}^0 is the maximum energy of attraction (potential well depth), and σ_{ij} satisfies $\phi_{ij}(\sigma_{ij}) = 0$ for $\delta = 0$ (non-polar case). When either species is non-polar, $\delta = 0$ and Eq. (4.22) reduces to the Lennard-Jones (12-6) potential. The Stockmayer potential permits the use of pre-tabulated collision integrals $\bar{Q}_{ij}^{(l,s)}(T^*, \delta)/\sigma_{ij}^2$ as a function of reduced temperature $T^* = k_B T_h/\phi_{ij}^0$ and species dipole moments. Monchick and Mason [204] provide accurate tables for $\bar{Q}_{ij}^{(1,1)}$, $\bar{Q}_{ij}^{(2,2)}$, A_{ij}^*, B_{ij}^*, C_{ij}^*, F_{ij}^*, and G_{ij}^*. The Lennard-Jones potential parameters and dipole moments are available for many interactions in the literature. For interactions not found in the literature, the Lorentz and Berthelot combination rules may be used to approximate the potential parameters from pure species interaction data, namely

$$\phi_{ij}^0 \approx \frac{1}{2}(\phi_{ii}^0 + \phi_{jj}^0), \quad \text{and} \tag{4.23}$$

$$\sigma_{ij} \approx \sqrt{\sigma_{ii}\sigma_{jj}}. \tag{4.24}$$

Other combination rules may also be used (see for example [205]).

The Lennard-Jones (12-6) potential provides a reasonably accurate description of the long range

interaction for many collision pairs. At higher temperatures, the short range interaction dominates and more accurate potentials are necessary. The Born-Mayer type potential,

$$\phi_{ij}(r) = a_{ij} \exp(-b_{ij} r), \tag{4.25}$$

parameterized by the parameters a_{ij} and b_{ij}, can be fit to a more complicated potential or experimental data [206] to provide accurate short-range interactions. Sokolova and Magin [207] have developed a "sewing" method for combining the Born-Mayer and Lennard-Jones potentials into a potential which is accurate at short and long separation distances. Bellemans and Magin [208] have computed curve-fits of the form,

$$\bar{Q}_{ij}^{(l,s)}(x = \ln T) = \exp(A_{ij}x^3 + B_{ij}x^2 + C_{ij}x + D_{ij}), \tag{4.26}$$

for several collision pairs relevant to carbon-phenolic ablation mixtures based on numerical integration of the sewn potential.

Other potentials have also been developed to model short and long range interactions in a consistent way. For example, the Tang-Toennies potential, described in the next section, combines both Born-Mayer and Lennard-Jones-like terms for the short and long range interactions. Pirani [209–211] has developed the phenomenalogical potential

$$\phi_{ij}(r) = \phi_{ij}^0 \left[\frac{m}{n(x) - m} \left(\frac{1}{x} \right)^{n(x)} - \frac{n(x)}{n(x) - m} \left(\frac{1}{x} \right)^{m} \right], \tag{4.27}$$

where $x = r/r_m$, ϕ_{ij}^0 and r_m are the maximum depth and location of the potential well, $n(x) = \beta + 4x^2$, β is a model parameter ranging from 6 to 10 based on the hardness of the of the interacting electronic distribution densities, and m depends on the type of interaction ($m = 6$ for neutral-neutral, $m = 4$ for ion induced dipole, $m = 2$ for ion permanent dipole, and $m = 1$ for ion-ion collisions). Correlation formulas provide estimates of the potential features ϕ_{ij}^0, r_m, and β based on fundamental physical properties of colliding species (polarizability, charge, and number of electrons effective in polarization). Laricchiuta *et al.* [212] have fitted reduced collision integrals over a wide range of reduced temperatures in the form

$$\ln\left(\frac{\bar{Q}_{ij}^{(l,s)}}{\pi \sigma_{\mathrm{HS}}^2} \right) = [a_1 + a_2 x] \frac{\exp\{[x - a_3]/a_4\}}{\exp\{[x - a_3]/a_4\} + \exp\{[a_3 - x]/a_4\}} + a_5 \frac{\exp\{[x - a_6]/a_7\}}{\exp\{[x - a_6]/a_7\} + \exp\{[a_6 - x]/a_7\}}, \tag{4.28}$$

$$a_i = \sum_{j=0}^{2} c_{ij} \beta^j, \tag{4.29}$$

where $x = \ln k_B T/\phi_i^0 j$ and the equivalent rigid-sphere radius is given as $\sigma_{\mathrm{HS}} = \xi_1 \beta^{\xi_2} r_m$ and $(\xi_1, \xi_2) = (0.8002, 0.049256)$ for neutral-neutral interactions and $(0.7564, 0.064605)$ for ion-neutral interactions.

Ion-neutral interactions

The Langevin (polarization) potential has been used extensively for modeling ion-neutral interactions and represents a special case of the inverse power potential,

$$\phi_{ij}(r) = -\frac{d}{r^\delta} \tag{4.30}$$

for $\delta = 4$ and $d = z_j^2 q_e^2 \alpha_i / 8\pi\epsilon_0$, where α_i is the dipole polarizability of the neutral species and z_j represents the elementary charge of the ion. The inverse power potential permits a closed form

Table 4.3.: *Ratios of $\bar{Q}_{ij}^{(l,s)}/\bar{Q}_{ij}^{(1,1)}$ for the Langevin potential.*

l,s	2	3	4	5
1	0.833	0.729	0.656	0.602
2	0.870	0.761	0.685	
3		0.842		

solution of the collision integrals, such that

$$\bar{Q}_{ij}^{(l,s)} = \frac{4\pi(l+1)}{(s+1)![2l+1-(-1)^l]} A^{(l)}(\delta) \sqrt{\frac{d\,\delta}{k_B T_h}} \Gamma\left(s+2-\frac{2}{\delta}\right), \tag{4.31}$$

where $A^{(1)}(4) = 0.5523$, $A^{(2)}(4) = 0.3846$, $A^{(3)}(4) = 0.6377$, and Γ is the gamma function for real numbers. Using the parameters for the Langevin potential, the diffusion integral is given as,

$$\bar{Q}_{ij}^{(1,1)} = 424.443 z_j \pi \sqrt{\frac{\alpha_i}{T_h}}. \tag{4.32}$$

Other integrals are constant ratios of the above. These ratios are given in Table 4.3 for the necessary integrals. The Langevin potential is useful when no data is available for a given collision as it only requires the polarizability of the neutral species, which may be found easily for most gases. Polarizabilities for neutral species considered in this work are provided in Appendix D. Levin and Wright [213] have compared this potential with accurate collision data for some important ion-neutral collisions in air and found the accuracy to be about 40 % over the temperature range of interest. Capitelli [214] has shown that this error can be as high as 100 % for the K^+-Ne and K^+-Xe collisions, suggesting that care should be taken when using this potential.

Levin and Wright [213] have proposed to use an effective Tang-Toennies potential for ion-neutral collisions,

$$\phi_{ij}(r) = \phi_{ij}^0 \exp(-r/\beta) - \sum_{n=2}^{\infty} \left[1 - \exp(-r/\beta) \sum_{k=0}^{2n} \frac{(r/\beta)^k}{k!}\right] \frac{C_{2n}}{r^{2n}}, \tag{4.33}$$

which combines an exponential repulsion term, dominate at short-range, with damped dispersion and polarization terms for the long-range interaction. For $n > 5$, the dispersion coefficients C_{2n} are given by the recursive relation

$$C_{2n+4} = C_{2n-2}(C_{2n+2}/C_{2n})^3. \tag{4.34}$$

The lower order dispersion coefficients and the short-range coefficients ϕ_0 and β may be estimated given C_6 and the dipole, quadrupole, and octopole polarizabilities of the ion and neutral species as discussed in [213].

For collisions between ions and their parent neutral, resonant charge transfer can significantly increase the momentum-transfer cross-section and should be taken into account for collision integrals with odd l. Charge transfer does not affect the viscosity cross-section due to symmetry. Typically, resonant charge transfer is considered through the simple mixing rule [215], such that

$$\bar{Q}_{ij}^{(l,s)} = \sqrt{\left(\bar{Q}_{ij,\text{ex}}^{(l,s)}\right)^2 + \left(\bar{Q}_{ij,\text{el}}^{(l,s)}\right)^2}, \quad \text{odd } l, \tag{4.35}$$

where $\bar{Q}_{ij,\text{ex}}^{(l,s)}$ and $\bar{Q}_{ij,\text{el}}^{(l,s)}$ are the collision integrals computed with pure charge transfer and elastic momentum-transfer cross-sections, respectively.

Collision integral data for ion-neutral collisions have been taken from several sources. Levin and Wright [213] provide tabulated diffusion and viscosity integrals for air interactions based on integrated Tang-Toennies potentials. In addition, Wright *et al.* [201] suggest that constant values of 1.2 and 0.85 are sufficient for the ratios B^* and C^* which has been used as a default for all

ion-neutral interactions when no other data is available. In a second work, Wright *et al.* [202] have also computed ion-neutral integrals for Mars and Venus mixtures, based on a combination of Langevin and Tang-Toennies models. Bruno *et al.* [203] provide accurate collision integral data for Jupiter species as well. Finally, the Langevin potential has been used for all other ion-neutral interactions required in this work.

Electron-neutral interactions

Unfortunately, it is difficult to use engineering approximations when computing electron-neutral collision integrals, due to the complexity of the interactions. Often these data are assembled from elastic or momentum cross sections as functions of energy, as determined from beam scattering or swarm measurements [201]. The most accurate method for computing collision integrals for electron-neutral interactions is through numerical integration of the differential elastic cross sections, $d\sigma/d\Omega$. Differential cross sections can be integrated over all scattering angles to provide integral cross sections versus energy,

$$Q_{ei}^{(l)}(E) = 2\pi \int_0^\pi \frac{d\sigma}{d\Omega}(1 - \cos^l \chi) \sin \chi d\chi. \tag{4.36}$$

The resulting cross sections can then be integrated over energy, assuming a Boltzmann energy distribution, to determine the required collision integrals versus temperature.

Wright *et al.* [201, 202] provide tables for Air, Mars, and Venus, electron-neutral collision integrals based on integrated differential cross sections, obtained from a careful review of the literature. A selection of these integrals are plotted in Fig. (4.7).

Charged interactions

Collisions between charged particles can be accurately modeled using the screened Coulomb potential shielded by the Debye length (Debye-Hückel potential),

$$\phi_{ij}(r) = \frac{z_i z_j}{r} \frac{q_e^2}{4\pi\epsilon_0} \exp\left(-\frac{r}{\lambda_D}\right), \tag{4.37}$$

where z_i and z_j are the elementary charges of colliding species. The Debye length (radius) represents the characteristic length over which charged particles in a plasma are shielded from other charged particles. When both electrons and ions are considered in the shielding, the Debye length is given as

$$\lambda_D^2 = \frac{\epsilon_0 k_B / q_e^2}{n_e/T_e + \sum_{j\in\mathcal{H}} z_j^2 n_j / T_h}. \tag{4.38}$$

It is not clear whether ions should be included in the shielding or not. When they are neglected, the sum in the denominator should be removed. For neutral plasmas with $T_e = T_h$, the Debye length simplifies to

$$\lambda_D^2 = \frac{\epsilon_0 k_B T_e}{2 q_e^2 n_e}. \tag{4.39}$$

Mason, Munn, and Smith [216] have accurately integrated the Coulomb potential and provide tabulated attractive and repulsive diffusion and viscosity integrals, as well as the ratios A^*, B^*, C^*, E^*, F^*, and G^* versus a reduced temperature,

$$T^* = \frac{\lambda_D k_B T}{q_e^2/(4\pi\epsilon_0)}. \tag{4.40}$$

Devoto [200] later extended these tabulations to include $\bar{Q}_{ij}^{(1,4)}$, $\bar{Q}_{ij}^{(1,5)}$, and $\bar{Q}_{ij}^{(2,4)}$ which are necessary for the third-order electron transport coefficients, as shown in Table 4.2. From Eq. (4.40), the reduced temperature is a function of the electron temperature and number density through the dependence on the Debye length. The tables provided by Devoto are valid for reduced temperatures

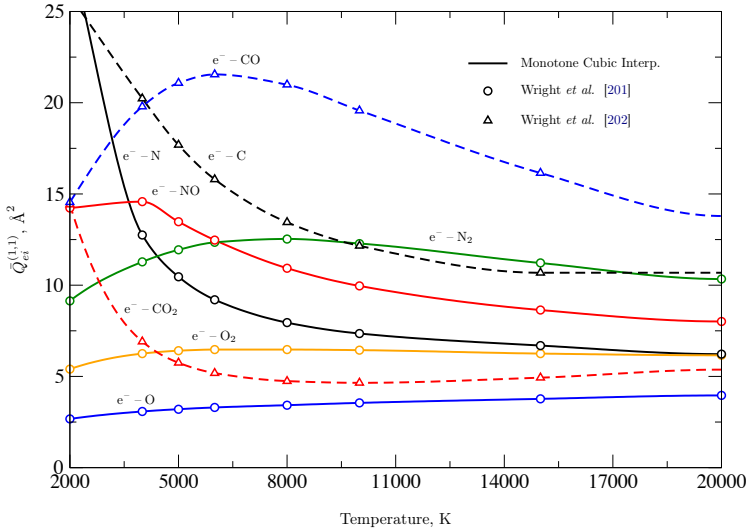

(a) *Electron-neutral interactions.*

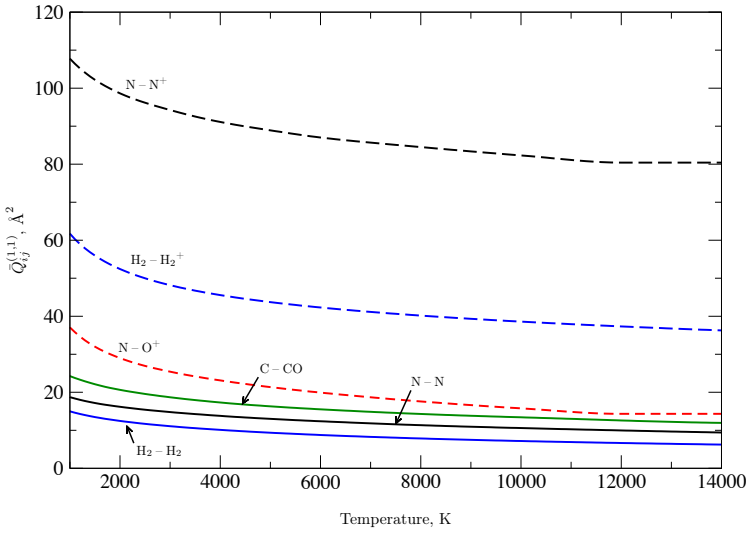

(b) *Neutral-neutral and neutral-ion interactions.*

Figure 4.7.: *Selected reduced collision integrals for various types of interactions.*

ranging from 0.1 to 10000, which is a stricter limit than those provided by Mason, Munn, and Smith. Fig. (4.8) shows T^* versus T for equilibrium air and Jupiter mixtures as well as a fictitious fully ionized gas ($x_e = 0.5$) over a large pressure range representative of atmospheric entry. At high temperatures, all the curves coincide with the fully ionized gas, as expected. At temperatures lower than 5000 K, ionization is negligible and thus Coulomb interactions are unimportant. It is therefore clear from the figure that the range of T^* provided by Devoto is sufficient to describe all conditions of interest for atmospheric entry applications.

Fig. (4.9) provides an example of the attractive and repulsive Coulomb collision integrals for equilibrium air at 1 atm. When compared to the neutral interactions shown in Fig. (4.7), Coulomb collision integrals are orders of magnitude larger. This is due to the fact that the Coulomb forces acting on colliding ions is much stronger than those acting on non-charged interactions.

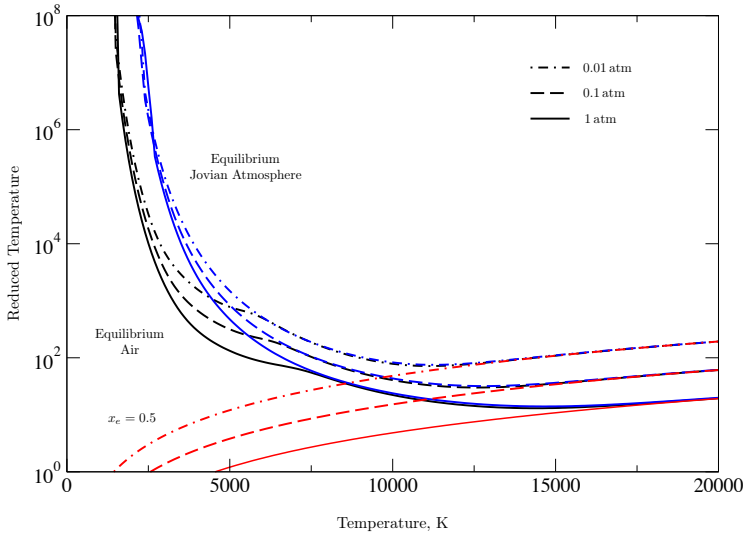

Figure 4.8.: *Reduced temperature used for Coulomb interactions calculated for various mixtures.*

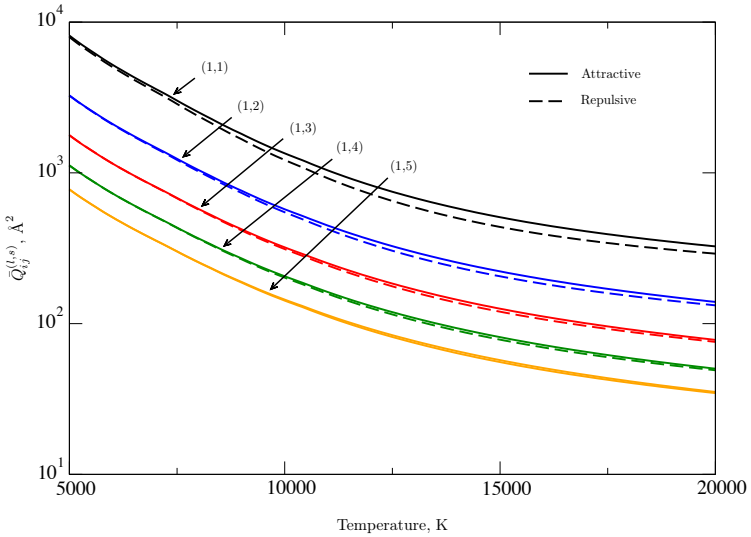

Figure 4.9.: *Coulomb collision integrals for equilibrium air mixture.*

Recurrence relations

Differentiating Eq. (4.15) yields the following recurrence relation,

$$\bar{Q}_{ij}^{(l,s+1)} = \bar{Q}_{ij}^{(l,s)} + \frac{T_{ij}}{s+2} \frac{d\bar{Q}_{ij}^{(l,s)}}{dT_{ij}}. \tag{4.41}$$

This expression provides a method for computing any collision integral with order $(l, s+1)$ from the integral (l, s) and its first derivative. Applying the recurrence relation for successive orders yields a more general expression,

$$\bar{Q}_{ij}^{(l,s+n)} = \sum_{k=0}^{n} a_k^n \, T_{ij}^k \, \frac{d^k \bar{Q}_{ij}^{(l,s)}}{dT_{ij}^k}, \tag{4.42}$$

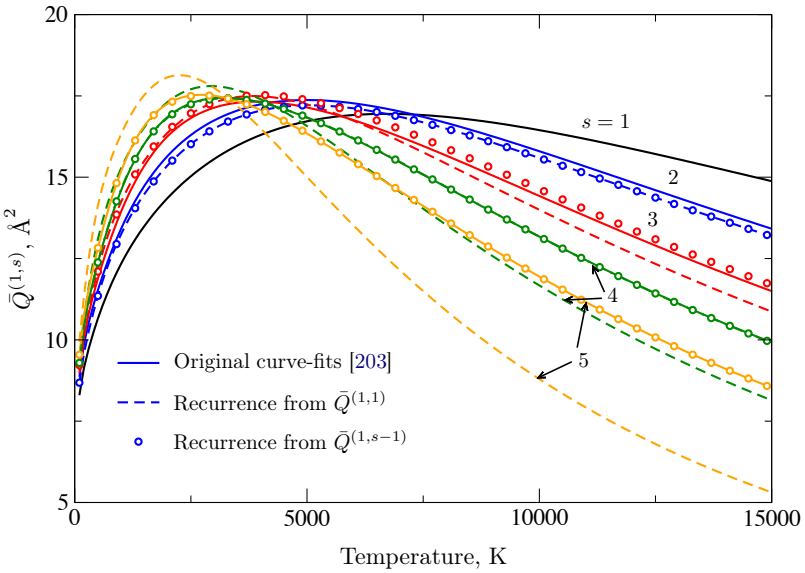

Figure 4.10.: *Comparison of $\bar{Q}^{(1,s)}$ for the (e^-, H_2) collision pair using the recurrence relations.*

for any integer $n \geq 0$. The coefficients a_k^n satisfy the recurrence relationship $(s+2)a_k^n = (s+2+k)a_k^{n-1} + a_{k-1}^{n-1}$ with $a_0^n = 1$ and $a_n^n = (s+2)^{-n}$. It is easily verified that Eq. (4.41) is retrieved for $n = 1$. In principle, Eq. (4.42) could be used to compute all necessary collision integrals in Table 4.2 given only the integrals corresponding to an (l, s) – order of (1,1) and (2,2) and their derivatives (up to fourth order for $l = 1$ and second order for $l = 2$). In practice, however, it is difficult to evaluate higher order derivatives from the data generally given in the literature.

Fig. (4.10) shows a typical example using the $\bar{Q}_{ij}^{(1,s)}$ integrals for the (e^-, H_2) collision pair for $1 \leq s \leq 5$. In the figure, solid lines represent the original curve-fits provided by Bruno *et al.* [203]. Dashed lines represent the same integrals computed using the general recurrence expression in Eq. (4.42) from order (1,1) while the symbols represent recurrence from the original data at one order lower. All derivatives were computed using a simple first order finite-difference scheme. From the figure, we can see that the error in the recurrence relation increases as the level of recurrence increases. This is due to error in the derivative approximations as well as errors in the original curve-fits which get propagated through each level of recurrence. However, using only one level of recurrence yields a reasonable approximation to the original data. The recurrence results for (1,4) and (1,5) are in excellent agreement, suggesting that Bruno *et al.* probably used Eq. (4.41) to compute these integrals in the first place.

4.5.2. Transport Algorithms

The solution of the transport fluxes typically represents a significant portion of the required CPU time for many CFD applications. In principle, the computation of transport coefficients can be split into two steps: 1) calculation of the necessary collision integrals and 2) formation and solution of the linear transport systems. Several solution methodologies have been proposed in the literature for reducing the necessary CPU cost of one or both of these steps. A review of transport algorithms has been given by Magin and Degrez [106]. Some key points are discussed here.

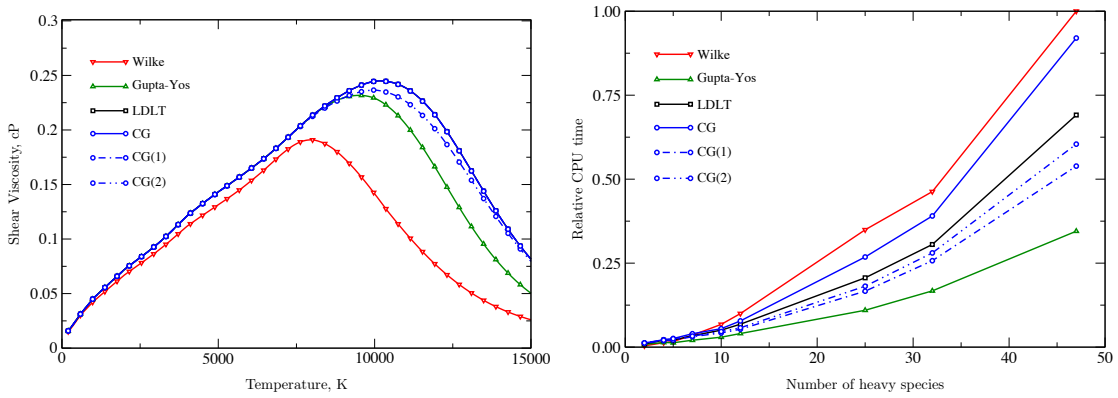

(a) *Air viscosity.* **(b)** *Relative CPU time.*

Figure 4.11.: *Comparison of shear viscosity of air at* 1 atm *and the relative CPU time required for different solution algorithms.*

Heat flux and stress tensor

Viscosity, heavy-particle thermal conductivity, and thermal diffusion ratios all require the solution of a linear system of the form

$$\begin{aligned} \mu &= \sum_{i\in\mathcal{H}^*} \alpha_i^\mu x_i, \\ \sum_{j\in\mathcal{H}^*} G_{ij}^\mu \alpha_j^\mu &= x_i \quad \forall\, i \in \mathcal{H}^*, \end{aligned} \tag{4.43}$$

as shown in Section 2.5 where μ is η or λ_h. Classical approaches [198] to solve these systems either use a determinant method whereby $\mu = \{\eta, \lambda_h\}$ is computed via

$$\mu = -\begin{vmatrix} G^\mu & x \\ x^T & 0 \end{vmatrix} / |G^\mu|, \tag{4.44}$$

or simplified mixture rules such as those developed by Gupta and Yos [217] or Wilke [218]. Ern and Giovangigli [219, 220] propose instead to formulate symmetric positive definite transport systems allowing the linear systems to be solved quickly using a direct method such as the Cholesky (LDL^T) decomposition or with iterative methods such as the Conjugate-Gradient (CG) method. Solution via LDL^T requires a computational cost which scales with $\mathcal{O}(n^3/6)$ while the CG method is $\mathcal{O}(mn^2)$, where m is the number of iterations performed. It is therefore obvious that iterative methods are competitive when the number of iterations does not exceed $n/6$.

Fig. (4.11) shows the performance comparison of the Wilke, Gupta-Yos, CG, and LDL^T methods. Three CG solutions are presented in the figure: the first iterated until convergence was reached to machine precision, the second and third cases represent using only 1 and 2 iterations respectively. Fig. (4.11a) provides the computed shear viscosity for equilibrium air (11 species) at 1 atm obtained with each method. Fig. (4.11b) shows the required CPU time to compute the viscosity versus the number of heavy species, relative to the maximum time. From the figure it is clear that the Gupta-Yos method can be competitive below about 9000 K, however at higher temperatures the accuracy decreases significantly. The CG method converges to the exact LDL^T solution after only 2 iterations and is slightly faster, as expected. In practice however, the direct method should be prefered when finite-differences are used to compute the Jacobians necessary in implicit time integration schemes since the iterative procedures may introduce small oscillations in the result. These results are consistent with those obtained by Magin and Degrez [106] who studied the performance of these methods for equilibrium air.

Diffusion velocities

Diffusion velocities can be computed using multicomponent diffusion coefficients or, equivalently, a generalized Stefan-Maxwell equation as shown in Section 2.5.2. When internal energy is neglected, the multicomponent diffusion coefficients require the solution of $n^{\mathcal{S}}$ linear systems of size $\xi n^{\mathcal{S}}$, where $n^{\mathcal{S}}$ is the number of species and ξ is the Sonine polynomial order [219]. Ern and Giovangigli [221] have developed iterative algorithms to compute the multicomponent diffusion coefficient matrix which have been shown to be competitive with direct solvers.

In this work, the generalized Stefan-Maxwell system of Eqs. (2.86) and (2.87) is preferred over the transport systems for the multicomponent diffusion matrix. The Stefan-Maxwell system can be written as,

$$\sum_{j\in\mathcal{S}^*} G_{ij}^V(\xi)\boldsymbol{V}_j(\xi) = -\boldsymbol{d}_i^{\Theta\prime} + \kappa_i^{\Theta}\boldsymbol{E}, \quad i \in \mathcal{S}^*, \tag{4.45}$$

for Sonine polynomial order ξ and with the mass constraint

$$\sum_{j\in\mathcal{S}^*} y_j \boldsymbol{V}_j = 0, \tag{4.46}$$

where $\kappa_i^{\Theta} = \kappa_i\Theta_i$, $\boldsymbol{d}_i^{\Theta\prime} = \boldsymbol{d}_i'\Theta_i$ and $\Theta_i = T_h/T_i$. The matrix $\mathbf{G}^V \in \mathcal{R}^{n^{\mathcal{S}}\times n^{\mathcal{S}}}$, given in Appendix A, is symmetric positive semi-definite. Magin and Degrez [106] have shown that $\mathbf{G}^V$ can be replaced with the non-singular form, $\mathbf{G}^V + \alpha\boldsymbol{y}\boldsymbol{y}^T$, where α is a constant with the same order as the $\mathbf{G}^V$, such as $1/\max_{ij}\mathscr{D}_{ij}$. For a known electric field, Eq. (4.45) can be solved using the CG algorithm for constrained systems, with projector $\mathbf{P} = \bar{\boldsymbol{I}} - \boldsymbol{R}^V\boldsymbol{y}^T/(\boldsymbol{y}^T\boldsymbol{R}^V)$, where $R_i^V = 1, i \in \mathcal{H}^*$ and $R_e^V = T_e/T_h$. Alternatively, the non-singular form can be solved using the LDL^T decomposition.

When the electric field is ambipolar, the Stefan-Maxwell system is supplied with the ambipolar constraint, $\sum_{j\in\mathcal{S}^*}\kappa_j\boldsymbol{V}_j = 0$, and the electric field is solved along with the diffusion velocities,

$$\begin{bmatrix} \mathbf{G}^V(\xi) & -\boldsymbol{\kappa}^{\Theta}/s \\ -\boldsymbol{\kappa}^T/s & 0 \end{bmatrix} \begin{bmatrix} \boldsymbol{V}(\xi) \\ s\boldsymbol{E} \end{bmatrix} = - \begin{bmatrix} \boldsymbol{d}^{\Theta\prime} \\ 0 \end{bmatrix}, \tag{4.47}$$

where $s = \|\boldsymbol{\kappa}\|$ is a scaling factor used to improve numerical robustness. This system is indefinite and non-symmetric. A nonsingular form can be created using the mass constraint as above and solved using standard Gaussian elimination with pivoting. The singular form can be solved with the Krylov iterative technique, such as the Generalized minimum residual (GMRES) algorithm [222] with projector $\mathbf{P}$. Both the known electric field and ambipolar cases of the Stefan-Maxwell equations retain the same form at any Sonine polynomial order.

Approximations to the Stefan-Maxwell equations can also be obtained for partially ionized plasmas. For an ambipolar electric field, a generalization of Ramshaw and Chang's diffusion model [106] leads to the solution of heavy species diffusion velocities via the linear system

$$\sum_{j\in\mathcal{H}^*} \hat{G}_{ij}^V(\xi)\boldsymbol{V}_j(\xi) = -\boldsymbol{d}_i' + \frac{\kappa_i}{\kappa_e}\boldsymbol{d}_e', \tag{4.48}$$

under the mass constraint

$$\sum_{j\in\mathcal{H}^*} y_j \boldsymbol{V}_j(\xi) = 0, \tag{4.49}$$

where $\hat{\mathbf{G}}^V$ is given in Appendix A. The electron diffusion velocity and ambipolar electric field are then obtained from $x_e q_e \boldsymbol{V}_e = \sum_{j\in\mathcal{H}^*} x_j q_j \boldsymbol{V}_j$ and $\boldsymbol{E} = \boldsymbol{d}_e'/\kappa_e$, respectively. The matrix $\hat{\mathbf{G}}^V$ is symmetric and singular. A non-singular form is again introduced as $\hat{\mathbf{G}}^V + a\hat{\boldsymbol{y}}\hat{\boldsymbol{y}}^T$, where $\hat{\boldsymbol{y}}$ is the vector of heavy-species mass fractions. As with the full Stefan-Maxwell system, the non-singular form of Eq. (4.48) can be solved using the Cholesky factorization or the singular form can be solved using the CG algorithm with an appropriate projector. Magin and Degrez [106] have shown that Ramshaw's model provides reasonably accurate diffusion velocities for a significantly reduced cost as compared to solving the full generalized Stefan-Maxwell system. In addition, it was shown that

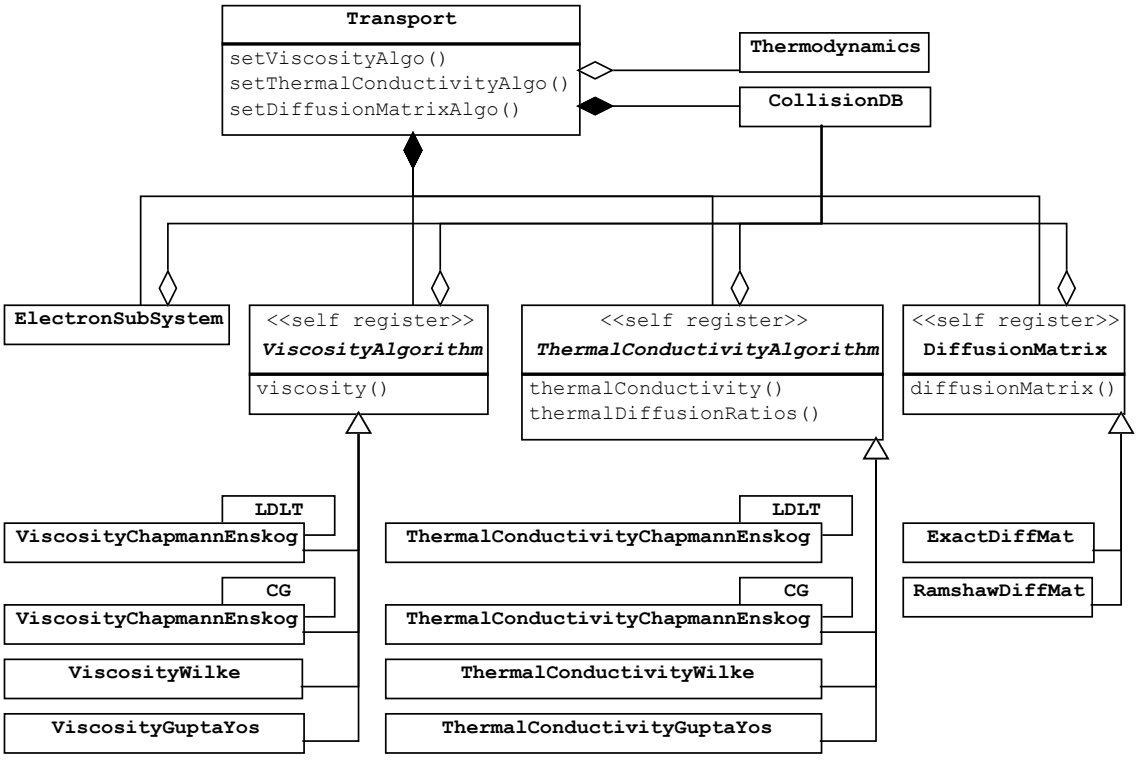

Figure 4.12.: *Simplified UML diagram for the design of the transport module.*

only first order Sonine polynomial terms are required for convergence.

4.5.3. Object-Oriented Design

A simplified class diagram of the transport module is given in Fig. (4.12). The module is responsible for providing all functions relevant to the computation of transport fluxes in MUTATION^{++}. Transport algorithms are implemented through the use of self registering algorithm classes. For example, the abstract class **`ThermalConductivityAlgorithm`** provides the necessary interface that all thermal conductivity algorithms must include, namely functions for computing the thermal conductivity and thermal diffusion ratios. Specific algorithms are then implemented by creating a concrete class which implements the interface. For thermal conductivity, four algorithms have been implemented in this work: the Wilke and GuptaYos mixture rules and the solution of the Chapman-Enskog linear transport system, solved either with the Cholesky decomposition ($LDLT$) or with iterative CG method. This pattern has also been used for the calculation of the multicomponent diffusion matrix and shear viscosity. Collision integral data is fed to each algorithm via the **`CollisionDB`** class which manages the efficient computation of the necessary collision integrals.

Collision integral database

An overview of the collision integral database is provided in Fig. (4.13). The design of the collision integral database has several important features, including

1. Collision integrals are only loaded when needed. This prevents the unnecessary errors from not finding data which isn't actually used and ensures that certain algorithms only compute the desired collision integrals. For example, the Wilke algorithm only requires integrals of collisions between the same species.

2. The database is self documenting. The XML format allows references to be included with the

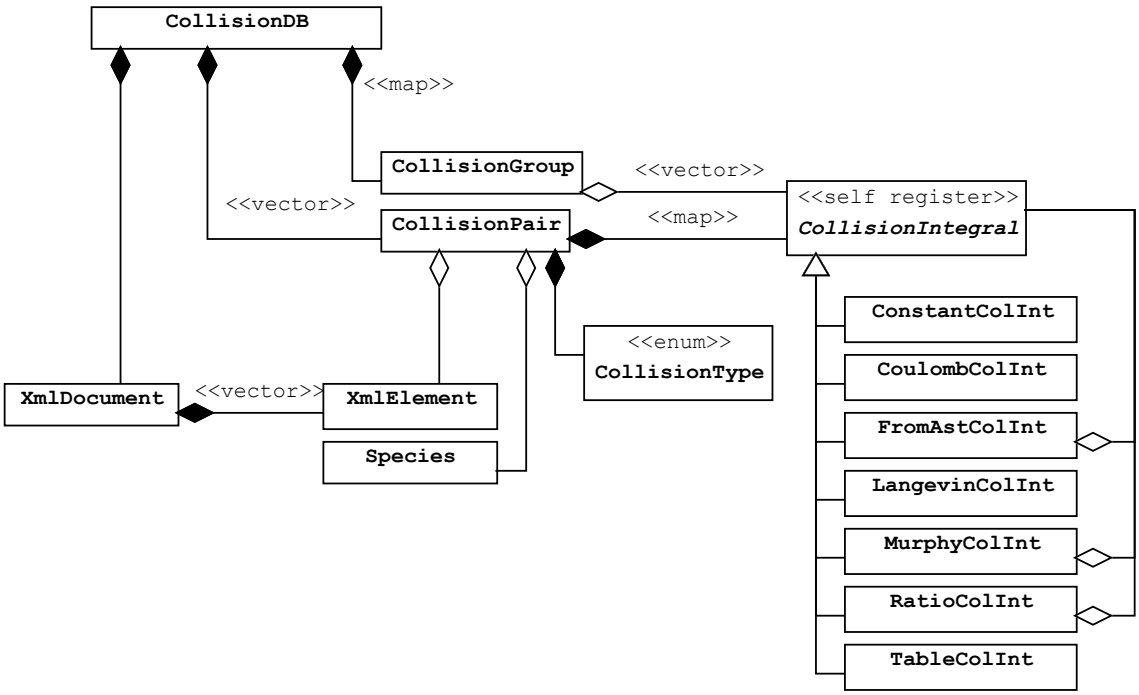

Figure 4.13.: *Simplified UML diagram for the design of the collision integral database.*

data and by providing the data in the same format as the data source, there is no guesswork in determining exactly what data is being used.

3. Users can easily add new data formats without having to recompile the library. This is enabled through the self registration of the collision integral types.
4. The default behavior used when data is missing can be easily configured inside the input file. For example, when a specific ion-neutral collision pair is not explicitly given in the database, the Langevin potential could be used if the polarizability of the neutral is provided.
5. Collision integral tables can be computed at run-time to improve the performance of the database.
6. Consistency between integrals and defined ratios are automatically enforced.

CollisionDB is organized into a map of **CollisionGroup** objects and a vector of **CollisionPair**s. The collision pairs represent each possible pair of species in the mixture and are responsible for determining the type of collision and loading collision integrals from the XML database when needed. The map of collision groups hold a collection of groups of collision integrals which can be identified by a given name. For example, the group "Q11ij" represents the set of reduced collision integrals of order (1,1) for all pairs of heavy species. **CollisionDB** is responsible for providing the **CollisionGroup** corresponding to the given name on demand. If a group is not already loaded, then it will first use the collision pairs to load all of the necessary integrals in the group. The temperature dependence of the collision integrals is also determined by the group name.

Collision integrals themselves are implemented by extending the self registering **CollisionIntegral** type. The base class provides a consistent interface so that all collision integral types know whether or not they can be tabulated, what convention they adhere to (should there be a factor of π applied or not), etc. Concreate **CollisionIntegral** types may even be functions of other collision integrals. For example, the **FromAstColInt** type can compute either $\bar{Q}_{ij}^{(1,1)}$, $\bar{Q}_{ij}^{(2,2)}$, or A_{ij}^{*} given the other two integrals. Using this framework, any collision integral format can be used in the database by simply creating a new concrete **CollisionIntegral** type and implementing the correct function for computing the integral from the given data.

4.5.4. Transport Properties

This section serves to both demonstrate and validate the calculation of transport coefficients for several equilibrium, partially ionized mixtures. For reference, Fig. (4.14) shows the equilibrium compositions of the three mixtures considered here. The first mixture represents equilibrium air, considering the eleven species comprised of N, N_2, O, O_2, NO, and their first ions plus free electrons. The second mixture is equilibrium carbon-dioxide. Eight species are considered: CO_2, CO, O_2, O, C, O^+, C^+, and e^-. The last mixture is equilibrium Jovian atmosphere consisting of the nine species H_2, $H_2{}^+$, H, H^+, H^-, He, He^+, He^{++}, and e^-. The equilibrium compositions have been computed using the Gibbs energy minimization procedure detailed in Chapter 5 at constant pressure of 1 atm.

Viscosity

The equilibrium shear viscosities of each of the mixtures shown in Fig. (4.14) are presented in Fig. (4.15). In addition, the viscosity of several frozen mixtures corresponding to the equilibrium compositions at specified temperatures are also shown. For the air and CO_2 cases, these temperatures are 300 K, 5000 K, 10 000 K, 15 000 K, and 20 000 K. For the Jupiter mixture, the temperatures are taken to be 300 K, 3500 K, 13 000 K, 30 000 K, and 50 000 K in order to accommodate the larger temperature range.

Two general trends can be seen in Fig. (4.15). The first is that viscosity tends to increase with temperature for a fixed mixture composition as is visible from the frozen cases. The second is that viscosity decreases with increasing levels of ionization. Both trends are easily predicted by considering the viscosity of a pure gas i (given in Appendix A),

$$\eta_i = \frac{5}{16}\frac{\sqrt{\pi k_B T m_i}}{\bar{Q}_{ii}^{(2,2)}}, \tag{4.50}$$

where m_i and $\bar{Q}_{ii}^{(2,2)}$ are the mass and reduced collision integral of the gas. As was noted in Section 4.5.1, the collision integrals for resonant charge transfer and charged interactions are significantly larger than other collisions due to Coulomb forces. Thus, as the level of ionization increases, these interactions dominate and the viscosity decreases due to the inverse proportionality with $\bar{Q}_{ii}^{(2,2)}$.

Fig. (4.15) includes comparisons with literature results for both the air and Jupiter mixtures. For air, the computed viscosity is compared to the result obtained by D'Angola *et al.* [197] who have developed a set of accurate curve-fits for equilibrium air thermodynamic and transport properties. The Jupiter result is compared with the calculations of Bruno *et al.* [203] based on a review of accurate collision integral data for Jupiter mixtures. Only minor differences can be seen in both cases. In the air case, the differences can be attributed small differences in the collision integral data used in this work compared to [197], while in the Jupiter case, the differences are a result of slightly different equilibrium compositions as a result of the thermodynamic data used in [203].

Diffusion fluxes

For a mixture in thermochemical equilibrium with constant pressure and element fractions, species diffusion velocities may be expressed from Eqs. (2.84) and (2.85) as,

$$\boldsymbol{V}_i = -\sum_{j\in\mathcal{S}} D_{ij}\left[\frac{\partial x_j}{\partial T} + \frac{(\chi_j^h + \chi_j^e)}{T}\right]\boldsymbol{\nabla} T + \boldsymbol{E}\sum_{j\in\mathcal{S}} D_{ij}\kappa_j, \quad \forall\, i \in \mathcal{S}, \tag{4.51}$$

where $\partial x_j/\partial T$ are the derivatives of equilibrium species mole fractions with respect to temperature. It will be shown in Chapter 5 that these derivatives can be evaluated cheaply during the solution of the equilibrium compositions. In principle, when element fractions are assumed constant, the mole fraction derivatives should be constrained to prevent elemental demixing [224, 225] through the diffusion of elements. The electric field $\boldsymbol{E}$ can either be specified in Eq. (4.51), or

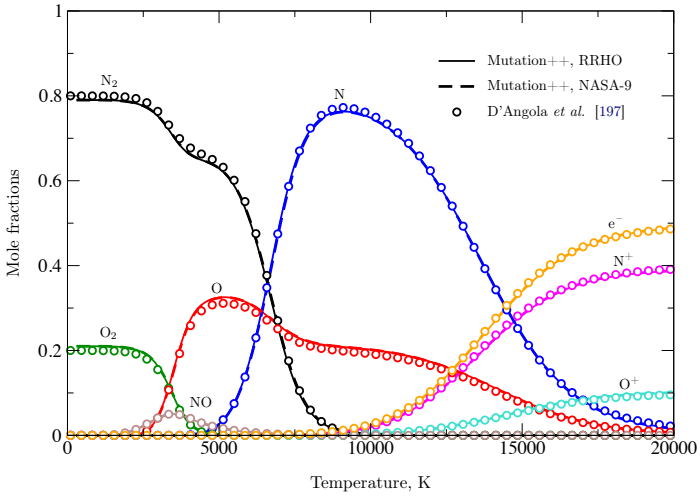

(a) *11-species air,* 79 % N_2 - 21 % O_2 *by volume.*

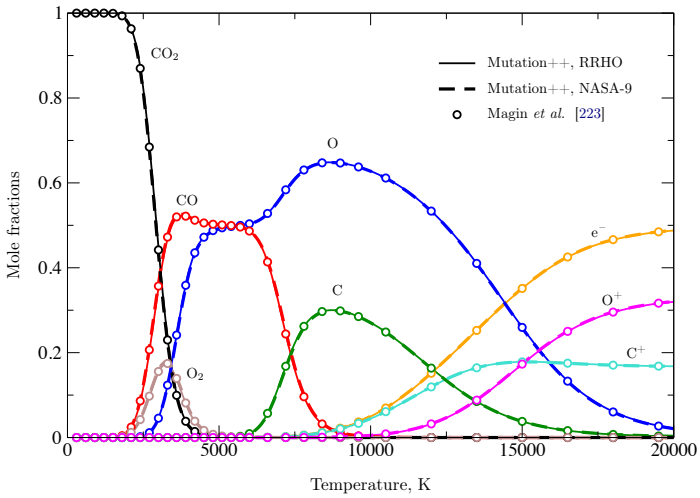

(b) *8-species* CO_2, 100 % CO_2 *by volume.*

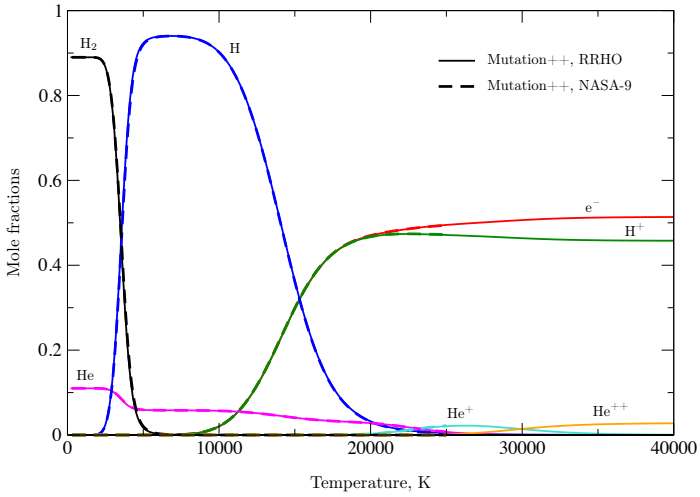

(c) *9-species Jupiter,* 11 % *He* - 89 % H_2 *by volume.*

Figure 4.14.: *Equilibrium compositions of selected mixtures at* 1 atm.

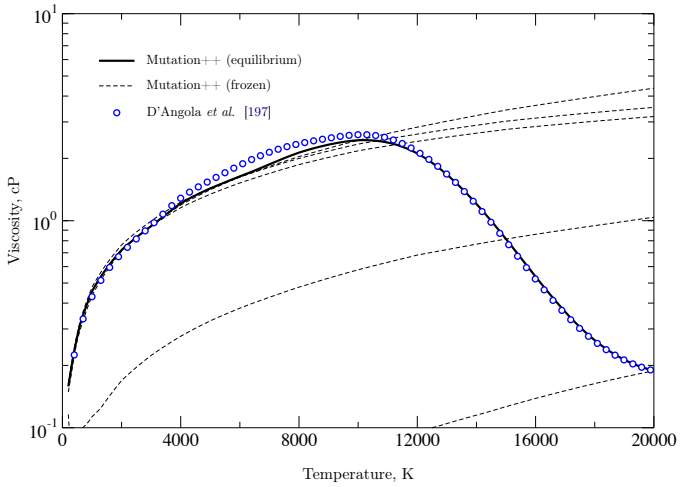

(a) *11-species air.*

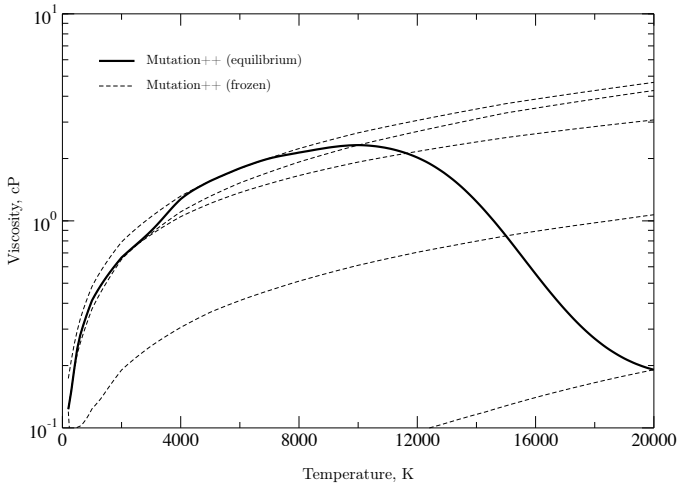

(b) *8-species CO_2.*

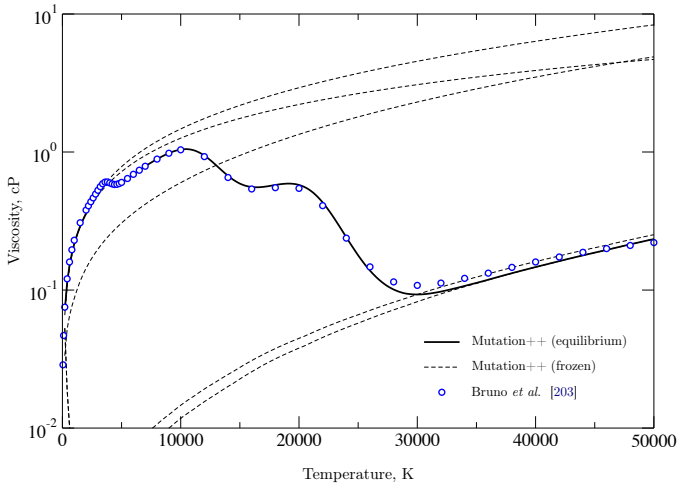

(c) *9-species Jovian atmosphere.*

Figure 4.15.: *Viscosities of selected mixtures at* 1 atm.

determined explicitly from the ambipolar constraint which assumes that there is no net electric current, $\sum_{i\in\mathcal{S}} n_i q_i \boldsymbol{V}_i = 0$. Under this assumption, the ambipolar electric field is given as

$$\begin{aligned} \boldsymbol{E}_\mathrm{a} &= E_\mathrm{a}^{\boldsymbol{\nabla} T} \boldsymbol{\nabla} T \\ E_\mathrm{a}^{\boldsymbol{\nabla} T} &= \frac{\sum_{i\in\mathcal{S}} n_i q_i \sum_{j\in\mathcal{S}} D_{ij} \left[\frac{\partial x_j}{\partial T} + \frac{(\chi_j^h + \chi_j^e)}{T}\right]}{\sum_{i\in\mathcal{S}} n_i q_i \sum_{j\in\mathcal{S}} D_{ij} \kappa_j}, \end{aligned} \tag{4.52}$$

where $E_\mathrm{a}^{\boldsymbol{\nabla} T}$ denotes the ambipolar electric field per temperature gradient. The computed ambipolar electric fields for equilibrium air and CO_2 at 1 atm are shown in Fig. (4.16). The effect of thermal nonequilibrium is also simulated by artificially increasing the heavy particle translational temperature after computing the equilibrium compositions. As can be seen in the figure, $\boldsymbol{E}_\mathrm{a}$ increases unbounded with decreasing temperature as a result of the denominator in Eq. (4.52) going to zero as the degree of ionization vanishes. The bumps present in the electric field of both mixtures from 5000 K to 8000 K correspond to the dissociation of N_2 and CO which increase the magnitude of the mole fraction derivatives for air and CO_2, respectively.

Species equilibrium diffusion fluxes per temperature gradient are shown in Fig. (4.17) for the first and second Sonine polynomial approximations for both air and CO_2. The diffusion fluxes were computed using the equivalent formulation of the Stefan-Maxwell system, for constant pressure, equilibrium mixtures, neglecting thermal diffusion. It is clear from the figure that the diffusion fluxes correctly sum to zero at all temperatures, according to the conservation of mass and the definition of the diffusion velocities. Positive values of the diffusion fluxes in Fig. (4.17) indicate that those species diffuse along the direction of the temperature gradient, while negative fluxes indicate moving against the gradient. For example, consider the diffusive fluxes of N_2 and N which are nearly balanced around 7000 K in Fig. (4.17a). In this region, the level of N_2 dissociation is increasing with increasing temperature, resulting in nearly equal and opposite gradients in the mole fractions of N_2 and N, with respect to temperature. As the temperature increases, the equilibrium mixture has more nitrogen atoms and less molecules, resulting in N_2 diffusing towards the higher temperature region and N diffusing away due to Fickian diffusion.

Heat flux

Using Eq. (4.51), the equilibrium, isobaric mixture heat flux can be expressed as

$$\boldsymbol{q} = -(\lambda_h + \lambda_e + \lambda_\mathrm{int} + \lambda_\mathrm{r} + \lambda_\mathrm{s}) \boldsymbol{\nabla} T, \tag{4.53}$$

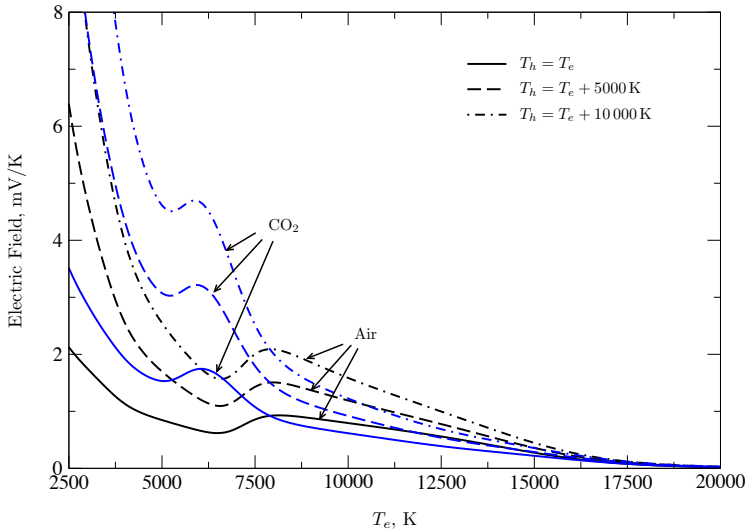

Figure 4.16.: *Ambipolar electric field per temperature gradient for equilibrium mixtures at* 1 atm.

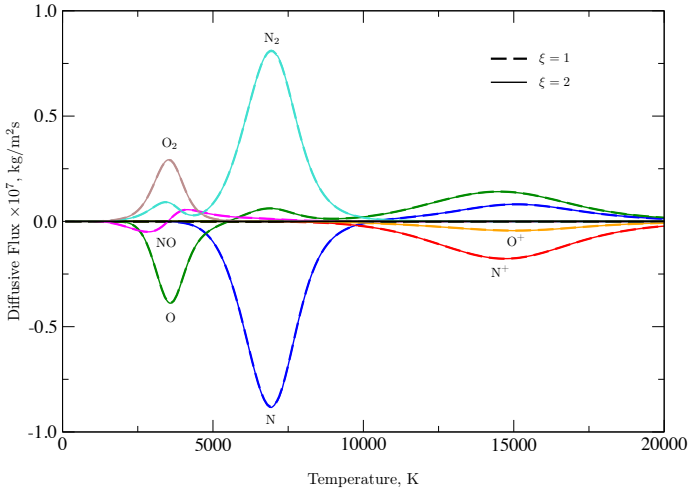

(a) *Air*

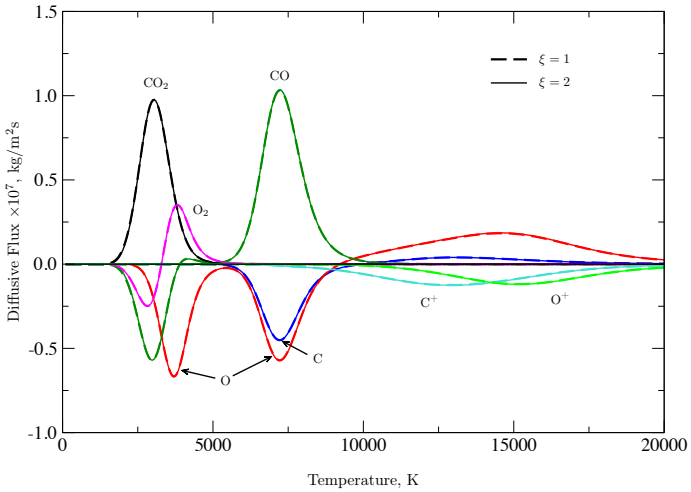

(b) *CO_2*

Figure 4.17.: *Species diffusion fluxes per temperature gradient for equilibrium mixtures at* 1 atm *using the ambipolar constraint on the electric field with first and second Sonine polynomial orders. Thermal diffusion is neglected.*

where λ_r and λ_s are the reactive and Soret thermal conductivities written as

$$\lambda_\mathrm{r} = \sum_{i,j\in\mathcal{S}} \rho_i h_i D_{ij} \left[\frac{\partial x_j}{\partial T} + \frac{(\chi_j^h + \chi_j^e)}{T} - \kappa_j E_\mathrm{a}^{\nabla T} \right], \quad \text{and} \tag{4.54}$$

$$\lambda_\mathrm{s} = p \sum_{i,j\in\mathcal{S}} (\chi_i^h + \chi_i^e) D_{ij} \left[\frac{\partial x_j}{\partial T} + \frac{(\chi_j^h + \chi_j^e)}{T} - \kappa_j E_\mathrm{a}^{\nabla T} \right]. \tag{4.55}$$

These terms act as effective thermal conductivities which arise from the dependence on temperature for equilibrium mole fractions. Here, the reactive thermal conductivity includes the effect of elemental demixing.

Butler and Brokaw [224, 226] developed a formulation of the reactive thermal conductivity which enforces zero elemental demixing by considering a set of $n^r = n^\mathcal{S} - n^\mathcal{E}$ formation reactions at equilibrium and neglecting thermal diffusion and external forces. The Butler-Brokaw formula

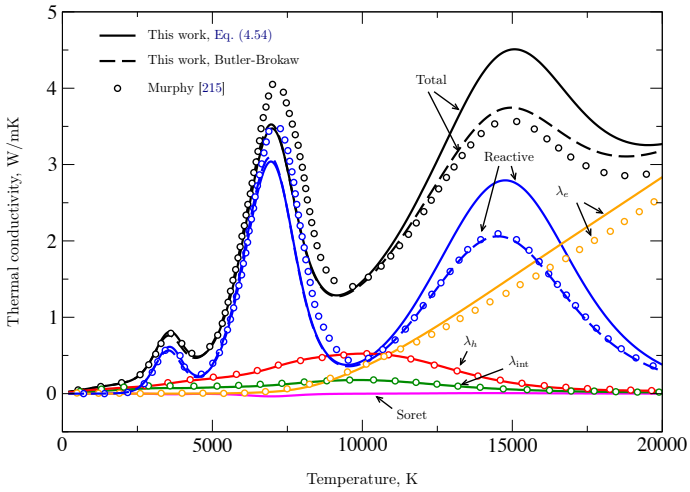

Figure 4.18.: *Components of thermal conductivity for equilibrium air at* 1 atm.

can be written in terms of the solution of a linear system [226],

$$\begin{aligned} \lambda_r &= \frac{1}{k_B T^2} \sum_{i=1}^{n^r} w_i \Delta H_i, \\ \sum_{j=1}^{n^r} A_{ij} w_j &= \Delta H_i, \end{aligned} \tag{4.56}$$

where ΔH_i is the enthalpy change across the formation reaction i and A_{ij} is an $n^r \times n^r$ symmetric positive definite matrix, which is a function of species mole fractions, formation reaction stoichiometric coefficients, and binary diffusion coefficients. Eq. (4.56) has been widely used to compute the reactive thermal conductivity for equilibrium gases because it does not require the explicit calculation of the multicomponent diffusion coefficients or mole fraction derivatives as is required by Eq. (4.54). In addition, the formula can provide better agreement with experimentally determined thermal conductivities, which can be attributed to the absence of elemental demixing. However, for CFD simulations of flows in thermochemical equilibrium, the expression in Eq. (4.54), resulting from the Chapman-Enskog solution of the Boltzmann equation, should be used since elemental demixing can occur.

Fig. (4.18) compares the contributions of each of the thermal conductivies presented in Eq. (4.53) for equilibrium air. Below about 2500 K, the heat flux is solely due to conduction of translational and internal energy of heavy particles. As the temperature rises and chemical reactions produce gradients in species mole fractions, diffusion becomes the dominant mode of heat transport, reflected in the reactive thermal conductivity. The three peaks in the reactive term in Fig. (4.18) can be attributed to (from left to right) dissociation of O_2, dissociation of N_2, and ionization of N and O. Good agreement is obtained between the Butler-Brokaw formula and Eq. (4.54) below 10 000 K, however Butler-Brokaw underestimates the reactive thermal conductivity in the third peak. Above about 17 000 K, ionization of N and O produce enough free electrons to make conduction of electron energy the dominant term in the heat flux. The Soret thermal conductivity is negligible at all temperatures.

The thermal conductivities shown in Fig. (4.18) are compared with the results of Murphy [215]. Excellent agreement is obtained for the conduction of heavy particle energy. Good agreement is also found for the reactive thermal conductivity computed using the Butler-Brokaw formula, which was used by Murphy. However, the second peak of the reactive thermal conductivity of Murphy is about 15 % higher than computed in this work with the Butler-Brokaw formula. This is most likely a result of different collision integral data used for the N_2-N interaction.

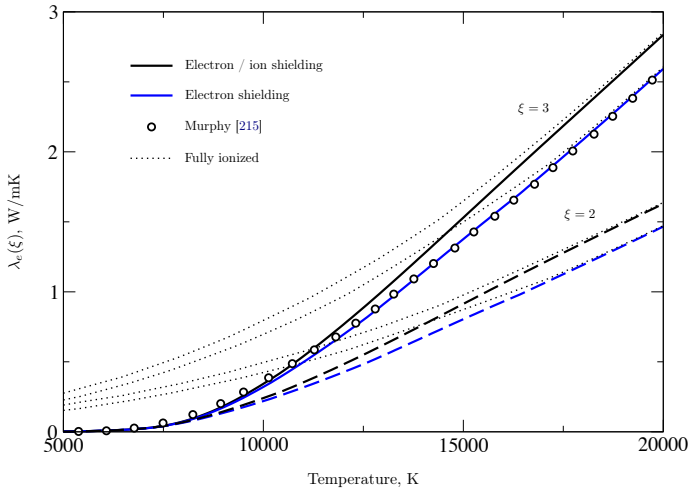

Figure 4.19.: *Electron thermal conductivity of equilibrium air at* 1 atm *for Sonine polynomial orders of 2 and 3 and considering electron and electron / ion shielding for the Debye length.*

A small difference can also be seen in the electron thermal conductivity at high temperatures. Fig. (4.19) compares the electron thermal conductivity of equilibrium air at 1 atm computed at both second and third Sonine polynomial orders. Both electron shielding and electron / ion shielding are considered for the calculation of the Debye length in the shielded Coulomb potential. For reference, the electron thermal conductivity of a fully ionized mixture is also shown. Several observations can be made. The first is that the electron thermal conductivity requires a polynomial order of 3, following the conventional convergence rule of two nonvanishing Sonine polynomials for ionized mixtures [227]. Second, ion shielding increases the electron thermal conductivity by decreasing the effective range of the shielded Coulomb potential for electron-ion interactions. As expected, all results converge to the fully ionized case at high temperatures. The result of Murphy is in excellent agreement when only electron shielding is considered, explaining the difference observed in Fig. (4.18), in which ion shielding is considered as well.

Finally, Fig. (4.20) compares the total thermal conductivity of air at 1 atm to those computed numerically by D'Angola *et al.* [197], Capitelli *et al.* [228], and Murphy [215] using the Butler-Brokaw formula, and the results obtained experimentally by Azinovsky *et al.* [229]. Similar agreement is obtained as was detailed for the result of Murphy. The difference between the experimental data and the computation in the second peak around 7000 K is due to the N_2-N collision integral data based on more accurate calculations, as previously discussed.

4.6. Chemical Kinetics

The goal of the chemical kinetics module in MUTATION^{++} is the efficient and robust computation of species production rates due to finite-rate chemical reactions. The derivation of the production rate of a species $k \in \mathcal{S}^*$ due to homogeneous chemical reactions was presented in Section 2.6.1. We consider production rates in the form

$$\begin{aligned}\dot{\omega}_k &= M_k \sum_{r\in\mathcal{R}} \nu_{kr}\mathfrak{R}_r \\ &= M_k \sum_{r\in\mathcal{R}} (\nu''_{kr} - \nu'_{kr}) \left[k_{f,r}(T_{fr}) \prod_{j\in\mathcal{S}^*} \hat{\rho}_j{}^{\nu'_{jr}} - k_{b,r}(T_{br}) \prod_{j\in\mathcal{S}^*} \hat{\rho}_j{}^{\nu''_{jr}} \right] \Theta_r,\end{aligned} \tag{4.57}$$

where $\Theta_r = \sum_{j\in\mathcal{S}^*} \alpha_{jr}\hat{\rho}_j$ if reaction r is a thirdbody reaction and $\Theta_r = 1$ otherwise. The forward reaction rate is assumed to be a function of a single, reaction-dependent temperature T_{fr} and the backward rate is determined from equilibrium as $k_{b,r}(T_{br}) = k_{f,r}(T_{br})/K_{\mathrm{eq},r}(T_{br})$ where T_{br} is a

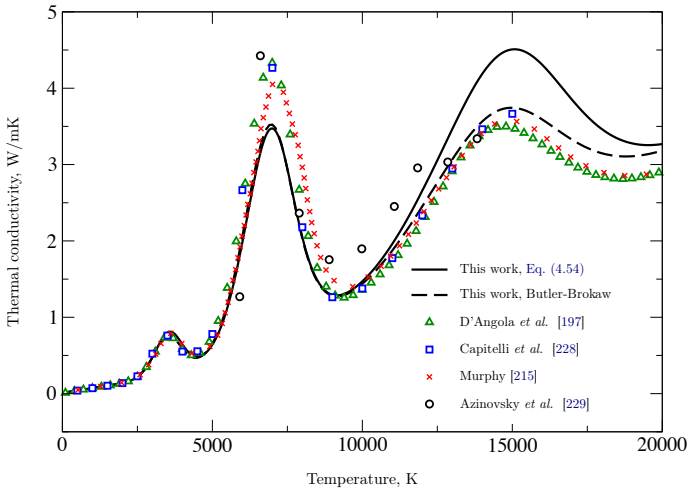

Figure 4.20.: *Thermal conductivity of equilibrium air at* 1 atm.

reaction-dependent temperature for the backward rate.

In principle, the evaluation of Eq. (4.57) is straight-forward. However, several features of the chemical kinetics module are worth mentioning, regarding the object-oriented and efficient solution of species production rates. A simplified class diagram of the module is presented in Fig. (4.21). The module contains a list of **`Reaction`** objects which are loaded from an XML reaction mechanism file, provided by the user. The rest of the module is comprised of a set of computational "managers", which are responsible for the efficient evaluation of individual parts of Eq. (4.57). These include the evaluation of reaction rates, operations associated with the reaction stoichiometry (the sum and products in Eq. (4.57)), and the evaluation of the thirdbody term, Θ_r. An additional manager class is responsible for evaluating the Jacobian of species production rates, necessary for implicit time-stepping CFD algorithms. Finally, the **`Kinetics`** class orchestrates the use of each of these managers to build up the evaluation of Eq. (4.57) and its Jacobian with respect to species densities and temperatures. A more detailed discussion of a few specific points is presented in the following subsections.

4.6.1. Automatic Reaction Type Recognition

As was mentioned previously, the temperature dependence of reaction rates is determined by the type of reaction. This differs from typical combustion applications which are in thermal equilibrium. The temperature dependence can either be input by the user or determined from the type of reaction. When reactions are loaded by MUTATION++, their type is automatically determined in order to associate the correct forward and backward temperatures necessary to evaluate the reaction rates. A list of reactions considered and their corresponding forward and backward temperatures is provided in Table 2.1.

The problem of automatically determining the type of a given reaction is well posed in the context of a *classification tree* [230]. Classification trees are a specialization of *decision trees* in which the result of the tree is to classify a list of objects into a finite set of discrete classes given a set of predictor variables which characterize the objects. Several algorithms have been developed in the literature for the automatic creation of classification trees from a set of training data, however these are not necessary in this context since reactions can be categorized from a relatively small set of predictors. As an example, the classification tree developed in this work for all non-STS reactions in Table 2.1 is presented in Fig. (4.22). The tree is traversed from left to right, starting at a root node. The root and internal nodes are colored yellow and represent properties of the reaction in consideration. In particular, they have all been formulated in terms of three basic yes/no questions.

1. Is there an electron / ion in the reactants / products?

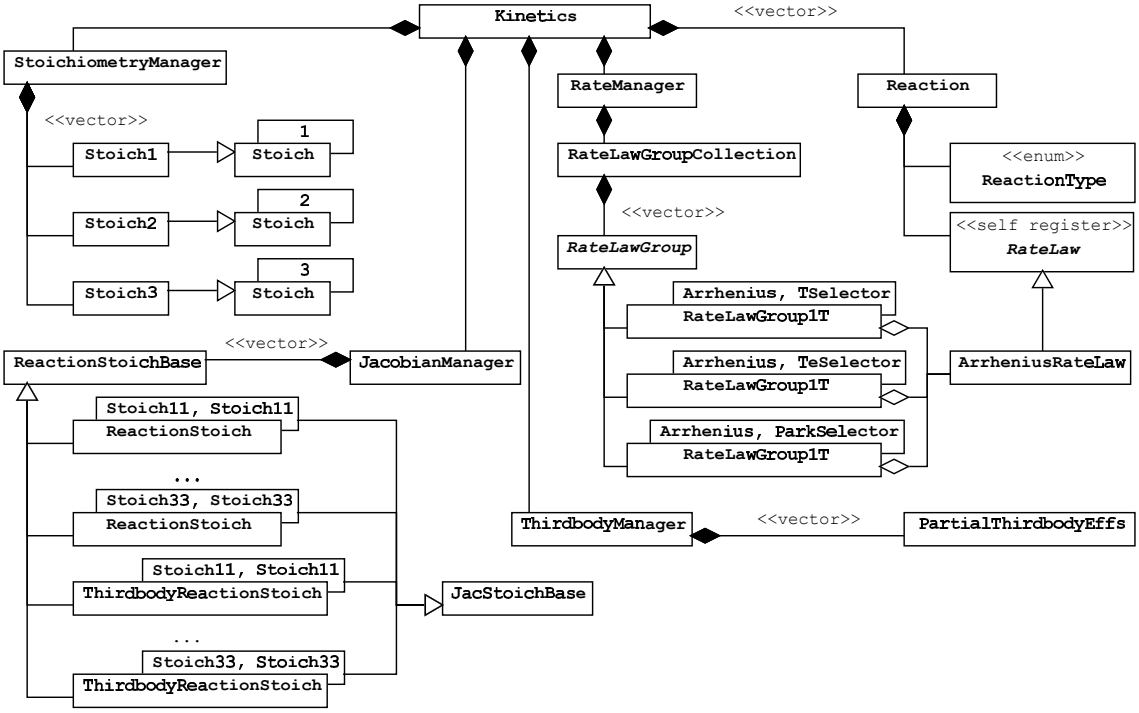

Figure 4.21.: *Simplified UML diagram of the kinetics module.*

2. Is there an inert electron / heavy species?
3. Are there more reactants than products?

These properties are easily determined from the reaction stoichiometry. The red leaf nodes in the tree represent the result of the classification tree which in this case is the fourteen reaction types considered. In practice, classification trees can be represented as tree or graph data structures. However, for this simple case the usual "if/else if/else" construct has been used.

The use of a classification tree has several advantages. To begin, the logic can be represented and easily understood through the use of a flow diagram like Fig. (4.22). If a considered reaction is one of the considered types, then it is guaranteed to be correctly classified. In addition, Fig. (4.22) represents a fairly well balanced tree, leading to a correct result in as little as two and at most five branches. A disadvantage with this approach is that an incorrect classification will be made for a reaction with a type not considered in the tree and in general it is not possible to know if this has happened. Therefore, it is up to the user to know which reaction types have been implemented, and those which have not.

4.6.2. Efficient Evaluation of MT Reaction Rates

The evaluation of reaction rate coefficients can occupy a considerable amount of CPU time when large reaction mechanisms are considered. The **`RateManager`** class, shown in Fig. (4.21), is responsible for optimizing as much as possible this process. This section provides an overview of the necessary steps for decomposing the rate coefficient calculation into efficient parts.

We first recall that for Arrhenius type reaction rates, the rate coefficients for reaction r are given as

$$k_{f,r}(T_{fr}) = A_r T_{fr}^{\beta_r} \exp\left(-\frac{\theta_r}{T_{fr}}\right), \quad \text{and} \tag{4.58}$$

$$k_{b,r}(T_{br}) = \frac{k_{f,r}(T_{br})}{K_{\mathrm{eq},r}(T_{br})}, \tag{4.59}$$

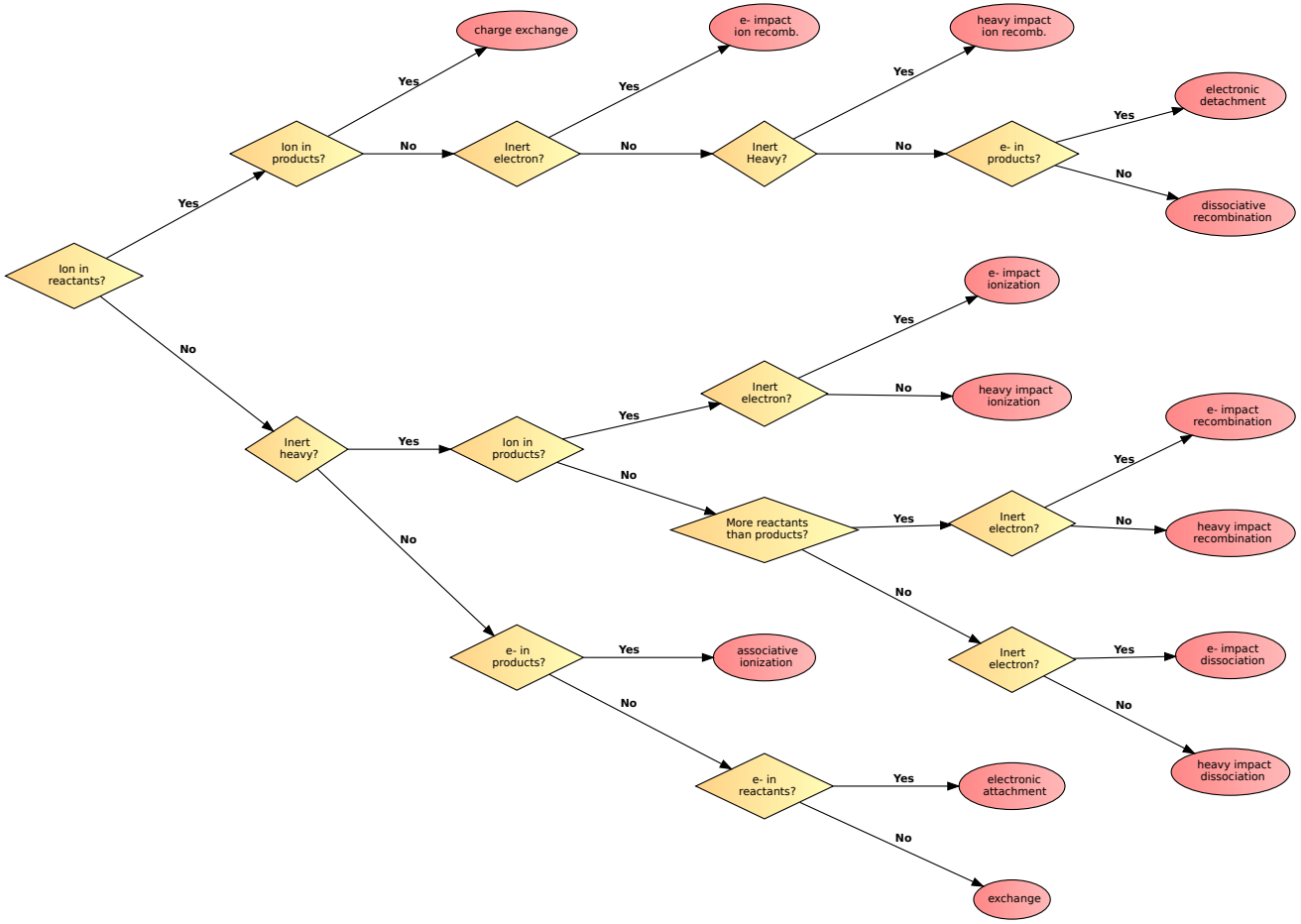

Figure 4.22.: *Classification tree for determining types of non-STS reactions.*

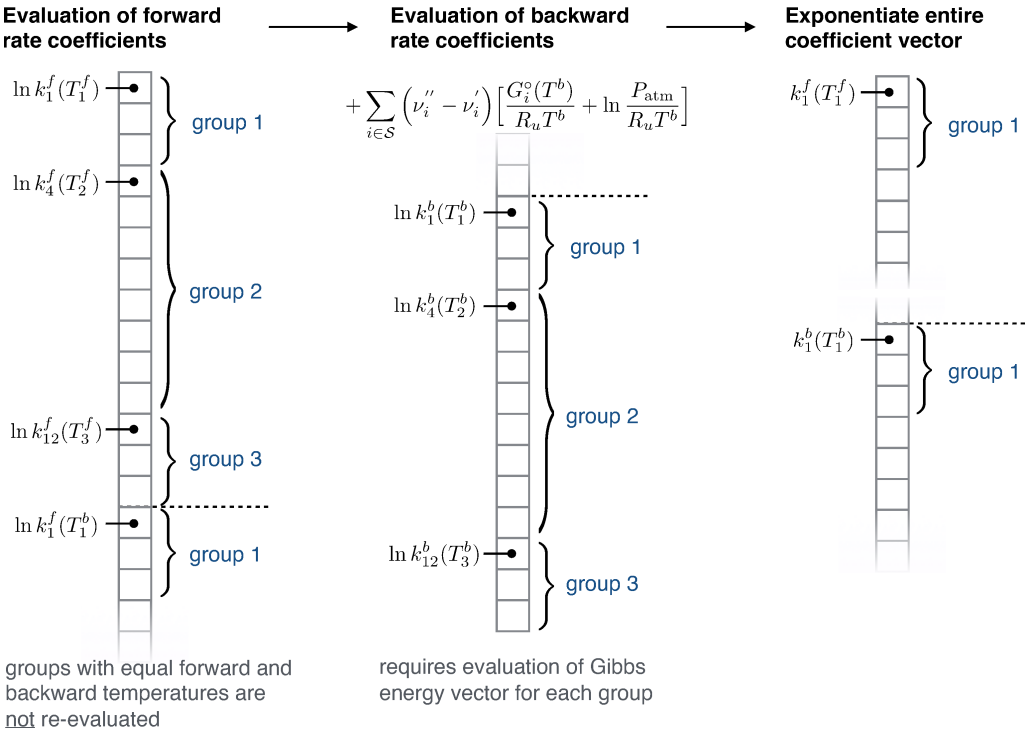

Figure 4.23.: *Order of operations for efficient evaluation of MT rate coefficients.*

where $K_{\mathrm{eq},r}$ is the equilibrium constant

$$K_{\mathrm{eq},r}(T_{br}) = \left(\frac{p^\circ}{R_uT_{br}}\right)^{\Delta\nu_r} \exp\left(-\frac{\Delta G_r^\circ(T_{br})}{R_uT_{br}}\right). \tag{4.60}$$

From a numerical standpoint, evaluating Eqs. (4.58 - 4.60) requires $2(n^{\mathcal{S}}+1)$ add/multiply operations, 3 divisions, 2 powers, and 2 exponentials per reaction (not including the calculation of species standard-state Gibbs energies). The division, power, and exponential operations remain expensive on modern computer architectures, requiring anywhere from 4 to 50 times more clock cycles. The situation is improved conventionally by considering the natural logarithm of the rate coefficients,

$$\ln k_{f,r}(T_{fr}) = \ln A_r + \beta_r \ln T_{fr} - \frac{\theta_r}{T_{fr}}, \quad \text{and} \tag{4.61}$$

$$\ln k_{b,r}(T_{br}) = \ln k_{f,r}(T_{br}) + \sum_{j\in\mathcal{S}^*}\left(\nu_{rj}^{''}-\nu_{rj}^{'}\right)\left[\frac{G_j^\circ}{R_uT_{br}} - \ln\left(\frac{p^\circ}{R_uT_{br}}\right)\right]. \tag{4.62}$$

Evaluating the logarithm of the rate coefficients and then exponentiating requires only $n^{\mathcal{S}}+4$ add/multiply operations and 2 exponentials per reaction, avoiding the power and division operations altogether, assuming the necessary $\ln T$, $1/T$, and $\ln p/R_uT$ terms are pre-computed for each group of reactions which share the same temperature dependence. The number of add/multiply operations can also be significantly reduced by recognizing that the maximum number of non-thirdbody species participating in any single reaction is 4 and therefore at most 4 terms will be nonzero in the summation in Eq. (4.62). Optimizations of this type are discussed in the next section.

Based on this analysis, Fig. (4.23) shows an example of the order of operations used by the **`RateManager`** class to compute the rate coefficients in an efficient way. In this example, the reaction mechanism consists of 14 reactions which have 3 separate **`RateLawGroup`**s, corresponding to 3 rate law and temperature dependence combinations. In the first step, the natural logarithms

of the forward rate coefficients are computed, including those used in the backward rate coefficient evaluation. Note that for Arrhenius rate laws, Eq. (4.61) can be efficiently evaluated for a whole group using a matrix-vector product in order to minimize the effect of cache thrashing. In the example, groups 2 and 3 share the same rate law and temperature dependence in both the forward and backward directions, therefore the forward coefficient at the backward temperature is not reevaluated. In a second step, the logarithm of the backward rate coefficients are evaluated using Eq. (4.62). Finally, the entire vector of forward and backward rate coefficients are exponentiated. Evaluating the entire vector at once allows for additional compiler optimizations, such as vectorization.

4.6.3. Stoichiometric Operations

The result of the summations and products in Eqs. (4.57) and (4.62) are functions of the stoichiometric coefficients for all species in the species set for a given reaction. An important observation however, is that at most four species can have non-zero stoichiometric coefficients for any given reaction. It is therefore inefficient to evaluate these summations and products by looping explicitly over all species. The class **`StoichiometryManager`** shown in Fig. (4.21) is responsible for evaluating these operations in an efficient way by keeping track of species indices which contribute to each reaction and providing suitable stoichiometric operations.

4.7. Concluding Remarks

This chapter detailed the design of MUTATION++, a new software library written in C++ for providing physicochemical models, data, and algorithms for use in hypersonic CFD codes. The library has been designed using modern OOP techniques in an effort to maximize its extendability and efficiency. The driving principle behind MUTATION++ is the ability to separate the underlying thermochemical model from the set of governing equations solved by the CFD tool. A generic set of governing equations was presented which encompasses all of the energy partitioning and thermochemical nonequilibrium models presented in Chapter 2. The concept of a state model was also introduced to provide the link between CFD and MUTATION++. At a high level, the library is organized into three modules: thermodynamics, transport, and chemical kinetics.

Two separate thermodynamic databases were presented in the framework of the thermodynamics module: one based on the RRHO energy partitioning model and the other based on the NASA thermodynamic polynomials. Pure species thermodynamic properties were derived based on the RRHO assumption and a summary of the resulting analytical expressions for these properties was presented using fundamental properties of the molecules. Using an object-oriented approach, both databases are seamlessly integrated and can be selected by the user at run-time. A comparison of mixture thermodynamic properties for equilibrium air, using both databases and the work of D'Angola *et al.* [197], serves to validate the implementation of the module.

The transport module was split roughly into the calculation of transport collision integrals and a discussion of transport algorithms. The collision integrals were defined for a multitemperature gas in which heavy species and free electrons thermalize at different temperatures. A summary of the necessary collision integrals required to compute all of the transport properties presented in Chapter 2 was provided. In addition, an extensive review of common interaction potentials used to compute collision integrals was made for neutral-neutral, ion-neutral, electron-neutral, and charged particle interactions. It was shown that collision integral data comes in a wide variety of formats in the literature and that the OOP approach used in the design of the MUTATION++ collision integral database allows for each of these formats to be integrated in a simple and efficient way. Transport algorithms were also reviewed in this chapter based on a previous work by Magin and Degrez [107]. Transport properties for equilibrium air, CO_2, and Jupiter were compared with relevant literature results in order to validate the transport module.

A few important aspects of the chemical kinetics module were also presented in this chapter including an object-oriented approach for the efficient calculation of species chemical production rates. In addition, a classification tree was developed to enable the automatic classification of

chemical reactions in order to determine the correct temperature dependence of individual reaction rates in a multitemperature context.

The MUTATION^{++} library has been coupled to the computational tools presented in Chapter 6 and applied to several atmospheric entry simulations in Chapter 7. Apart from the direct contribution to this thesis, it is worth mentioning that MUTATION^{++} has contributed to a number of other applications as well. These include the study of biomass pyrolysis [231], state-to-state catalytic recombination of nitrogen flows, [232], transport properties of carbon-phenolic ablation mixtures [208], atmospheric entry of meteors [233, 234], and uncertainty quantification for high enthalpy, plasma wind tunnels [235]. Finally, the library is available for download, open source, at `https://sync.vki.ac.be/mpp/mutationpp`.

CHAPTER 5

Linearly Constrained Multiphase Equilibria

"Gibbs is the greatest mind in American history."

— Albert Einstien, *(c. 1925)*

5.1. Introduction

The efficient and robust computation of multiphase, constrained equilibrium compositions is an important topic over a wide range of fields including combustion, aerospace and (bio)chemical engineering, metallurgy, paper processes, and the design of thermal protection systems for atmospheric entry vehicles (e.g., [236–241]). For a detailed history and list of applications, the reader is referred to the treatises by van Zeggeren and Storey [242] or Smith and Missen [243].

Prior to the work of White *et al.* [244], the equilibrium constant formulation was primarily used to compute equilibrium compositions for ideal, gas phase mixtures. The equilibrium constant formulation works by assigning formation reactions to each species based on a set of base or component species which are chosen *a priori* for the given reaction system. Kuo [117] cites several disadvantages that hindered researches using this method including difficulties in extending the method to non ideal equations of state, testing for the presence of condensed species and numerical complications with the use of component species.

In 1958, White, Johnson, and Dantzig [244] introduced the concept of free-energy minimization and proposed a numerical solution technique using the method of steepest decent. White [245] later elaborated on the advantages of free-energy minimization and the use of element potentials in the solution of equilibrium compositions, including the possibility to treat any general chemical system without the necessity of specifying the formation reactions. In addition, the use of element potentials allowed for the solution of linear systems whose size scaled with the number of elements rather than species, present in the mixture. This fact alone offers a significant computational advantage when considering large chemical systems.

Today, both the equilibrium constant formulation and the free-energy minimization methods are widely used. Most commercial and general purpose research codes implement various numerical methods for solving the free-energy minimization problem, however the equilibrium constant formulation is still used in certain applications [103, 239]. Perhaps one of the most widely used equilibrium codes today is the Stanford-JANAF (STANJAN) code by Reynolds [246] who popularized the element potential method for constrained Gibbs free-energy minimization by developing a numerical solution procedure to the minimization problem which solves the so-called "dual problem." Part of the success of the STANJAN method lies in its powerful initialization and preconditioning procedures which help make STANJAN extremely robust for most problems. The CEA code developed by Gordon and McBride [166, 182] is also used heavily, helped by the success of the detailed thermodynamic database developed at NASA Glenn Research Center [181], which it employs.

In addition to the normal mass balance constraints, so called "generalized constraints" [247] on the equilibrium solution have been used in a wide range of applications [238] and in particular, are an integral component of the Rate-Controlled Chemical Equilibrium (RCCE) [247–261] method. Some important examples of constraints used in the RCCE method include constraints on the

total number of moles, the number of free valence electrons, and the number of O−O bonds, among many others [238, 260]. Bishnu *et al.* [262, 263] added the ability to include general linear constraints on the equilibrium solutions to both STANJAN and CEA. They found that, under certain conditions, both the constrained versions of STANJAN and CEA failed to converge to a solution. In general, these situations arise when the linear constraints force the equilibrium composition near the boundary of the feasible region imposed by the hyperplane defined by the constraints.

In an effort to provide a provably robust, constrained equilibrium solver, Pope [264, 265] developed the Gibbs function continuation (GFC) method which solves the element potential equations for an ideal gas mixture under general linear constraints. Since its development, the GFC method has been successfully embedded into a variety of more complex turbulent combustion modeling algorithms, including the Eddy Dissipation Concept (EDC) [266, 267], RCCE using greedy algorithm with local improvement (RCCE-GALI) [259], and the Relaxa tion-Redistribution method (RRM) [268]. One drawback of the GFC method however, is that it is only capable of computing equilibrium compositions of gas phase mixtures.

The purpose of this chapter is to present a generalization of the GFC method to mixtures with multiple ideal phases and to provide a more rigorous mathematical analysis of its robustness and stability. The new method is referred to as the multiphase Gibbs function continuation (MPGFC) method. This work was recently published in [269]. In Section 5.2, the necessary equations to describe constrained chemical equilibrium for any number of ideal phases are reviewed. Section 5.3 develops the mathematical basis of the MPGFC method, followed by a detailed overview of a practical implementation of the algorithm in Section 5.4.1. Finally, two numerical test cases will be presented to demonstrate some key features of the algorithm in Section 5.4.2.

5.2. Constrained Chemical Equilibrium

5.2.1. Free Energy Minimization

Consider a chemical system composed of any number of ideal phases. The set of indices which denote all species in this system is $\mathcal{S} = \{1, \dots, n^{\mathcal{S}}\} = \cup_{m\in\mathcal{P}}\mathcal{S}_m$ where $n^{\mathcal{S}}$ is the total number of species considered, $\mathcal{P} = \{1, \dots, n^{\mathcal{P}}\}$ is the set of phase indices with $n^{\mathcal{P}}$ the number of phases, and $\mathcal{S}_m$ denotes the set of species indices belonging to phase m. Note that each species belongs to a single phase. If a particular chemical species occurs in (for example) three phases, then it is treated as three different species. Since all phases are ideal, the normalized Gibbs function for this system is

$$\tilde{G} \equiv \frac{G}{R_u T} = \sum_{m\in\mathcal{P}} \sum_{j\in\mathcal{S}_m} N_j \left(\tilde{g}_j + \ln N_j - \ln \bar{N}_m\right), \tag{5.1}$$

where N_j is the number of moles of species j and $\tilde{g}_j(T,p)$ is the non-dimensional Gibbs function of pure species j at the system temperature T and pressure p, R_u is the molar universal gas constant, and $\bar{N}_m$ is the total moles in phase m, sometimes referred to as the phase moles of phase m.

$$\bar{N}_m = \sum_{j\in\mathcal{S}_m} N_j, \quad \forall\, m \in \mathcal{P}. \tag{5.2}$$

The vector of $n^{\mathcal{P}}$ phase moles, $\bar{\boldsymbol{N}}$, can thus be expressed as

$$\bar{\boldsymbol{N}} = \mathbf{P}^T \boldsymbol{N}, \tag{5.3}$$

where $\boldsymbol{N} \in \mathcal{R}^{n^{\mathcal{S}}}$ is the vector of species moles and $\mathbf{P} \in \mathcal{R}^{n^{\mathcal{S}}\times n^{\mathcal{P}}}$ is a "phase summation matrix" whose elements are defined as

$$P_{jm} \equiv \delta_{p_j m}. \tag{5.4}$$

The symbol $\delta_{p_j m}$ is the familiar Kronecker Delta function and the subscript p_j is used to denote the index of the phase in $\mathcal{P}$ to which the species j belongs. In other words, for all m in $\mathcal{P}$ and all

j in $\mathcal{S}_m$, $p_j = m$. The two notations of the phase index are used for convenience, depending on the situation. For instance, Eq. (5.1) may be equivalently written as

$$\tilde{G} = \sum_{j\in\mathcal{S}} N_j\Big(\tilde{g}_j + \ln N_j - \ln \sum_{k\in\mathcal{S}_{p_j}} N_k\Big). \tag{5.5}$$

The non-dimensional Gibbs function for a pure species j is given by

$$\tilde{g}_j(T,p) = \frac{H_j(T)}{R_u T} - \frac{S_j^\circ(T)}{R_u} + \begin{cases} \ln\frac{p}{p^\circ}, & j \in \text{gas phase} \\ 0, & \text{otherwise} \end{cases}, \tag{5.6}$$

where H_j is the molar enthalpy of pure species j and S_j°, its molar entropy evaluated at the standard state pressure p°.

If the total moles of each element i in the mixture is denoted by c_i^{e}, then conservation of mass dictates that

$$\sum_{j\in\mathcal{S}} B_{ji}^{\mathrm{e}} N_j = c_i^{\mathrm{e}} \quad \forall\, i \in \mathcal{E}, \tag{5.7}$$

where B_{ji}^{e} is the stoichiometric coefficient for the i^{th} element in species j. $\mathcal{E} = \{1,\ldots,n^{\mathcal{E}}\}$ denotes the set of element indices for the $n^{\mathcal{E}}$ considered elements in the mixture. Eq. (6.40) is often referred to as the mass balance relations or constraints. It states that the available atoms in a mixture must be shared amongst each of the species in the mixture (regardless of phase). In addition to these physically imposed constraints, it is often useful to impose other constraints on the system. Therefore, we consider the set of $n^{\mathcal{G}}$ additional linear constraints on the number of moles of each species, $\mathcal{G} = \{1,\ldots,n^{\mathcal{G}}\}$, such that

$$\sum_{j\in\mathcal{S}} B_{ji}^{\mathrm{g}} N_j = c_i^{\mathrm{g}} \quad \forall\, i \in \mathcal{G}. \tag{5.8}$$

Using matrix notation, the total constraints imposed on the composition are thus given by

$$\mathbf{B}^T \boldsymbol{N} = \boldsymbol{c}, \tag{5.9}$$

where

$$\mathbf{B} = \begin{bmatrix}\mathbf{B}^{\mathrm{e}} & \mathbf{B}^{\mathrm{g}}\end{bmatrix} \in \mathcal{R}^{n^{\mathcal{S}}\times n^{\mathcal{C}}}, \quad \boldsymbol{c} = \begin{bmatrix}\boldsymbol{c}^{\mathrm{e}} \\ \boldsymbol{c}^{\mathrm{g}}\end{bmatrix} \in \mathcal{R}^{n^{\mathcal{C}}}, \tag{5.10}$$

and $n^{\mathcal{C}} = n^{\mathcal{E}} + n^{\mathcal{G}}$ are the total number of linear constraints whose indices compose the set $\mathcal{C} = \{1,\ldots,n^{\mathcal{C}}\}$. As a clarifying example, consider a 5-species mixture composed of four gaseous species, C, CO, CO_2, and O_2, and solid graphite, C(gr), with an imposed constraint on the total mixture moles, $\bar{N}_{\text{mix}}$. Table 5.1 shows the corresponding $\mathbf{B}$ and $\mathbf{P}$ matrices associated with this system. Note that the first two columns of $\mathbf{B}$ correspond to the mass balance constraints in Eq. (6.40) while the last column corresponds to the constraint on the total mixture moles.

For a given $\mathbf{B}$, $\boldsymbol{c}$, and a fixed temperature and pressure, the LTE composition for a chemical system is the one which minimizes $\tilde{G}$, Eq. (5.1), while satisfying the linear constraints in Eq. (5.9).

5.2.2. Constraint Potentials

The Lagrange multiplier method is a well known technique for solving constrained minimization problems and will be used here. To begin, the Gibbs function and mass balance constraints are combined to form the Lagrangian, L,

$$\begin{aligned} L &= \tilde{G} - \sum_{i\in\mathcal{C}} \lambda_i\Big(\sum_{j\in\mathcal{S}} B_{ji}N_j - c_i\Big) \\ &= \sum_{j\in\mathcal{S}} N_j\Big(\tilde{g}_j + \ln N_j - \ln \sum_{k\in\mathcal{S}_{p_j}} N_k\Big) - \sum_{i\in\mathcal{C}} \lambda_i\Big(\sum_{j\in\mathcal{S}} B_{ji}N_j - c_i\Big) \end{aligned} \tag{5.11}$$

Table 5.1.: *Example constraint matrices* **B** *and* **P** *for a 5-species CO_2 mixture with constraints placed on the total mixture moles, $\bar{N}_{mix}$.*

	B columns			**P** columns	
Species	C	O	$\bar{N}_{\text{mix}}$	Gas	C (gr)
C	1	0	1	1	0
CO	1	1	1	1	0
CO_2	1	2	1	1	0
O_2	0	2	1	1	0
C(gr)	1	0	1	0	1

through the use of Lagrange multipliers, λ_i. Setting the derivative of the Lagrangian with respect to the species moles to zero provides the necessary conditions for the solution of the minimization problem. Namely,

$$\begin{aligned}\frac{\partial L}{\partial N_j} &= \frac{\partial \tilde{G}}{\partial N_j} - \sum_{i\in\mathcal{C}} \lambda_i B_{ji} \\ &= \tilde{g}_j + \ln N_j - \ln \sum_{k\in\mathcal{S}_{p_j}} N_k - \sum_{i\in\mathcal{C}} \lambda_i B_{ji} \\ &= 0, \quad \forall\, j \in \mathcal{S}.\end{aligned} \tag{5.12}$$

The physical meaning of the Lagrange multipliers is evident when Eq. (5.11) is differentiated with respect to the constraint constants, c_i, yielding

$$\frac{\partial L}{\partial c_i} = \frac{\partial \tilde{G}}{\partial c_i} + \lambda_i = 0 \Rightarrow \lambda_i = -\frac{\partial \tilde{G}}{\partial c_i}. \tag{5.13}$$

Therefore, λ_i is a dimensionless number which represents the negative rate of change in the normalized Gibbs energy of the equilibrium system with respect to a change in the constraint constant, c_i. In addition, Eq. (5.12) may be rewritten such that

$$\sum_{i\in\mathcal{C}} \lambda_i B_{ji} = \frac{\partial \tilde{G}}{\partial N_j} \equiv \frac{\mu_j}{R_u T}, \quad \forall\, j \in \mathcal{S}, \tag{5.14}$$

where μ_j is called the chemical potential of species j for the given chemical system. Because of this relationship, the Lagrange multipliers are often referred to as element potentials when they are associated with elemental mass balance constraints, or simply constraint potentials for a general constraint.

Finally, Eq. (5.12) may also be rewritten to yield the Element Potential Equations (EPE)[246],

$$N_j = \bar{N}_{p_j} \exp\Big(-\tilde{g}_j + \sum_{i\in\mathcal{C}} \lambda_i B_{ji} \Big), \quad \forall j \in \mathcal{S}, \tag{5.15}$$

which show that the number of moles of each species, N_j, in a mixture at equilibrium are functions of only their phase moles, $\bar{N}_{p_j}$, and the $n^{\mathcal{C}}$ constraint potentials, λ_i, corresponding to each constraint i. Note that when written in terms of species mole fractions, $x_j = N_j/\bar{N}_{p_j}$, the constraint potentials λ_i completely define the equilibrium composition of each phase for a fixed temperature and pressure (but not the amount of each phase present in the mixture). Substitution of Eq. (5.15) into Eqs. (5.3) and (5.9) leads to a nonlinear system of $n^{\mathcal{P}} + n^{\mathcal{C}}$ equations and as many unknowns: $\bar{N}_m$, $\forall\, m \in \mathcal{P}$, and λ_i, $\forall\, i \in \mathcal{C}$. The robust solution of this nonlinear system is the focus of the following sections.

5.2.3. Coordinate Transfer and Matrix-Vector Representation

The following sections make use of a coordinate transformation which simplifies the development of the multiphase Gibbs function continuation method. This transformation is similar to the one made by Pope in the original development of the single-phase method. Instead of dealing directly with species moles, it is convenient to use their square-root,

$$y_i \equiv \sqrt{N_i}. \tag{5.16}$$

The purpose of this change of variables will become evident later. Using Eq. (5.15), the vector $\boldsymbol{y} \in \mathcal{R}^{n^{\mathcal{S}}}$ may be expressed in matrix-vector notation as a function of the element potential vector, $\boldsymbol{\lambda} \in \mathcal{R}^{n^{\mathcal{C}}}$, and phase mole vector $\bar{\boldsymbol{N}} \in \mathcal{R}^{n^{\mathcal{P}}}$ by

$$\boldsymbol{y} = \exp\left(-\tilde{\boldsymbol{g}} + \mathbf{B}\boldsymbol{\lambda} + \mathbf{P}\ln\bar{\boldsymbol{N}}\right)^{\frac{1}{2}}. \tag{5.17}$$

Here, the exponential, logarithm, and square-root operators act element-wise on their vector argument. Note also that $\mathbf{P}$ in Eq. (5.17) is used to transform the $n^{\mathcal{P}}$-sized vector $\ln\bar{\boldsymbol{N}}$ into a $n^{\mathcal{S}}$-sized vector with repeated values depending on the phase of each species. This construction will be used throughout the paper. Finally, the matrices $\mathbf{Y} \in \mathcal{R}^{n^{\mathcal{S}}\times n^{\mathcal{S}}}$, $\tilde{\mathbf{B}} \in \mathcal{R}^{n^{\mathcal{S}}\times n^{\mathcal{C}}}$, and $\tilde{\mathbf{P}} \in \mathcal{R}^{n^{\mathcal{S}}\times n^{\mathcal{P}}}$ are defined as

$$\mathbf{Y} \equiv \operatorname{diag}(\boldsymbol{y}), \quad \tilde{\mathbf{B}} \equiv \mathbf{Y}\mathbf{B}, \quad \tilde{\mathbf{P}} \equiv \mathbf{Y}\mathbf{P}. \tag{5.18}$$

Using the above notation, the constrained chemical equilibrium problem defined in Eqs. (5.3) and (5.9) may be written as

$$\tilde{\mathbf{P}}^T\boldsymbol{y} = \bar{\boldsymbol{N}} \tag{5.19}$$

$$\tilde{\mathbf{B}}^T\boldsymbol{y} = \boldsymbol{c} \tag{5.20}$$

5.3. Multiphase Gibbs Function Continuation

Newton's method, or a variant thereof, is the most common method for solving nonlinear equations such as Eqs. (5.19) and (5.20)). In general, the convergence of Newton's method for a Lipshitz continuous, nonlinear system, $\boldsymbol{F}(\boldsymbol{x}) = 0$, is q-quadratic when the initial iterate, $\boldsymbol{x}^0$, is close enough to a root of $\boldsymbol{F}$, $\boldsymbol{x}^*$, and the system Jacobian within the region around the root is nonsingular [270]. In fact, quadratic convergence is only guaranteed when the initial guess, $\boldsymbol{x}^0$, is close enough to the real solution, $\boldsymbol{x}^*$, to satisfy the condition

$$\|\boldsymbol{x}^0 - \boldsymbol{x}^*\|_2 < \frac{\|\mathbf{F}'(\boldsymbol{x}^*)\|_2}{\gamma\kappa(\mathbf{F}'(\boldsymbol{x}^0))}, \tag{5.21}$$

where $\mathbf{F}'(\boldsymbol{x})$ is the system Jacobian evaluated at $\boldsymbol{x}$, γ is the Lipschitz constant for $\mathbf{F}'$, and $\kappa(\mathbf{F}'(\boldsymbol{x}))$ is the condition number of $\mathbf{F}'(\boldsymbol{x})$. The condition number is a measure of how close a matrix is to being singular, increasing to infinity when the matrix is singular. Thus, as the Jacobian of the system approaches a singular matrix, the corresponding bound on the initial guess's proximity to the actual solution becomes nearly zero. For the equilibrium problem of Eqs. (5.19) and (5.20), situations often arise in which the system Jacobian approaches a singular matrix causing the Newton convergence to stagnate.

The MPGFC method avoids the above difficulties by converting Eqs. (5.19) and (5.20) into an initial value problem which may be integrated robustly through the use of a continuation parameter. To begin, the multiphase residual vector, $\boldsymbol{R} \in \mathcal{R}^{n^{\mathcal{C}}+n^{\mathcal{P}}}$, is formally expressed as a function of the solution vector, $\tilde{\boldsymbol{x}}$, and the Gibbs vector, $\tilde{\boldsymbol{g}}(T,p)$, such that

$$\boldsymbol{R}(\tilde{\boldsymbol{x}},\tilde{\boldsymbol{g}}) = \begin{bmatrix}\tilde{\mathbf{B}}^T\\ \tilde{\mathbf{P}}^T\end{bmatrix}\boldsymbol{y} - \begin{bmatrix}\boldsymbol{c}\\ \bar{\boldsymbol{N}}\end{bmatrix}, \quad \text{and} \quad \tilde{\boldsymbol{x}} \equiv \begin{bmatrix}\boldsymbol{\lambda}\\ \ln\bar{\boldsymbol{N}}\end{bmatrix}, \tag{5.22}$$

where $\tilde{\mathbf{B}}$, $\tilde{\mathbf{P}}$, and $\boldsymbol{y}$ are implicit functions of $\tilde{\boldsymbol{x}}$ as shown in Eqs. (5.17) and (5.18). Eqs. (5.19) and (5.20) may now be written in terms of the residual vector as $\boldsymbol{R}(\tilde{\boldsymbol{x}}^*, \tilde{\boldsymbol{g}}) = 0$, which implicitly defines the equilibrium point $\tilde{\boldsymbol{x}}^*$ for a fixed T and p. The solution of this nonlinear system via Newton's method is not guaranteed to succeed, based on the arguments made above. Instead, we define a new Gibbs energy vector $\hat{\boldsymbol{g}}$, linearly parameterized by a continuation parameter s, such that

$$\hat{\boldsymbol{g}}(s) = \hat{\boldsymbol{g}}(0) + s\left[\tilde{\boldsymbol{g}} - \hat{\boldsymbol{g}}(0)\right], \tag{5.23}$$

where $\hat{\boldsymbol{g}}(0)$ denotes $\hat{\boldsymbol{g}}$ at $s = 0$. Replacing $\tilde{\boldsymbol{g}}$ with $\hat{\boldsymbol{g}}$, the equation $\boldsymbol{R}(\hat{\boldsymbol{x}}, \hat{\boldsymbol{g}}(s)) = 0$ now implicitly defines a path of pseudo-equilibrium points $\hat{\boldsymbol{x}}(s)$, parameterized by s, where $\hat{\boldsymbol{x}}(1) = \tilde{\boldsymbol{x}}^*$. As $\hat{\boldsymbol{g}}(0)$ is arbitrary, there are an infinite number of such paths, however, given a set of initial values of $\hat{\boldsymbol{g}}(0)$ and $\hat{\boldsymbol{x}}(0)$ which satisfy $\boldsymbol{R}(\hat{\boldsymbol{x}}(0), \hat{\boldsymbol{g}}(0)) = \mathbf{0}$, the equilibrium point can be determined by tracing the path of pseudo-equilibrium points from $s = 0$ to $s = 1$, via

$$\tilde{\boldsymbol{x}}^* = \hat{\boldsymbol{x}}(1) = \int_0^1 \frac{d\hat{\boldsymbol{x}}}{ds} ds + \hat{\boldsymbol{x}}\,(0)\,, \tag{5.24}$$

where the tangent vector, $d\hat{\boldsymbol{x}}/ds = [d\boldsymbol{\lambda}/ds, d\ln\bar{\boldsymbol{N}}/ds]^T$, can be derived from the implicit relation $d\boldsymbol{R}(\hat{\boldsymbol{x}}, \hat{\boldsymbol{g}}(s))/ds = 0$. Note that the 'hat' symbol is left off of λ and $\bar{\boldsymbol{N}}$ for convenience but their dependence on s will be clear based on the context. Given a $\hat{\boldsymbol{g}}(0)$, the path $\hat{\boldsymbol{x}}(s)$ is smooth and unique because $\hat{\boldsymbol{g}}(s)$ is linear from Eq. (5.23) and the existence and uniqueness of the equilibrium problem is well known (see for example [271]).

In its most basic form, the MPGFC method solves for the equilibrium point $\tilde{\boldsymbol{x}}^*$ by numerically integrating the initial value problem of Eq. (5.24) using a simple Euler scheme.The derivatives, $d\boldsymbol{\lambda}/ds$ and $d\ln\bar{\boldsymbol{N}}/ds$, can be computed robustly by exploiting a feature of least-squares solutions. In addition, special care must be taken to ensure that the correct condensed phases are included in the equilibrium solution. Further improvements to the efficiency and global accuracy of the method are obtained by using an adaptive step-size, Δs, as well as Newton's method (when possible) to reduce errors in the numerical integration. The mathematical basis for each of these issues are presented in the following subsections while Section 5.4.1 will detail the exact MPGFC solution algorithm.

5.3.1. Initial Conditions

The initial conditions, $\hat{\boldsymbol{g}}(0)$, $\boldsymbol{\lambda}(0)$, and $\ln\bar{\boldsymbol{N}}(0)$, must satisfy the constraint $\boldsymbol{R}(\hat{\boldsymbol{x}}(0), \hat{\boldsymbol{g}}(0)) = \mathbf{0}$. Therefore, the initial species moles vector, $\boldsymbol{N}(0)$, must satisfy Eqs. (5.19) and (5.20). There are an infinite number of species mole vectors which can satisfy the underdetermined constraint system in Eq. (5.20). The vector space of all such vectors will be denoted by

$$\mathcal{B} = \left\{ \boldsymbol{N} \in \mathcal{R}^{n^{\mathcal{S}}} \,:\, \mathbf{B}^T\boldsymbol{N} = \boldsymbol{c},\ N_j \geq 0 \right\}. \tag{5.25}$$

We now define two species compositions contained in this vector space. The Min-G composition,

$$\boldsymbol{N}_{\text{min-g}} = \underset{\boldsymbol{N}\in\mathcal{B}}{\arg\min}\, \boldsymbol{N}^T\tilde{\boldsymbol{g}}, \tag{5.26}$$

minimizes the sum of species Gibbs energies while satisfying the constraints in Eq. (5.20), approximating the minimization of Eq. (5.1) without regard to the energy of mixing. The Max-Min composition,

$$\boldsymbol{N}_{\text{max-min}} = \underset{\boldsymbol{N}\in\mathcal{B}}{\arg\max} \left(\min_{j\in\mathcal{S}} N_j \right), \tag{5.27}$$

is the composition which maximizes the smallest single species moles and still satisfies Eq. (5.20). Both compositions can be formulated as the solution to a linear programming problem which can be easily solved via the Simplex algorithm [272]. The Min-G composition is useful because it estimates the equilibrium moles of the major species. However, at most $n^{\mathcal{C}}$ species in $\boldsymbol{N}_{\text{min-g}}$ will

be non-zero, while the rest are exactly zero. The Max-Min composition is strictly positive but far from the equilibrium composition as it does nothing to minimize $\tilde{G}$. Therefore, Pope [264] has suggested that a linear combination of the Min-G and Max-Min compositions,

$$\boldsymbol{N}(0) = \boldsymbol{N}_{\text{min-g}}(1-\alpha) + \boldsymbol{N}_{\text{max-min}}\alpha, \tag{5.28}$$

provides a good approximation of the major equilibrium species while ensuring that all species moles are strictly positive and that Eq. (5.20) is satisfied. The value of α is typically taken to be 0.01 such that the Min-G composition dominates, and the major species moles are still well approximated by the initial solution.

The Gibbs phase rule [273] says that, for a fixed temperature and pressure, the maximum number of phases allowed in an equilibrium solution are the total number of constraints imposed on it, $n^{\mathcal{C}}$. In order to ensure that the initial conditions satisfy the phase rule, only the phases which have non-zero moles in the Min-G solution are kept for the Max-Min solution. As the maximum number of non zero species in the Min-G solution is equal to the number of constraints, this is sufficient to ensure the phase rule is satisfied.

Eq. (5.19) is then directly satisfied by taking

$$\ln \bar{\boldsymbol{N}}(0) = \ln\left(\mathbf{P}^T \boldsymbol{N}(0)\right). \tag{5.29}$$

Note the necessity of having a strictly positive $\boldsymbol{N}(0)$ in order for the logarithm above to be well defined.

Eqs. (5.28) and (5.29) ensure that $\boldsymbol{R} = 0$ (recall that $\boldsymbol{y} = \sqrt{\boldsymbol{N}}$ from Eq. (5.16)). All that remains is to determine $\hat{\boldsymbol{g}}(0)$ and $\boldsymbol{\lambda}(0)$ which are consistent with $\boldsymbol{N}(0)$ through the EPE, Eq. (5.17). First, $\boldsymbol{\lambda}(0)$ is computed as the least-squares solution of the EPE using the Gibbs energy vector, $\tilde{\boldsymbol{g}}$.

$$\boldsymbol{\lambda}(0) = \arg\min_{\boldsymbol{\lambda}} \left\| \mathbf{B}\boldsymbol{\lambda} - \ln \boldsymbol{N}(0) + \mathbf{P} \ln \bar{\boldsymbol{N}}(0) - \tilde{\boldsymbol{g}} \right\|_2 \tag{5.30}$$

Finally, $\hat{\boldsymbol{g}}(0)$ is chosen such that Eq. (5.17) is exactly satisfied.

$$\hat{\boldsymbol{g}}(0) = \mathbf{B}\boldsymbol{\lambda}(0) - \ln \boldsymbol{N}(0) + \mathbf{P} \ln \bar{\boldsymbol{N}}(0) \tag{5.31}$$

5.3.2. Computing the Tangent Vector

The derivatives, $d\boldsymbol{\lambda}/ds$ and $d \ln \bar{\boldsymbol{N}}/ds$, at constant $\boldsymbol{R}$, are obtained from the implicit relations found when the residual is differentiated with respect to s and set equal to zero, such that

$$\frac{d\boldsymbol{R}}{ds} = \frac{d}{ds}\begin{bmatrix} \tilde{\mathbf{B}}^T \boldsymbol{y} \\ \tilde{\mathbf{P}}^T \boldsymbol{y} - \bar{\boldsymbol{N}} \end{bmatrix} = \mathbf{0}. \tag{5.32}$$

From Eq. (5.17), the following relationship can be easily determined.

$$\begin{aligned} \frac{d}{ds}(\mathbf{Y}\boldsymbol{y}) &= \mathbf{Y}^2 \left[\mathbf{B}\frac{d\boldsymbol{\lambda}}{ds} - \frac{d\hat{\boldsymbol{g}}}{ds} + \mathbf{P}\frac{d}{ds}(\ln \bar{\boldsymbol{N}}) \right] \\ &= \mathbf{Y} \left[\tilde{\mathbf{B}}\frac{d\boldsymbol{\lambda}}{ds} - \mathbf{Y}\frac{d\hat{\boldsymbol{g}}}{ds} + \tilde{\mathbf{P}}\frac{d}{ds}(\ln \bar{\boldsymbol{N}}) \right] \end{aligned} \tag{5.33}$$

Note that $d\hat{\boldsymbol{g}}/ds$ is a known function from Eq. (5.23), namely $d\hat{\boldsymbol{g}}/ds = \tilde{\boldsymbol{g}} - \hat{\boldsymbol{g}}(0)$. Using Eq. (5.33), the first term in Eq. (5.32) can be written as

$$\frac{d}{ds}\left(\tilde{\mathbf{B}}^T \boldsymbol{y}\right) = \tilde{\mathbf{B}}^T \left[\tilde{\mathbf{B}}\frac{d\boldsymbol{\lambda}}{ds} - \mathbf{Y}\frac{d\hat{\boldsymbol{g}}}{ds} + \tilde{\mathbf{P}}\frac{d}{ds}(\ln \bar{\boldsymbol{N}}) \right]. \tag{5.34}$$

We now seek a $d\boldsymbol{\lambda}/ds$ such that $d(\tilde{\mathbf{B}}^T \boldsymbol{y})/ds = \mathbf{0}$ is satisfied regardless of the value of $d \ln \bar{\boldsymbol{N}}/ds$.

To begin, $d\boldsymbol{\lambda}/ds$, is decomposed into two components,

$$\frac{d\boldsymbol{\lambda}}{ds} = \dot{\boldsymbol{\lambda}}^{\boldsymbol{g}} - \dot{\boldsymbol{\Lambda}}^{\boldsymbol{y}} \frac{d}{ds}(\ln \bar{\boldsymbol{N}}), \tag{5.35}$$

where $\dot{\boldsymbol{\lambda}}^{\boldsymbol{g}} \in \mathcal{R}^{n^{\mathcal{C}}}$ and $\dot{\boldsymbol{\Lambda}}^{\boldsymbol{y}} \in \mathcal{R}^{n^{\mathcal{C}} \times n^{\mathcal{P}}}$ are obtained via the minimum-norm solutions to the following least-squares problems

$$\dot{\boldsymbol{\lambda}}^{g} = \arg\min_{\dot{\boldsymbol{\lambda}}} \left\| \tilde{\mathbf{B}}\dot{\boldsymbol{\lambda}} - \mathbf{Y}\frac{d\hat{\boldsymbol{g}}}{ds} \right\|_2, \tag{5.36}$$

$$\dot{\boldsymbol{\Lambda}}^{\boldsymbol{y}} = \arg\min_{\dot{\boldsymbol{\Lambda}}} \left\| \tilde{\mathbf{B}}\dot{\boldsymbol{\Lambda}} - \tilde{\mathbf{P}} \right\|_2. \tag{5.37}$$

The solutions of Eqs. (5.36) and (5.37) may be stably computed using the singular value decomposition of $\tilde{\mathbf{B}}$, regardless of its rank. In addition, their residuals reside in the null space of $\tilde{\mathbf{B}}^T$, based on a general property of least squares solutions. Thus,

$$\tilde{\mathbf{B}}^T \left(\tilde{\mathbf{B}}\dot{\boldsymbol{\lambda}}^{\boldsymbol{g}} - \mathbf{Y}\frac{d\hat{\boldsymbol{g}}}{ds} \right) = \mathbf{0}, \tag{5.38}$$

$$\tilde{\mathbf{B}}^T \left(\tilde{\mathbf{B}}\dot{\boldsymbol{\Lambda}}^{\boldsymbol{y}} - \tilde{\mathbf{P}} \right) = \mathbf{0}. \tag{5.39}$$

Using this fact and substituting Eq. (5.35) into Eq. (5.34) and rearranging, we then have

$$\tilde{\mathbf{B}}^T \left[\tilde{\mathbf{B}}\dot{\boldsymbol{\lambda}}^{\boldsymbol{g}} - \mathbf{Y}\frac{d\hat{\boldsymbol{g}}}{ds} - \left(\tilde{\mathbf{B}}\dot{\boldsymbol{\Lambda}}^{\boldsymbol{y}} - \tilde{\mathbf{P}} \right) \frac{d}{ds}(\ln \bar{\boldsymbol{N}}) \right] = \mathbf{0}. \tag{5.40}$$

The usefulness of the decomposition of $d\boldsymbol{\lambda}/ds$ in Eq. (5.35) is now evident because it ensures that the first term in Eq. (5.32) is always satisfied, regardless of the value of $d\ln\bar{\boldsymbol{N}}/ds$.

The phase moles derivatives, $d\ln\bar{\boldsymbol{N}}/ds$, are determined from the second implicit relation defined in Eq. (5.32), namely

$$\frac{d}{ds}\left(\tilde{\mathbf{P}}^T\boldsymbol{y} - \bar{\boldsymbol{N}} \right) = \tilde{\mathbf{P}}^T \left(\tilde{\mathbf{P}}\frac{d}{ds}(\ln \bar{\boldsymbol{N}}) - \mathbf{Y}\frac{d\hat{\boldsymbol{g}}}{ds} + \tilde{\mathbf{B}}\frac{d\boldsymbol{\lambda}}{ds} \right) - \frac{d\bar{\boldsymbol{N}}}{ds} = 0 \tag{5.41}$$

Making use of the following relationship for $d\ln\bar{\boldsymbol{N}}/ds$ when $\boldsymbol{R} = \mathbf{0}$,

$$\frac{d}{ds}(\ln \bar{\boldsymbol{N}}) = \mathrm{diag}(\bar{\boldsymbol{N}})^{-1}\frac{d\bar{\boldsymbol{N}}}{ds} = \left(\tilde{\mathbf{P}}^T\tilde{\mathbf{P}} \right)^{-1}\frac{d\bar{\boldsymbol{N}}}{ds}, \tag{5.42}$$

and substituting in Eq. (5.35) for $d\boldsymbol{\lambda}/ds$, Eq. (5.41) may be written as

$$\tilde{\mathbf{P}}^T\tilde{\mathbf{B}}\dot{\boldsymbol{\Lambda}}^{\boldsymbol{y}}\frac{d}{ds}(\ln \bar{\boldsymbol{N}}) = \tilde{\mathbf{P}}^T \left(\tilde{\mathbf{B}}\dot{\boldsymbol{\lambda}}^{\boldsymbol{g}} - \mathbf{Y}\frac{d\hat{\boldsymbol{g}}}{ds} \right). \tag{5.43}$$

Eq. (5.43) represents a linear system of equations for the solution of $d\ln\bar{\boldsymbol{N}}/ds$. We now introduce the matrix $\mathbf{M} \equiv \tilde{\mathbf{P}}^T\tilde{\mathbf{B}}\dot{\boldsymbol{\Lambda}}^{\boldsymbol{y}} \in \mathcal{R}^{n^{\mathcal{P}} \times n^{\mathcal{P}}}$ for convenience. The structure of this matrix is studied in detail in Appendix B. In particular, $\mathbf{M}$ is symmetric and positive definite when the phase moles are non zero. In fact, the eigenvalues of $\mathbf{M}$, denoted $\beta_1 \geq \beta_m \geq \beta_{n^{\mathcal{P}}}$, have the following upper and lower bounds:

$$\bar{N}_m \geq \beta_m(\mathbf{M}) \geq \frac{\beta_m(\mathbf{C}^T\mathbf{C})}{\|\tilde{\mathbf{B}}\|_2^2} \geq 0, \quad \forall\, m \in \mathcal{P}, \tag{5.44}$$

where $\mathbf{C} \equiv \tilde{\mathbf{B}}^T\tilde{\mathbf{P}} \in \mathcal{R}^{n^{\mathcal{C}} \times n^{\mathcal{P}}}$ has column vectors, $\boldsymbol{c}_m$, which represent the amount of elements or constraint constants which are associated with the phase m. It is trivial to show that $\sum_{m\in\mathcal{P}} \boldsymbol{c}_m = \boldsymbol{c}$. For the single phase case, $\mathbf{M}$ becomes a scalar M and the bounds on the eigenvalues given in Eq. (5.44) become the bounds on M itself. In this special case, the lower bound on M is readily

given as $M \geq \|\boldsymbol{c}\|_2^2 / \|\tilde{\mathbf{B}}\|_2^2$, which is strictly positive. In the development of the single phase GFC method, Pope [265] derived a similar equation as Eq. (5.43) (divided by the total moles of the mixture) and placed an identical lower bound on the scalar quotient (D in Pope's notation) through other means. In Pope's derivation, the physical meaning of the scalar was unknown, and furthermore, the proof of positivity cannot be readily extended to consider multiple phases. However, the eigenvalue analysis given in Appendix B, and whose result is given by the bounds in Eq. (5.44), directly relates the eigenvalues of $\mathbf{M}$ to the moles in each phase and is applicable to any number of phases (including the single phase case). Furthermore, the upper bound of $\bar{N}_m$ on the eigenvalues of $\mathbf{M}$ informs a practical method for determining when $\mathbf{M}$ approaches a positive semidefinite matrix.

With a careful treatment of nearly empty phases, Eq. (5.43) can be solved in a robust and efficient manner using the Cholesky factorization for symmetric positive definite systems, ensuring that the derivatives $d\boldsymbol{\lambda}/ds$ and $d\ln \bar{\boldsymbol{N}}/ds$ can be determined in a fully robust way.

5.3.3. Newton's Method

As the Euler integration scheme approximates the pseudo-equilibrium path in a linear way, errors may accumulate during the course of the numerical integration. Therefore, after each new solution is obtained in the numerical integration of Eq. (5.24), Newton's method is used to attempt to reduce the residual below a specified global error tolerance for a fixed value of s (fixed $\hat{\boldsymbol{g}}$). Newton's method corresponds to solving the following linear system for successive updates in the pseudo-equilibrium solution,

$$\mathbf{J}\left(\tilde{\boldsymbol{x}}^{k+1} - \tilde{\boldsymbol{x}}^{k}\right) = -\mathbf{R}(\tilde{\boldsymbol{x}}^{k}, \hat{\boldsymbol{g}}), \tag{5.45}$$

where the superscript k denotes the k^{th} solution iterate and the system Jacobian, $\mathbf{J}$, is determined to be

$$\mathbf{J} \equiv \frac{\partial \mathbf{R}}{\partial \tilde{\boldsymbol{x}}} = \begin{bmatrix} \tilde{\mathbf{B}}^T\tilde{\mathbf{B}} & \tilde{\mathbf{B}}^T\tilde{\mathbf{P}} \\ \tilde{\mathbf{P}}^T\tilde{\mathbf{B}} & \tilde{\mathbf{P}}^T\tilde{\mathbf{P}} \end{bmatrix} - \begin{bmatrix} \mathbf{0} & \mathbf{0} \\ \mathbf{0} & \operatorname{diag}\left(\bar{\boldsymbol{N}}\right) \end{bmatrix}. \tag{5.46}$$

Note that the parentheses on the right hand side of Eq. (5.45) denote that the residual is evaluated at $(\tilde{\boldsymbol{x}}^k, \hat{\boldsymbol{g}})$, while those on the left simply distribute the matrix vector product to both $\tilde{\boldsymbol{x}}^{k+1}$ and $\tilde{\boldsymbol{x}}^k$.

In some situations, the above system may be singular, making it impossible to converge the solution further after taking a continuation step. In such cases, the Newton iterations are abandoned and the residual is reduced by reducing the step-size used for the numerical integration and retaking the step.

5.3.4. Inclusion of Condensed Phases

The initialization procedure presented in Section 5.3.1 typically does a good job of predicting which condensed phases should be present in the equilibrium mixture through the Min-G solution. However, it is possible that the phases present in the initial solution are not the correct ones which minimize the Gibbs free energy. Furthermore, it is also possible that some phases, which are correctly included in the initial solution, are removed during the course of the integration of Eq. (5.24). Therefore, at the end of the integration of Eq. (5.24), a check must be performed to determine whether or not a previously neglected phase can in fact minimize the system Gibbs energy further. Since the equilibrium solution represents a stationary point of the Lagrange function ($\partial L = 0$), Eq. (5.12) yields the necessary condition for a new phase to be included. Namely, if

$$\tilde{g}_c - \sum_{i \in \mathcal{C}} \lambda_i^* B_{ci} < 0, \tag{5.47}$$

for any condensed species c, which has not yet been included in the equilibrium solution, then adding the phase to which species c belongs will decrease the overall Gibbs energy at equilibrium. This is sometimes referred to as the vapor pressure test. When multiple phases meet this criteria, the one with the most negative change in the Gibbs energy is added.

When it is determined that a new phase should be included, a phase redistribution procedure is performed which distributes moles of the largest (in terms of quantity) species into the new phase while satisfying the mass balance constraint of Eq. (5.20). This is done in the following way. First, the current solution of the species moles vector, $\boldsymbol{N}$, is extended by the number of species in the new phase. If the new phase has index m, then the extended species vector, denoted by $\boldsymbol{N}^{\text{ext}}$, is computed as

$$N_j^{\text{ext}} = \begin{cases} N_j, & j \in \mathcal{S} \\ \bar{N}_m / n_m^{\mathcal{S}}, & j \in \mathcal{S}_m \end{cases}. \tag{5.48}$$

where $\bar{N}_m$ is the desired number of initial moles in the phase m, and $n_m^{\mathcal{S}}$ denotes the number of species in that phase. The constraint matrix $\mathbf{B}$, the phase summation matrix $\mathbf{P}$, and the species index set are also extended accordingly.

We then search for an update in the $n^{\mathcal{C}}$ largest species of $\boldsymbol{N}^{\text{ext}}$ which will satisfy the mass balance constraints through the solution of the linear system,

$$\mathbf{B}^T \Delta \boldsymbol{N}^{\max} = \boldsymbol{c} - \mathbf{B}^T \boldsymbol{N}^{\text{ext}}, \tag{5.49}$$

where the vector $\Delta \boldsymbol{N}^{\max}$ is defined to be a vector of zeros except for the elements representing the $n^{\mathcal{C}}$ largest species. Note that Eq. (5.49) represents a linear system with $n^{\mathcal{C}}$ equations and $n^{\mathcal{C}}$ unknowns. Furthermore, a suitable update can always be obtained by using the singular value decomposition of the sub matrix of $\mathbf{B}^T$ representing the $n^{\mathcal{C}}$ maximum species, even when that matrix is rank deficient.

Finally, a new initial species moles vector is computed by applying the update to $\boldsymbol{N}^{\text{ext}}$,

$$\boldsymbol{N}(0) = \boldsymbol{N}^{\text{ext}} + \Delta \boldsymbol{N}^{\max}. \tag{5.50}$$

It is easy to verify that that this new $\boldsymbol{N}(0)$ vector satisfies Eq. (5.20). With a new $\boldsymbol{N}(0)$, the solution is then reinitialized and the integration procedure is repeated to solve Eq. (5.24). This whole process must be repeated until all necessary phases are included in the equilibrium mixture according to Eq. (5.47).

5.4. Practical Implementation

5.4.1. Solution Algorithm

The previous section detailed the mathematical basis for the MPGFC method. However, in order to create an efficient and robust equilibrium solver, several algorithmic details must be developed. An overview of the full MPGFC algorithm is presented in this section.

For a fixed temperature, pressure, and constraint vector, the initial moles of each species are determined using Eqs. (5.26 - 5.28). Following initialization, the proceeding steps are then used to compute the integral in Eq. (5.24).

1. The initial solution $\hat{\boldsymbol{x}}(0)$ and Gibbs energy vector $\hat{\boldsymbol{g}}(0)$ are computed according to Eqs. (5.29 - 5.31). The continuation parameter and step size are also initialized as $s = 0$ and $\Delta s = 1$.

2. Compute the tangent vector of the pseudo-equilibrium path, $d\hat{\boldsymbol{x}}/ds$ at s using Eqs. (5.35 - 5.37), and Eq. (5.43).

3. Next, integrate the solution forward along the pseudo-equilibrium path with an Euler integration over Δs,

$$\tilde{\boldsymbol{x}}^0(s + \Delta s) = \hat{\boldsymbol{x}}(s) + \frac{d\hat{\boldsymbol{x}}}{ds} \Delta s. \tag{5.51}$$

   The superscript 0 is used to denote the initial iterate for the Newton iteration procedure. The Gibbs energy vector is also updated via Eq. (5.23) at $s + \Delta s$.

4. Newton's method is then used to reduce the residual vector below a specified tolerance, ϵ_{abs}, using Eq. (5.45) and Eq. (5.46). The Newton iterations are stopped when either (i) the iterations converge, such that

$$\|\boldsymbol{R}(\tilde{\boldsymbol{x}}^k, \hat{\boldsymbol{g}}(s + \Delta s))\|_2 \leq \epsilon_{\text{abs}}, \tag{5.52}$$

(ii) a maximum number of iterations is reached, or (iii) the residual norm increases above the norm of the previous iterate.

5. Following the Newton iterations, the new solution vector is tested against the following criteria:

$$\|\boldsymbol{R}(\tilde{\boldsymbol{x}}^k, \hat{\boldsymbol{g}}(s + \Delta s))\|_2 \leq \max\left[(1 + \epsilon_{\text{rel}})\left\|\boldsymbol{R}(\hat{\boldsymbol{x}}(s), \hat{\boldsymbol{g}}(s))\right\|_2, \epsilon_{\text{abs}}\right]. \tag{5.53}$$

If the above inequality holds true, then the iterate k is accepted and the solution is updated as $\hat{\boldsymbol{x}}(s) = \tilde{\boldsymbol{x}}^k$, $s = s + \Delta s$, and the step-size Δs is increased via

$$\Delta s = \min\left(s - 1,\ 2\Delta s\right). \tag{5.54}$$

Otherwise, the solution is not updated and Δs is reduced by a factor of 2 and the algorithm continues at Step 3. Note that the term $(1+\epsilon_{\text{rel}})$ in Eq. (5.53) prevents the step-size Δs from decreasing to zero, allowing the solution to progress with a small increase in the residual.

6. If $s = 1$ after the above step, then the solution vector corresponds to the equilibrium solution for the included phases. If not, the solution procedure is continued starting from Step 2.

7. The phase inclusion test is checked to see if any additional phases should be included in the equilibrium mixture, according to Eq. (5.47). If it is determined that a previously excluded phase can reduce the Gibbs energy of the equilibrium solution, then Eqs. (5.48 - 5.50) are used to compute a new initial species moles vector $\boldsymbol{N}(0)$ with the addition of the new phase, and Eq. (5.24) must be reintegrated starting from Step 1.

Figure (5.1) provides a graphical overview of the MPGFC method to help clarify the algorithm, of which several aspects are worth elaborating on. To start with, while the Newton iteration procedure attempts to bring the residual below an absolute tolerance, ϵ_{abs}, it is indicated in Step 5 that the solution is accepted as long as Eq. (5.53) is valid for some small ϵ_{rel}. This is done to allow the integration to proceed for a small enough Δs even when the Newton procedure cannot converge. Typically, if such a situation is encountered, allowing the solution to proceed forward will eventually allow the Newton iterations to converge and maintain an acceptable error tolerance on the solution. In the worst case scenario, the MPGFC method breaks down to a simple Euler integration with small step sizes.

In some cases, a particular phase tends towards zero as the integration in s is computed. Since the robustness of the MPGFC method relies on including only nonempty phases, these phases must be removed when the number of moles fall below some tolerance. Because of this, a small adaptation is included in the Newton procedure which first removes any phases meeting this criteria, before computing the system Jacobian. If the Newton iteration is rejected in Step 5, then the original phase ordering must be remembered. This introduces some extra book keeping in the algorithm, though it does not greatly affect the overall complexity or the necessary coding required to implement it.

Finally, the choice of solution variable $\ln \bar{\boldsymbol{N}}$ as opposed to $\bar{\boldsymbol{N}}$ for the phase moles is an important one for two reasons. First, the algebra necessary to develop the method is made more simple. Second, and more importantly, is that this choice automatically guaranties that the phase moles are strictly positive, further guarantying the species moles are strictly positive as well. This makes the necessary coding far easier because negative moles and mole fractions do not have to be dealt with as in other equilibrium solution methods (see for example, CEA [166]).

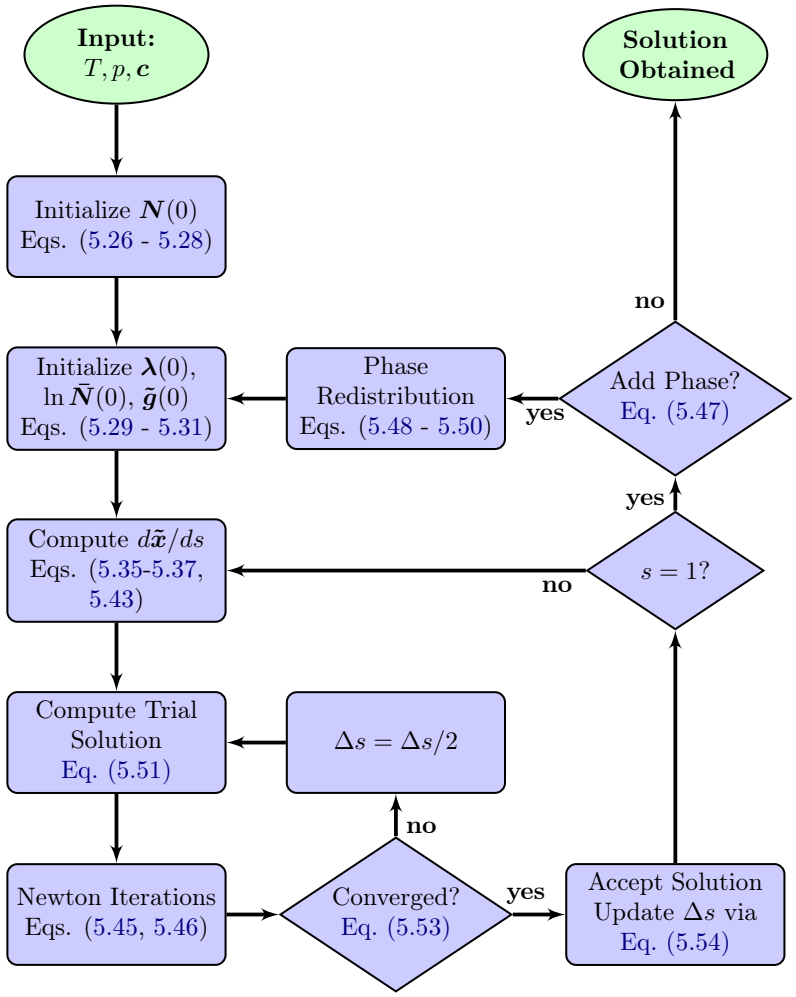

Figure 5.1.: *Flow diagram of the solution procedure for the MPGFC method at a given fixed temperature and pressure.*

5.4.2. Some Examples

The MPGFC method has been implemented in the Multicomponent Thermodynamic and Transport Properties for Ionized Gases in C++ (MUTATION^{++}) library[1][274]. Among other things, MUTATION^{++}provides thermodynamic properties of individual species and has an option of including the thermodynamic database [181] used in the NASA CEA [166, 182] code which will be used for all of the results presented here.

Constrained Single Phase Mixture

As previously mentioned in the introduction, Bishnu *et al.* [262] developed a linearly constrained version of the CEA and STANJAN codes and performed several numerical experiments to judge the overall robustness of the two methods with constraints in addition to the mass balance constraints. One such set of calculations used a simple 8-species H_2O mixture comprised of H, O, OH, H_2, O_2, H_2O, HO_2, and H_2O_2 in which the total moles of the mixture were constrained. This constraint may be written as

$$\sum_{j \in \mathcal{S}} N_j = N_{\text{mix}} \tag{5.55}$$

[1] Available for download at https://www.mutationpp.org

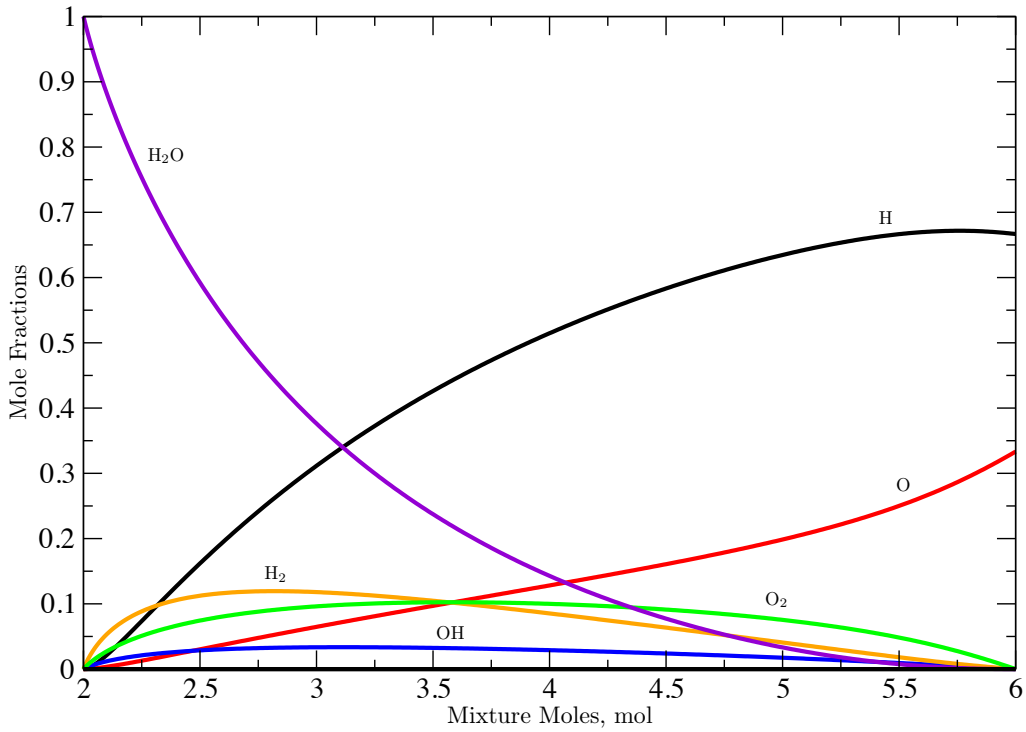

Figure 5.2.: *Water mixture composed of 4 moles of H and 2 moles of O at* 1500 K *and* 1 atm *with total number of moles constrained between the limits of 2 and 6 moles.*

Note that this is the same constraint as was used for the example in Table 5.1.

If the elemental moles of H and O are 4 mol and 2 mol respectively, then the above constraint on the total moles of the mixture limits the feasible region of equilibrium solutions to $2 \leq N_{\text{mix}} \leq 6$. On the boundaries of this feasible region, the species moles are determined completely by the constraints themselves: at $N_{\text{mix}} = 2$, $N_{\text{H}_2\text{O}} = 2$ while all other species are zero, and at $N_{\text{mix}} = 6$, $N_{\text{H}} = 4$ and $N_{\text{O}} = 2$ with the other species zero. Bishnu found that at these boundaries, CEA failed to converge to a solution at 1500 K and 1 atm.

Figure (5.2) shows the equilibrium mole fractions obtained using the MPGFC method for this H_2O mixture at 1500 K and 1 atm with the mixture moles constrained over the span of the feasible region. It is clear from the figure that the MPGFC method can successfully solve the equilibrium solution even at the boundaries of the feasible region. Perhaps more importantly, the use of the Simplex algorithm when determining the initial conditions (Eqs. (5.26) and (5.27)) allows the method to detect when a set of input constraints have no feasible region, and an appropriate error message may be presented to the user.

A Multiphase Example

In many fields, multiphase equilibrium solutions are used to make engineering calculations or to understand complex chemical processes. As an example of a multiphase problem, a calculation has been performed with a Silicon-Phenolic mixture which has been used to study complex ablation phenomena occurring at the surface of some ablator materials during atmospheric entry [275]. Figure (5.3) shows the results of a calculation with the complex $Si-C_6H_5OH$ mixture. Because CEA treats all condensed phases as pure phases, each condensed phase was treated separately in the MPGFC calculation (though the algorithm described here can be used on any general set of ideal phases).

It is clear from Fig. (5.3) that the results obtained with the MPGFC method compare exactly with those obtained using CEA. It should also be noted that CEA was not able to converge

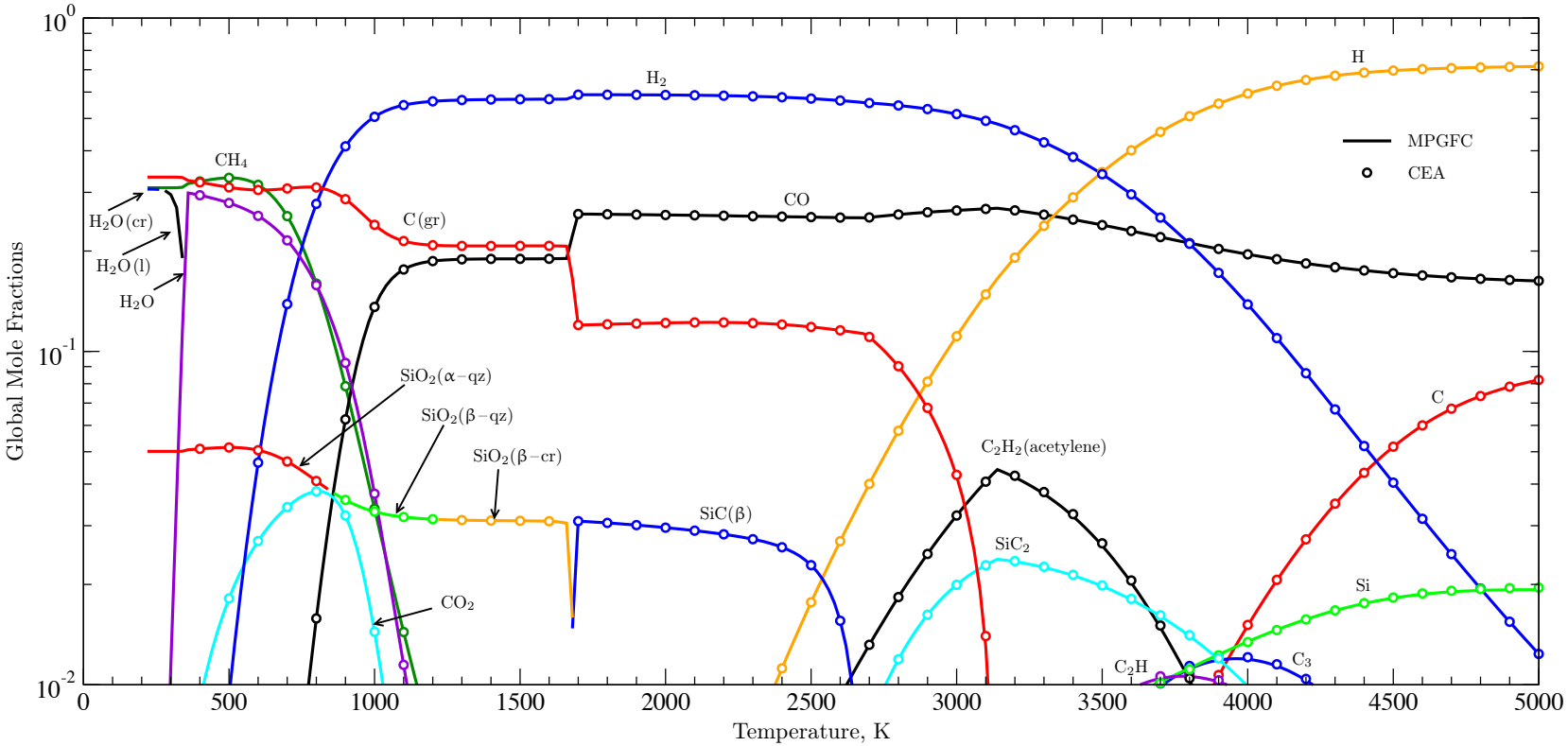

Figure 5.3.: *Global mole fractions of the major equilibrium species for a mixture consisting of* 90 % *Phenol* (C_6H_5OH) *and* 10 % *Si by moles. Comparison between results obtained with CEA and the MPGFC method. All condensed species are considered as separate, pure phases.*

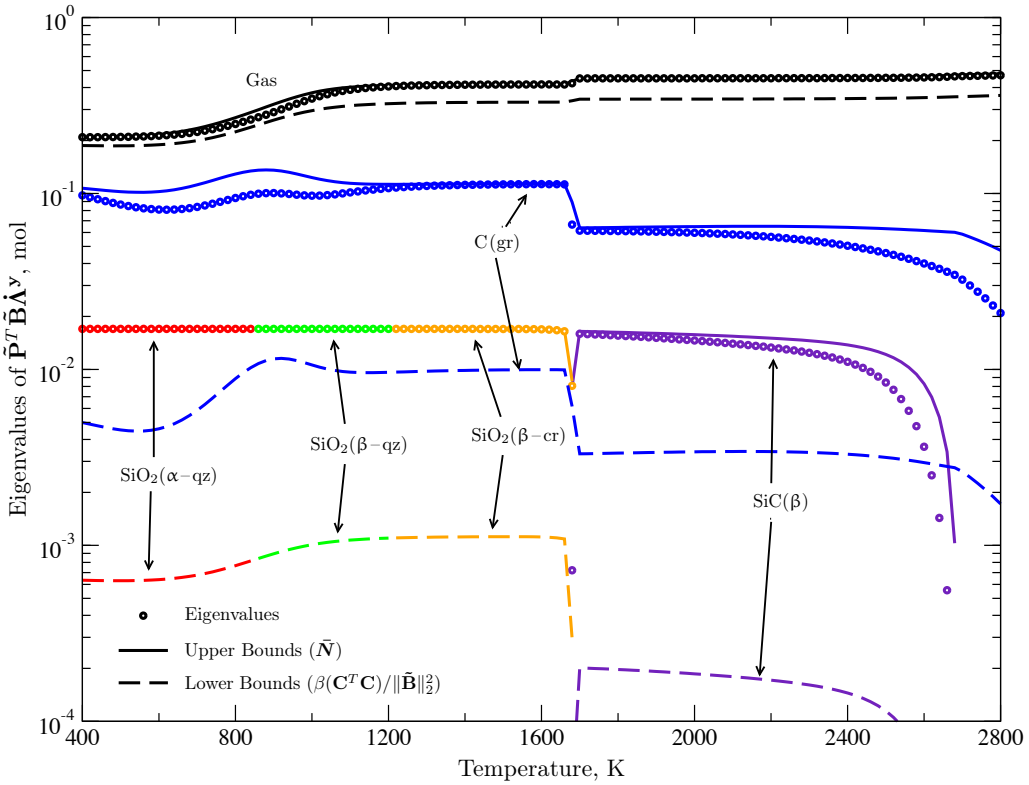

Figure 5.4.: *Eigenvalues of the matrix* $\tilde{\mathbf{P}}^T\tilde{\mathbf{B}}\dot{\mathbf{\Lambda}}^{\mathbf{y}}$ *at* $s = 1$ *for the equilibrium solution in Fig. (5.3) with the associated upper and lower bounds from Eq. (5.44).*

for temperatures below 400 K due to its poor initial estimate of the solution. Therefore, the CEA solution begins at 400 K in Fig. (5.3).

One interesting feature of the solution is how the solid silicon-oxide transforms between each of its 3 stable forms. Due to the pure condensed phase assumption, there is a discontinuity in the mole fractions around 1700 K when it becomes more preferential for the Si to combine with C to form solid SiC(β) rather than combining with O to form solid SiO_2 in its β-crystalline state. The carbon needed to form SiC is taken from the graphite when this change occurs, causing a steep drop in the C(gr) mole fraction at 1700 K.

Figure (5.4) shows the computed eigenvalues of the linear system matrix, $\mathbf{M} \equiv \tilde{\mathbf{P}}^T\tilde{\mathbf{B}}\dot{\mathbf{\Lambda}}^{\mathbf{y}}$, from Eq. (5.43), along with the corresponding eigenvalue bounds given in Eq. (5.44). It is interesting to note that the eigenvalues tend to stay close to their upper limit, which is equal to the phase moles of the phase corresponding to each eigenvalue. This may be explained by decomposing $\mathbf{M}$ as,

$$\mathbf{M} = \tilde{\mathbf{P}}^T\tilde{\mathbf{P}} + \tilde{\mathbf{P}}^T\boldsymbol{r}^{\boldsymbol{y}}. \tag{5.56}$$

where $\boldsymbol{r}^{\boldsymbol{y}} = \tilde{\mathbf{B}}\dot{\mathbf{\Lambda}}^{\boldsymbol{y}} - \tilde{\mathbf{P}}$ is the residual of the least squares solution for $\dot{\mathbf{\Lambda}}^{\boldsymbol{y}}$ in Eq. (5.37). From this, it is easy to see that the m^{th} eigenvalue of $\mathbf{M}$ is exactly

$$\beta_m(\mathbf{M}) = \bar{N}_m + \beta_m\left(\tilde{\mathbf{P}}^T\boldsymbol{r}^{\boldsymbol{y}}\right), \tag{5.57}$$

because $\tilde{\mathbf{P}}^T\tilde{\mathbf{P}}$ is diagonal with diagonal entries equal to the phase moles of each phase. From Eq. (5.57), it is clear that the eigenvalues of $\mathbf{M}$ tend towards the phase moles as the residual in Eq. (5.37) decreases. Note also that the m^{th} column of $\boldsymbol{r}^{\boldsymbol{y}}$ is essentially the residual of Eq. (5.37) corresponding to the phase m. Therefore, when the least squares system can be exactly satisfied for a given phase, the eigenvalue of $\mathbf{M}$ corresponding to that phase is exactly the number of phase

moles. In Fig. (5.4), this is clearly evident for the eigenvalues of the solid phases of SiO_2. Since all of the Si in the equilibrium solution is contained in solid SiO_2 (see Fig. (5.3)), the least squares problem in Eq. (5.37) corresponding to SiO_2 can be exactly satisfied.

5.5. Mole Fraction Derivatives

It is often necessary to know the derivative of the equilibrium species mole fractions with respect to temperature, pressure, or elemental mole fractions. Indeed, all of these are required in the full computation of diffusion driving forces for mixtures in LTE, as shown in Section 2.5. From Eq. (5.15), it is easy show that the derivative of equilibrium mole fractions with respect to any variable α must satisfy

$$\frac{\partial x_j}{\partial \alpha} = x_j \left(-\frac{\partial \tilde{g}_j}{\partial \alpha} + \sum_{i \in \mathcal{C}} B_{ji} \frac{\partial \lambda_i}{\partial \alpha} \right), \quad j \in \mathcal{S}. \tag{5.58}$$

Gibbs free energy derivatives are easily derived for temperature and pressure as

$$\frac{\partial \tilde{g}_j}{\partial T} = -\frac{H_j(T)}{R_u T^2}, \quad \text{and} \quad \frac{\partial \tilde{g}_j}{\partial p} = \begin{cases} \frac{1}{p}, & j \in \text{gas phase} \\ 0, & \text{otherwise} \end{cases}. \tag{5.59}$$

The element potential derivatives can be stably computed using the same procedure as in Section 5.3.2. In particular, the derivatives are split such that

$$\frac{\partial \boldsymbol{\lambda}}{\partial \alpha} = \dot{\boldsymbol{\lambda}}^{\alpha} - \dot{\boldsymbol{\Lambda}}^{\alpha} \frac{\partial}{\partial \alpha} (\ln \bar{\boldsymbol{N}}), \tag{5.60}$$

where $\dot{\boldsymbol{\lambda}}^{\alpha} \in \mathcal{R}^{n^{\mathcal{C}}}$ and $\dot{\boldsymbol{\Lambda}}^{\alpha} \in \mathcal{R}^{n^{\mathcal{C}} \times n^{\mathcal{P}}}$ are obtained via the minimum-norm solutions to the following least-squares problems

$$\dot{\boldsymbol{\lambda}}^{\alpha} = \arg\min_{\dot{\boldsymbol{\lambda}}} \left\| \tilde{\mathbf{B}} \dot{\boldsymbol{\lambda}} - \mathbf{Y} \frac{\partial \tilde{\boldsymbol{g}}}{\partial \alpha} \right\|_2, \tag{5.61}$$

$$\dot{\boldsymbol{\Lambda}}^{\alpha} = \arg\min_{\dot{\boldsymbol{\Lambda}}} \left\| \tilde{\mathbf{B}} \dot{\boldsymbol{\Lambda}} - \tilde{\mathbf{P}} \right\|_2, \tag{5.62}$$

and the phase mole derivatives are computed via the solution of the linear system

$$\tilde{\mathbf{P}}^T \tilde{\mathbf{B}} \dot{\boldsymbol{\Lambda}}^{\alpha} \frac{\partial}{\partial \alpha} (\ln \bar{\boldsymbol{N}}) = \tilde{\mathbf{P}}^T \left(\tilde{\mathbf{B}} \dot{\boldsymbol{\lambda}}^{\alpha} - \mathbf{Y} \frac{\partial \tilde{\boldsymbol{g}}}{\partial \alpha} \right). \tag{5.63}$$

The solution of the above linear system is well posed based on the arguments made in Section 5.3.2 and Appendix B.

Figure (5.5) compares the mole fraction derivatives for the water mixture in Fig. (5.2) obtained with Eqs. (5.58 - 5.63) and a finite-difference approximation. While the results are in perfect agreement as expected, the analytical solution offers a significant savings in computation effort compared to the finite-difference approximation.

5.6. Concluding Remarks

In this chapter, the single phase Gibbs function continuation method has been extended to a general multiphase algorithm. To the author's best knowledge, this represents the first time the Gibbs function continuation method has been extended to a general multiphase system and that the MPGFC method is the first multiphase, constrained equilibrium solution algorithm which is guaranteed to converge for all well posed constraints. The major contributions are listed as follows:

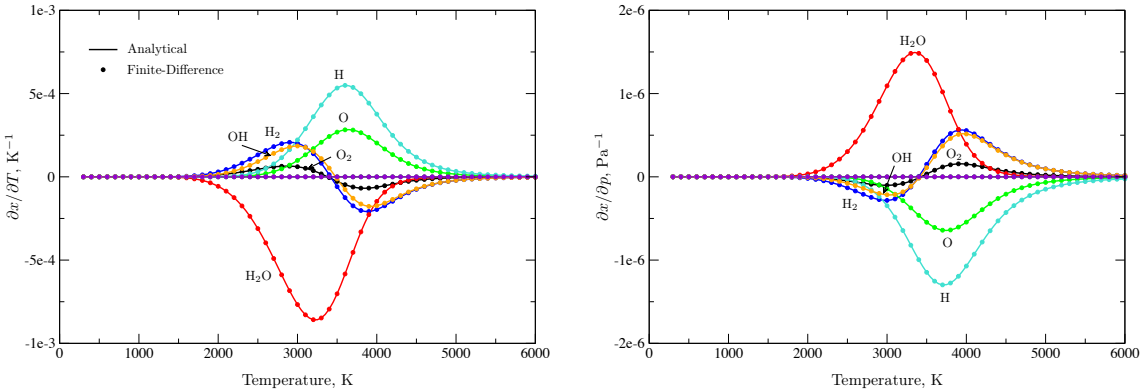

(a) *With respect to temperature.* **(b)** *With respect to pressure.*

Figure 5.5.: *Mole fraction derivatives with respect to temperature and pressure for the water mixture from Fig. (5.2). The expressions in Eqs. (5.58 - 5.63) were used to compute the analytical results and are compared against results obtained using a finite-difference approximation.*

- The phase moles have been added to the solution vector with the necessary mathematical adjustments developed for the GFC methodology.
- A procedure to ensure that the Gibbs phase rule is satisfied has been included in the initialization procedure along with a phase redistribution technique to ensure all phases are correctly included.
- Strictly positive (upper and lower) bounds have been placed on the eigenvalues of the linear system matrix necessary for computing the tangent vector of the pseudo-equilibrium path in a robust manner.
- Furthermore, it was shown that the eigenvalues tend toward the moles of each included phase as the residual of the least squares solution for $\dot{\mathbf{\Lambda}}^{\mathbf{y}}$ decreases.
- The eigenvalue analysis has been used to develop a sensible procedure for removing phases from the equilibrium solution, namely when the moles in a phase drop below a specified tolerance.

The above points were demonstrated on two numerical test cases which serve to highlight some of the features of the method. A single phase case demonstrated the use of constraints on the equilibrium mixture and the robustness of the method when the solution lies on the edge of the feasible region. A multiphase example was used to show, first and foremost, that the method provides the correct solution when compared to the well established CEA code, and secondly that the underlying eigenvalue analysis is correct.

Finally, the MPGFC method is shown to be a reliable and robust algorithm for computing linearly constrained, multiphase, chemical equilibrium solutions. The method has been included in the MUTATION^{++} library, presented in Chapter 4, which is available as a free, open source, software package.

CHAPTER 6

Numerical Methods and Codes

6.1. Introduction

The purpose of this chapter is to present the numerical tools developed in this thesis which are used in the following chapter to study coupled flow, radiation, and ablation phenomena for atmospheric entry vehicles. Unsteady, three-dimensional, coupled simulations of atmospheric entry vehicles with ablative heat shields remain extremely costly undertakings due to the large number of species, chemical reactions, and physical phenomena involved. As a result, these types of simulations are often performed with lower fidelity modeling and approximate coupling strategies between radiation, ablation, and flow solutions.

Since the primary focus of this work is to study these complex interactions, only the steady-state stagnation stream line is considered. As will be shown, considering only the stagnation line of an atmospheric entry vehicle substantially reduces the cost in terms of CPU time required to obtain meaningful solutions. These savings can then be reinvested by using higher fidelity physicochemical models and coupling strategies. In addition, this approach provides the ability to make accurate engineering predictions of stagnation point heating in a relatively short time. A few drawbacks of this approach is that 3D and unsteady effects are not considered. However, such effects are out of the scope of this thesis.

The chapter is organized as follows. Section 6.2 details the derivation and discretization of the governing equations for the flow field along the stagnation line of an atmospheric entry vehicle. Coupling with the material response is approximately modeled through a steady-state ablative boundary condition. Section 6.3 presents the development of two numerical tools which are used in this work for the solution of radiative transport along the stagnation line using the LBL and HSNB methodologies. Finally, Section 6.4 discusses the strategies used to compute coupled simulations.

6.2. Stagnation Line Flow

This section details the code developed for modeling the stagnation line flow field. The governing equations, numerical methods, and boundary conditions used in this work are summarized in the following sections. The two-temperature thermochemical nonequilibrium model presented in Chapter 2 is used to illustrate the governing equations derived for the stagnation line. In principle, however, any thermochemical nonequilibrium model could be used with this approach.

6.2.1. Dimensionally Reduced Navier-Stokes Equations

We follow the methodology of Klomfass and Müller [276] for deriving a 1D plasma flow model along the stagnation-line of a spherical body with radius R_0 as shown in Fig. (6.1). Non-spherical bodies are modeled using an equivalent sphere radius R_0 which correctly reproduces certain desired flow features. For example, Turchi *et al.* [277] have shown that the Local Heat Transfer Simulation (LHTS) methodology can be used to define an equilivalent sphere radius to match subsonic plasma wind tunnel conditions with actual flight conditions, through appropriate similarity conditions. In this work, equivalent sphere radii have been determined in order to match expected shock standoff

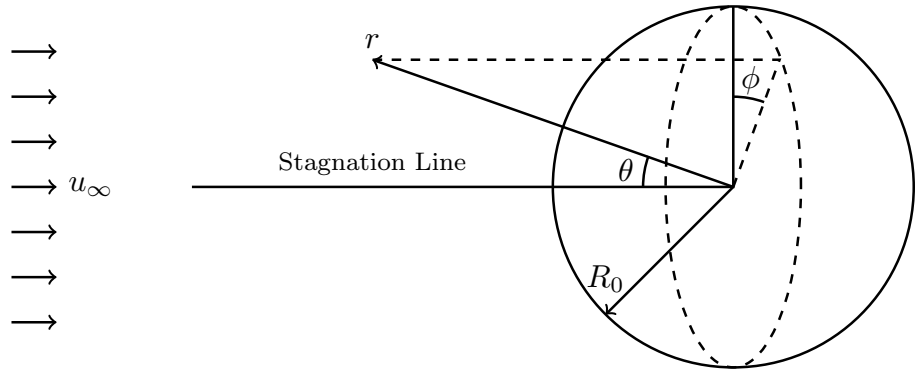

Figure 6.1.: *Spherical body of radius R_0 subjected to a hypersonic flow with uniform velocity u_∞. Azimuth and zenith angles are ϕ and θ, respectively.*

distances, based on the work of Park [278] for the Apollo 4 vehicle. More details, specific to each case considered, are given in Chapter 7.

Using physical considerations and the assumption of axi-symmetric flow ($\partial/\partial\phi = 0$), Klomfass and Müller assume the following radial dependence for mass fractions and temperatures,

$$y_s = \bar{y}_s(r), \tag{6.1}$$
$$T = \bar{T}(r), \tag{6.2}$$
$$T^{ve} = \bar{T}^{ve}(r), \tag{6.3}$$

while velocities and pressures are split into radial and tangential components following

$$u_r = \bar{u}_r(r)\cos\theta, \tag{6.4}$$
$$u_\theta = \bar{u}_\theta(r)\sin\theta, \tag{6.5}$$
$$p - p_\infty = \bar{p}(r)\cos^2\theta, \tag{6.6}$$
$$p_e - p_{e,\infty} = \bar{p}_e(r)\cos^2\theta, \tag{6.7}$$

where the pressure is assumed to follow a Newtonian approximation [104] and the overline symbol indicates stagnation line quantities. Introducing this decomposition into the 3D Navier-Stokes equations in spherical coordinates and then taking the limit when θ tends to zero leads to the Dimensionally Reduced Navier Stokes (DNRS) equations for the stagnation-streamline quantities of the form

$$\frac{\partial \mathbf{U}}{\partial t} + \frac{\partial \mathbf{F}^c}{\partial r} + \frac{\partial \mathbf{F}^d}{\partial r} = \mathbf{S}^c + \mathbf{S}^d + \mathbf{S}^k + \mathbf{S}^r, \tag{6.8}$$

where $\mathbf{U}$ is the conservative variable vector and $\mathbf{F}^c$ and $\mathbf{F}^d$ are the convective and diffusive fluxes,

$$\mathbf{U} = \begin{bmatrix} \rho_s \\ \rho u_r \\ \rho u_\theta \\ \rho E \\ \rho e^{ve} \end{bmatrix}, \quad \mathbf{F}^c = \begin{bmatrix} \rho_s u_r \\ \rho u_r^2 + p \\ \rho u_r u_\theta \\ \rho u_r H \\ \rho u_r e^{ve} \end{bmatrix}, \quad \text{and} \quad \mathbf{F}^d = \begin{bmatrix} J_{rs} \\ -\tau_{rr} \\ -\tau_{r\theta} \\ q_r - \tau_{rr} u_r \\ q_r^{ve} \end{bmatrix}. \tag{6.9}$$

$\mathbf{S}^c$ and $\mathbf{S}^d$ are convective and diffusive source terms resulting from the expansion along the

stagnation-line and are written as

$$\mathbf{S}^c = -\frac{(u_r+u_\theta)}{r}\begin{bmatrix} 2\rho_s \\ 2\rho u_r \\ 3\rho u_\theta - 2\frac{p-p_\infty}{u_r+u_\theta} \\ 2\rho H \\ 2\rho e^{ve} \end{bmatrix}, \quad \text{and} \tag{6.10}$$

$$\mathbf{S}^d = -\frac{1}{r}\begin{bmatrix} 2J_{rs} \\ 2(\tau_{\theta\theta} - \tau_{rr} + \tau_{r\theta}) \\ \tau_{\theta\theta} - 3\tau_{r\theta} \\ 2(q_r - \tau_{rr}u_r - \tau_{r\theta}u_r - \tau_{\theta\theta}u_\theta) \\ 2q_r^{ve} \end{bmatrix}. \tag{6.11}$$

Finally $\mathbf{S}^k$ and $\mathbf{S}^r$ are the internal kinetic and energy transfer and radiative source term vectors, respectively, where

$$\mathbf{S}^k = \begin{bmatrix} \dot{\omega}_s \\ 0 \\ 0 \\ 0 \\ \Omega^{ve} \end{bmatrix}, \quad \text{and} \quad \mathbf{S}^r = \begin{bmatrix} \dot{\phi}_s \\ 0 \\ 0 \\ \mathcal{P} \\ \mathcal{P}_{ve} \end{bmatrix}. \tag{6.12}$$

The overline symbol introduced in Eqs. (6.1 - 6.7) to designate stagnation-line quantities has been omitted for the sake of clarity. The DNRS equations are supplied with appropriate boundary conditions at the free-stream radius $r = R_\infty$ and the vehicle surface $r = R_0$. The boundary conditions used in this work are discussed in Section 6.2.3.

The total energy and the vibrational-electronic-electron energy per unit volume are defined as $\rho E = \sum_s \rho_s e_s + \rho u_r^2/2$ and $\rho e^{ve} = \sum_s \rho_s e_s^{ve}$. Only the radial velocity component contributes to the kinetic energy due to the ansatz Eqs. (6.4 - 6.7). Note that the formation energy is not included in e^{ve}. This point is important for the source terms described below. The total enthalpy is defined as usual by $H = E + p/\rho$.

The radial species diffusion fluxes J_{rs} are obtained by solving the approximate Stefan-Maxwell equations for heavy species with an ambipolar electric field as discussed in Section 4.5.2. The radial heat fluxes are defined by

$$q_r = \sum_s J_{rs}h_s - \lambda^{tr}\frac{\partial T}{\partial r} - \lambda^{ve}\frac{\partial T^{ve}}{\partial r}, \tag{6.13}$$

$$q_r^{ve} = \sum_s J_{rs}h_s^{ve} - \lambda^{ve}\frac{\partial T^{ve}}{\partial r}, \tag{6.14}$$

where λ^{tr} and λ^{ve} are the thermal conductivities of the energy modes in equilibrium with the temperatures T and T^{ve} respectively, $h_s = e_s + p_s/\rho_s$, $h_s^{ve} = e_s^{ve}$ for $s \neq e$ and $h_e^{ve} = e_e^{ve} + p_e/\rho_e$. The components of the viscous stress tensor τ_{rr}, $\tau_{r\theta}$ and $\tau_{\theta\theta}$ are given by

$$\tau_{rr} = \frac{4}{3}\eta\left(\frac{\partial u_r}{\partial r} - \frac{u_r+u_\theta}{r}\right), \tag{6.15}$$

$$\tau_{r\theta} = \eta\left(\frac{\partial u_\theta}{\partial r} - \frac{u_r+u_\theta}{r}\right), \tag{6.16}$$

$$\tau_{\theta\theta} = -\frac{1}{2}\tau_{rr}, \tag{6.17}$$

where η is the shear viscosity.

In Eq. (6.12) $\dot{\omega}_s$ are the collisional species mass production rates. Reaction rate constants are assumed to follow an Arrhenius law (see Section 2.6.1). Forward reaction constants are taken from the literature depending on the mixture considered. Backward reaction constants are computed

such that equilibrium relations are satisfied [7]. The nonequilibrium temperatures used for the forward and backward rates in this work have already been presented in Table 2.1. Ω^{ve} represents the rate of translational energy being converted to vibration-electronic-electron energy and is written as

$$\Omega^{ve} = -p_e \left(\frac{\partial u_r}{\partial r} + 2\frac{u_r + u_\theta}{\partial r} \right) + \sum_{s \in \mathcal{M}} \rho_s \frac{e_s^{v0} - e_s^v}{\tau_s^{VT}} + \rho_e \frac{e_e^{t0} - e_e^t}{\tau^{ET}} + \sum_s e_s^{ve} \dot{\omega}_s - \sum_{p \in \mathcal{R}} \Delta H_p \mathfrak{R}_p. \quad (6.18)$$

The first term on the right-hand-side of Eq. (6.18) represents the internal work done by the electron pressure. The second term represents vibration-translation energy exchange where e_s^{v0} and e_s^v are vibrational energies of species s at the temperature T and T^{ve}, respectively. The third term corresponds to electron-heavy translation energy exchange where e_e^{t0} and e_e^t are translational energies of electrons at the temperature T and T^{ve}, respectively. The expressions shown in Eq. (2.129) and Eq. (2.135) are used in this work for the associated relaxation times τ_s^{VT} and τ_s^{ET}, respectively. The fourth term represents the coupling between chemistry and vibrational-electronic energy. Finally, the fifth term accounts for the energy removed from the electron bath due to the set $\mathcal{R}$ of electron impact ionization and dissociation reactions, where $\mathfrak{R}_p$ is the molar rate of progress and $\Delta H_p = \sum_s \nu_{sp} e_s^f / M_s$ is the chemical heat released per unit mole (ν_{sp} is the stoichiometric coefficient for reaction p and M_s is the molar mass of species s) of reaction p.

Lastly, $\dot{\phi}_s$ represents the mass production rate of species s due to photochemical reactions, $\mathcal{P}$ is the total radiative energy source term and $\mathcal{P}_{ve}$ is the radiative energy source term for the energy modes in equilibrium with T^{ve}. The numerical solution of the radiative source terms is presented in Section 6.3.

6.2.2. Discretization

The numerical solution of the DNRS stagnation-line equations derived in the previous section has been developed by Munafò [97] for nitrogen STS flows. This implementation has been extended in this work to general thermochemical non-equilibrium models, however the numerical methods remain unchanged from the original work of Munafò. The stagnation-line equations of Eq. (6.8) are solved via the method-of-lines. The spatial and temporal discretizations are summarized below.

Spatial Discretization

The stagnation-line equations are discretized in space between the surface radius R_0 and free-stream radius R_∞ using the Finite Volume (FV) method. The resulting discretization yields the following Ordinary Differential Equation (ODE) for the temporal variation of the cell-averaged conservative variables in cell i,

$$\frac{\partial \mathbf{U}_i}{\partial t} \Delta r_i + \tilde{\mathbf{F}}^c_{i+\frac{1}{2}} - \tilde{\mathbf{F}}^c_{i-\frac{1}{2}} + \mathbf{F}^d_{i+\frac{1}{2}} - \mathbf{F}^d_{i-\frac{1}{2}} = \left(\mathbf{S}^c_i + \mathbf{S}^d_i + \mathbf{S}^k_i + \mathbf{S}^r_i \right) \Delta r_i, \quad (6.19)$$

where $\Delta r_i = r_{i+\frac{1}{2}} - r_{i-\frac{1}{2}}$ is length of cell i. The numerical inviscid flux $\tilde{\mathbf{F}}^c_{i+\frac{1}{2}}$ is computed using Roe's approximate Riemann solver [279], such that

$$\tilde{\mathbf{F}}^c_{i+\frac{1}{2}} = \frac{1}{2}\Big[\mathbf{F}^c(\mathbf{U}_{i+1}) + \mathbf{F}^c(\mathbf{U}_i) \Big] - \frac{1}{2} \big| \mathbf{A}(\hat{\mathbf{U}}) \big| \Big[\mathbf{U}_{i+1} - \mathbf{U}_i \Big]. \quad (6.20)$$

$\big|\mathbf{A}(\hat{\mathbf{U}})\big|$ is the dissipation matrix, defined as $\big|\mathbf{A}(\hat{\mathbf{U}})\big| = \mathbf{R}(\hat{\mathbf{U}}) \big|\mathbf{\Lambda}(\hat{\mathbf{U}})\big| \mathbf{L}(\hat{\mathbf{U}})$, where $\mathbf{R}$, $\mathbf{L}$, and $\mathbf{\Lambda}$ are the right eigenvector, left eigenvector, and diagonal eigenvalue matrices associated with the inviscid flux Jacobian $\mathbf{A} = \partial \mathbf{F}^c / \partial \mathbf{U} = \mathbf{R}\mathbf{\Lambda}\mathbf{L}$. The exact expressions used for the eigensystem matrices are provided in Appendix C. The hat symbol on the conservative variable vector in Eq. (6.20) denotes the Roe averaged state, evaluated using the linearization of Prabhu [280] with the entropy fix of Harten and Hyman [281] in order to prevent the occurrence of expansion shocks.

Second-order accuracy in space is achieved by reconstructing upwind variables at the cell interface. For robustness, the reconstruction is performed on primitive variables, $\mathbf{P} = [\rho_s, u_r, u_\theta, T, T^{ve}]^T, s \in \mathcal{S}^*$ [27]. For a generic primitive variable p, the reconstructed "left" (L) and "right" (R) values at an interface $i + 1/2$ are computed using the Monotone Upstream Centered Schemes for Conservation Laws (MUSCL) scheme [282],

$$p^L_{i+1/2} = p_i + \frac{1}{2}\phi(r^L_i)(p_i - p_{i-1}), \tag{6.21}$$

$$p^R_{i+1/2} = p_{i+1} - \frac{1}{2}\phi(1/r^R_{i+1})(p_{i+2} - p_{i+1}), \tag{6.22}$$

where $\phi(r)$ is a slope limiter function. Here, r represents the ratios of consecutive differences, such that

$$r^L_i = \frac{p_{i+1} - p_i}{p_i - p_{i-1}}, \tag{6.23}$$

$$r^R_{i+1} = \frac{p_{i+2} - p_{i+1}}{p_{i+1} - p_i}. \tag{6.24}$$

The van Albada limiter [283] has been used in this work, following the implementation of Munafò [97]. Conservative variables are then built from reconstructed primitive variables and the second-order numerical flux is computed according to $\tilde{\mathbf{F}}^c_{i+1/2} = \tilde{\mathbf{F}}^c_{i+1/2}(\mathbf{U}^L_{i+1/2}, \mathbf{U}^R_{i+1/2})$.

The diffusive fluxes and source terms are computed using primitive variables. Primitive variables are computed at the face $i + \frac{1}{2}$ for the diffusive fluxes using a simple weighted average, such that for a generic primitive variable p

$$p_{i+\frac{1}{2}} = \frac{p_{i+1}\Delta r_{i+1} + p_i \Delta r_i}{\Delta r_{i+1} + \Delta r_i}. \tag{6.25}$$

Likewise, primitive variable gradients are computed using a central difference scheme at the face,

$$\left(\frac{\partial p}{\partial r}\right)_{i+\frac{1}{2}} = 2\left(\frac{p_{i+1} - p_i}{\Delta r_{i+1} + \Delta r_i}\right). \tag{6.26}$$

Cell-centered gradients are computed using a two point central finite difference for the diffusive flux source term, such that

$$\left(\frac{\partial p}{\partial r}\right)_{i} = 2\left(\frac{p_{i+1} - p_{i-1}}{\Delta r_{i+1} + 2\Delta r_i + \Delta r_{i-1}}\right). \tag{6.27}$$

Temporal Discretization

Eq. (6.19) is integrated in time from an initial time level of $n = 0$ using the implicit Backward-Euler method,

$$\frac{\delta \mathbf{U}^n_i}{\Delta t_i}\Delta r_i + \tilde{\mathbf{F}}^{c\ n+1}_{i+\frac{1}{2}} - \tilde{\mathbf{F}}^{c\ n+1}_{i-\frac{1}{2}} + \mathbf{F}^{d\ n+1}_{i+\frac{1}{2}} - \mathbf{F}^{d\ n+1}_{i-\frac{1}{2}} = \left(\mathbf{S}^{c\ n+1}_i + \mathbf{S}^{d\ n+1}_i + \mathbf{S}^{k\ n+1}_i + \mathbf{S}^{r\ k}_i\right)\Delta r_i, \tag{6.28}$$

where $\delta \mathbf{U}^n_i = \mathbf{U}^{n+1}_i - \mathbf{U}^n_i$ and Δt_i is the local time-step based on the Courant-Friedrichs-Lewy (CFL) number according to Blazek [284],

$$\Delta t_i = \frac{\mathrm{CFL}\Delta r_i}{\left[|u_r| + a + \frac{1}{\Delta r}\max\left(\frac{4}{3}\frac{\eta}{\rho}, \frac{\lambda}{c_v}\right)\right]_i}, \tag{6.29}$$

where a is the numerical speed of sound presented in Appendix C. In practice, the CFL number

is typically ramped up from about 0.01 to 100 by multiplying by 10 every 1000 iterations or so. For simplicity, the initial solution for uncoupled simulations is taken as the free-stream conditions. Coupled simulations are discussed in Section 6.4. The radiative source term in Eq. (6.28) is treated explicitly at a lagged time level $k = n - (n \bmod n^r)$ where n^r is the number of flow time-steps computed between updates to the radiative source term and $(n \bmod n^r)$ represents the modulus of the integer division of n by n^r.

The numerical inviscid flux is linearized using the method of Liou and van Leer [285],

$$\tilde{\mathbf{F}}^{c\,n+1}_{i+\frac{1}{2}} \approx \tilde{\mathbf{F}}^{c\,n}_{i+\frac{1}{2}} + \mathbf{A}^{+}_{i}\delta\mathbf{U}^{n}_{i} + \mathbf{A}^{-}_{i+1}\delta\mathbf{U}^{n}_{i+1}, \tag{6.30}$$

where the positive-negative split Jacobians are $\mathbf{A}^{\pm} = \mathbf{R}\mathbf{\Lambda}^{\pm}\mathbf{L}$. Their expressions are provided in Appendix C. The diffusive fluxes and source term are linearized in two steps. In the first step, the fluxes and source terms are rewritten as a sum of the terms which are linearly dependent on the gradient of conservative variables plus those which are not, such that

$$\mathbf{F}^{d\,n}_{i+\frac{1}{2}} = \mathbf{A}^{d\,n}_{i+\frac{1}{2}}\left(\frac{\partial\mathbf{U}}{\partial r}\right)^{n}_{i+\frac{1}{2}} + \mathbf{B}^{d\,n}_{i+\frac{1}{2}}, \tag{6.31}$$

$$\mathbf{S}^{d\,n}_{i} = \mathbf{A}^{d\,n}_{s\,i}\left(\frac{\partial\mathbf{U}}{\partial r}\right)^{n}_{i} + \mathbf{B}^{d\,n}_{s\,i}. \tag{6.32}$$

To simplify the linearization procedure, the matrices $\mathbf{A}^d$ and $\mathbf{A}^d_s$ are computed assuming a Fickian diffusion model using the self-consistent effective diffusion coefficients of Ramshaw and Chang [286]. Expressions for the matrices $\mathbf{A}^d$, $\mathbf{A}^d_s$, $\mathbf{B}^d$, and $\mathbf{B}^d_s$ are provided in Appendix C. In the second step, the gradients in Eqs. (6.31) and (6.32) are computed according to Eqs. (6.26) and (6.27) and the resulting expressions are linearized around time-level n, such that

$$\mathbf{F}^{d\,n+1}_{i+\frac{1}{2}} \approx \mathbf{F}^{d\,n}_{i+\frac{1}{2}} + 2\mathbf{A}^{d\,n}_{i+\frac{1}{2}}\left(\frac{\delta\mathbf{U}_{i+1} - \delta\mathbf{U}_{i}}{\Delta r_{i+1} + \Delta r_{i}}\right) + \frac{\partial\mathbf{B}^{d\,n}_{i+1/2}}{\partial\mathbf{U}^{n}_{i}}\delta\mathbf{U}^{n}_{i} + \frac{\partial\mathbf{B}^{d\,n}_{i+1/2}}{\partial\mathbf{U}^{n}_{i+1}}\delta\mathbf{U}^{n}_{i+1}, \tag{6.33}$$

$$\mathbf{S}^{d\,n+1}_{i} \approx \mathbf{S}^{d\,n}_{i} + 2\mathbf{A}^{d\,n}_{s\,i}\left(\frac{\delta\mathbf{U}_{i+1} - \delta\mathbf{U}_{i}}{\Delta r_{i+1} + 2\Delta r_{i} + \Delta r_{i-1}}\right) + \frac{\partial\mathbf{B}^{d\,n}_{s\,i}}{\partial\mathbf{U}^{n}_{i}}\delta\mathbf{U}^{n}_{i}, \tag{6.34}$$

where the matrices $\mathbf{A}^d$ and $\mathbf{A}^d_s$ have been assumed constant during the linearization. For simplicity, the last two Jacobians in Eq. (6.33) are approximated as

$$\frac{\partial\mathbf{B}^{d\,n}_{i+1/2}}{\partial\mathbf{U}^{n}_{i}} \approx \frac{\partial\mathbf{B}^{d\,n}_{i}}{\partial\mathbf{U}^{n}_{i}}, \tag{6.35}$$

$$\frac{\partial\mathbf{B}^{d\,n}_{i+1/2}}{\partial\mathbf{U}^{n}_{i+1}} \approx \frac{\partial\mathbf{B}^{d\,n}_{i+1}}{\partial\mathbf{U}^{n}_{i+1}}, \tag{6.36}$$

where the expressions for $\partial\mathbf{B}^d/\partial\mathbf{U}$ and $\partial\mathbf{B}^d_s/\partial\mathbf{U}$ are given in Appendix C.

Finally, the convective and kinetic source terms are linearized through a simple Taylor series expansion, such that

$$\mathbf{S}^{c\,n+1}_{i} \approx \mathbf{S}^{c\,n}_{i} + \frac{\partial\mathbf{S}^{c\,n}_{i}}{\partial\mathbf{U}^{n}_{i}}\delta\mathbf{U}^{n}_{i}, \tag{6.37}$$

$$\mathbf{S}^{k\,n+1}_{i} \approx \mathbf{S}^{k\,n}_{i} + \frac{\partial\mathbf{S}^{k\,n}_{i}}{\partial\mathbf{U}^{n}_{i}}\delta\mathbf{U}^{n}_{i}. \tag{6.38}$$

The source term Jacobians are computed analytically to increase stability and the resulting expressions are presented in Appendix C.

The substitution of Eqs. (6.30 - 6.38) into Eq. (6.28) leads to a block-tridiagonal linear system of equations which is solved at each time-step using the Thomas algorithm [281] for the update in the conservative variables. This procedure is repeated until a steady-state solution is reached.

6.2.3. Boundary Conditions

Boundary conditions are imposed using primitive variables at ghost-cells [281]. The different boundary conditions used in this work are described below. The wall boundary conditions are imposed at a radius $r = R_0$, while free-stream conditions are imposed at $r = R_\infty$.

Isothermal, non-catalytic, no-slip wall

When ablation coupling is neglected, the wall of the vehicle is assumed to be non-ablative, non-catalytic, and isothermal at $T = T^{ve} = T_w$ for a prescribed wall temperature T_w. A no-slip condition for the velocity is prescribed, where $(\rho u_r)_w = (\rho u_\theta)_w = 0$. Finally, species partial pressures are assumed constant across the wall.

Isothermal, steady-state ablation

Coupling with ablation and pyrolysis phenomena is obtained by way of a steady-state ablation boundary condition using the procedure detailed by Turchi *et al.* [287]. A detailed species mass balance at the surface yields the following relationship,

$$(\rho_i u_r)_w + (J_{ri})_w = \dot{m}_{c,i} + \dot{m}_{g,i}, \quad \forall\, i \in \mathcal{S}, \tag{6.39}$$

in which the first two terms are the convective and diffusive mass fluxes of species i at the surface and $\dot{m}_{c,i}$ and $\dot{m}_{g,i}$ represent the char and pyrolysis gas blowing rates respectively at the surface for species i. Summing the species mass balance over all species, we have

$$(\rho u_r)_w = \dot{m}_c + \dot{m}_g, \tag{6.40}$$

where $\dot{m}_c = \sum_{i\in\mathcal{S}} \dot{m}_{c,i}$ and $\dot{m}_g = \sum_{i\in\mathcal{S}} \dot{m}_{g,i}$. The recession rate of the surface, $\dot{s}_c$, and the virgin layer, $\dot{s}_v$, are given as

$$\dot{s}_c = \frac{\dot{m}_c}{\rho_c}, \quad \dot{s}_v = \frac{\dot{m}_g}{\rho_v - \rho_c} \tag{6.41}$$

where ρ_c and ρ_v are the densities of the char and virgin materials respectively. Under the steady-state ablation assumption, the surface and virgin layer recess at the same rate, leading to the following expression for the pyrolysis blowing rate:

$$\dot{m}_g = \left(\frac{\rho_v}{\rho_c} - 1\right) \dot{m}_c. \tag{6.42}$$

The ratio ρ_v/ρ_c is by definition greater than one and may be determined experimentally for a given TPS material. Substituting Eqs. (6.40) and (6.42) into Eq. (6.39), we have

$$\frac{\rho_v}{\rho_c}\dot{m}_c \left(\frac{\rho_i}{\rho}\right)_w + (J_{ri})_w = \dot{m}_{c,i} + \left(\frac{\rho_v}{\rho_c} - 1\right) y_{g,i}\dot{m}_c, \quad \forall\, i \in \mathcal{S}, \tag{6.43}$$

where $y_{g,i}$ is the mass fraction of species i in the pure pyrolysis gas. When equilibrium is assumed for the pyrolysis gas composition, $y_{g,i}$ is fixed based on the surface temperature, pressure, and the given elemental composition of the pyrolysis gas. The char mass blowing rate is determined from the following four elementary reactions considered at a pure carbon surface.

$$\mathrm{C(s)} + \mathrm{O} \longrightarrow \mathrm{CO} \tag{6.44}$$

$$2\,\mathrm{C(s)} + \mathrm{O_2} \longrightarrow 2\,\mathrm{CO} \tag{6.45}$$

$$\mathrm{C(s)} + \mathrm{N} \longrightarrow \mathrm{CN} \tag{6.46}$$

$$3\,\mathrm{C(s)} \rightleftharpoons \mathrm{C_3} \tag{6.47}$$

The reaction probabilities for the two oxidation reactions and the sublimation reaction have been taken from Park [69], while the nitridation reaction probability is taken from Suzuki [288] based

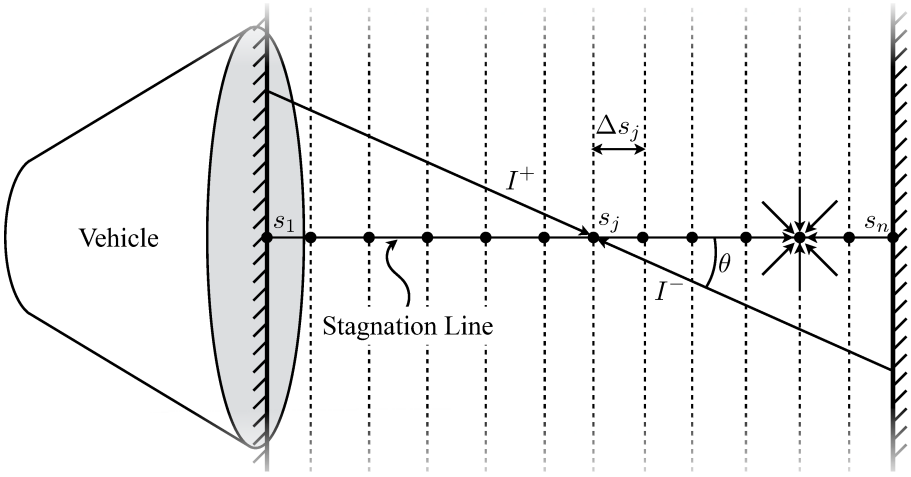

Figure 6.2.: *Diagram of the tangent slab approximation.*

on a recent experimental investigation by Helber *et al.* [8] on the nitridation of Graphite in a pure Nitrogen plasma. Note that the sublimation reaction is considered reversible such that carbon may condense on the surface. In addition to the heterogeneous reactions listed above, all ions are recombined at the wall in order to ensure that there is no electrical charge across the surface. Catalytic recombination of neutral species is neglected. For a fixed wall temperature and pressure, Eq. (6.43) represents a nonlinear system of $n^{\mathcal{S}}$ equations for the $n^{\mathcal{S}}$ unknown species densities at the wall which can be solved using a simple Newton iterative procedure. An energy balance could also be coupled to this system to solve for the temperature at the wall, however we will only consider a fixed wall temperature in this work in order to simplify the analysis. Finally, the ablative boundary condition is closed with the addition of the following constraints at the wall:

$$(T)_w = (T^{ve})_w = T_w, \tag{6.48}$$

$$\left(\frac{\partial p}{\partial r}\right)_w = 0, \tag{6.49}$$

$$(u_\theta)_w = 0. \tag{6.50}$$

Free-stream

Free-stream boundary conditions are implemented as a supersonic inlet [281] in which temperature, velocity and species mass densities are imposed.

6.3. 1D Radiative Transfer

This section describes the tools developed for the solution of the radiative source terms along the stagnation line. The tangent slab approximation has been used to model the radiative properties in the flow field. The tangent slab approximation assumes that the flow field can be divided into constant property slabs which extend to infinity in all directions tangent to the stagnation line as shown in Fig. (6.2). In the figure, the stagnation line is divided into n discrete points s_j with $1 \leq j \leq n$ which separate $n-1$ constant property slabs. Under this assumption, a radiative property ϕ_σ can then be expressed as only a function of the tangential distance from the stagnation point $\phi_\sigma(s) = \phi_\sigma(s_j)$ for $s_j \leq s < s_{j+1}$. This simplification greatly reduces the numerical complexity of computing radiative source terms.

Two separate codes have been developed in this work for computing the radiative source terms along the stagnation line, under the tangent slab approximation. The first is specialized for full LBL calculations, while the second is used with the HSNB model. Each code is summarized below.

6.3.1. LBL Tangent Slab

The tangent slab geometry depicted in Fig. (6.2) allows the RTE given in Eq. (3.1) to be greatly simplified to,

$$\cos\theta \frac{\partial}{\partial s} I_\sigma(s,\theta) = \eta_\sigma(s) - \kappa_\sigma(s) I_\sigma(s,\theta), \tag{6.51}$$

where θ is the angle between the ray direction and the stagnation line and s is the normal coordinate between the two walls in Fig. (6.2) or along the stagnation line in this work. Note that this s is distinctly different than the s used in Eq. (3.1) which is the coordinate along the ray. Writing $\mu = \cos\theta$, the formal solution to Eq. (6.51) is given by

$$I_\sigma(s,\mu) = I_\sigma(b,\mu)\,\tau_\sigma(b,s,\mu) + \frac{1}{\mu}\int_b^s \eta_\sigma(s')\,\tau_\sigma(s',s,\mu)\,ds', \tag{6.52}$$

where b represents the tangential coordinate of the boundary from which a ray with angle cosine μ starts from. The spectral transmissivity is given as

$$\tau_\sigma(s',s,\mu) = \exp\left(-\int_{s'}^{s} \frac{\kappa_\sigma(s'')}{\mu} ds''\right). \tag{6.53}$$

Using the formalism of Section 3.4.1, the intensity at a point s_j in the direction μ for the constant property slab geometry in Fig. (6.2) is found to be

$$I_\sigma(s_j,\mu) = I_\sigma(s_1,\mu)\,\tau(s_1,s_j,\mu) + \sum_{i=1}^{j-1} \frac{\eta}{\kappa}(s_i)\big[\tau(s_{i+1},s_j,\mu) - \tau(s_i,s_j,\mu)\big], \qquad 0 \le \mu \le 1, \tag{6.54}$$

and

$$I_\sigma(s_j,\mu) = I_\sigma(s_n,\mu)\,\tau(s_n,s_j,\mu) + \sum_{i=j}^{n-1} \frac{\eta}{\kappa}(s_i)\big[\tau(s_i,s_j,\mu) - \tau(s_{i+1},s_j,\mu)\big], \qquad -1 \le \mu < 0. \tag{6.55}$$

The radiative heat flux can then be computed as

$$q^r_\sigma(s_j) = 2\pi \int_{-1}^{1} I_\sigma(s_j,\mu)\,\mu\,d\mu. \tag{6.56}$$

Assuming black walls, the integrals over the angle cosine may be computed analytically, resulting in the final expression for the tangent slab heat flux,

$$\begin{aligned} q^r_\sigma(s_j) = 2\pi\Bigg\{ & I^b_\sigma(T_1)\,E_3\Bigg(\sum_{i=1}^{j-1}\kappa_i\Delta s_i\Bigg) - I^b_\sigma(T_2)\,E_3\Bigg(\sum_{i=j}^{n-1}\kappa_i\Delta s_i\Bigg) \\ & + \sum_{i=1}^{j-1} \frac{\eta_\sigma}{\kappa_\sigma}\bigg|_i \Bigg[E_3\Bigg(\sum_{k=i+1}^{j-1}\kappa_k\Delta s_k\Bigg) - E_3\Bigg(\sum_{k=i}^{j-1}\kappa_k\Delta s_k\Bigg)\Bigg] \\ & - \sum_{i=j}^{n-1} \frac{\eta_\sigma}{\kappa_\sigma}\bigg|_i \Bigg[E_3\Bigg(\sum_{k=j}^{i-1}\kappa_k\Delta s_k\Bigg) - E_3\Bigg(\sum_{k=j}^{i}\kappa_k\Delta s_k\Bigg)\Bigg]\Bigg\}, \end{aligned} \tag{6.57}$$

where κ_i and η_i are respectively the spectral absorption and emission coefficients for slab i, T_1 and T_2 are the temperatures of the boundaries at s_1 and s_n, and $\Delta s_i = s_{i+1} - s_i$ is the thickness of

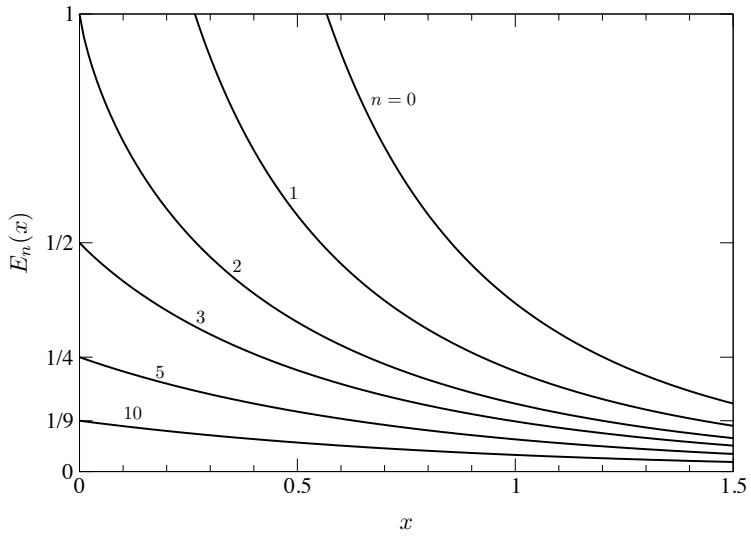

Figure 6.3.: *Selected exponential integrals $E_n(x)$.*

the i^{th} slab. E_3 is the exponential integral function, where

$$E_n(x) = \int_0^1 \mu^{n-2} \exp\left(-\frac{x}{\mu}\right) d\mu, \quad n \geq 0. \tag{6.58}$$

The exponential integral functions satisfy the recurrence relation $nE_{n+1}(x) = \exp(-x) - xE_n(x)$, leading to the expression

$$E_n(x) = \frac{1}{(n-1)!}\left[(-x)^{n-1}E_1(x) + \exp(-x)\sum_{i=0}^{n-2}(n-i-2)!(-x)^i\right], \tag{6.59}$$

which relates all the exponential integral functions with $n > 1$ to E_1. The case of $n = 1$ is usually approximated using curve-fits based on accurate numerical integration or series expansions. For $n = 0$, the simple analytical expression, $E_0(x) = x^{-1}\exp(-x)$, can be used. The general behavior of the exponential integrals is shown in Fig. (6.3).

The tangent slab approximation allows for a significant reduction in computational effort necessary to evaluate the radiative heat flux and source term along the stagnation line when LBL calculations are performed. All LBL calculations performed in this work are computed using Eq. (6.57). The spectral coefficients are provided by the HTGR library discussed in Chapter 3. The average radiative source term in the slab bounded by s_j and s_{j+1} is readily obtained from,

$$-\boldsymbol{\nabla}\cdot\boldsymbol{q}^r(s_{j+\frac{1}{2}})\Delta s_j = q^r(s_j) - q^r(s_{j+1}), \tag{6.60}$$

where $s_{j+\frac{1}{2}} = (s_j + s_{j+1})/2$ denotes the location of the center of the slab.

6.3.2. HSNB Tangent Slab

Unfortunately, the HSNB methodology does not allow for the analytical treatment of the angular integration using exponential integrals as was shown for the LBL case in the previous section. This is most easily seen by considering the expression for the mean transmissivity in Eq. (6.53) applied to a homogeneous path between points s_1 and s_2. From Eq. (6.53), the average transmissivity over

a narrow spectral band, integrated over the direction cosine μ may be written as

$$\int_0^1 \overline{\tau_\sigma}^{\Delta\sigma}\, d\mu = \frac{1}{\Delta\sigma}\int_{\Delta\sigma} E_2\left(\kappa_\sigma(s_2 - s_1)\right) d\sigma. \tag{6.61}$$

If instead, we compute the band-average assuming a tailed-inverse exponential distribution for Lorentz broadening (see Table 3.2), then we have

$$\int_0^1 \overline{\tau_\sigma}^{\Delta\sigma}\, d\mu = \int_0^1 \exp\left(-2\beta\left(\sqrt{1 + \frac{k(s_2 - s_1)}{\beta\mu}} - 1\right)\right) d\mu, \tag{6.62}$$

where k and β are the SNB model parameters. These two equations show that transmissivity integrated over the direction cosine can be calculated using the E_2 exponential integral in the monochromatic case, but when averaged over a narrow band, an angular discretization must be used to perform the integration due to the non-Beerian expression of the narrow band transmissivity.

Discretizing the direction cosine space into discrete intervals $\Delta\mu_i$ with center μ_i, the heat flux is numerically integrated at each point s_j according to

$$\begin{aligned} q^r(s_j) &= 2\pi\int_0^\infty\int_{-1}^1 I_\sigma(s_j,\mu)\,\mu\, d\mu\, d\sigma \\ &\approx 2\pi\sum_{\Delta\sigma}\sum_{i=1}^{n_\mu} \overline{I_\sigma}^{\Delta\sigma}(s_j,\mu_i)\,\mu_i\,\Delta\mu_i\,\Delta\sigma, \end{aligned} \tag{6.63}$$

where $\overline{I_\sigma}^{\Delta\sigma}(s_j,\mu_i)$ is the band-averaged intensity at the point s_j in the direction corresponding to μ_i for band $\Delta\sigma$, and the sum over $\Delta\sigma$ corresponds to the sum over all narrow bands. The band-averaged intensity is computed using the HSNB method detailed in Section 3.4 for a path constructed from the tangent slab geometry ending at point s_j and beginning at the appropriate boundary corresponding to the direction cosine μ_i.

Eq. (6.63) represents four nested loops. The inner-most loop is performed over the line-of-sight necessary to compute the band-averaged intensity at a given spatial point and direction, $\overline{I_\sigma}^{\Delta\sigma}(s_j,\mu_i)$. The angular integration is then performed by looping over each point in the angular discretization. Next the spectral integration is performed by looping over each narrow band of the HSNB model. Finally, this procedure must be performed at all spatial locations along the stagnation line. Thus the numerical complexity for the integration of the radiative flux using Eq. (6.63) is proportional to $n(n-1)n_\mu n_b/2$. Once the flux has been calculated, its divergence is calculated according to Eq. (6.60).

The band-averaged spectral incident radiation at a point s_j may be computed using the same angular integration strategy used for the flux, namely

$$\overline{G}^{\Delta\sigma}(s_j) = 2\pi\int_{-1}^1 \overline{I_\sigma}^{\Delta\sigma}(s_j,\mu)\, d\mu \approx 2\pi\sum_{i=1}^{n_\mu}\overline{I_\sigma}^{\Delta\sigma}(s_j,\mu_i)\,\Delta\mu_i. \tag{6.64}$$

Finally, the species photochemical production rate for species s may be computed at the center of each slab through the discretization of Eq. (3.14),

$$\begin{aligned} \dot{\phi}_s(s_{j+\frac{1}{2}}) &= \frac{m_s}{hc}\sum_p \nu_{ps}\int_0^\infty \left[\kappa_\sigma^p(s_j)\, G_\sigma(s_{j+\frac{1}{2}}) - 4\pi\,\eta_\sigma^p(s_j)\right]\frac{d\sigma}{\sigma}, \\ &\approx \frac{m_s}{hc}\sum_p \nu_{ps}\sum_{\Delta\sigma}\left[\overline{\kappa^p}^{\Delta\sigma}(s_j)\,\overline{G}^{\Delta\sigma}(s_{j+\frac{1}{2}}) - 4\pi\,\overline{\eta^p}^{\Delta\sigma}(s_j)\right]\frac{\Delta\sigma_b}{\sigma}, \end{aligned} \tag{6.65}$$

where the sums over p and $\Delta\sigma$ represent the sums over all bound-free processes and spectral narrow bands, respectively, and $\sigma = (\sigma_1 + \sigma_2)/2$ is the center of each narrow band. $\overline{\kappa^p}^{\Delta\sigma}$ and $\overline{\eta^p}^{\Delta\sigma}$ are the narrow band absorption and emission coefficients, respectively, for the photochemical process

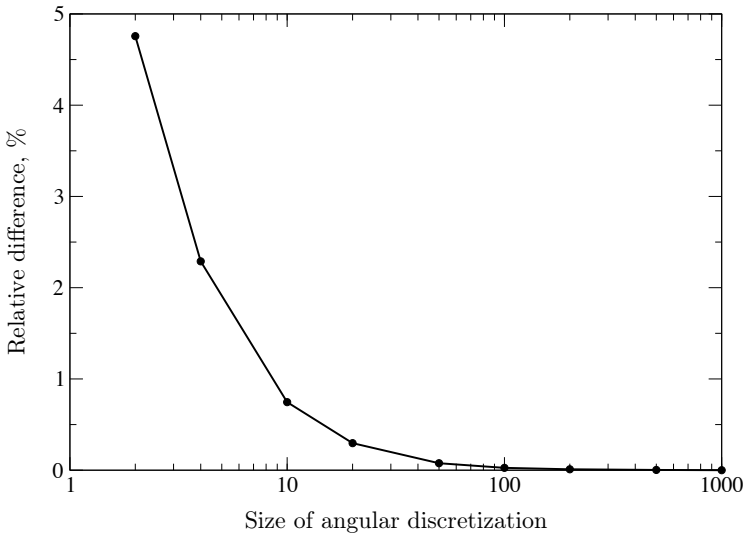

Figure 6.4.: *Difference in computed wall radiative flux versus different sizes of the angular discretization with 1000 angular points taken as reference. Flow field taken from the Fire II* 1634 s *case presented in Section 7.3.1.*

p as provided by the HSNB database. The incident radiation is approximated at the slab center by averaging, $\overline{G}^{\Delta\sigma}(s_{j+\frac{1}{2}}) = (\overline{G}^{\Delta\sigma}(s_j) + \overline{G}^{\Delta\sigma}(s_{j+1}))/2$.

The treatment of the angular discretization and boundary conditions are discussed in the following subsections.

Angular discretization

A uniform angular discretization is constructed via

$$\mu_i = 1 - (i - 0.5)\Delta\mu_i, \tag{6.66}$$

$$\Delta\mu_i = \frac{2}{n_\mu}, \tag{6.67}$$

where $1 \leq i \leq n_\mu$ and n_μ is number of angular points. A total of 20 points over the range $-1 \leq \mu \leq 1$ has been used for all calculations presented in this work. This choice is based on an angular grid convergence study for typical flow fields. An example convergence result is shown in Fig. (6.4) for the Fire II 1634 s case presented in Section 7.3.1. The relative precision loss on the wall radiative flux with 20 angular points is about 0.3 % when compared to a reference solution with 1000 points. This is about one order of magnitude smaller than the accuracy that can be expected with the HSNB method compared to full LBL results. Thus, 20 points is a reasonable choice for the angular discretization.

Reflecting boundaries

The boundary condition in Eq. (3.5) is discretized as

$$\overline{I}_\sigma^{\Delta\sigma}(s_1, \mu_j) = \epsilon_1 \overline{I}_\sigma^{b\,\Delta\sigma}(T_1) + \frac{1-\epsilon_1}{\pi} \sum_{\mu_i<0} \overline{I}_\sigma^{\Delta\sigma}(s_1, \mu_i)\,|\mu_i|\,\Delta\mu_i, \qquad \mu_j > 0, \tag{6.68}$$

$$\overline{I}_\sigma^{\Delta\sigma}(s_n, \mu_j) = \epsilon_2 \overline{I}_\sigma^{b\,\Delta\sigma}(T_2) + \frac{1-\epsilon_2}{\pi} \sum_{\mu_i>0} \overline{I}_\sigma^{\Delta\sigma}(s_n, \mu_i)\,|\mu_i|\,\Delta\mu_i, \qquad \mu_j < 0, \tag{6.69}$$

where ϵ_1 and ϵ_2 are the emissivities of the first and second wall respectively. These equations represent a coupling between the outgoing intensity of each wall through reflection of the incoming

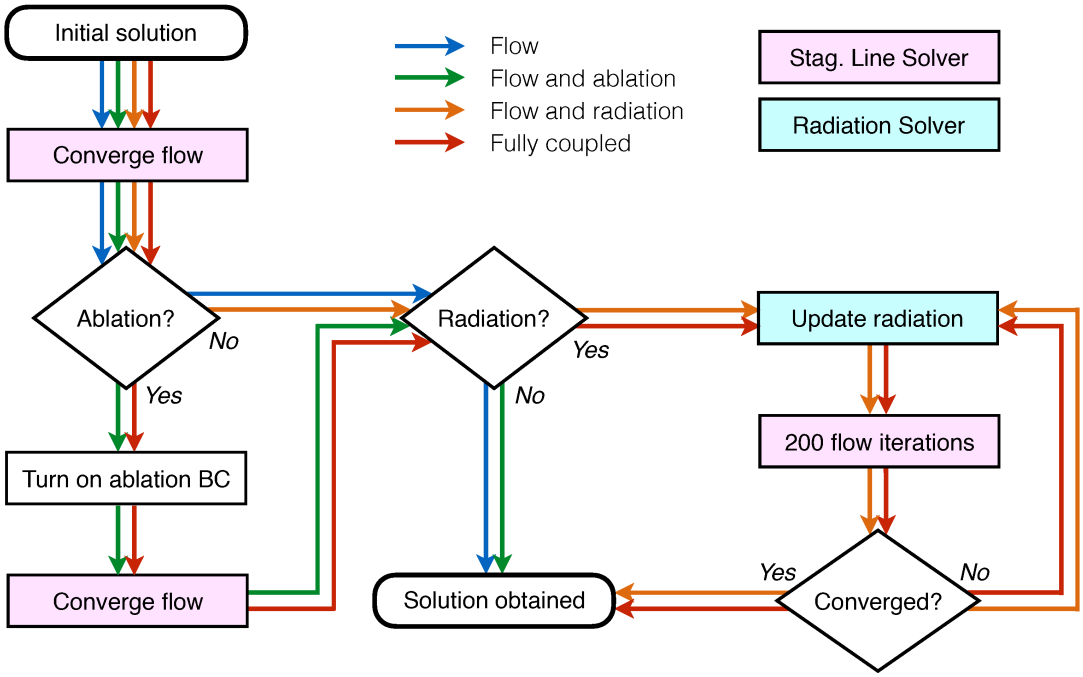

Figure 6.5.: *Flowchart representing the strategy used for each type of coupling considered in this work.*

intensity. When one or both walls in Fig. (6.2) are treated as reflecting boundaries, the outgoing average intensity at the walls is solved iteratively. The process begins by initializing the outgoing intensities using black walls at the wall temperatures. Eqs. (6.68) and (6.69) are then evaluated to update the outgoing intensities at each wall. This process is repeated until the outgoing intensities differ between successive iterations by less than $10^{-6}\,\mathrm{W/cm-sr}$ in each narrow band. Typically, this condition was met after only two iterations for the cases presented in this work.

6.4. Coupling Strategies

Four different coupling strategies are considered in Chapter 7: flow only, coupled flow and radiation, coupled flow and ablation, and fully coupled. This section describes how each coupled solution type is obtained using the stagnation line flow solver and radiation transport codes presented in the previous sections. An overview of each coupling strategy is shown in Fig. (6.5).

Uncoupled

When radiation and ablation are both ignored, the stagnation line code is used to solve the DNRS equations presented in Section 6.2.1 with $\mathbf{S}^r = 0$ and an isothermal, non-catalytic, and no-slip boundary condition. The solution is iterated implicitly from an initial solution until a steady state solution is obtained using the methods described in Section 6.2.2. The convergence criteria used in this thesis for all solutions is a drop in the initial residual by six orders of magnitude.

Coupled flow and radiation

When radiation coupling is considered the radiative source terms are added explicitly to the previous algorithm. The radiative source terms are updated typically every 200 flow iterations using the code described in Section 6.3.2. Starting from an uncoupled solution, time integration is performed until steady state is reached. In order to reduce the computational time, radiative calculations are carried out on a coarse mesh in which the convective cells are grouped by five based on an

extensive grid convergence analysis. Finally, radiative source terms are linearly interpolated from the cell centers of the radiation mesh to the cell centers of the flow mesh.

Coupled flow and ablation

Ablation coupling is obtained via the steady-state ablation boundary condition described in Section 6.2.3. Starting from an uncoupled solution, a new solution is converged with the updated boundary condition. The uncoupled flow solution is first obtained considering only the species relevant to the shock layer chemistry. Once converged, the additional products of ablation and pyrolysis are added to the mixture and initialized with negligible densities. The chemical mechanism is also updated accordingly. This solution is then used as the initial conditions for coupled flow and ablation calculation.

Fully coupled

Fully coupled solutions are obtained using a mix of the partially coupled methods described above. An uncoupled solution is first obtained and used as initial conditions for a coupled ablation solution. This solution is then used as the initial conditions for the fully coupled solution. Computing intermediate solutions in this way helps to avoid numerical difficulties associated with trying to compute the radiative source terms and ablation boundary condition before the shock and boundary layers have developed.

6.5. Concluding Remarks

This chapter presented the numerical tools developed to study coupled flow, radiation, and ablation effects for atmospheric entry flows. The focus was placed on modeling the stagnation streamline in an effort to maximize the fidelity of the phyiscochemical models and coupling strategies. Three codes have been developed to model flow and radiative transfer along the stagnation line.

The dimensionally reduced Navier-Stokes equations for multicomponent, reacting, and radiating flows along the stagnation streamline were presented. The equations have been discretized in space using a second-order FV method and their steady-state solution via the method-of-lines was also presented. Ablation coupling is achieved through a steady-state ablation boundary condition.

Radiation coupling is treated explicitly. Two treatments of the RTE have been considered: 1) a full LBL solution using spectra produced by the HTGR database discussed in Chapter 3, and 2) solution via the HSNB methodology. Both solutions make use of the tangent-slab approximation for the three-dimensional geometry of the radiation field ahead of the vehicle. An analytical treatment of the angular integration via exponential integrals is used for the LBL case in order to significantly reduce the solution cost. It was shown that this is not possible when the HSNB model is used, due to the non-Beerian nature of the SNB approximation. Instead, numerical integration is performed on a discretized angular domain and it was shown that 20 angular points provides sufficient accuracy, based on a grid convergence study.

Finally, four coupling strategies are envisaged: no coupling, coupled flow and ablation, coupled flow and radiation, and fully coupled. The methodology used for each strategy has been presented. While it was not discussed in this chapter, it is important to mention that the codes developed in this work have been verified against other numerical solutions [72, 289]. The tools developed in this chapter are used in Chapter 7 to study several atmospheric entry vehicles.

CHAPTER 7

Applications and Results

7.1. Introduction

Previous chapters have been dedicated to the description of the physico-chemical models and algorithms developed in this thesis for atmospheric entry simulations. In this chapter, several applications are presented in which the HSNB methodology is analyzed in terms of its overall accuracy and efficiency. The model is then used to study the effects of flow-radiation and flow-radiation-ablation coupling on the predicted convective and radiative heating to different atmospheric vehicles using the numerical tools developed in the previous chapter.

Two key questions regarding the use of the HSNB method are addressed, namely

1. How does the HSNB model compare to LBL results for flight conditions relevant to atmospheric entry?
2. What is the cost/benefit analysis in terms of speed and accuracy of the adaptive HSNB method presented in Chapter 3 as compared to the high-resolution HSNB method?

The effects of coupled flow, radiation, and ablation are discussed, based on stagnation line simulations of real flight vehicles. Finally, the various conclusions drawn in this chapter are summarized in the last section.

7.1.1. Vehicles and Flight Conditions

This section details the various vehicles and flight conditions considered in the rest of the chapter. A summary of the different flight conditions is presented in Table 7.1 for each vehicle. In addition, the specific thermodynamic, transport, and chemistry data used for each of the mixtures presented in the following sections is summarized in Appendix D.

Fire II

The Fire II vehicle was the second of two early successful reentry flight tests conducted during the Apollo era in order to help reduce uncertainties in the predicted aerothermal environment surrounding the Apollo reentry capsule. Launched on May 22, 1965, Fire II reentered Earth's atmosphere with a velocity of 11.35 km/s at a flightpath angle of $-14.7°$. The Fire reentry package consisted of a blunt spherical forebody with a conical afterbody as shown in Fig. (7.1) and flew with a nominal 0° angle of attack. The forebody was constructed of three beryllium calorimeter shields designed to be ejected before reaching their melting point. Each shield was sandwiched between phenolic-asbestos insulation layers for protection until the desired exposure times. Thus, Fire II data is split into three distinct data-gathering periods, each with a different nose radius. A series of sensor plugs embedded with thermocouples provided in-depth temperature profiles of each beryllium shield allowing estimation of the surface temperature of the stagnation region during each data-gathering period [290]. In addition, three total radiometers provided integrated intensities over a wavelength range of 0.2 µm to 4.0 µm at the stagnation point and two off-axis locations [291]. A spectral radiometer was also located at the stagnation point, providing a 0.004 µm wavelength resolution from 0.3 µm to 0.6 µm.

Table 7.1.: *Conditions for the vehicle trajectory points considered in this work. Altitude h, equivalent sphere radius of the vehicle R_0, wall temperature T_w and free stream conditions (temperature T_∞, velocity u_∞, total mass density ρ_∞ and mass fractions y_∞).*

Atmosphere y_∞ [%]	Vehicle	Flight Time s	h km	R_0 m	T_w K	T_∞ K	u_∞ km/s	ρ_∞ kg/m^3
Earth	Fire II	1634.0	76.42	0.935	615.0	195.0	11.36	3.72×10^{-5}
77.6 - 23.3 (N_2-O_2)		1642.66	53.87	0.805	480.0	273.0	10.56	7.17×10^{-4}
		1645.0	48.40	0.805	1520.0	285.0	9.83	1.32×10^{-3}
	Apollo 4	30 032.0	59.79	2.85	2500.0	246.04	10.25	3.41×10^{-4}
Titan	Huygens	189.0	273.2	1.25	2000.0	176.6	5.13	2.96×10^{-4}
98.84 - 1.16 (N_2-CH_4)		191.0	267.9	1.25	1000.0	183.0	4.79	3.18×10^{-4}

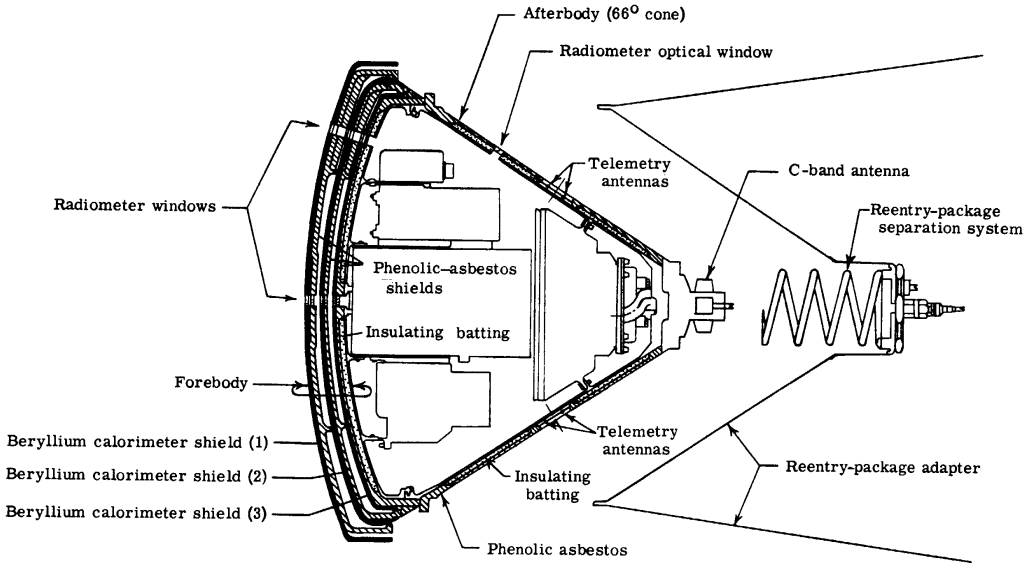

Figure 7.1.: *Schematic of Fire II entry vehicle from [290].*

Three trajectory points of the Fire II reentry are considered in this chapter, corresponding to the first two data-gathering periods. A summary of the free-stream flow parameters at each trajectory point is presented in Table 7.1. Since the forebody of Fire II was spherical, the exact nose radius is used for the stagnation-line simulations presented in the following sections. The 11-species, two temperature, air mechanism by Park [69] is used to model the flow field chemistry. A description of the reactions and their rate constants are provided in Table D.2. The EM2C-HTGR database has been used for the calculation of spectral emission and absorption coefficients, both for the LBL and HSNB calculations. The contributions of 19 diatomic systems of N_2, N_2^+, NO, and O_2 as listed in Table 3.1 have been included in the calculations, as well as atomic lines of N, O, N^+, O^+, and continuum processes.

Apollo 4

Apollo 4 was the first all-up unmanned flight test of the Saturn V rocket and Apollo vehicle. The flight test was conducted on November 9, 1967, and was designed to test many of the onboard systems during real flight conditions, including a test of the Apollo heat shield at simulated lunar return speed and angle. To this day, the flight test remains one of only a hand-full of successful flights of a fully instrumented heat shield into Earth's atmosphere, providing valuable flight data which can be used to validate computational tools.

The Apollo 4 command module was a 33° sphere-segment with a nose radius of 4.69 m and at peak heating conditions, flew at an angle of attack of 25° [5]. Peak radiative heating occurred 30 032 s after launch during reentry at an altitude of 59.79 km and with a velocity of 10.252 km/s [292]. The free-stream density was determined by Ried *et al.* [292] to be $3.41 \times 10^{-4}\,\mathrm{kg/m^3}$ based on pressure measurements onboard which results in a free-stream temperature of about 246 K. At these conditions, Park [278] determined an equivalent sphere radius of 2.85 m to reproduce the shock standoff distance measured by Ried *et al.* [292] using Schlieren imagery. In addition, Park [278] assumed a fixed wall temperature of 2500 K which will also be used in this analysis. Finally, the TPS material is assumed to have a virgin to char density ratio of $\rho_v/\rho_c = 2$ and an emissivity value of $\epsilon = 0.85$ following Johnston *et al.* [16].

The air mechanism presented for the Fire II vehicle above has also been used for all Apollo 4 simulations when ablation is not considered (uncoupled and flow-radiation coupling). When ablation is considered, the air mechanism has been supplied with additional species relevant to carbon-phenolic ablation and pyrolysis, namely C, C^+, H, H^+, C_2, C_2H, C_3, CO, CO_2, CN, HCN,

and H_2. To reduce the number of species considered, the minor air species N_2^+, O_2^+, and NO^+ are neglected, making the total number of species 20. The resulting reaction mechanism is given in Table D.3. Lastly, all of the available radiative mechanism listed in Table 3.1 corresponding to the 20 species air-ablation mechanism have been considered.

Huygens

The Huygens probe, developed by the European Space Agency (ESA), successfully landed on the surface of Titan, one of Saturn's moons, on January 14, 2005. The probe was designed to spend a few hours in the Titan atmosphere to study its composition and gather other important data [293] as it descended to the surface. Huygens entered the Titan atmosphere with a relatively low velocity of 6.2 km/s. The reentry vehicle geometry was comprised of a 60° half-angle sphere-cone forebody with a diameter of 2.7 m and nose radius of 1.25 m. The nominal angle of attack was 0°. The forebody heatshield comprised of a small layer of AQ60, a phenolic-silica ablator. Since the angle of attack was 0°, the nose radius of 1.25 m has been used in this work as the equivalent sphere radius.

The nominal Titan atmosphere is about 98.4 % N_2 and 1.4 % CH_4 by volume (as measured by Huygens [293]). Small amounts of CN are created in the shock-heated gas which can produce significant radiative heating. The Huygens entry is therefore interesting from a radiation modeling standpoint due to the strong molecular radiation emitted by the CN violet and red systems. In addition, it has been shown that thermal nonequilibrium effects play an important role, namely the non-Boltzmann population of the CN(B) state during the early trajectory points significantly reduces the predicted radiative heating [7, 294].

For the trajectory points considered in this work (Table 7.1), thermal nonequilibrium effects are weak and ionization is insignificant. A mixture of 13 species (N, C, H, N_2, C_2, H_2, CN, NH, CH, CH_2, CH_3, CH_4, HCN) at thermal equilibrium is envisaged. Chemical reactions and rates are taken from the work of Gokcen [295] and are presented in Table D.4. The electronic band systems of N_2 (Birge-Hopfield 1 and 2, Worley-Jenkins, Worley, Caroll-Yoshino), CN (violet, red, LeBlanc), and C_2 (Philips, Mulliken, Deslandres-D'Azambuja, Ballik and Ramsay, Fox-Herzberg, Swan) (presented in Table 3.1) have been considered for the coupled calculations.

7.2. Accuracy and Efficiency of HSNB Model

This section analyzes the accuracy and efficiency of different aspects of the HSNB model including the LBL spectral grid adaptation schemes for atomic lines and the difference between the Curtis-Godson and Lindquist-Simmons methods for computing mean black equivalent line widths. The aim is to understand the accuracy of the HSNB methodology, compared to reference LBL results for uncoupled simulations over a variety of flight conditions. The lessons learned in this section are then applied to the following sections for coupled simulations.

7.2.1. Adaptive HSNB

In Section 3.4.3, two algorithms were introduced for generating an adaptive spectral mesh for the LBL treatment of atomic lines in the HSNB method. The first consisted of a fixed 11-point stencil based on the Voigt half-width of each atomic line. The second extended this methodology by bisecting the areas between lines in order to better capture line wing regions. In this section, the accuracy and efficiency of both algorithms are compared to full LBL results (including the treatment of molecular lines) for realistic flow fields. LBL solutions are obtained using a fixed spectral mesh, consisting of 4 420 667 points spaced logarithmically from a spacing of $0.01\,\mathrm{cm}^{-1}$ at $1000\,\mathrm{cm}^{-1}$ to a spacing of $0.12\,\mathrm{cm}^{-1}$ at $200\,000\,\mathrm{cm}^{-1}$. In order to quantify the error in the HSNB approximation without an adaptive spectral mesh, an additional HSNB case is considered, in which the spectral mesh used for atomic lines is taken to be the high resolution spectral mesh used for the full LBL case. This method will be denoted as HSNB Hi-Res.

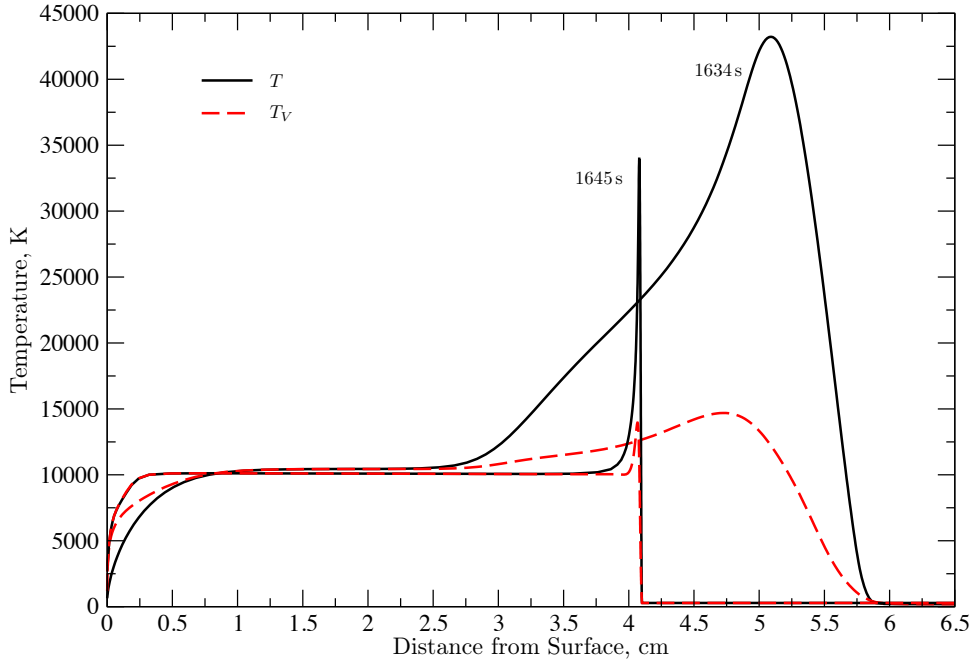

Figure 7.2.: *Simulated temperature profiles along the stagnation line of the Fire-II vehicle.*

The Fire II flight experiment [290, 291] has been widely used to validate and compare coupled and uncoupled flow/radiation simulations [40, 55, 296] for two primary reasons: (i) the flight conditions provide both strong thermochemical nonequilibrium and equilibrium conditions in the shock layer, and (ii) (perhaps more importantly) there is little other flight data to be used for such purposes. For these reasons, the Fire II conditions will also be used here. Specifically, the 1634 s and 1645 s trajectory points have been considered since they produce strong thermochemical nonequilibrium and equilbrium flow fields.

The computed stagnation line temperature distribution for both trajectory points are shown in Fig. (7.2). It is clear from the figure that a significant thermochemical nonequilibruim exists at 1634 s in the shock and boundary layer regions due to the low free stream density. However, by 1645 s, the density has risen two orders of magnitude, causing the shock layer to be nearly in thermal equilibrium.

Fig. (7.3) shows a comparison of the radial and stagnation point radiative heat fluxes for the 1634 s trajectory point. The radial heat flux is defined as the net radiative flux in the direction away from the surface and is given by Eq. (6.57) for the LBL case and Eq. (6.63) for the HSNB cases. Therefore, a negative radial flux indicates the flux is towards the vehicle. The stagnation point radiative flux is plotted in Fig. (7.3) as positive going into the body for convenience. The radial heat flux profile appears as expected, with emission in the hot shock layer into the free stream and boundary layer. All of the HSNB results compare reasonable well with that of the LBL solution, but over-predict the heat flux at the stagnation point. The HSNB with high resolution and bisection grid results are essentially the same, showing better agreement with the full LBL solution than the HSNB 11 point fixed stencil mesh.

The spectral wall directed heat flux shown in Fig. (7.3) shows the contribution of the error in the total stagnation point radiative heat flux due to each wavenumber band. Note that a significant portion of the differences between the fixed stencil and the other methods occur in the higher wavenumber region between 50 000 cm^{-1} to 100 000 cm^{-1}. This is due to the fact that the radiative flux in the VUV region is dominated by a few strong atomic lines. For strong lines, the line wing regions contribute significantly to the radiative transfer. With the fixed point stencil, the far line wing regions are not well resolved as previously discussed in Section 3.4.3.

The same comparison is made for the 1645 s trajectory point in Fig. (7.4). Note that the radial

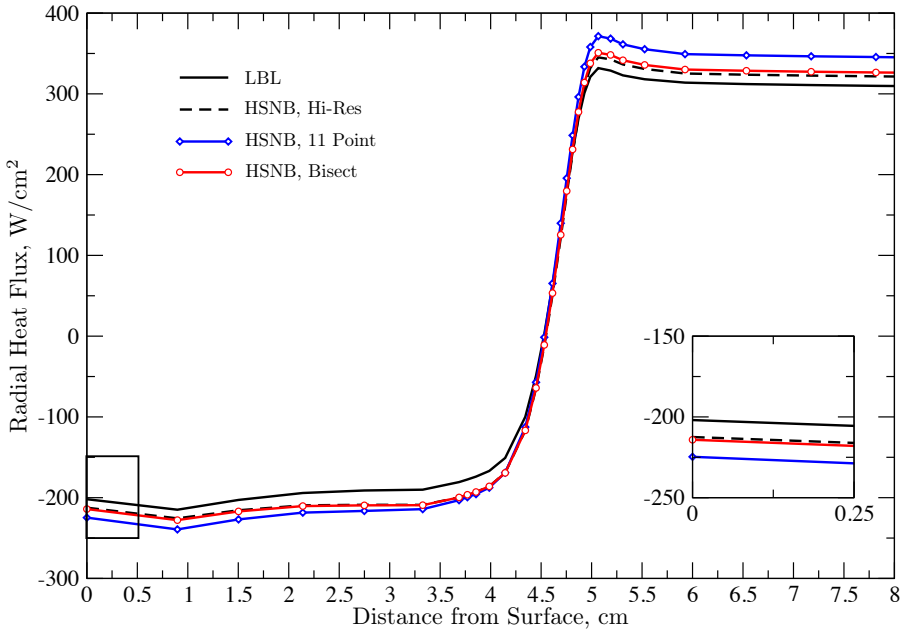

(a) *Heat flux.*

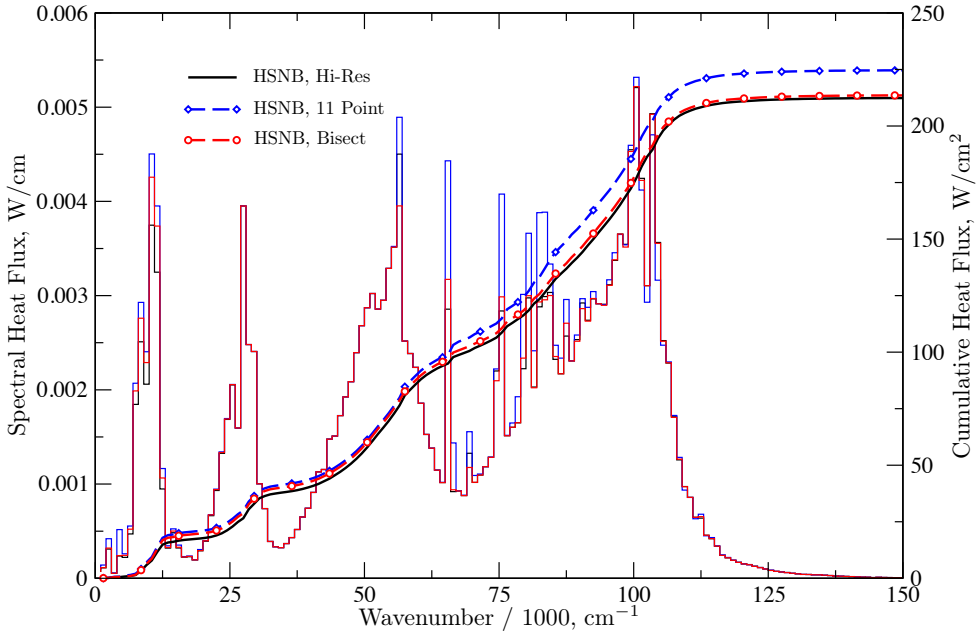

(b) *Wall directed heat flux.*

Figure 7.3.: *Comparison of radiative heat fluxes for the 1634* s *case obtained using different methods.*

flux field has a slightly different behavior than in the 1634 s case due to the thin shock region. Again, the results obtained with HSNB using the high resolution spectral mesh and that obtained using the bisection algorithm have excellent agreement with the full LBL solution. However, the fixed point adaptive mesh yields significant errors in the radial flux field. The spectral flux obtained at the stagnation point shows why. Unlike the 1634 s case, which was at a relatively low pressure condition, the 1645 s has a significant Lorentz broadening of the atomic lines. Increased broadening leads to more significant self absorption in the line centers, further magnifying the contribution of

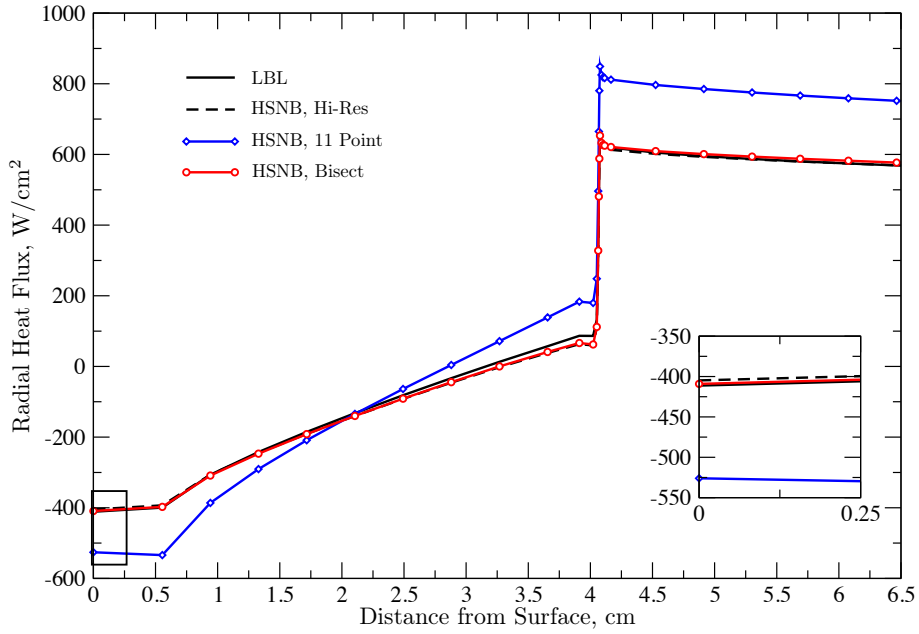

(a) *Heat flux.*

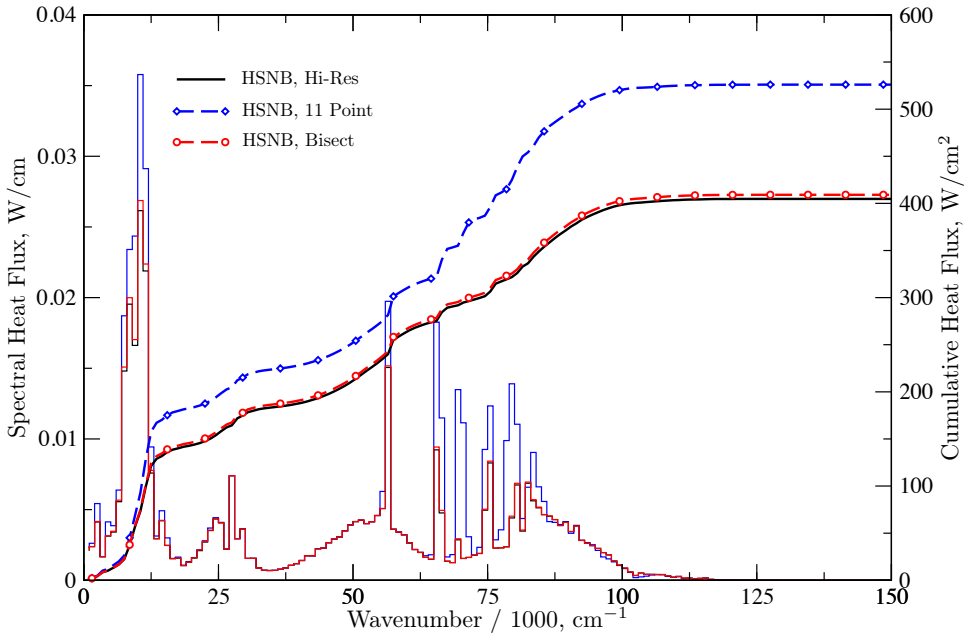

(b) *Wall directed heat flux.*

Figure 7.4.: *Comparison of radiative heat fluxes for the 1645* s *case obtained using different methods.*

the line wings to the radiative transfer. Thus, poorly resolved line wings with the fixed point mesh results in significant errors in the radiative flux.

Table 7.2 summarizes the results for each of the methods at both trajectory points, including errors in the calculated wall heat flux, and the CPU time required to compute the radiative flux, relative to the time with the bisection method. The CPU time required for the full flux calculation is two orders of magnitude less for the adaptive HSNB methods compared to the LBL solution, while the high-resolution HSNB model allows a one order of magnitude reduction. In practice,

Table 7.2.: *Timing and error statistic comparison for adaptive HSNB methods for the uncoupled Fire II* 1634 s *and* 1645 s *cases. CPU times are relative to that obtained with the HSNB-Bisect method and were obtained using a single processor. The number of spectral grid points per atomic line is based on the total 3,333 atomic lines included in the database for N, O, N^+, and O^+, though not all lines fall within the considered spectral range of* $1000\,\mathrm{cm}^{-1}$ *to* $200\,000\,\mathrm{cm}^{-1}$.

Trajectory Point	Method	Spectral Grid Size	Points per Atomic Line	Relative CPU Time	% Spectra	% Integration	$\frac{q_{r,\mathrm{wall}}-q_{r,\mathrm{wall}}^{\mathrm{LBL}}}{q_{r,\mathrm{wall}}^{\mathrm{LBL}}}$, %
1634 s	LBL	4,420,667	-	146.7	99.0	1.0	-
	HSNB, Hi-Res	4,420,667	1,326.3	21.7	59.2	40.8	5.2
	HSNB, 11 Point	33,735	10.1	0.96	14.9	85.1	11.3
	HSNB, Bisect	40,976	12.3	1.00	16.8	83.2	6.0
1645 s	LBL	4,420,667	-	131.6	99.0	1.0	-
	HSNB, Hi-Res	4,420,667	1,326.3	24.7	63.0	37.0	-1.6
	HSNB, 11 Point	33,735	10.1	0.95	17.1	82.9	27.9
	HSNB, Bisect	41,669	12.5	1.00	19.3	80.7	-0.55

the adaptive HSNB methods required between 60 s to 90 s for 30 spatial grid points, while the LBL solution was completed in about 2.5 h, running on a single core of an Intel(R) Core(TM) i7-4770K CPU. Differences in CPU times for the different trajectory points are caused primarily by the assigned spectral window for each atomic line which was taken to be 10 000 times the Voigt half-width for these calculations. The 1645 s case has significantly more Lorentz broadening of the atomic lines, which increases the number of spectral grid points that the line shape of each atomic line must be computed over. This is reflected in the fact that the percentage of time required to compute the line spectra is proportionally more at 1645 s than at 1634 s.

It can also be seen in Table 7.2 that for the full LBL calculations, 99 % of the total CPU time is spent just generating the spectra, and only 1 % is spent performing the spatial, angular, and spectral integration. This is in large contrast to the HSNB methods which clearly tend to spend more time in the integration as the number of atomic spectral grid points is reduced. This is to be expected, when it is considered that the time required for the computation of the spectra is proportional to the product of the number of lines with the number of spectral and spatial grid points. The integration time, however, is proportional to the product of the spectral and spatial grid points only. Therefore, it is clear that since the number of lines considered is significantly lowered using the HSNB methodology (by a factor of ≈ 1000), a significant amount of the overall reduction in CPU time is due to the spectral property calculation. It should also be noted that the HSNB formulation does not permit the use of the E_n integral exponential functions to "analytically" perform the angular integration in the tangent slab formulation as is typically done in most RTE solvers. Therefore, there is an additional cost required to compute the angular integration included in the HSNB results. This additional complexity and cost is justified when the overall CPU cost requirements are considered.

Finally, the accuracy of the adaptive HSNB methods are compared to LBL. The relative percent difference of the stagnation point radiative heat flux between the HSNB solutions and that of the LBL calculations are given in the last column of Table 7.2. In all cases the high resolution HSNB result provides a very good estimate of the full LBL heat flux, with a maximum error of just 5.2 %. For the fixed point adaptive grid, the HSNB formulation provides a reasonable result for the 1634 s case with an 11.3 % difference from LBL results. However, there is a 27.9 % difference observed for 1645 s, which is likely not acceptable for most applications. When the fixed point mesh is augmented with the bisection method, this error is seen to disappear, and the adaptive mesh provides a flux estimate close to the high resolution HSNB formulation. Interestingly, this adaptive approach provides an even better estimate to the LBL solution than the high resolution spectral mesh for the 1645 s case. However, since the total error is less than 1 %, it is assumed that this was just a lucky outcome, and that the high resolution and adaptive HSNB methods should be considered to provide essentially the same results. Therefore, the bisection method will be used throughout the remainder of this chapter where ever the HSNB method is considered.

7.2.2. Curtis-Godson versus Lindquist-Simmons

For a homogeneous optical path, analytical expressions can be derived for the mean black equivalent width $\overline{W}/\delta$ introduced in Eq. (3.55) for mean transmissivity calculations. These expressions depend on the broadening mechanism and a prescribed distribution law for line intensities within the narrow band and are functions of two parameters: a mean absorption coefficient $\overline{k}$ and an overlapping parameter $\overline{\beta}$.

For a non homogeneous optical path, the Curtis-Godson approximation consists in using the expressions derived for homogeneous media with averaged parameters $\overline{ku^*}$ and $\overline{\beta^*}$ that we define according to

$$\overline{ku^*} = \int_{s'}^{s} p(s'')\overline{k(s'')}ds'', \tag{7.1}$$

$$\overline{\beta^*} = \frac{1}{\overline{ku^*}} \int_{s'}^{s} \overline{\beta(s'')}p(s'')\overline{k(s'')}ds''. \tag{7.2}$$

Expressions of the mean black equivalent width $\overline{W_L(s',s)}/\delta$ and $\overline{W_D(s',s)}/\delta$ for both Lorentz and

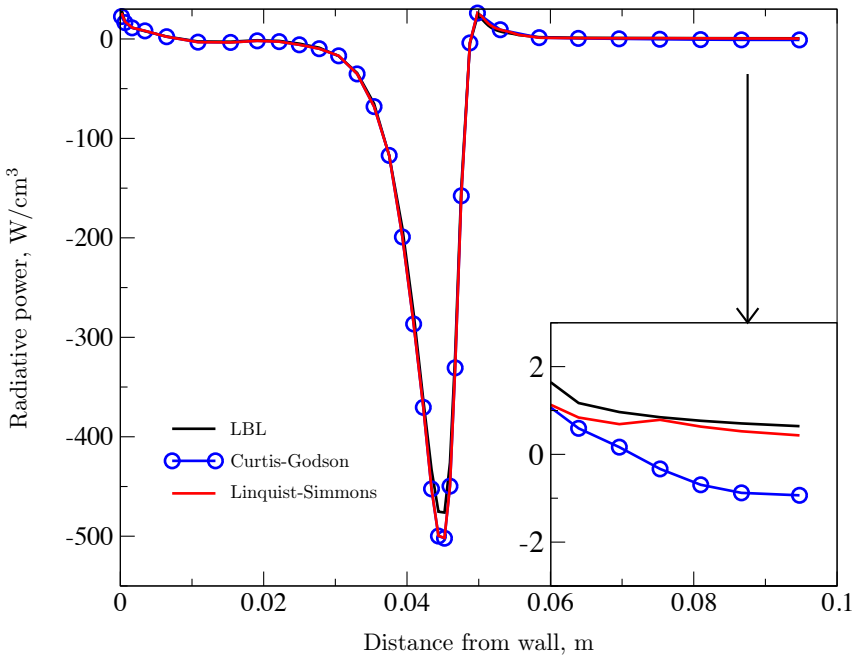

Figure 7.5.: *Radiative power comparison between Curtis-Godson and Lindquist-Simmons approximations for the Fire II* 1634 s *test case.*

Doppler broadening are given in Table 3.2. Eq. (3.57) is used to obtain the mean black equivalent width in the Voigt broadening regime, as proposed by Ludwig *et al.* [158].

An alternative approach for treating non-uniform optical paths is the Lindquist-Simmons approximation [159]. It consists in finding an expression for the space derivative of the mean black equivalent width and then integrating it over the path in order to get the mean transmissivity

$$\overline{\tau_\sigma(s',s)}^{\Delta\sigma} = \exp\left(\frac{1}{\delta}\int_{s'}^{s}\frac{\partial\overline{W(s'',s)}}{\partial s''}ds"\right). \tag{7.3}$$

The expressions of $\partial\overline{W_L(s'',s)}/\partial s''$ and $\partial\overline{W_D(s'',s)}/\partial s''$ for Lorentz and Doppler broadening used in this work are given in Table 3.3. They involve both local parameters $\overline{k(s'')}$, $\overline{\beta(s'')}$ and averaged parameters $\overline{ku}^*$, $\overline{\beta}^*$. After the spatial integration, Eq. (3.57) is used to get the mean black equivalent width in the Voigt regime, as is done in the Curtis-Godson approach.

A comparison between the HSNB Curtis-Godson and the HSNB Lindquist-Simmons is given in Fig. (7.5) for the Fire II (1634 s) test case. The difference between the two approximations is very tiny and for most of the points is much lower than the difference between HSNB Lindquist-Simmons and LBL calculations. However, we can see a much larger discrepancy in the free stream, where the radiative power predicted by the HSNB Curtis-Godson model becomes negative while it remains positive for the HSNB Lindquist-Simmons and LBL models. A negative energy source term in this cold region is a major computational issue for coupling as negative temperatures can be predicted after a few iterations. Therefore, the Lindquist-Simmons approximation has been chosen for all coupled simulations presented in this work, though it requires around three times more computational time.

7.2.3. Comparison with Smeared Rotational Band Model

In order to assess the accuracy and the efficiency of the HSNB model, a comparison with the rigorous Line-By-Line (LBL) method is carried out. In LBL calculations, radiative properties of the plasma are computed from the spectroscopic HTGR database, presented in Chapter 3, on a

Table 7.3.: *Comparison between LBL, HSNB-Weak and HSNB models for Fire II (1634 s), Fire II (1642.66 s) and Huygens (191 s) cases. Incident radiative fluxes and computational times for one radiation calculation.*

Case	Quantity	LBL	HSNB-Weak	HSNB
Fire II (1634 s)	Wall flux [W/cm^2]	146.78	151.94	150.85
	CPU time [s]	20480	41	242
Fire II (1642.66 s)	Wall flux [W/cm^2]	553.78	578.81	581.97
	CPU time [s]	19140	51	250
Huygens (191 s)	Wall flux [W/cm^2]	82.68	104.26	86.24
	CPU time [s]	13158	5	105

high resolution spectral grid of 4.4×10^6 points in order to capture correctly all the atomic and molecular lines.

It is also interesting to compare the HSNB model with the Smeared-Rotational-Band model, which is often used as a simple model to treat molecular radiation but may lead to a strong over-estimation of radiative fluxes. For this purpose, we implemented a model similar to the Smeared-Rotational-Band that will be called hereafter HSNB-Weak. It consists in computing the mean transmissivity of thick molecular systems using the simple Box model (Eq. (3.64)) instead of the SNB model described in Section 3.4.1.

For the three entry conditions described previously (Fire II (1634 s, 1642.66 s) and Huygens (191 s)), calculations have been performed with the LBL, HSNB-Weak and HSNB models from the same flow field corresponding to the coupled result obtained with the HSNB model. Table 7.3 gives the incident radiative flux at the wall, together with the total computational time for one radiation calculation, for the different combinations of models and test cases. Compared to the reference LBL solutions, the HSNB model provides an accurate prediction of the incident radiative flux, with an error between 3 and 5 % and a speed up factor around 80 for the computational time. Most of the computational gain comes from the calculation of LBL molecular spectra which is very expensive due to the large number of molecular lines.

From Table 7.3, the HSNB-Weak model provides reasonably accurate results for Earth entry with a difference of 3.5 and 4.5 % for the two trajectory points. However, for the Titan entry case, the incident radiative flux is over-predicted by 26 %. These are expected results based on a previous assessment of Smeared-Rotational-Band models in Ref. [46]. Concerning the computational times, the HSNB-Weak model is 5 times faster than the HSNB model for Earth entry cases. The Lindquist-Simmons approximation used for computing mean transmissivities over non homogeneous paths for thick molecular systems (see Section 7.2.2) is responsible for the lower computational efficiency of the HSNB model.

The spectral and cumulated incident radiative fluxes at the wall are displayed in Fig. (7.6) for the early trajectory point (1634 s) of the Fire II experiment. It can be seen that the complex structure of the LBL spectral flux is correctly captured by both HSNB and HSNB-Weak models, with a good agreement on the total cumulated flux (see Table 7.3 for numerical values). The incoming radiation mostly arises from molecular and atomic transitions in the Vacuum Ultraviolet. The accuracy of the HSNB model should also be assessed regarding the total radiative energy source term along the stagnation line. Fig. (7.6) also shows this distribution together with the difference with LBL calculations normalized by the absolute maximum value of the total radiative source term. The differences do not exceed 5 % for both HSNB and HSNB-Weak models. The highest discrepancies are located near the shock position, where the radiation emission is at a maximum.

The spectral and cumulated incident radiative fluxes at the wall and the total radiative source term along the stagnation line are shown for the Titan test case in Fig. (7.7). While the HSNB model reproduces with a good accuracy the LBL calculation, both the spectral flux and the total radiative source term are strongly over-predicted by the HSNB-Weak model. This failure comes from an incorrect treatment of the CN-Violet molecular system in the spectral range [25,000 -

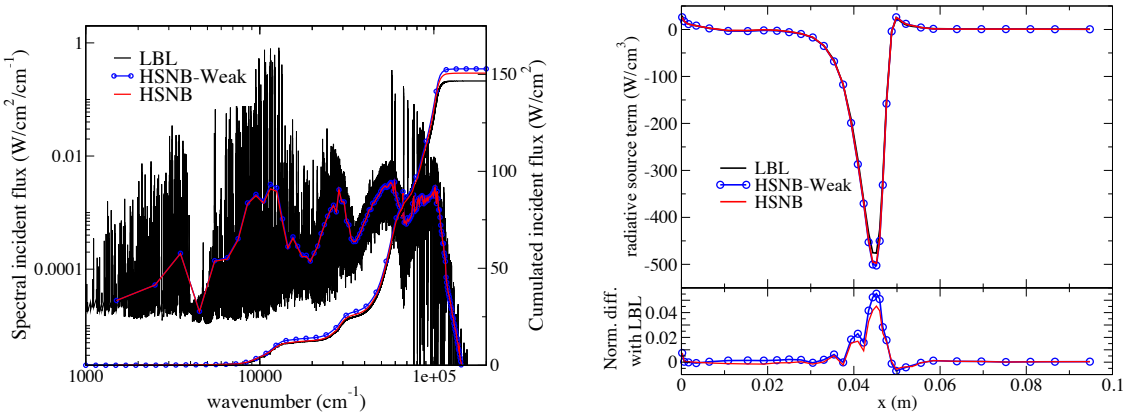

Figure 7.6.: *Fire II 1634 s. Comparison between LBL, HSNB-Weak and HSNB models. Left: spectral and cumulated incident fluxes at the wall. Right: total radiative source term along the stagnation line and differences with LBL calculations normalized by the maximum absolute value.*

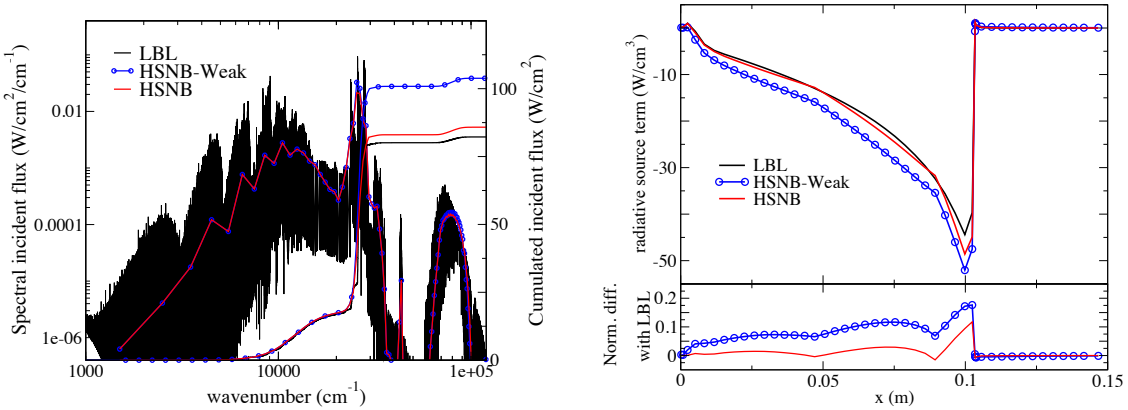

Figure 7.7.: *Huygens* 191 s. *Comparison between LBL, HSNB-Weak and HSNB models. Left: spectral and cumulated incident fluxes at the wall. Right: total radiative source term along the stagnation line and differences with LBL calculations normalized by the maximum absolute value.*

29,000 cm^{-1}]. For this case, the value of the HSNB model is clearly realized.

7.2.4. Comparison with literature results

The accuracy of the HSNB model has been assessed in the previous sections by comparison with LBL results, where both HSNB parameters and LBL radiative properties were obtained from the HTGR spectroscopic database. The purpose of this section is to compare the HSNB model with results obtained by other researchers.

Huygens (189 s)

We have considered the LBL radiation simulation of Bansal and Modest [53] of the trajectory point $t = 189$ s of the Huygens probe entry from an uncoupled flow field taken from Johnston [297] where nonequilibrium populations of the CN electronic states were considered.

In order to compare with their results we have computed the radiative source term along the stagnation line with both the HSNB model and the LBL approach. For the CN electronic states, both Boltzmann populations and nonequilibrium populations based on the QSS model of Bose et al. [298] have been taken into account. The flow field computed by Johnston [297] is reproduced in Fig. (7.8) and the comparison is shown in Fig. (7.9) for the CN red and violet systems. It can

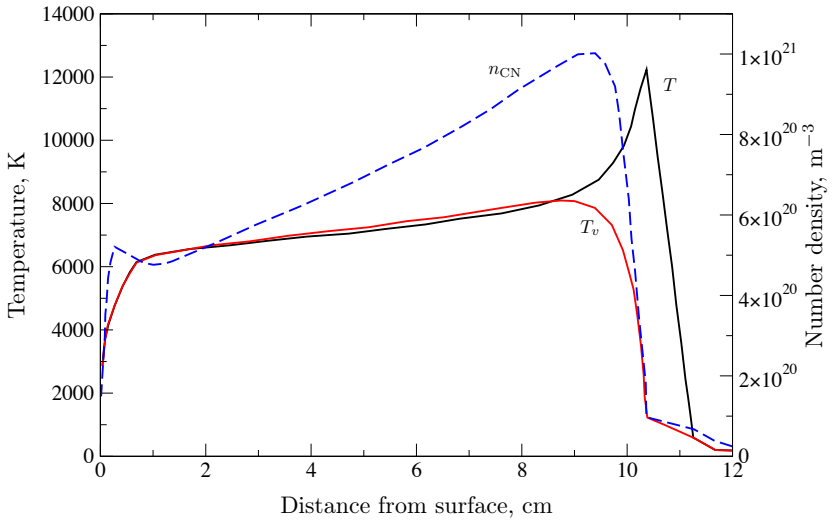

Figure 7.8.: *Flow field of Huygens stagnation line at* 189 s*, reproduced from Johnston et al. [297].*

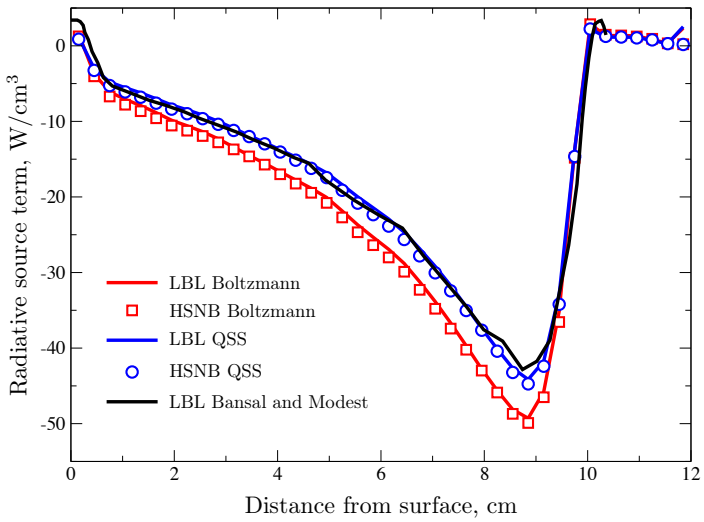

Figure 7.9.: *Huygens* 189 s*. Comparison between LBL, HSNB and LBL results from Bansal and Modest [53]. Contribution of the CN red and violet systems to the radiative source term along the stagnation line.*

be seen for a given population assumption, the LBL and HSNB results computed in this work provide similar results. When the QSS model is used, good agreement is obtained between the LBL results of Bansal and Modest [53] with both LBL and HSNB. Note that nonequilibrium effects are non-negligible in the considered simulation and lead to about 16 % difference at the peak value of the radiative source term.

7.3. Flow-Radiation Coupling

In this section, the results of coupled flow-radiation simulations obtained with the HSNB model are compared to the results of uncoupled simulations to show how radiative transfer affects the aerothermodynamic fields and heat fluxes at the wall of the vehicle. Three cases are considered, namely the 1634 s and 1642.66 s Fire II and 191 s Huygens flow fields. Flow-radiation coupling for these simulations is performed using the methodology presented in Section 6.4.

Table 7.4.: *Fire II* 1634 s. *Standoff distance* δ*, conductive flux at the wall* q_w*, radiative flux at the wall* q_w^{rad} *and incoming radiative intensity at the wall* I_w *over spectral intervals* $\Delta\sigma_1 =]16\,667\,\mathrm{cm}^{-1}$ *to* $33\,333\,\mathrm{cm}^{-1}[$ *and* $\Delta\sigma_2 =]2500\,\mathrm{cm}^{-1}$ *to* $50\,000\,\mathrm{cm}^{-1}[$*.*

Case	δ cm	q_w W/cm^2	q_w^{rad} W/cm^2	$I_w(\Delta\sigma_1)$ W/cm^{2}sr	$I_w(\Delta\sigma_2)$ W/cm^{2}sr
Uncoupled	5.36	94.9	203.6	2.05	8.57
Coupled	5.05	76.3	150.0	2.12	7.16
Coupled QSS	5.21	76.5	74.7	1.28	4.71
Flight Data	-	-	-	0.1	1.3

7.3.1. Fire II (1634 s)

The Fire II flight conditions of the early trajectory point at 1634 s correspond to a high velocity entry into a low density atmosphere (see Table 7.1). The plasma flow around the vehicle is then in strong thermal nonequilibrium that may not be correctly described by multi-temperature models [92].

In order to investigate non-Boltzmann effects, we implemented for this particular case the Quasi-Steady State (QSS) model proposed by Johnston [297]. For each radiation calculation, non-Boltzmann populations of electronic levels of N and O as well as the first electronic levels (X, A, B, C) of N_2 and N_2^+ are determined from simple correlations depending on the macroscopic state of the flow (electron temperature, total number densities). An additional assumption is made concerning N_2 VUV systems (Birge-Hopfield 1 and 2, Worley-Jenkins, Worley, Caroll-Yoshino) in which the population of the upper energy levels of these transitions, which are above the dissociation limit, are computed according to a chemical equilibrium assumption with atomic nitrogen. The non-Boltzmann populations are taken into account in the HSNB model using Eqs. (3.26) and (3.27) for atomic radiation and using expressions given by Lamet *et al.* [55] for band parameters of molecular systems. It should be underlined that this QSS model used for radiation is not consistent with the flow modeling, though it provides a first approximation of thermal non-equilibrium effects. The full consistent state-to-state coupling between flow and radiation has been recently achieved for instance in [44] for atomic electronic states.

Table 7.4 compares the uncoupled, coupled (Boltzmann, 2T), and coupled QSS results concerning the shock standoff distance, the conductive flux, and the radiative flux at the wall. The coupling effect is to decrease all of these quantities due to the radiative cooling associated with the strong radiative emission in the shock layer. The shock layer thickness decreases because the plasma density increases and the heat fluxes decrease because the temperature levels are lower. In the coupled QSS case, the same trends are obtained but to a lesser extent. Table 7.4 also shows the incoming radiative intensity at the wall over two specific spectral ranges corresponding to the experimental flight data, given with an uncertainty of 20 %. All uncoupled, coupled, and coupled QSS results are far from the flight data, although the QSS case is much closer than the two others.

Fig. (7.10) displays temperatures along the stagnation line for the uncoupled, coupled, and coupled QSS cases. The uncoupled temperature profile can be split into four regions from right to left: the free-stream, the shock, the equilibrium plateau and the boundary layer close to the wall. Because of the low density, the shock region is wide and in strong thermal nonequilibrium. In the boundary layer, T_v is slightly greater than T, because of atomic recombination which creates vibrational energy. When radiation is considered (coupled case), the temperature distributions are significantly affected. The shock layer spreads out and the equilibrium zone is shortened. Radiative cooling lowers the peak and plateau temperatures. In particular, the maximum of T_v decreases from 14 670 K (uncoupled) to 13 470 K (coupled). Another interesting feature is that the free-stream region is no longer at thermal equilibrium because the radiation absorption from the shock increases electronic and vibrational energy.

Fig. (7.10) also shows the species molar fractions along the stagnation line. For the uncoupled case, the main chemical mechanisms are the dissociation of molecular nitrogen and oxygen and

Table 7.5.: *Fire II* 1642.66 s. *Standoff distance* δ*, conductive flux at the wall* q_w*, radiative flux at the wall* q_w^{rad} *and incoming radiative intensity at the wall* I_w *over spectral intervals* $\Delta\sigma_1 = [16\,667\,\mathrm{cm}^{-1}$ *to* $33\,333\,\mathrm{cm}^{-1}]$ *and* $\Delta\sigma_2 = [2500\,\mathrm{cm}^{-1}$ *to* $50\,000\,\mathrm{cm}^{-1}]$.

Case	δ cm	q_w W/cm^2	q_w^{rad} W/cm^2	$I_w(\Delta\sigma_1)$ W/cm^{2}sr	$I_w(\Delta\sigma_2)$ W/cm^{2}sr
Uncoupled	4.06	635.6	791.3	11.65	71.01
Coupled	4.01	617.0	581.7	9.28	53.63
Flight Data	-	-	-	10.5	63.0

the ionization of atomic nitrogen and oxygen through the shock. A significant amount of nitrogen monoxide is also produced in the shock region. The ionization level is quite important in the plateau as the electron molar fraction reaches 0.15. In the boundary layer, the ionization level drops down and atomic nitrogen starts recombining. For the coupled case, the fall of the two temperatures slows down the ionization reactions and the electron molar fraction reaches a maximum of 0.08. The free-stream region ahead of the shock becomes chemically reacting under the effect of radiation: atomic oxygen is produced by photodissociation and electrons are produced mainly by photoionization of molecular oxygen.

These coupling effects on temperature and composition are also noticeable in Fig. (7.10) for the coupled QSS case, however they are much weaker. In order to understand this behavior, the radiative source term along the stagnation line is plotted in Fig. (7.11) and split according to the atomic, molecular, and continua emission contributions. From uncoupled to coupled calculations, the peak of the radiative source term is decreased by a factor two due to radiative cooling. From coupled to coupled QSS calculations, the peak of the radiative source term is further reduced and atomic contribution almost vanishes at the shock location. The reason is that the T_v Boltzmann distribution leads to an overestimation of the population of the highest electronic energy levels of atomic N and O, as well as N_2 and N_2^+. In particular, for the N_2 VUV systems, the dissociation equilibrium assumption makes the population of the upper electronic energy level associated with these systems close to zero and thus cancels their contribution to radiation. The remaining molecular emission peak in Fig. (7.11) comes mostly from NO radiation, of which electronic energy levels are assumed to be populated according to the temperature T_v. An incorrect treatment of the thermal state of NO might be responsible of the remaining discrepancies between the coupled QSS results and the flight data.

7.3.2. Fire II (1642.66 s)

The Fire 2 flight conditions of the trajectory point $t = 1642.66$ s correspond to a quasi-thermal equilibrium situation. Due to the higher density, the kinetic energy transfer between the internal energy modes is much faster than for the trajectory point $t = 1634$ s. Thus, the QSS model has not been considered in this case.

Table 7.5 shows the computed shock standoff distance and conductive and radiative flux at the wall for the coupled and uncoupled simulations. As can be seen, the standoff distance and the conductive flux slightly decrease and the radiative flux diminishes by around 25 % when radiation is coupled to the flow. In addition, coupled results are in fair agreement with flight data which are given with an uncertainty of 20 %. Temperatures and composition along the stagnation line are shown in Fig. (7.12). For the uncoupled case, the flow is in thermal equilibrium everywhere except in the shock region. A chemical equilibrium zone with flat molar fraction profiles is clearly distinguishable between the boundary layer and the shock. The electron molar fraction is around 0.07 in this zone. When radiation is considered, as for the previous trajectory point, the vibration-electronic-electron temperature T_v increases and a slight fraction of O, e^- and O_2^+ are produced in the free stream by photodissociation and photoionization of O_2. The temperature is slightly decreased in the shock layer, leading to a lower ionization level.

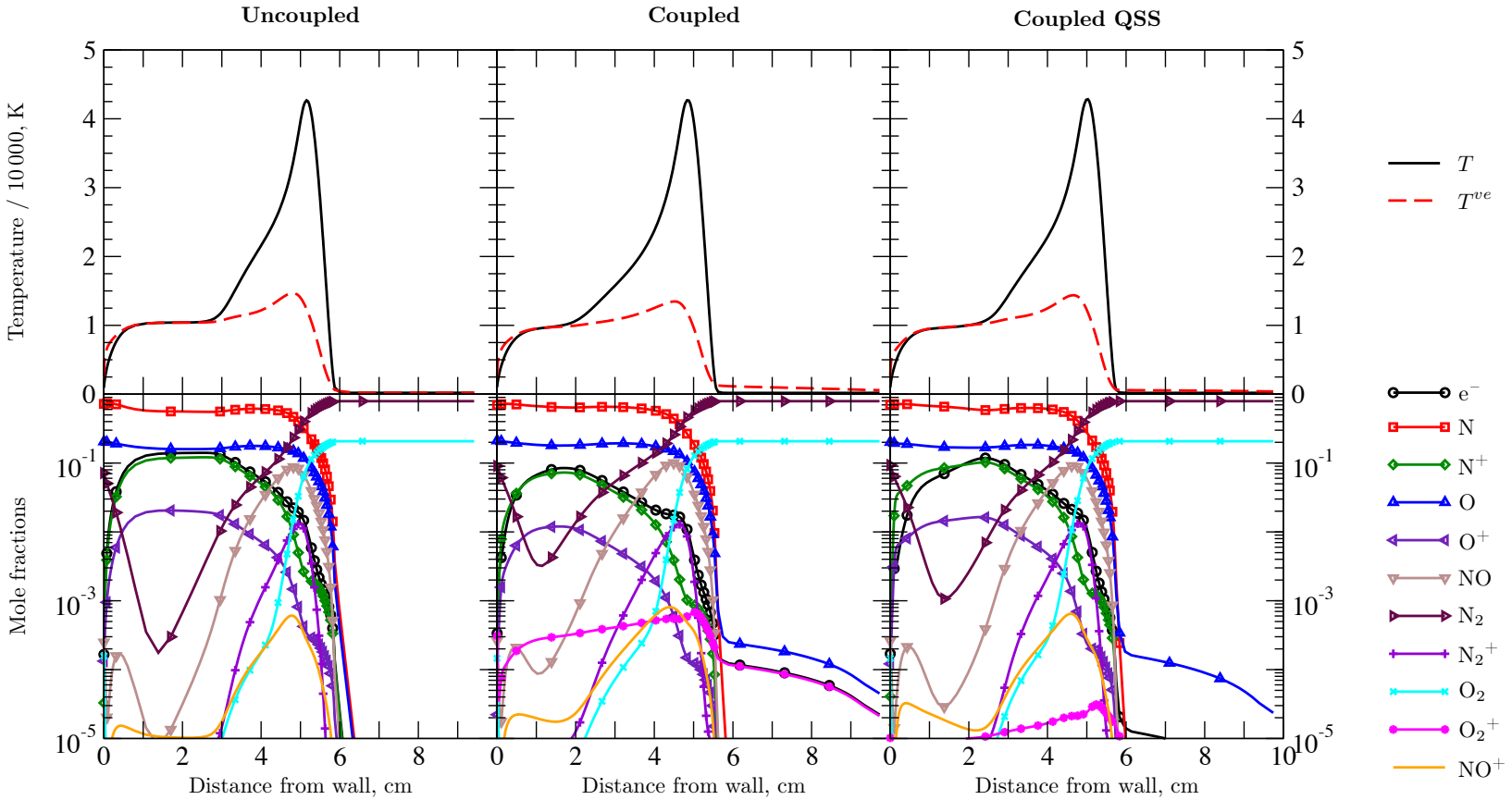

Figure 7.10.: *Fire II* 1634 s. *Temperatures and composition along the stagnation line.*

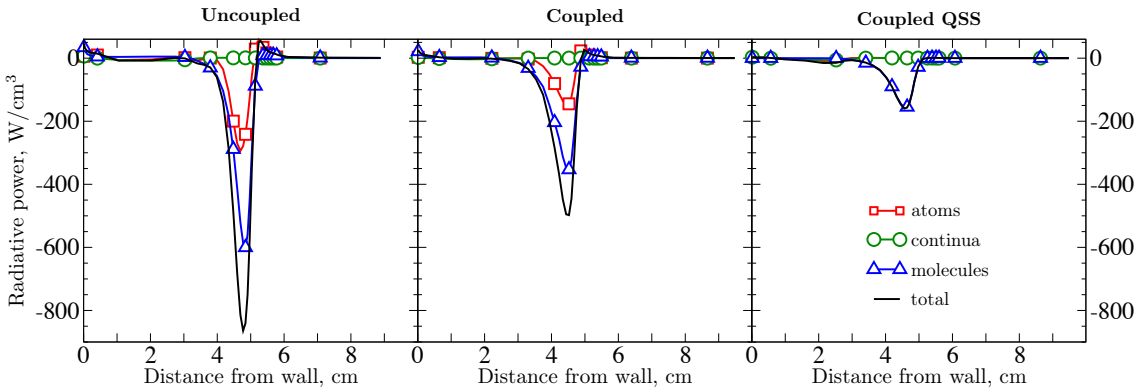

Figure 7.11.: *Fire II* 1634 s. *Total radiative source term along the stagnation line.*

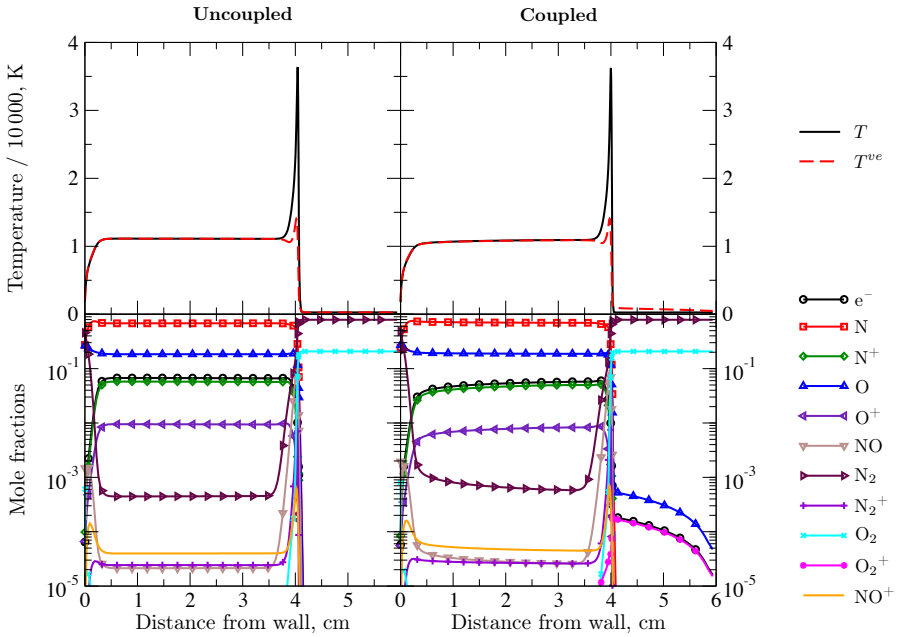

Figure 7.12.: *Fire II* 1642.66 s. *Temperatures and composition along the stagnation line.*

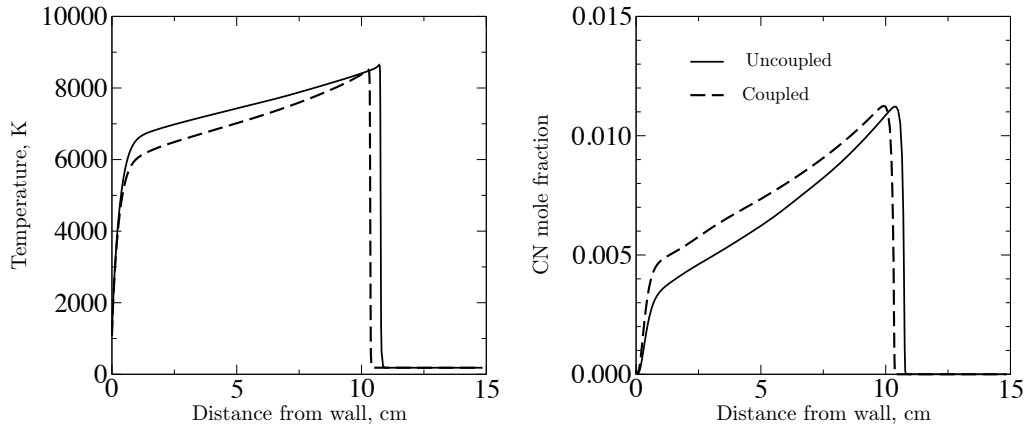

Figure 7.13.: *Huygens* 191 s. *Temperature and CN molar fraction along the stagnation line.*

7.3.3. Huygens (191 s)

This Titan entry case has been selected to show the ability of the HSNB model to handle strong optically thick molecular radiation. For early trajectory points, a state-to-state electronic specific model of the CN molecule is required [7, 297] as was shown in Section 7.2.4. As thermal nonequilibrium modeling has been already discussed for the Fire II $t = 1634$ s case, we will focus here on an quasi-equilibrium case at the trajectory point $t = 191$ s.

The temperature and CN molar fraction along the stagnation line are plotted in Fig. (7.13). In the shock layer, we can notice a lower temperature due to radiative cooling and a higher CN molar fraction because of lower dissociation rates. When coupled radiation effects are taken into account, the standoff distance decreases from 10.77 cm (uncoupled) to 10.33 cm (coupled), the conductive heat flux decreases from 24.2 W/cm^2 to 22.0 W/cm^2 and the radiative flux decreases from 95.6 W/cm^2 to 80.57 W/cm^2. The radiative flux obtained in the uncoupled case is in agreement with [294]. They found a radiative flux of 75 W/cm^2 but they applied to their results a correction coefficient of 0.75 to model the 3D effects.

The role of CN radiation, especially the CN-violet system, has been highlighted when discussing the accuracy of the HSNB model in Section 7.2.3. Indeed, it can be seen in Fig. (7.14) that the dominant contributors to radiation are the CN-violet, followed by the CN-red molecular systems. N_2 radiation also contributes significantly at the emission peak. However, C_2 radiation is weak. When radiation is coupled to the flow, the emission is reduced at the peak because of the lower temperature.

7.4. Ablation-Flow-Radiation Coupling

This section presents a study of the effects associated with the coupling between flow, ablation, and radiation. In particular, the study is aimed at carbon-phenolic thermal protection systems ablating in air.

7.4.1. Radiative Absorption by Ablation Products

Before studying the effects of coupled radiation and ablation, it is useful to first see the impact ablation products might have on the absorptivity of the boundary layer. Following Johnston *et al.* [16], a typical hypersonic boundary layer is simulated as a 1 cm constant property slab at 5000 K and 0.5 bar. The composition of the gas in the slab is computed as an equilibrium mixture with elemental mass fractions taken as a linear combination of pure air and a pure ablation product composition,

$$y_k = y_k^{\text{air}}(1-\alpha) + \alpha y_k^{\text{abl}}, \quad 0 \leq \alpha \leq 1. \tag{7.4}$$

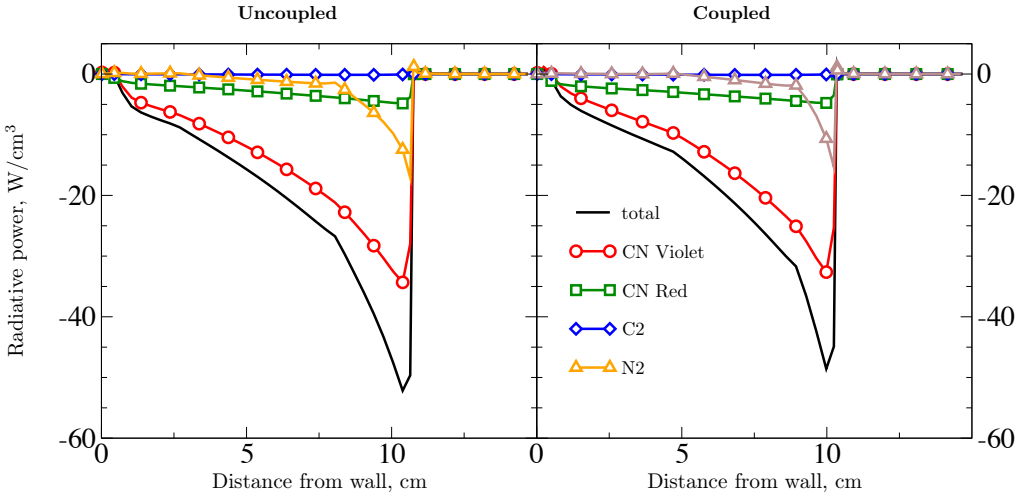

Figure 7.14.: *Huygens (191 s). Total radiative source term along the stagnation line.*

Table 7.6.: *Elemental mass fractions used to simulate a hypersonic boundary layer contaminated with ablation products based on Ref. [16].*

Gas	y_N	y_O	y_C	y_H
Air	0.76	0.24	0.0	0.0
Ablation Products	0.04	0.01	0.9	0.05

When $\alpha = 0$, a pure air composition is obtained, when $\alpha = 1$ a pure ablation and pyrolysis gas. Table 7.6 gives the elemental compositions which were used in the following analysis. The ablation gas composition is taken from [16] and roughly corresponds to a mixture of 60 % pyrolysis gas and 40 % char by volume for a linear resin with 56 % char yield with nitrogen impurities.

For reference, Fig. (7.15) shows the resulting equilibrium species mole fractions versus the α parameter for this fictitious boundary layer. When $\alpha < 0.2$, all of the carbon introduced by the ablation mixture is consumed by the available oxygen from the air mixture, producing CO. As the ratio of ablation to air mixtures increases, all of the available oxygen is consumed and the remaining carbon goes into the formation of atomic carbon, and to a lesser extent CN. Finally as α surpasses 0.5, the abundance of carbon in the slab forms pure carbonaceous species C_2 and C_3.

Fig. (7.16) shows the total mean transmissivities, $\overline{\tau_\sigma}^{\Delta\sigma}$, for several values of α for the simulated boundary layer, as well as the individual mean transmissivities, $\overline{\tau_\sigma^k}^{\Delta\sigma}$, of the major contributions to absorption for a 50 % air and 50 % ablation products mixture using the HSNB model. From the figure, it is clear that even with a small amount of carbonaceous species present, the spectral transmittance of the gas is significantly reduced in the visible and UV spectral regions. The two most absorptive molecular band systems are the CO 4$^{\text{th}}$ positive and the C_3 UV systems, however the CN Violet and Red systems as well as the C_2 Deslandres-d'Azambuja, Mulliken, and Swan systems also play an important role below 50 000 cm^{-1}. When enough carbon is present in the mixture, the gas becomes opaque in the vacuum UV due to the addition of photoionization of C atoms. It is also important to note that a significant difference in the spectral transmissivities exists between the $\alpha = 0.2$ and $\alpha = 0.5$ cases. This is because at low carbon concentrations, most of the carbon goes into forming CO and to a lesser extent, CN as shown in Fig. (7.15). As the carbon concentration increases however, a significant amount of it is used to form C atoms, and C_2 and C_3 molecules which are shown to contribute significantly to the absorptivity of the mixture. It is therefore important to accurately model the amount of carbon which enters the boundary layer in order to correctly determine the amount of radiation which may be absorbed before reaching the surface of the vehicle.

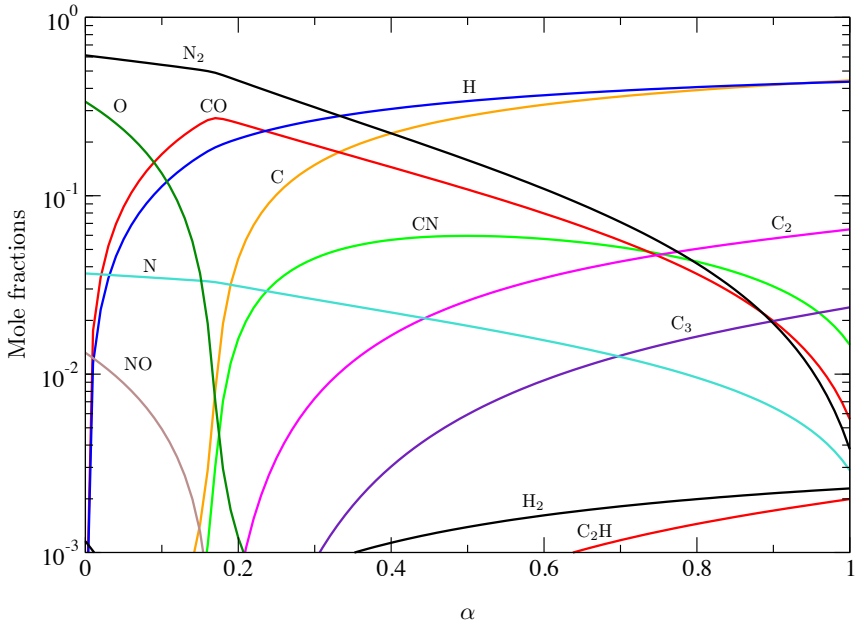

Figure 7.15.: *Equilibrium species mole fractions versus α for the elemental compositions given by Eq. (7.4) and Table 7.6 at* 5000 K *and* 0.5 atm.

7.4.2. Apollo 4 Peak Radiative Heating Analysis

The proposed model has been used to study the effects of coupled ablation and radiation phenomena occurring along the stagnation line of the Apollo 4 vehicle during atmospheric entry at peak radiative heating.

Fig. (7.17) shows the computed stagnation line temperature profiles for the four coupling strategies: flow only, flow with radiation, flow with ablation, and fully coupled. As can be seen from the figure, the dominant effect on the shock standoff distance and equilibrium temperature profile is due to the addition of the radiation source terms in the governing equations. As the energy is radiated out of the shock layer, the shock standoff distance is decreased, a phenomenon known as radiative cooling. Looking at the temperature profile in the boundary layer, it is clear that absorption of the shock layer radiation in the boundary layer, serves to increase the temperature gradient at the wall. This is most clearly seen in the case of flow and radiation coupling because the boundary layer is not being cooled by the relatively cold ablation and pyrolysis outgassing. In front of the shock, the vibrational-electronic-electron temperature is increased due to radiative absorption and photochemical processes.

Fig. (7.18) shows the effect of coupled ablation on the species concentrations in the boundary layer. As can be seen, the major products of the ablation and pyrolysis gas injection are CO, C, H_2, and H. The CO is largely formed by the oxidation reaction at the wall which consumes the incoming oxygen diffusing in from the boundary layer edge. Nitridation plays a far less import role as the CN number densities show. In fact, the CN formed by nitridation is quickly destroyed through dissociation reactions before being reproduced by several exchange reactions occurring a few mm from the surface. This behavior has been well characterized by Turchi *et al.* [287] for modeling plasmatron and arc-jet experiments with ablators. As was shown in Fig. (7.16), C_2 and C_3 can be major absorbers, however from Fig. (7.18) it is clear that the relative concentrations of those carbonaceous species is too low to make a significant impact.

Table 7.7 shows the individual components of the wall heat flux at the stagnation point of Apollo 4 using the various coupling strategies considered. Each component is related through the surface energy balance for charring ablators,

$$q_w^{\text{conv}} + \epsilon(q_{\text{in}}^r - \sigma T_w^4) - \dot{m}_g(h_w - h_g) - \dot{m}_c(h_w - h_c) - q_{\text{cond}} = 0, \tag{7.5}$$

Table 7.7.: *Components of stagnation point heat flux in* $\mathrm{W/cm^2}$ *for Apollo 4 at* 30 032 s *after launch using different coupling strategies. The wall temperature was fixed at* 2500 K *for each case.*

Coupling	$\epsilon q_{\mathrm{in}}^{r}$	$-\epsilon\sigma T_w^4$	$q_{\mathrm{w}}^{\mathrm{diff}}$	$q_{\mathrm{w}}^{\mathrm{cond}}$	$q_{\mathrm{w}}^{\mathrm{conv}}$	$-\dot{m}_g(h_w - h_g)$	$-\dot{m}_c(h_w - h_c)$	q_{cond}
Flow	279.92	−188.28	0.0	119.77	119.77	-	-	211.41
Flow / Abl.	254.74	−188.28	38.62	95.31	133.93	1.55	−5.99	195.95
Flow / Rad.	196.64	−188.28	0.0	168.42	168.42	-	-	176.78
Fully Coupled	194.44	−188.28	37.77	97.38	135.15	1.70	−5.79	137.22

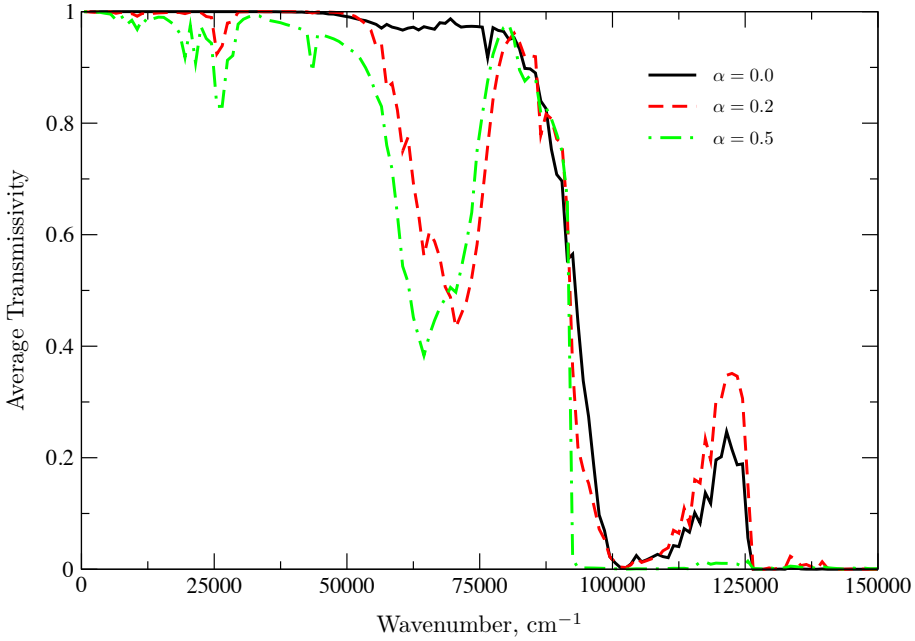

(a) *Comparison of different mixing ratios.*

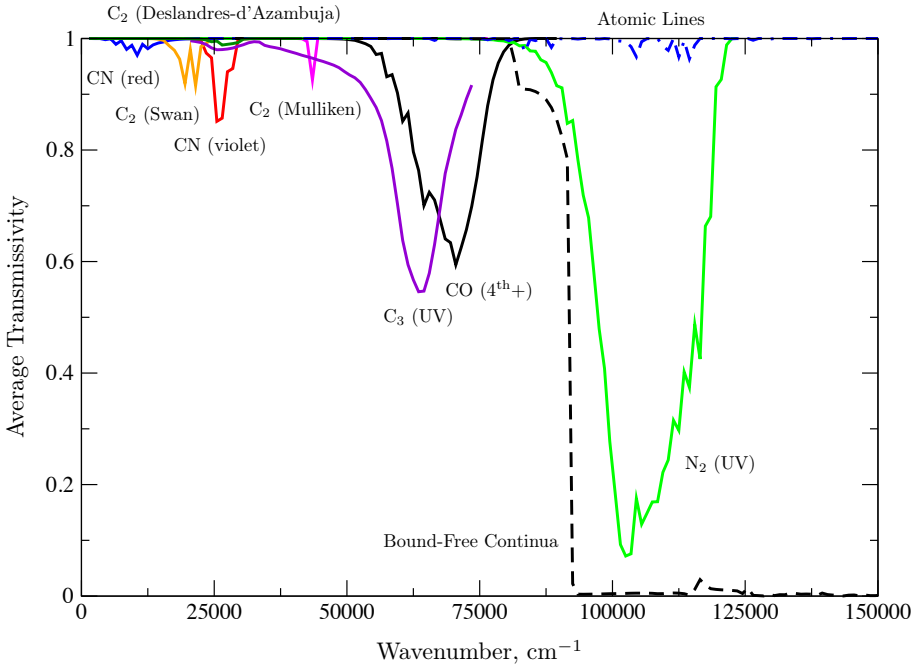

(b) *Major contributions for* $\alpha = 0.5$.

Figure 7.16.: *Average spectral transmissivities for a* 1 cm *slab of several equilibrium mixtures of air and ablation gases at* 5000 K *and* 0.5 bar. *The mixture elemental mass fraction for element* k *is determined by* $y_k^{air}(1-\alpha)+\alpha y_k^{abl}$ *such that* $\alpha = 0$ *results in a pure air mixture while an* $\alpha = 1$ *is a pure ablation gas. Note that the total transmissivity of the mixture as plotted in (a) is obtained as the product of each contribution which is shown for the* $\alpha = 0.5$ *case in (b).*

where the convective heat flux $q_w^{\text{conv}} = q_w^{\text{diff}} + q_w^{\text{cond}}$ is the sum of the diffusive and conductive heating from the gas, ϵq_{in}^r is the radiative flux from the flow field absorbed at the surface, and $\epsilon\sigma T_w^4$ accounts for energy emitted by the ablator surface. The next two terms represent the enthalpy of the injected

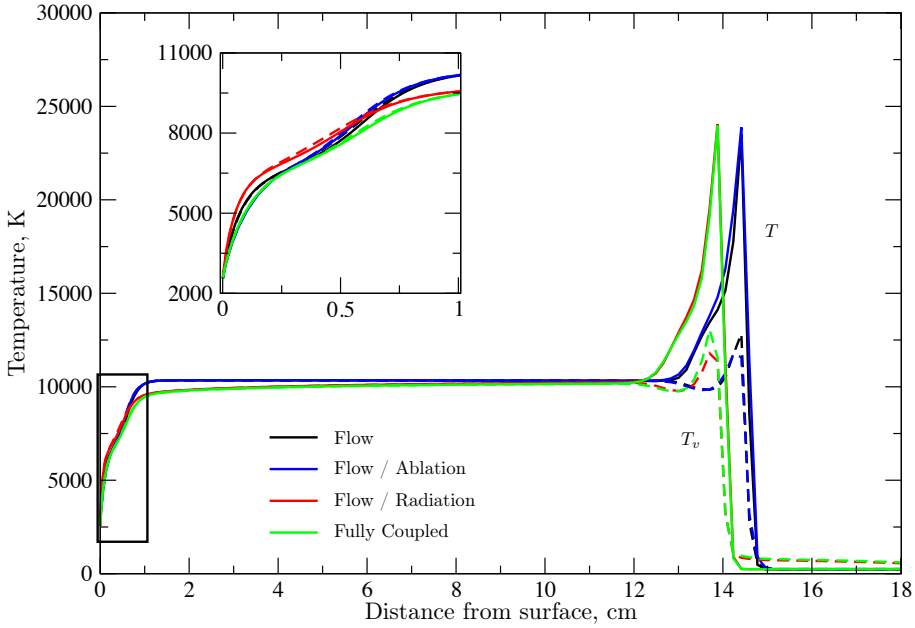

Figure 7.17.: *Computed temperature profiles along the stagnation line of Apollo 4 at* 30 032 s *after launch with various levels of flow/radiation/ablation coupling.*

pyrolysis and char gases. h_w is the enthalpy of the gas at the surface determined from the gas composition and temperature while h_c and h_g are the enthalpies of the solid char and pyrolysis gas, respectively. For this work, the char enthalpy is taken to be the enthalpy of pure graphite at 2500 K and the pyrolysis gas enthalpy is computed assuming an equilibrium composition at the surface temperature and pressure. Finally, q_{cond} is the heat conducted into the ablator and represents the inability to relieve the convective and radiative heating through emission, ablation, and pyrolysis. For a fixed surface temperature, q_{cond} is computed using the surface energy balance in Eq. (7.5).

Based on Table 7.7, radiation coupling is the dominant contributor to the overall difference in the heat flux between no coupling and the fully coupled solution. Radiative cooling reduces the net radiative flux to the surface by as much as 90 % while absorption of radiation in the boundary layer increases the conductive heat flux by about 40 %. In total, coupling with radiation reduces the heat conducted into the surface from 211.41 W/cm^2 to 176.78 W/cm^2, or by about 16 %. When coupled ablation is considered, the diffusive heat flux becomes important, adding up to about 38 W/cm^2. However, the outgassing due to ablation and pyrolysis reduces the conductive heat flux by about 20 % such that the overall effect on the convective heating rate is nearly unchanged when compared to no coupling. Ablation products in the boundary layer also contribute about a 28 % reduction in the net radiative heating rate due to increased absorption in the boundary layer. In total, the combined effects of coupled radiation and ablation reduce the heat conducted in the material from 211.41 W/cm^2 to 137.22 W/cm^2, or 35 %.

The individual contributions to the incoming band-averaged radiant intensity at the stagnation point for a ray along the stagnation line are shown in Fig. (7.19) for both the flow/radiation coupling and fully coupled simulations. Here, the individual intensities are defined as the emitted intensity of each contribution (molecular system, atomic lines, or continuum process) reaching the wall. Using the SNB formulation from Eq. (3.49), the band-averaged intensity from a contribution k is given by

$$\overline{I_\sigma^k(s)}^{\Delta\sigma} = \int_0^s \overline{\eta_\sigma^k(s')\tau_\sigma^k(s',s)}^{\Delta\sigma} \prod_{k'\neq k} \overline{\tau_\sigma^{k'}(s',s)}^{\Delta\sigma} ds'. \tag{7.6}$$

From Fig. (7.19), it is clear the addition of ablation products in the boundary layer has little

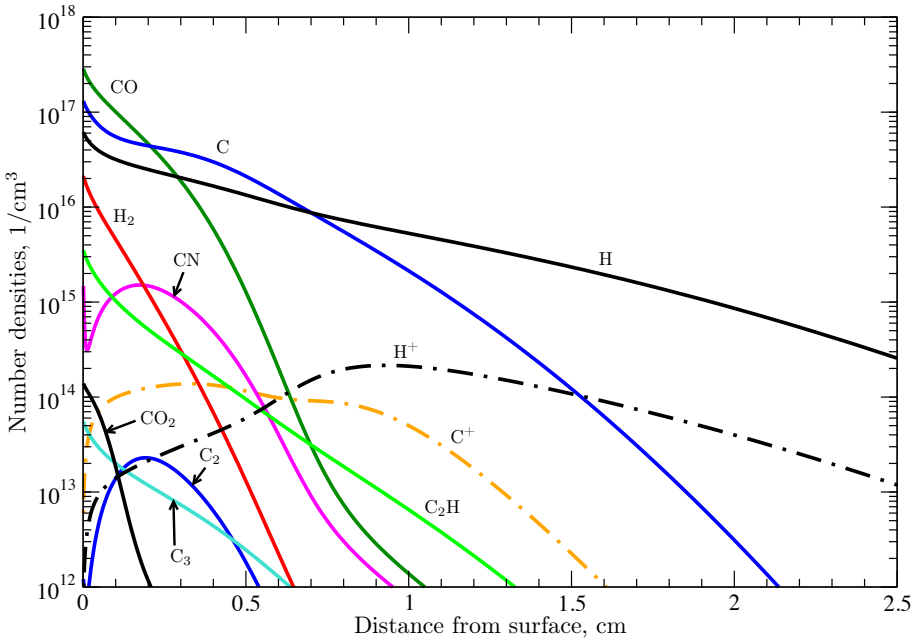

(a) *Ablation and pyrolysis products.*

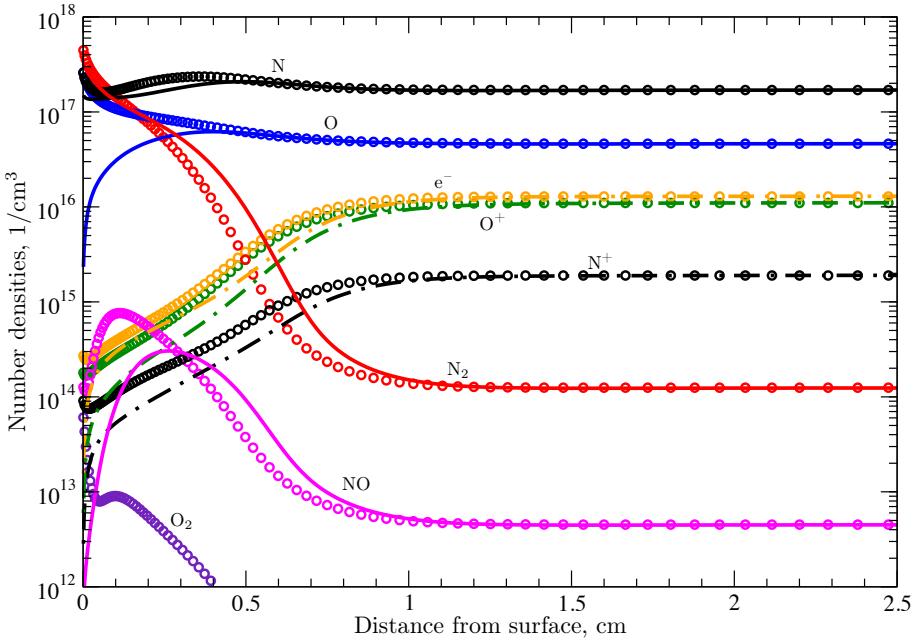

(b) *Air species. Symbols represent solution with no ablation.*

Figure 7.18.: *Number densities for coupled flow/ablation calculation for Apollo 4 30 032 s trajectory point. The symbols represent the number densities of Air species when ablation coupling is neglected.*

effect on the incoming intensities at the wall. Based on the simplified boundary layer analysis in Section 7.4.1, this is likely due to the low carbon mass flux from the wall. In both the radiation coupling and fully coupled solutions, the dominant contributions to the radiative heat flux are atomic lines, nitrogen photoionization, and the N_2 UV systems. The major effects due to ablation seem to be from the CN violet system and the absorption due to C photoionization above about 100 000 cm^{-1}. However, the cumulative heat flux for the entire spectrum shows only about

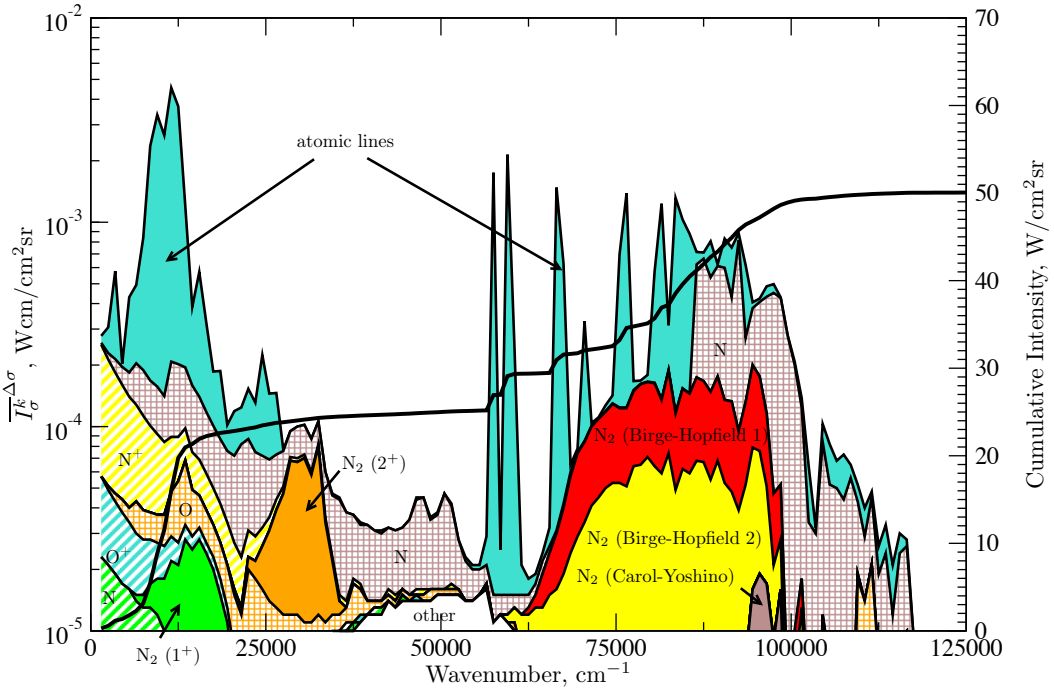

(a) *Flow / Radiation Coupling.*

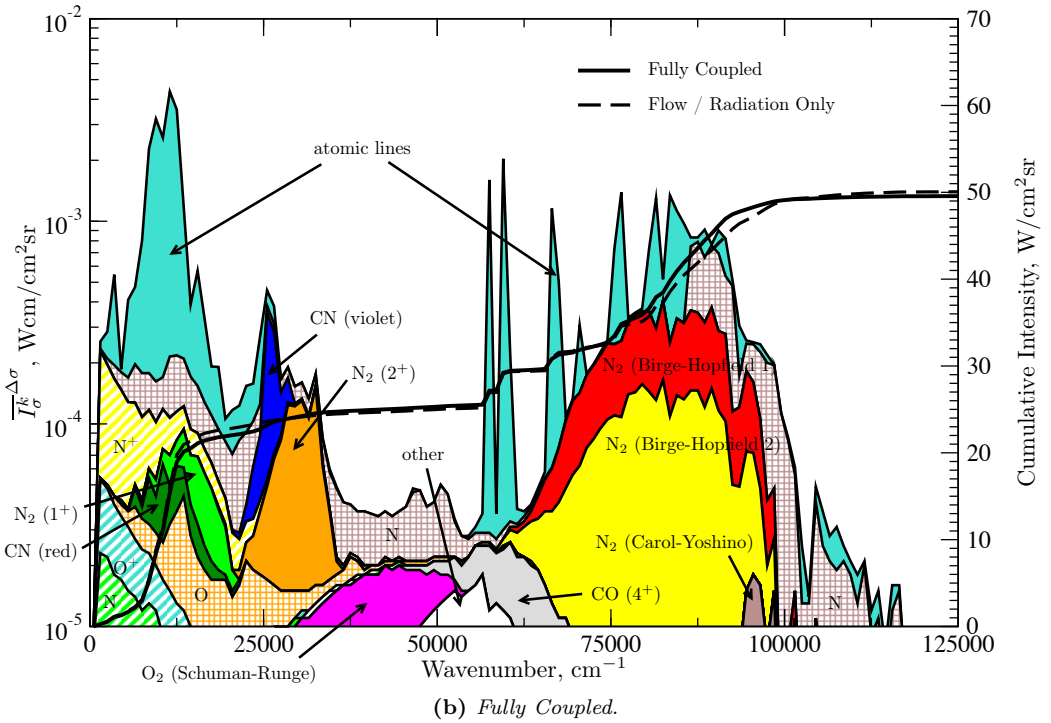

(b) *Fully Coupled.*

Figure 7.19.: *Wall-directed average spectral and cumulative intensities for a ray along the stagnation line for Apollo 4 at* 30 032 s *after launch for both flow/radiation and fully coupled solutions. The spectral intensity is stacked based on individual contributions. Diagonal bars represent free-free contributions, cross-hatching represents bound-free contributions, and solid shading indicates bound-bound contributions.*

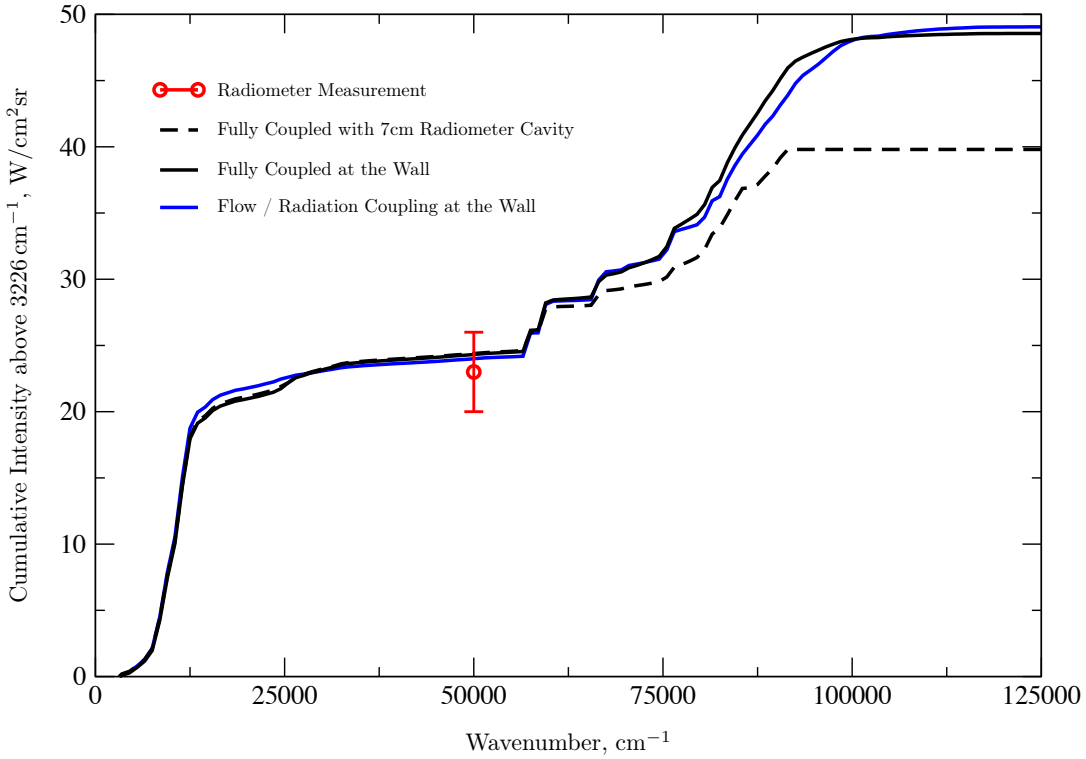

Figure 7.20.: *Comparison of the cumulative intensity above* $3226\,\mathrm{cm}^{-1}$ *to the onboard radiometer measurement reported by Ried et al. [292].*

$1\,\mathrm{W/cm^2sr}$ difference between the solutions with and without ablation coupling.

Finally, Fig. (7.20) compares the cumulative intensity to the radiometer measurement made onboard Apollo 4 at 30 032 s after launch. The radiometer had a spectral range between 0.4 eV to 6.2 eV ($3226\,\mathrm{cm}^{-1}$ to $50\,006\,\mathrm{cm}^{-1}$) and was recessed about 7 cm below the surface of the ablator at the peak heating condition[16]. At the peak heating point, the measured intensity was about $23\,\mathrm{W/cm^2sr}$ with a noise of about $3\,\mathrm{W/cm^2sr}$ according to Ried *et al.* [292]. In Fig. (7.20), the measurement is compared to the intensities computed with both the radiation coupling only and the fully coupled solutions. In addition, the influence of the radiometer cavity is also considered by adding a 7 cm constant property slab with the temperature, pressure, and species densities of the surface behind the ablator wall as was done by Johnston *et al.* [16]. The surface temperature was fixed at 2500 K and the pressure is found to be about 0.34 atm. The species number densities at the surface can be obtained from Fig. (7.18).

Good agreement with the radiometer measurement is obtained for all three cases. The radiometer cavity has little effect on the cumulative intensity over the spectral range measured by the radiometer which supports the assumption by Park [278] that carbon was only present in small amounts in the radiometer cavity based on the lack of observed carbon residue on the radiometer window post-flight. This result varies from that of Johnston *et al.* [16] who performed a similar comparison and found that agreement with the radiometer measurement could only be obtained when absorption in the cavity was considered. This is most likely due to the differences in ablation models imposed, whereby the fixed mass flux imposed by Johnston increases the amount of carbon injected into the boundary layer, which in turn generates significantly more C_2 and C_3 that can act as strong absorbers as shown in the previous section. Such sensitivities in the model therefore provide a clear motivation for increased fidelity in the ablation and pyrolysis modeling.

7.5. Concluding Remarks

This chapter has proven the ability of the HSNB model to accurately and efficiently predict radiation effects on hypersonic entry flows. In general, the method provides a speedup of at least two orders of magnitude and can accurately predict wall radiative heat fluxes to within 5 % compared to LBL calculations. The novel spectral grid adaptation method developed in this thesis for atomic lines was shown to provide nearly identical results with 20 times speedup compared to the original high-resolution HSNB method. This significant improvement is possible due to the small amount of atomic lines as compared to those typically treated for molecular systems. Concerning molecular radiation, the HSNB model provides a significant improvement compared to the Smeared-Rotational-Band model in the case of Titan entry dominated by optically thick CN radiation.

The Lindquist-Simmons and Curtis-Godson approximations to the mean black equivalent line width for non-uniform media were also compared in this chapter. The Lindquist-Simmons method was found to be about three times slower than the Curtis-Godson method for Fire II. It was also shown that the Curtis-Godson approach can provide small negative radiative source terms in the free-stream region, causing numerical instabilities in coupled calculations. For this reason, all coupled cases were computed using the Lindquist-Simmons approach.

Taking into account the coupling with radiation, both convective and radiative heat fluxes at the wall decrease. The standoff distance is reduced due to radiative cooling of the shock layer. For Earth entry cases, we observed slower ionization levels as well as the appearance of O, e^- and O_2^+ in the free stream produced by the photodissociation and the photoionization of O_2.

The analysis of the first trajectory point of the Fire II experiment has shown that the two temperature approach was not satisfactory to model the thermal nonequilibrium state of the plasma. The results obtained using non-Boltzmann electronic populations provided by the QSS model of Johnston [297] were closer to the flight data even if discrepancies still remain. For such entry conditions (high velocity, low density), a self-consistent electronic specific collisional-radiative model should be developed. The HSNB model could be used since it is compatible with arbitrary populations of electronic states.

Finally, the effects of coupled ablation and radiation were studied for Earth entries. It was shown that for a simulated boundary layer, ablation products in the boundary layer can significantly increase the radiation blockage to the surface of the vehicle. In particular, the C_3 UV and CO fourth positive band systems as well as photoionization of C atoms contribute significantly to absorption when enough carbon is present. An analysis of the Apollo 4 peak heating condition showed that coupled radiation and ablation effects can reduce the conducted heat flux by as much as 35 % for a fixed wall temperature of 2500 K. Comparison with the radiometer data taken during the Apollo 4 flight showed excellent agreement for the peak heating condition, partially validating the coupling methodology and radiation database. In addition, the importance of accurately modeling the amount of carbon which is blown into the boundary layer was demonstrated by contrasting the results of this study to those obtained by Johnston *et al.* [16].

CHAPTER 8

Conclusions and Perspectives

This thesis presented the development of physicochemical models and numerical methods for the study of the complex, coupled, multiphysics phenomena associated with atmospheric entry flows. In particular, the research focused on the coupling between the flow, ablation, and radiation phenomena encountered in the stagnation region of atmospheric entry vehicles with carbon-phenolic thermal protection systems. Broadly speaking, the following objectives have been achieved, based on the goals outlined in Chapter 1.

1. Development of a new software library capable of providing a centralized repository for the basic physicochemical models, algorithms, and data relevant to nonequilibrium plasma flows.

2. Development of a numerical approach for calculating coupled flow, radiation, and ablation solutions along the stagnation line of atmospheric entry vehicles and to assess the accuracy and efficiency of HSNB model using the tools developed.

3. Application of these tools to study real flight conditions of interest in an effort to gain a greater understanding of the coupled flow, radiation, and ablation phenomena occurring in atmospheric entry flows.

In the next section, the specific conclusions and contributions of this thesis are summarized in more detail. Lastly, some perspectives on future work are given in Section 8.2.

8.1. Contributions of This Work

In Chapter 2, a review of the thermochemical nonequilibrium models and the corresponding governing equations used to simulate hypersonic flows was made. From this review, a generalized notation was developed, capable of describing most of the popular nonequilibrium models in use today, including state-to-state, multitemperature, and local thermodynamic equilibrium models. Using this notation, a general set of governing equations were derived from the standard conservation of mass, momentum, and energy equations for multicomponent, reacting, radiating, partially ionized and weakly magnetized plasmas. The thermodynamic, transport, chemical kinetic, and energy transfer models necessary to close the governing equations were then presented, consistent with the generalized notation. While the models presented in Chapter 2 are not original, the development of a consistent notation capable of encompassing most thermochemical nonequilibrium models of interest is a valuable contribution for a number of reasons. For starters, a vast literature is available describing numerous thermochemical nonequilibrium models relevant to atmospheric entry. As was shown in Chapter 2, these models can be derived from many different assumptions with varying levels of fidelity and are often inconsistent with one another. By placing each model into a consistent mathematical framework, the similarities and differences between them can be readily assessed. Perhaps more importantly, the generalized model presented in this work provides the machinery needed to abstract the physicochemical models used in modern hypersonic CFD tools away from the implementation of the discretization and solution of the governing equations.

This concept was demonstrated through the development of the MUTATION^{++} software library, presented in Chapter 4. Written using modern, objected oriented programming techniques in C++,

MUTATION^{++} provides thermodynamic, transport, chemistry, and energy transfer models, data, and algorithms, relevant to flows in thermochemical nonequilibrium as well as LTE flows. The driving principle behind MUTATION^{++} is the ability to separate the underlying thermochemical model from the set of governing equations solved by CFD tools, using the framework from Chapter 2. The library builds on previous Fortran libraries developed at the von Karman Institute for the efficient computation of accurate thermodynamic [103] and transport [163] properties for partially ionized gas mixtures. In particular, the scope of the thermodynamic and transport data has been vastly expanded through implementation of the NASA thermodynamic polynomial databases and the creation of a specialized XML format for the storage of binary collision integrals. In addition, MUTATION^{++} implements a novel method for the robust calculation of linearly constrained, multiphase equilibria, a crucial component of many thermal protection material response codes. To the author's best knowledge, the MPGFC algorithm presented in Chapter 5, is the first such algorithm guaranteed to converge for all well-posed constraints. While it was originally developed to improve the robustness of multiphase equilibrium routines required in certain ablation models, the MPGFC algorithm has wide ranging applications.

Chapter 6 presented the other numerics tools developed in this work. The steady-state flow along the stagnation line of an atmospheric entry vehicle is computed using a one-dimensional, finite-volume code, based on the dimensionally reduced Navier-Stokes equations for stagnation line flows. The flow solver was developed in a previous thesis for modeling STS nitrogen flows [72] and has been extended in this work to general thermochemical nonequilibrium mixtures, by coupling with the MUTATION^{++} library. Coupling with ablation is achieved through a steady-state ablation boundary condition using finite-rate heterogeneous reactions at the surface and imposed equilibrium compositions of pyrolysis outgassing.

Concerning radiation coupling, the HTGR database from the laboratory EM2C at CentraleSupélec has been used to provide accurate LBL spectra. Based on a review of the major radiative mechanisms contributing to the radiative heat flux for atmospheric entry vehicles, several contributions were added to the HTGR database in this work, including hydrogen lines, C_3 Swings and UV systems, as well as the photoionization of H, H_2, and CH. The HSNB model has also been implemented in this work in order to significantly reduce the computational resources required to compute accurate radiative heating calculations when many species are present in the flow field. SNB parameters have been computed for the H_2 Lyman and Werner systems, by adjusting the Doppler and Lorentz overlap parameters to fit curves of growth for each narrow band. Comparisons with band-averaged transmissivities computed with the LBL approach show excellent agreement with the resulting SNB parameters for these systems. In general, the method provides a speedup of at least two orders of magnitude and can accurately predict wall radiative heat fluxes to within 5 % compared to LBL calculations. In addition, a novel spectral grid adaptation method has been developed for atomic lines and was shown to provide nearly identical results as compared to the original high-resolution HSNB method with a 20-fold decrease in the computational time. Concerning molecular radiation, the HSNB model provides a significant improvement compared to the Smeared-Rotational-Band model in the case of Titan entry, dominated by optically thick CN radiation.

Finally, the effects of coupled ablation and radiation have been studied for Earth entries in Chapter 7. It was shown that for a simulated boundary layer, ablation products in the boundary layer can significantly increase the radiation blockage to the surface of the vehicle. In particular, the C_3 UV and CO fourth positive band systems as well as photoionization of C atoms contribute significantly to absorption when enough carbon is present. This is the first time that the HSNB model has been used to simulate ablation contaminated boundary layer flows. An analysis of the Apollo 4 peak heating condition showed that coupled radiation and ablation effects can reduce the conducted heat flux by as much as 35 % for a fixed wall temperature of 2500 K. Comparison with the radiometer data taken during the Apollo 4 flight showed excellent agreement for the peak heating condition, partially validating the coupling methodology and radiation database. In addition, the importance of accurately modeling the amount of carbon which is blown into the boundary layer was demonstrated by contrasting the results of other researchers.

8.2. Future Work and Perspectives

This work represents a first step in the direction of understanding fully coupled flow, radiation, and ablation phenomena for atmospheric entry vehicles. The effectiveness of the HSNB model for accurately and efficiently computing radiative heating in highly nonhomogeneous, nonequilibrium flow fields has been clearly demonstrated. However, the steady-state ablation boundary condition used in this work is not sufficient to gain a complete picture of the possible radiation-ablation coupling mechanisms at work in real atmospheric entry flows. In addition, the effects of a 3-dimensional flow field have been completely ignored in an effort to limit the scope of the thesis to a manageable workload. Using the tools developed in this work only, it is not possible to draw conclusions regarding the interaction of ablation products and the radiative heating on the backshell of an entry vehicle. A reasonable step in this direction could be the use of a 3D radiation transport code based on the Monte Carlo Ray Tracing (MCRT) technique and the HSNB method, coupled with a single domain flow / material response solver like the one recently developed by Schrooyen [18]. For example, Rouzaud *et al.* have developed MCRT/SNB code for studying the radiative heating on a Martian orbiter [299]. This tool was later extended to use the full HSNB model for nonequilibrium air flows by Lamet *et al.* [300], however the presence of ablation products has not yet been studied.

As discussed in Chapter 4, the MUTATION^{++} library has already been used by other researchers for a variety of applications related to hypersonics and ablation. These include the study of biomass pyrolysis [231], state-to-state catalytic recombination of nitrogen flows, [232], transport properties of carbon-phenolic ablation mixtures [208], atmospheric entry of meteors [233, 234], and uncertainty quantification for high enthalpy, plasma wind tunnels [235]. However, the library is useful for many other applications which are not directly obvious upon first glance. One interesting example is the study of the Sun's chromosphere which shares many of the phenomena experienced during atmospheric entry, including thermochemical nonequilibrium and strong radiation coupling. A major difference however, is the presence of strong electromagnetic fields which dominate the Sun's landscape. Under such conditions, transport properties are no longer isotropic for ionized plasmas due to the gyroscopic motion of free electrons (and to a lesser extent, ions) around the magnetic field lines. Current approaches for the simulation of the solar chromosphere use simplified models like the one of Braginskii [301] for computing anisotropic transport coefficients [302, 303]. Recently, Graille, Magin, and Massot developed a unified fluid model for multicomponent plasmas in thermal nonequilibrium accounting for the influence of the electromagnetic field [100]. While not presented in this thesis, explicit expressions for asymptotic solutions of the anisotropic transport properties have recently been derived using a spectral Galerkin projection, supplied with Laguerre-Sonine polynomial basis functions, and implemented in MUTATION^{++} [304]. Coupling this new model with the tools used in solar chromosphere studies is a straight forward avenue for future research which may lead to a better understanding of the complex processes involved in that region of our star.

Appendices

APPENDIX A

Transport Systems

This appendix describes the evaluation of the linear transport systems necessary for computing the multicomponent transport properties shown in Chapter 2. For the most part, these equations summarize the results of [106], and are reproduced here for completeness.

Binary diffusion coefficients are given as

$$n\mathscr{D}_{ij} = \frac{3}{16}\sqrt{\frac{2\pi k_B T_h (m_i + m_j)}{m_i m_j}}\frac{1}{\bar{Q}_{ij}^{(1,1)}}, \quad i,j \in \mathcal{H}, \tag{A.1}$$

$$n\mathscr{D}_{ie} = \frac{3}{16}\sqrt{\frac{2\pi k_B T_e}{m_e}}\frac{1}{\bar{Q}_{ie}^{(1,1)}}, \quad i \in \mathcal{H}, \tag{A.2}$$

$$n\mathscr{D}_{ee} = \frac{3}{8}\sqrt{\frac{\pi k_B T_e}{m_e}}\frac{1}{\bar{Q}_{ee}^{(1,1)}}. \tag{A.3}$$

Shear viscosity coefficients for heavy particles read

$$\eta_i = \frac{5}{16}\frac{\sqrt{\pi k_B T_h m_i}}{\bar{Q}_{ii}^{(2,2)}}, \quad i \in \mathcal{H}. \tag{A.4}$$

As discussed in Chapter 2, the transport systems result from Laguerre-Sonine polynomial approximations of the Chapmann-Enskog approximation to the nondimensionalized Boltzmann equation. The resulting systems are summarized in Table A.1 and Table A.2 for heavy-heavy interactions and all electron interactions, respectively. The correction functions for heavy-heavy interactions, $\phi_{ij}, i,j \in \mathcal{H}$, are given in first and second order approximations as

$$\phi_{ij}(1) = 0, \tag{A.5}$$

$$\phi_{ij}(2) = -\frac{25}{8}k_B\frac{n\mathscr{D}_{ij}}{x_i x_j}\sum_{k\in\mathcal{H}}\Lambda_{ik}^{01}\beta_{kj}, \tag{A.6}$$

$$\sum_{k\in\mathcal{H}} G_{ik}^{\lambda_h}\beta_{kj} = -2\Lambda_{ji}^{01}, \quad i,j \in \mathcal{H}, \tag{A.7}$$

and for heavy-electron interactions, $\phi_{ie}, i \in \mathcal{H}$, as

$$\phi_{ie}(1) = 0, \tag{A.8}$$

$$\phi_{ie}(2) = -\frac{25}{8}k_B\frac{n\mathscr{D}_{ie}}{x_i x_e}\frac{\Lambda_{ee}^{01}\Lambda_{ie}^{01}}{\Lambda_{ee}^{11}}. \tag{A.9}$$

Only first order solutions have been used in this work.

Table A.1.: *Summary of heavy particle transport subsystems, $i, j \in \mathcal{H}$.*

System	Formula
G_{ij}^{η}	$\frac{x_i x_j}{n\mathscr{D}_{ij}} \frac{1}{m_i + m_j} \left(\frac{6}{5} A_{ij}^* - 2 \right), \quad i \neq j$
G_{ii}^{η}	$\sum_{\substack{j \in \mathcal{H} \\ j \neq i}} \frac{x_i x_j}{n\mathscr{D}_{ij}} \frac{1}{m_i + m_j} \left(\frac{6}{5} \frac{m_j}{m_i} A_{ij}^* + 2 \right) + \frac{x_i^2}{\eta_i}$
$G_{ij}^{\lambda_h}$	$\frac{1}{25 k_B} \frac{x_i x_j}{n\mathscr{D}_{ij}} \frac{m_i m_j}{(m_i + m_j)^2} \left(16 A_{ij}^* + 12 B_{ij}^* - 55 \right), \quad i \neq j$
$G_{ii}^{\lambda_h}$	$\frac{1}{25 k_B} \sum_{\substack{j \in \mathcal{H} \\ j \neq i}} \frac{x_i x_j}{n\mathscr{D}_{ij}} \frac{m_i m_j}{(m_i + m_j)^2} \left(16 A_{ij}^* - 12 \frac{m_j}{m_i} B_{ij}^* + 25 \frac{m_j}{m_i} + 30 \frac{m_i}{m_j} \right) + \frac{4 m_i}{15 k_B} \frac{x_i^2}{\eta_i}$
$G_{ij}^{\boldsymbol{V}} = \tilde{G}_{ij}^{\boldsymbol{V}}$	$-\frac{x_i x_j}{\mathscr{D}_{ij}} (1 + \phi_{ij}), \quad i \neq j$
$G_{ii}^{\boldsymbol{V}}$	$\sum_{\substack{j \in \mathcal{H} \\ j \neq i}} \frac{x_i x_j}{\mathscr{D}_{ij}} (1 + \phi_{ij}) + \left(\frac{T_e}{T_h} \right)^2 \frac{x_i x_e}{\mathscr{D}_{ie}} (1 + \phi_{ie})$
$\tilde{G}_{ii}^{\boldsymbol{V}}$	$\sum_{\substack{j \in \mathcal{H} \\ j \neq i}} \frac{x_i x_j}{\mathscr{D}_{ij}} (1 + \phi_{ij})$
Λ_{ij}^{01}	$\frac{1}{25 k_B} \frac{x_i x_j}{n\mathscr{D}_{ij}} \frac{m_i}{m_i + m_j} \left(12 C_{ij}^* - 10 \right), \quad i \neq j$
Λ_{ii}^{01}	$-\frac{1}{25 k_B} \sum_{\substack{j \in \mathcal{H} \\ j \neq i}} \frac{x_i x_j}{n\mathscr{D}_{ij}} \frac{m_j}{m_i + m_j} \left(12 C_{ij}^* - 10 \right)$

For simplicity, the usual expressions for collision integral ratios,

$$A_{ij}^* = \frac{\bar{Q}_{ij}^{(2,2)}}{\bar{Q}_{ij}^{(1,1)}}, \tag{A.10}$$

$$B_{ij}^* = \frac{5 \bar{Q}_{ij}^{(1,2)} - 4 \bar{Q}_{ij}^{(1,3)}}{\bar{Q}_{ij}^{(1,1)}}, \tag{A.11}$$

$$C_{ij}^* = \frac{\bar{Q}_{ij}^{(1,2)}}{\bar{Q}_{ij}^{(1,1)}}, \tag{A.12}$$

have been used in Table A.1 as well as the following relationship in Table A.2,

$$\Lambda_{ie}^{kl} = \frac{64 x_e}{75 k_B} \sqrt{\frac{m_e}{2\pi k_B T_e}} \, \tilde{\Lambda}_{ie}^{kl}, \quad i \in \mathcal{S},\ k, l \in \{0, 1, 2\}. \tag{A.13}$$

Table A.2.: *Summary of heavy particle-electron and electron-electron transport subsystems, $i \in \mathcal{H}$.*

System	Formula
$G_{ie}^{\boldsymbol{V}} = \tilde{G}_{ie}^{\boldsymbol{V}}$	$-\frac{T_e}{T_h}\frac{x_i x_e}{\mathscr{D}_{ie}}(1+\phi_{ie})$
$G_{ee}^{\boldsymbol{V}} = \tilde{G}_{ee}^{\boldsymbol{V}}$	$\sum_{i\in\mathcal{H}} \frac{x_i x_e}{\mathscr{D}_{ie}}(1+\phi_{ie})$
$\tilde{\Lambda}_{ie}^{01}$	$x_i \frac{T_e}{T_h}\left(\frac{5}{2}\bar{Q}_{ej}^{(1,1)} - 3\bar{Q}_{ej}^{(1,2)}\right)$
$\tilde{\Lambda}_{ie}^{02}$	$x_i \frac{T_e}{T_h}\left(\frac{35}{8}\bar{Q}_{ej}^{(1,1)} - \frac{21}{2}\bar{Q}_{ej}^{(1,2)} + 6\bar{Q}_{ej}^{(1,3)}\right)$
$\tilde{\Lambda}_{ee}^{00}$	$\sum_{j\in\mathcal{H}} x_j \bar{Q}_{ej}^{(1,1)}$
$\tilde{\Lambda}_{ee}^{01}$	$\sum_{j\in\mathcal{H}} x_j \left(\frac{5}{2}\bar{Q}_{ej}^{(1,1)} - 3\bar{Q}_{ej}^{(1,2)}\right)$
$\tilde{\Lambda}_{ee}^{02}$	$\sum_{j\in\mathcal{H}} x_j \left(\frac{35}{8}\bar{Q}_{ej}^{(1,1)} - \frac{21}{2}\bar{Q}_{ej}^{(1,2)} + 6\bar{Q}_{ej}^{(1,3)}\right)$
$\tilde{\Lambda}_{ee}^{11}$	$\sum_{j\in\mathcal{H}} x_j \left(\frac{25}{4}\bar{Q}_{ej}^{(1,1)} - 15\bar{Q}_{ej}^{(1,2)} + 12\bar{Q}_{ej}^{(1,3)}\right) + x_e\sqrt{2}\bar{Q}_{ee}^{(2,2)}$
$\tilde{\Lambda}_{ee}^{12}$	$\sum_{j\in\mathcal{H}} x_j \left(\frac{175}{16}\bar{Q}_{ej}^{(1,1)} - \frac{315}{8}\bar{Q}_{ej}^{(1,2)} + 57\bar{Q}_{ej}^{(1,3)} - 30\bar{Q}_{ej}^{(1,4)}\right) + x_e\sqrt{2}\left(\frac{7}{4}\bar{Q}_{ee}^{(2,2)} - 2\bar{Q}_{ee}^{(2,3)}\right)$
$\tilde{\Lambda}_{ee}^{22}$	$\sum_{j\in\mathcal{H}} x_j \left(\frac{1225}{64}\bar{Q}_{ej}^{(1,1)} - \frac{735}{8}\bar{Q}_{ej}^{(1,2)} + \frac{399}{2}\bar{Q}_{ej}^{(1,3)} - 210\bar{Q}_{ej}^{(1,4)} + 90\bar{Q}_{ej}^{(1,5)}\right) + x_e\sqrt{2}\left(\frac{77}{16}\bar{Q}_{ee}^{(2,2)} - 7\bar{Q}_{ee}^{(2,3)} + 5\bar{Q}_{ee}^{(2,4)}\right)$

APPENDIX B

MPGFC M Matrix Properties

This appendix provides proof of several important properties of the matrix $\mathbf{M} \equiv \tilde{\mathbf{P}}^T \tilde{\mathbf{B}} \dot{\mathbf{\Lambda}}^{\mathbf{y}}$ from Eq. (5.43).

Definition. The so called hat matrix for the least squares problem $\tilde{\mathbf{B}} \dot{\mathbf{\Lambda}}^{\mathbf{y}} = \tilde{\mathbf{P}}$ is defined as

$$\mathbf{H} \equiv \tilde{\mathbf{B}} \left(\tilde{\mathbf{B}}^T \tilde{\mathbf{B}} \right)^{-1} \tilde{\mathbf{B}}^T, \tag{B.1}$$

The following results are trivial from the definition of the hat matrix, $\mathbf{H}$.

Result 1. $\mathbf{H}$ *is idempotent, meaning* $\mathbf{H}^k = \mathbf{H}$ *for all powers* k *and the eigenvalues of* $\mathbf{H}$ *are either* 0 *or* 1.

Result 2. $\mathbf{H}$ *is symmetric positive semidefinite,* $\mathbf{H} \succeq 0$.

Result 3. *The matrix* $(\mathbf{I} - \mathbf{H})$ *is idempotent and symmetric positive semidefinite,* $(\mathbf{I} - \mathbf{H}) \succeq 0$.

Definition. The matrix $\mathbf{M} \in \mathcal{R}^{n^{\mathcal{P}} \times n^{\mathcal{P}}}$ is defined for convenience such that

$$\mathbf{M} \equiv \tilde{\mathbf{P}}^T \tilde{\mathbf{B}} \dot{\mathbf{\Lambda}}^{\mathbf{y}}, \tag{B.2}$$

where $\tilde{\mathbf{P}}$ and $\tilde{\mathbf{B}}$ are defined in Eq. (5.18) and $\dot{\mathbf{\Lambda}}^{\mathbf{y}}$ solves the least squares problem, $\tilde{\mathbf{B}} \dot{\mathbf{\Lambda}}^{\mathbf{y}} = \tilde{\mathbf{P}}$. We further enforce that $\tilde{\mathbf{B}}$ is full rank, namely $\text{rank}(\tilde{\mathbf{B}}) = n^{\mathcal{C}}$.

Result 4. $\mathbf{M} = \tilde{\mathbf{P}}^T \mathbf{H} \tilde{\mathbf{P}}$

Proof. The normal equations solve the least squares problem, $\tilde{\mathbf{B}} \dot{\mathbf{\Lambda}}^{\mathbf{y}} = \tilde{\mathbf{P}}$, such that

$$\dot{\mathbf{\Lambda}}^{\mathbf{y}} = \left(\tilde{\mathbf{B}}^T \tilde{\mathbf{B}} \right)^{-1} \tilde{\mathbf{B}}^T \tilde{\mathbf{P}} \tag{B.3}$$

Substituting the above relation into Eq. (B.2) yields the result. □

Result 5. $\mathbf{M}$ *is symmetric positive semidefinite,* $\mathbf{M} \succeq 0$.

Proof. This is a trivial result following Results 2 and 4. □

Result 6. *When Eq. (5.19) is satisfied, the* k^{th} *largest eigenvalue of* $\mathbf{M}$ *is upper bounded by the* k^{th} *largest phase moles,* $\beta_k(\mathbf{M}) \leq \bar{N}_k$.

Proof. From Results 3 and 4, we may write

$$\tilde{\mathbf{P}}^T \tilde{\mathbf{P}} - \mathbf{M} = \tilde{\mathbf{P}}^T (\mathbf{I} - \mathbf{H}) \tilde{\mathbf{P}} \succeq 0, \tag{B.4}$$

which shows that $\tilde{\mathbf{P}}^T \tilde{\mathbf{P}} \succeq \mathbf{M}$. Therefore, the Courant minimax principle provides that

$$\beta_k \left(\tilde{\mathbf{P}}^T \tilde{\mathbf{P}} \right) \geq \beta_k (\mathbf{M}), \tag{B.5}$$

where $\beta_k(\cdot)$ represents the k^{th} largest eigenvalue of the matrix in parentheses. When Eq. (5.19) is satisfied, $\tilde{\mathbf{P}}^T \tilde{\mathbf{P}} = \text{diag}\left(\bar{\boldsymbol{N}}\right)$, and $\beta_k \left(\tilde{\mathbf{P}}^T \tilde{\mathbf{P}} \right) = \bar{N}_k$ where $\bar{N}_k$ is the phase moles of the k^{th} largest phase. □

Definition. The matrix $\mathbf{C} \in \mathcal{R}^{n^{\mathcal{C}} \times n^{\mathcal{P}}} \equiv \tilde{\mathbf{B}}^T \tilde{\mathbf{P}}$ has column vectors $\boldsymbol{c}_m = \sum_{k \in \mathcal{S}_m} N_k \tilde{\mathbf{B}}(k,:), \forall\, m \in \mathcal{P}$ which represent the amount of elements (or general constraints) contained in each phase m. Note that $\mathbf{C1} = \sum_{m \in \mathcal{P}} \boldsymbol{c}_m = \boldsymbol{c}$ where $\boldsymbol{c}$ is the constraint vector from Eq. (5.9).

Result 7. *If* $\mathbf{C} \in \mathcal{R}^{n^{\mathcal{C}} \times n^{\mathcal{P}}} \equiv \tilde{\mathbf{B}}^T \tilde{\mathbf{P}}$ *has full column rank (meaning* $\operatorname{rank} \mathbf{C} = n^{\mathcal{P}}$*), then the eigenvalues of* $\mathbf{M}$ *are lower bounded by the eigenvalues of the matrix* $\|\tilde{\mathbf{B}}\|_2^{-2} \mathbf{C}^T \mathbf{C}$ *which are strictly positive,* $\beta_k(\mathbf{M}) \geq \beta_k(\mathbf{C}^T \mathbf{C}) / \|\tilde{\mathbf{B}}\|_2^2 > 0$.

Proof. Letting $\sigma_1 = \|\tilde{\mathbf{B}}\|_2$ denote the largest singular value of $\tilde{\mathbf{B}}$, the difference $\mathbf{M} - \mathbf{C}^T \mathbf{C} / \sigma_1^2$ can be written as

$$\mathbf{M} - \frac{1}{\sigma_1^2} \mathbf{C}^T \mathbf{C} = \mathbf{C}^T \left[\left(\tilde{\mathbf{B}}^T \tilde{\mathbf{B}} \right)^{-1} - \frac{1}{\sigma_1^2} \mathbf{I} \right] \mathbf{C}. \tag{B.6}$$

The term inside the brackets is symmetric and positive semi-definite because the smallest eigenvalue of $(\tilde{\mathbf{B}}^T \tilde{\mathbf{B}})^{-1}$,

$$\beta_{\min} \left(\left(\tilde{\mathbf{B}}^T \tilde{\mathbf{B}} \right)^{-1} \right) = \frac{1}{\beta_{\max} \left(\tilde{\mathbf{B}}^T \tilde{\mathbf{B}} \right)} = \frac{1}{\sigma_1^2}, \tag{B.7}$$

is equal to the $n^{\mathcal{C}}$ repeated eigenvalue of $\mathbf{I} / \sigma_1^2$. Since $\mathbf{C}$ is full rank, we have

$$\mathbf{M} \succeq \frac{1}{\sigma_1^2} \mathbf{C}^T \mathbf{C}, \tag{B.8}$$

and invoking the Courant minimax principle again yields

$$\beta_k(\mathbf{M}) \geq \frac{1}{\sigma_1^2} \beta_k(\mathbf{C}^T \mathbf{C}). \tag{B.9}$$

Finally, since $\mathbf{C}$ is full rank, the product $\mathbf{C}^T \mathbf{C}$ forms the Gramian of the linearly independent column vectors of $\mathbf{C}$ which is guaranteed to be symmetric positive definite with strictly positive eigenvalues. □

Result 8. *When* $n^{\mathcal{P}} = 1$, $\mathbf{M} = M$ *is a strictly positive scalar with a lower bound,* $M \geq \|\boldsymbol{c}\|_2^2 / \|\tilde{\mathbf{B}}\|_2^2$.

Proof. From Result 7, with $n^{\mathcal{P}} = 1$, we have easily

$$M = \beta(\mathbf{M}) \geq \frac{1}{\sigma_1^2} \beta \left(\boldsymbol{c}^T \boldsymbol{c} \right) = \frac{\|\boldsymbol{c}\|_2^2}{\|\tilde{\mathbf{B}}\|_2^2}. \tag{B.10}$$

□

APPENDIX C

Stagnation Line Jacobians

C.1. Convective Flux Jacobian and Eigensystem

The convective Jacobian $\mathbf{A} = \partial \boldsymbol{F}^{\mathbf{c}}/\partial \boldsymbol{U}$ for stagnation line flows is derived for a general thermochemical nonequilibrium model using the notation defined in Section 2.3.1, where the conservative and convective flux vectors are given as

$$\boldsymbol{U} = [\rho_i, \rho u_r, \rho u_\theta, \rho E, \rho e^m]^T, \tag{C.1}$$

$$\boldsymbol{F}^{\mathbf{c}} = [\rho_i u_r, \rho u_r^2 + p, \rho u_r u_\theta, \rho u_r H, \rho u_r e^m]^T, \tag{C.2}$$

where the densities and energies expand for $i \in \mathcal{S}^*$ and $m \in \{2, \ldots, n^{\mathcal{M}}\}$, respectively. Before proceeding with the Jacobian calculation, the partial derivatives of the static pressure with respect to the conservative variables are first obtained as

$$\frac{\partial p}{\partial \boldsymbol{U}} = [\Phi_j,\ -\beta^1 u_r,\ 0,\ \beta^1,\ \beta^n - \beta^1], \tag{C.3}$$

where

$$\Phi_j \equiv \frac{\partial p}{\partial \rho_j} = R_j T_j + \rho \sum_{m \in \mathcal{M}} R^m \Upsilon_{mj}, \tag{C.4}$$

$$\Upsilon_{mj} \equiv \frac{\partial T_m}{\partial \rho_j} = \frac{\delta_{m1}(u_r^2/2 - \Delta h_{f,j}) - e_j^m}{\rho c_v^m}, \tag{C.5}$$

$$R^m = \alpha_h^m \sum_{k \in \mathcal{H}^*} y_k R_k + \alpha_e^m y_e R_e, \tag{C.6}$$

$$\beta^m = \frac{R^m}{c_v^m}. \tag{C.7}$$

Using the α_h^m and α_e^m parameters, the translational temperature associated with a species $j \in \mathcal{S}^*$ can be expressed in terms of the temperatures associated with the global energy modes $m \in \mathcal{M}$ as

$$T_j = \sum_{m \in \mathcal{M}} [\delta_{ej} \alpha_e^m + (1 - \delta_{ej}) \alpha_h^m]. \tag{C.8}$$

With these relations in hand, the convective Jacobian is straightforwardly computed after writing the flux vector with conserved quantities and pressure and differentiating, yielding

$$\mathbf{A} = \begin{bmatrix} u_r(\delta_{ij} - y_i) & y_i & 0 & 0 & 0 \\ \Phi_j - u_r^2 & u_r(2-\beta^1) & 0 & \beta^1 & \beta^n \\ -u_r u_\theta & u_\theta & u_r & 0 & 0 \\ u_r(\Phi_j - H) & H - \beta^1 u_r^2 & 0 & u_r(\beta^1+1) & u_r\beta^n \\ -u_r e^m & e^m & 0 & 0 & \delta_{mn}u_r \end{bmatrix}, \tag{C.9}$$

for $i, j \in \mathcal{S}^*$ and $m, n \in \{2, \ldots, n^{\mathcal{M}}\}$. Note that i and m expand in rows while j and n expand in columns. This notation is used throughout this appendix to simplify matrix expressions.

The eigensystem $\mathbf{A} = \mathbf{R}\mathbf{\Lambda}\mathbf{L}$ is derived using the similarity transformation

$$\boldsymbol{A} = \frac{\partial \boldsymbol{F^c}}{\partial \boldsymbol{U}} = \frac{\partial \boldsymbol{U}}{\partial \boldsymbol{V}}\frac{\partial \boldsymbol{V}}{\partial \boldsymbol{U}}\frac{\partial \boldsymbol{F^c}}{\partial \boldsymbol{U}}\frac{\partial \boldsymbol{U}}{\partial \boldsymbol{V}}\frac{\partial \boldsymbol{V}}{\partial \boldsymbol{U}} = \frac{\partial \boldsymbol{U}}{\partial \boldsymbol{V}}\tilde{\mathbf{A}}\frac{\partial \boldsymbol{V}}{\partial \boldsymbol{U}}, \tag{C.10}$$

where $\boldsymbol{V} = [\rho_i, u_r, u_\theta, p, e^m]$ is the natural variable vector, designed to simplify the eigenvalue problem for the matrix $\tilde{\mathbf{A}}$. Since the eigenvalues of $\tilde{\mathbf{A}}$ and $\mathbf{A}$ are the same, due to the similarity transformation, the calculation of the eigensystem for $\mathbf{A}$ proceeds as follows. First, the Jacobians associated with the natural variable vector V are computed and $\tilde{\mathbf{A}}$ is built from the straightforward matrix multiplication,

$$\tilde{\mathbf{A}} = \frac{\partial \boldsymbol{V}}{\partial \boldsymbol{U}}\frac{\partial \boldsymbol{F^c}}{\partial \boldsymbol{U}}\frac{\partial \boldsymbol{U}}{\partial \boldsymbol{V}}. \tag{C.11}$$

Next, the eigensystem of $\tilde{\mathbf{A}}$ is computed as $\tilde{\mathbf{A}} = \tilde{\mathbf{R}}\mathbf{\Lambda}\tilde{\mathbf{L}}$, where $\tilde{\mathbf{L}}$ and $\tilde{\mathbf{R}}$ are the left and right eigenvector matrices associated with the diagonal eigenvalue matrix $\mathbf{\Lambda}$. Finally, the left and right eigenvector matrices associated the convective Jacobian are then easily computed by

$$\mathbf{L} = \tilde{\mathbf{L}}\frac{\partial \boldsymbol{V}}{\partial \boldsymbol{U}}, \quad \mathbf{R} = \frac{\partial \boldsymbol{U}}{\partial \boldsymbol{V}}\tilde{\mathbf{R}}. \tag{C.12}$$

To begin, the Jacobians associated with the natural variable vector are found to be

$$\frac{\partial \boldsymbol{V}}{\partial \boldsymbol{U}} = \begin{bmatrix} \delta_{ij} & 0 & 0 & 0 & 0 \\ -u_r/\rho & 1/\rho & 0 & 0 & 0 \\ -u_\theta/\rho & 0 & 1/\rho & 0 & 0 \\ \Phi_j & -\beta^1 u_r & 0 & \beta^1 & \beta^n - \beta^1 \\ -e^m/\rho & 0 & 0 & 0 & \delta_{mn}/\rho \end{bmatrix}, \tag{C.13}$$

and

$$\frac{\partial \boldsymbol{U}}{\partial \boldsymbol{V}} = \begin{bmatrix} \delta_{ij} & 0 & 0 & 0 & 0 \\ u_r & \rho & 0 & 0 & 0 \\ u_\theta & 0 & \rho & 0 & 0 \\ \Theta_j & \rho u_r & 0 & 1/\beta^1 & \rho(1 - \dfrac{\beta^n}{\beta^1}) \\ e^m & 0 & 0 & 0 & \delta_{mn}\rho \end{bmatrix}, \tag{C.14}$$

where $\Theta_j = u_r^2 + [\sum_{k\in\mathcal{M}}(\beta^k - \beta^1)e^k - \Phi_j]/\beta^1$. Substitution of Eq. (C.9) and Eqs. (C.13) and (C.14) into Eq. (C.11) yields

$$\tilde{\mathbf{A}} = \begin{bmatrix} \delta_{ij}u_r & \rho_i & 0 & 0 & 0 \\ 0 & u_r & 0 & 1/\rho & 0 \\ 0 & 0 & u_r & 0 & 0 \\ 0 & p(1+\beta^1) & 0 & u_r & 0 \\ 0 & 0 & 0 & 0 & \delta_{mn}u_r \end{bmatrix}. \tag{C.15}$$

As can be seen, $\tilde{\mathbf{A}}$ is much more sparce than $\mathbf{A}$, which greatly simplifies the eigenvalue analysis. From Eq. (C.15), the following characteristic equation for the eigenvalue λ is readily obtained,

$$(u_r - \lambda)^{n^{\mathcal{S}^*}+n^{\mathcal{M}}}\left[(u_r-\lambda)^2 - \frac{p}{\rho}(1+\beta^1)\right] = 0. \tag{C.16}$$

Solution of Eq. (C.16) for λ yields the eigenvalues $\lambda = \{u_r, u_r + a, u_r - a\}$, where the eigenvalue $\lambda = u_r$ is repeated $n^{\mathcal{S}^*} + n^{\mathcal{M}}$ times and a is the numerical "sound speed" associated with the convective Jacobian, defined as

$$a^2 = \frac{p}{\rho}(1+\beta^1). \tag{C.17}$$

Note that for a single temperature model, the sound speed reduces to the conventional result, $a^2 = \gamma p/\rho$ where γ is the ratio of mixture specific heats. Writing the eigenvalue matrix as

$$\mathbf{\Lambda} = \begin{bmatrix} u_r\delta_{ij} & 0 & 0 & 0 & 0 \\ 0 & u_r + a & 0 & 0 & 0 \\ 0 & 0 & u_r - a & 0 & 0 \\ 0 & 0 & 0 & u_r & 0 \\ 0 & 0 & 0 & 0 & u_r\delta_{mn} \end{bmatrix}, \tag{C.18}$$

the right and left eigenvector matrices are obtained from the relations $\tilde{\mathbf{A}}\tilde{\mathbf{R}} = \tilde{\mathbf{R}}\mathbf{\Lambda}$ and $\tilde{\mathbf{L}}\tilde{\mathbf{A}} = \mathbf{\Lambda}\tilde{\mathbf{L}}$. After some algebra, we obtain

$$\tilde{\mathbf{R}} = \begin{bmatrix} \delta_{ij} & \rho_i & \rho_i & 0 & 0 \\ 0 & a & -a & 0 & 0 \\ 0 & 0 & 0 & 1 & 0 \\ 0 & \rho a^2 & \rho a^2 & 0 & 0 \\ 0 & 0 & 0 & 0 & \delta_{mn} \end{bmatrix}, \tag{C.19}$$

and

$$\tilde{\mathbf{L}} = \begin{bmatrix} \delta_{ij} & 0 & 0 & -y_i/a^2 & 0 \\ 0 & 1/(2a) & 0 & 1/(2\rho a^2) & 0 \\ 0 & -1/(2a) & 0 & 1/(2\rho a^2) & 0 \\ 0 & 0 & 1 & 0 & 0 \\ 0 & 0 & 0 & 0 & \delta_{mn} \end{bmatrix}. \tag{C.20}$$

Finally, using Eq. (C.12), the final solution for the right and left eigenvectors associated with the convective Jacobian are given as

$$\mathbf{R} = \begin{bmatrix} \delta_{ij} & \rho_i & \rho_i & 0 & 0 \\ u_r & \rho(u_r+a) & \rho(u_r-a) & 0 & 0 \\ u_\theta & \rho u_\theta & \rho u_\theta & \rho & 0 \\ \Theta_j & \rho(H+u_r a) & \rho(H-u_r a) & 0 & \rho(1-\frac{\beta^n}{\beta^1}) \\ e^m & \rho e^m & \rho e^m & 0 & \delta_{mn} \end{bmatrix}, \tag{C.21}$$

and

$$\mathbf{L} = \begin{bmatrix} \delta_{ij} - \frac{y_i \Phi_j}{a^2} & \frac{\beta^1 u_r y_i}{a^2} & 0 & -\frac{\beta^1 y_i}{a^2} & \frac{y_i(\beta^1-\beta^n)}{a^2} \\ \frac{(\Phi_j - u_r a)}{2\rho a^2} & \frac{(a-\beta^1 u_r)}{2\rho a^2} & 0 & \frac{\beta^1}{2\rho a^2} & \frac{(\beta^n-\beta^1)}{2\rho a^2} \\ \frac{(\Phi_j + u_r a)}{2\rho a^2} & \frac{(a+\beta^1 u_r)}{-2\rho a^2} & 0 & \frac{\beta^1}{2\rho a^2} & \frac{(\beta^n-\beta^1)}{2\rho a^2} \\ -u_\theta/\rho & 0 & 1/\rho & 0 & 0 \\ -e^m/\rho & 0 & 0 & 0 & \delta_{mn}/\rho \end{bmatrix}. \tag{C.22}$$

C.2. Positive-Negative Split Jacobians

In order to calculate the positive-negative split Jacobians,

$$\mathbf{A}^{\pm} = \mathbf{R}\mathbf{\Lambda}^{\pm}\mathbf{L}, \tag{C.23}$$

the eigenvalues are first labeled as

$$\lambda_1 = u_r, \quad \lambda_2 = u_r + a, \quad \lambda_3 = u_r - a, \tag{C.24}$$

and the positive-negative eigenvalues are defined

$$\lambda_i^{\pm} = \frac{\lambda_i \pm |\lambda_i|}{2}, \quad i = \{1,2,3\}. \tag{C.25}$$

Inserting the positive-negative eigenvalues into Eq. (C.18) yields the positive-negative eigenvalue matrix,

$$\boldsymbol{\Lambda}^{\pm} = \begin{bmatrix} \lambda_1^{\pm}\delta_{ij} & 0 & 0 & 0 & 0 \\ 0 & \lambda_2^{\pm} & 0 & 0 & 0 \\ 0 & 0 & \lambda_3^{\pm} & 0 & 0 \\ 0 & 0 & 0 & \lambda_1^{\pm} & 0 \\ 0 & 0 & 0 & 0 & \lambda_1^{\pm}\delta_{mn} \end{bmatrix}. \tag{C.26}$$

Note, from the definition of the positive-negative eigenvalues in Eq. (C.25), $\boldsymbol{\Lambda}^{+}$ is a diagonal matrix with only the positive eigenvalues along the diagonal while the negative eigenvalues are zeroed out. Conversely, $\boldsymbol{\Lambda}^{-}$ has only negative eigenvalues along the diagonal with the positive eigenvalues zeroed out. Substituting Eq. (C.26) into Eq. (C.23) yields the positive-negative split Jacobian matrices.

C.3. Convective Source Term Jacobian

For the general thermochemical nonequilibrium model, the convective source term vector for the stagnation line equations is given as

$$\boldsymbol{S}^{\boldsymbol{c}} = -\frac{(u_r + u_\theta)}{r}\left[2\rho_i, 2\rho u_r, 3\rho u_\theta - 2\frac{p - p_\infty}{u_r + u_\theta}, 2\rho H, 2\rho e^m\right], \tag{C.27}$$

where the indices $i \in \mathcal{S}^*$ and $m \in \{2, \ldots, n^{\mathcal{M}}\}$ expand accordingly. The convective source term Jacobian then follows from a straightforward differentiation, such that

$$\frac{\partial \boldsymbol{S}^{\boldsymbol{c}}}{\partial \boldsymbol{U}} = -\frac{2}{r}\begin{bmatrix} \bar{u}(\delta_{ij} - y_i) & y_i & y_i & 0 & 0 \\ -u_r\bar{u} & (u_r + \bar{u}) & u_r & 0 & 0 \\ -\frac{3}{2}u_\theta\bar{u} - \Phi_j & \frac{3}{2}u_\theta + u_r\beta^1 & \frac{3}{2}(\bar{u} + u_\theta) & -\beta^1 & -(\beta^n - \beta^1) \\ \bar{u}(\Phi_j - H) & H - u_r\bar{u}\beta^1 & H & \bar{u}(1 + \beta^1) & \bar{u}(\beta^n - \beta^1) \\ -\bar{u}e^m & e^m & e^m & 0 & \bar{u}\delta_{mn} \end{bmatrix}, \tag{C.28}$$

where $\bar{u} = u_r + u_\theta$ has been defined for convenience.

C.4. Diffusive Flux Jacobian

The stagnation line diffusive flux vector in the general thermochemical nonequilibrium model notation is given as

$$\boldsymbol{F}^d = [\rho_i V_{ri},\ -\tau_{rr},\ -\tau_{r\theta},\ q_r - \tau_{rr}u_r,\ q_r^m]^T, \tag{C.29}$$

where the indices $i \in \mathcal{S}^*$ and $m \in \{2, \ldots, n^{\mathcal{M}}\}$ expand as usual. Linearization of $\boldsymbol{F}^d$ is performed by first rewriting the flux vector as a sum of the terms which are linearly dependent on the gradient of conservative variables plus those which are not,

$$\boldsymbol{F}^d = \mathbf{A}^d\left(\frac{\partial \boldsymbol{U}}{\partial r}\right) + \boldsymbol{B}^d. \tag{C.30}$$

The diffusion fluxes are then approximated according to the method of Ramshaw and Chang by

$$\rho_i V_{ri} = \rho_i \sum_{j \in \mathcal{S}^*} D_{ij} \frac{\partial x_j}{\partial r}, \tag{C.31}$$

where D_{ij} is the multicomponent diffusion coefficient for species i and j. After some algebra, this relation may be written in terms of species density gradients via

$$\rho_i V_{ri} = \sum_{j \in \mathcal{S}^*} a_{ij} \frac{\partial \rho_j}{\partial r}, \tag{C.32}$$

where the a_{ij} coefficients are

$$a_{ij} = y_i \frac{M}{M_j} \left[D_{ij} - \sum_{k \in \mathcal{S}^*} D_{ik} x_k \right]. \tag{C.33}$$

The velocity and temperature gradients are similarly written in terms of gradients of conserved quantities such that

$$\frac{\partial u_r}{\partial r} = \frac{1}{\rho} \frac{\partial (\rho u_r)}{\partial r} - \frac{u_r}{\rho} \sum_{i \in \mathcal{S}^*} \frac{\partial \rho_i}{\partial r}, \tag{C.34}$$

$$\frac{\partial u_\theta}{\partial r} = \frac{1}{\rho} \frac{\partial (\rho u_\theta)}{\partial r} - \frac{u_\theta}{\rho} \sum_{i \in \mathcal{S}^*} \frac{\partial \rho_i}{\partial r}, \tag{C.35}$$

$$\frac{\partial T_1}{\partial r} = \frac{1}{\rho c_v^1} \left[\frac{\partial (\rho E)}{\partial r} - \sum_{m=2}^{n^{\mathcal{M}}} \frac{\partial (\rho e^m)}{\partial r} - u_r \frac{\partial (\rho u_r)}{\partial r} \right] + \sum_{i \in \mathcal{S}^*} \Upsilon_{1i} \frac{\partial \rho_i}{\partial r}, \tag{C.36}$$

$$\frac{\partial T_m}{\partial r} = \frac{1}{\rho c_v^m} \frac{\partial \rho e^m}{\partial r} + \sum_{i \in \mathcal{S}^*} \Upsilon_{mi} \frac{\partial \rho_i}{\partial r}, \quad \forall\, m \in \{2, \ldots, n^{\mathcal{M}}\}. \tag{C.37}$$

The stress tensor components and radial heat fluxes can then be written as

$$\tau_{rr} = \frac{4}{3} \eta \left(\frac{1}{\rho} \frac{\partial (\rho u_r)}{\partial r} - \frac{u_r}{\rho} \sum_{i \in \mathcal{S}^*} \frac{\partial \rho_i}{\partial r} - \frac{\bar{u}}{r} \right), \tag{C.38}$$

$$\tau_{r\theta} = \eta \left(\frac{1}{\rho} \frac{\partial (\rho u_\theta)}{\partial r} - \frac{u_\theta}{\rho} \sum_{i \in \mathcal{S}^*} \frac{\partial \rho_i}{\partial r} - \frac{\bar{u}}{r} \right), \tag{C.39}$$

$$\tau_{\theta\theta} = -\frac{1}{2} \tau_{rr}, \tag{C.40}$$

and

$$q_r = \sum_{i \in \mathcal{S}^*} b_i \frac{\partial \rho_i}{\partial r} + \alpha^1 u_r \frac{\partial (\rho u_r)}{\partial r} - \alpha^1 \frac{\partial (\rho E)}{\partial r} + \sum_{m=2}^{n^{\mathcal{M}}} \left(\alpha^1 - \alpha^m \right) \frac{\partial (\rho e^m)}{\partial r}, \tag{C.41}$$

$$q_r^m = \sum_{s \in \mathcal{S}^*} b_i^m \frac{\partial \rho_i}{\partial r} - \alpha^m \frac{\partial (\rho e^m)}{\partial r}, \quad \forall\, m \in \{2, \ldots, n^{\mathcal{M}}\}, \tag{C.42}$$

where $\alpha^m = \lambda^m / \rho c_v^m, \forall\, m \in \mathcal{M}$ and the b_i and b_i^m coefficients are

$$b_i = \sum_{k \in \mathcal{S}^*} h_k a_{ki} - \sum_{m \in \mathcal{M}} \lambda^m \Upsilon_{mi}, \tag{C.43}$$

$$b_i^m = \sum_{k \in \mathcal{S}^*} h_k^m a_{ki} - \lambda^m \Upsilon_{mi}. \tag{C.44}$$

Using the above relations, $\mathbf{A}^d$ and $\boldsymbol{B}^d$ are then found to be

$$\mathbf{A}^d = \begin{bmatrix} a_{ij} & 0 & 0 & 0 & 0 \\ \frac{4}{3}\frac{\eta}{\rho}u_r & -\frac{4}{3}\frac{\eta}{\rho} & 0 & 0 & 0 \\ \frac{\eta}{\rho}u_\theta & 0 & -\frac{\eta}{\rho} & 0 & 0 \\ b_j+\frac{4}{3}\frac{\eta}{\rho}u_r^2 & (\alpha^1-\frac{4}{3}\frac{\eta}{\rho})u_r & 0 & -\alpha^1 & \alpha^1-\alpha^n \\ b_j^m & 0 & 0 & 0 & -\alpha^m\delta_{mn} \end{bmatrix}, \tag{C.45}$$

and

$$\boldsymbol{B}^d = \bar{u}\frac{\mu}{r}\left[0,\ \frac{4}{3},\ 1,\ \frac{4}{3}u_r,\ 0\right]^T, \tag{C.46}$$

where the first and last zeros in $\boldsymbol{B}^d$ are expanded $n^{\mathcal{S}^*}$ and $n^{\mathcal{M}}-1$ times, respectively. Finally, the Jacobian of $\boldsymbol{B}^d$ with respect to the conservative variables is found to be

$$\frac{\partial \boldsymbol{B}^d}{\partial \boldsymbol{U}} = \frac{1}{r}\frac{\eta}{\rho}\begin{bmatrix} 0 & 0 & 0 & 0 & 0 \\ -\frac{4}{3}\bar{u} & \frac{4}{3} & \frac{4}{3} & 0 & 0 \\ -\bar{u} & 1 & 1 & 0 & 0 \\ -\frac{8}{3}\bar{u} & \frac{4}{3}(\bar{u}+u_r) & \frac{4}{3}u_r & 0 & 0 \\ 0 & 0 & 0 & 0 & 0 \end{bmatrix}, \tag{C.47}$$

where the first and last rows and columns are expanded $n^{\mathcal{S}^*}$ and $n^{\mathcal{M}}-1$ times, respectively.

C.5. Diffusive Source Term Jacobian

The diffusive source term vector written in the general thermochemical model notation is expressed as

$$\boldsymbol{S}^d = -\frac{2}{r}\left[\rho_i V_{ri},\ \tau_{\theta\theta}-\tau_{rr}+\tau_{r\theta},\ \frac{(\tau_{\theta\theta}-3\tau_{r\theta})}{2},\ q_r-\tau_{rr}u_r-\tau_{r\theta}u_r-\tau_{\theta\theta}u_\theta,\ q_r^m\right]^T, \tag{C.48}$$

where the indices $i \in \mathcal{S}^*$ and $m \in \{2,\ldots,n^{\mathcal{M}}\}$ are expanded. The linearization of $\boldsymbol{S}^d$ proceeds in the same way as was done for $\boldsymbol{F}^d$ in the previous section, by first decomposing the vector as

$$\boldsymbol{S}^d = \mathbf{A}_s^d\left(\frac{\partial \boldsymbol{U}}{\partial r}\right) + \boldsymbol{B}_{\boldsymbol{s}}^{\boldsymbol{d}}. \tag{C.49}$$

Using the procedure detailed in the previous section, $\mathbf{A}_s^d$ and $\boldsymbol{B}_s^d$ are given as

$$\mathbf{A_s^d} = -\frac{2}{r}\begin{bmatrix} a_{ij} & 0 & 0 & 0 & 0 \\ d & -2\dfrac{\mu}{\rho} & -\dfrac{\mu}{\rho} & 0 & 0 \\ f & -\dfrac{1}{3}\dfrac{\mu}{\rho} & -\frac{3}{2}\dfrac{\mu}{\rho} & 0 & 0 \\ c_j & c_r & -u_r\dfrac{\mu}{\rho} & -\alpha^1 & \alpha^1-\alpha^n \\ b_j^m & 0 & 0 & 0 & -\alpha^m\delta_{mn} \end{bmatrix} \tag{C.50}$$

where

$$c_i = b_i + \frac{\mu}{\rho}\frac{u_r}{3}\left(\bar{u}+3u_r\right), \tag{C.51}$$

$$c_r = \beta^1 u_r + \frac{\mu}{\rho}\frac{4}{3}\left(u_r - \frac{1}{2}u_\theta\right), \tag{C.52}$$

$$d = \frac{\mu}{\rho}(\bar{u}+u_r), \tag{C.53}$$

$$f = \frac{1}{6}\frac{\mu}{\rho}(2\bar{u}+7u_\theta), \tag{C.54}$$

and

$$\boldsymbol{B}_s^d = \frac{\mu}{r^2}\left[0,\ -6\bar{u},\ -\frac{11}{3}\bar{u},\ -\frac{2}{3}\bar{u}^\star,\ 0\right]^T, \tag{C.55}$$

where $\bar{u}^\star = 7u_r^2 + 5u_r u_\theta - 2u_\theta^2$. Finally, the Jacobian of $\boldsymbol{B}_s^d$ is found to be

$$\frac{\partial \boldsymbol{B}_s^d}{\partial \boldsymbol{U}} = \frac{1}{r^2}\frac{\mu}{\rho}\begin{bmatrix} 0 & 0 & 0 & 0 & 0 \\ 6\bar{u} & -6 & -6 & 0 & 0 \\ \dfrac{11}{3}\bar{u} & -\dfrac{11}{3} & -\dfrac{11}{3} & 0 & 0 \\ \dfrac{4}{3}\bar{u}^\star & g_r & g_t & 0 & 0 \\ 0 & 0 & 0 & 0 & 0 \end{bmatrix}, \tag{C.56}$$

where

$$g_r = \frac{2}{3}(15u_r - 5u_\theta), \tag{C.57}$$

$$g_t = \frac{2}{3}(4u_r - 5u_\theta). \tag{C.58}$$

C.6. Kinetic Source Term Jacobian

Lastly, the kinetic source term vector for the general thermochemical model is given as,

$$\boldsymbol{S^k} = \left[\dot{\omega}_i,\ 0,\ 0,\ 0,\ \Omega^m\right]^T, \tag{C.59}$$

where the the species and energy production rates are functions of species densities and temperatures,

$$\dot{\omega}_i = \dot{\omega}_i(\{\rho_k, k \in \mathcal{S}^*\}, \{T^n, n \in \mathcal{M}\}), \quad i \in \mathcal{S}^*, \tag{C.60}$$

$$\Omega^m = \Omega^m(\{\rho_k, k \in \mathcal{S}^*\}, \{T^n, n \in \mathcal{M}\}), \quad m \in \{2, \ldots, n^{\mathcal{M}}\}. \tag{C.61}$$

It is therefore convenient to calculate the kinetic source Jacobian using the chain rule,

$$\frac{\partial \boldsymbol{S^k}}{\partial \boldsymbol{U}} = \frac{\partial \boldsymbol{S^k}}{\partial \boldsymbol{P}} \frac{\partial \boldsymbol{P}}{\partial \boldsymbol{U}}, \tag{C.62}$$

where $\boldsymbol{P}$ is the primitive variable vector

$$\boldsymbol{P} = [\rho_i,\ u_r,\ u_\theta,\ T_1,\ T_m]^T. \tag{C.63}$$

The primitive variable Jacobian is found to be

$$\frac{\partial \boldsymbol{P}}{\partial \boldsymbol{U}} = \begin{bmatrix} \delta_{ij} & 0 & 0 & 0 & 0 \\ -u_r/\rho & 1/\rho & 0 & 0 & 0 \\ -u_\theta/\rho & 0 & 1/\rho & 0 & 0 \\ \Upsilon_{1j} & -u_r/(\rho c_v^1) & 0 & 1/(\rho c_v^1) & -1/(\rho c_v^1) \\ \Upsilon_{mj} & 0 & 0 & 0 & \delta_{mn}/(\rho c_v^n) \end{bmatrix}. \tag{C.64}$$

The source term Jacobian with respect to primitive variables is given as

$$\frac{\partial \boldsymbol{S^k}}{\partial \boldsymbol{P}} = \begin{bmatrix} \left(\frac{\partial \dot{\omega}_i}{\partial \rho_j}\right)_{\boldsymbol{P}} & 0 & 0 & \left(\frac{\partial \dot{\omega}_i}{\partial T_1}\right)_{\boldsymbol{P}} & \left(\frac{\partial \dot{\omega}_i}{\partial T_n}\right)_{\boldsymbol{P}} \\ 0 & 0 & 0 & 0 & 0 \\ 0 & 0 & 0 & 0 & 0 \\ 0 & 0 & 0 & 0 & 0 \\ \left(\frac{\partial \Omega^m}{\partial \rho_j}\right)_{\boldsymbol{P}} & 0 & 0 & \left(\frac{\partial \Omega^m}{\partial T_1}\right)_{\boldsymbol{P}} & \left(\frac{\partial \Omega^m}{\partial T_n}\right)_{\boldsymbol{P}} \end{bmatrix}, \tag{C.65}$$

where the subscript $\boldsymbol{P}$ is used to emphasize that the derivatives are with respect to primitive variables, rather than conservative ones. Multiplying the above two matrices yields

$$\frac{\partial \boldsymbol{S^k}}{\partial \boldsymbol{U}} = \begin{bmatrix} \frac{\partial \dot{\omega}_i}{\partial \rho_j} & \frac{\partial \dot{\omega}_i}{\partial (\rho u_r)} & 0 & \frac{\partial \dot{\omega}_i}{\partial (\rho E)} & \frac{\partial \dot{\omega}_i}{\partial (\rho e^n)} \\ 0 & 0 & 0 & 0 & 0 \\ 0 & 0 & 0 & 0 & 0 \\ 0 & 0 & 0 & 0 & 0 \\ \frac{\partial \Omega^m}{\partial \rho_j} & \frac{\partial \Omega^m}{\partial (\rho u_r)} & 0 & \frac{\partial \Omega^m}{\partial (\rho E)} & \frac{\partial \Omega^m}{\partial (\rho e^n)} \end{bmatrix}, \tag{C.66}$$

where the derivatives with respect to conservative variables are found to be

$$\frac{\partial X}{\partial \rho_j} = \left(\frac{\partial X}{\partial \rho_j}\right)_{\boldsymbol{P}} + \sum_{l \in \mathcal{M}} \Upsilon_{lj} \left(\frac{\partial X}{\partial T_l}\right)_{\boldsymbol{P}}, \tag{C.67}$$

$$\frac{\partial X}{\partial (\rho u_r)} = -\frac{u_r}{\rho c_v^1} \left(\frac{\partial X}{T_1}\right)_{\boldsymbol{P}}, \tag{C.68}$$

$$\frac{\partial X}{\partial (\rho E)} = \frac{1}{\rho c_v^1} \left(\frac{\partial X}{T_1}\right)_{\boldsymbol{P}}, \tag{C.69}$$

$$\frac{\partial X}{\partial (\rho e^n)} = \frac{1}{\rho c_v^n} \left(\frac{\partial X}{T_n}\right)_{\boldsymbol{P}} - \frac{1}{\rho c_v^1} \left(\frac{\partial X}{T_1}\right)_{\boldsymbol{P}}, \tag{C.70}$$

for $X = \{\dot{\omega}_i,\ \Omega^m\}$.

APPENDIX D

Mixtures and Data

This appendix details the various mixtures and data used for the simulations presented in Chapter 7, including the the species involved, specific reactions considered, as well as the collision integral data necessary to compute the transport coefficients.

D.1. Mixtures

The three mixtures described in Section 7.1.1 are summarized in Table D.1. The table provides a list of species included in each mixture, the thermal nonequilibrium model employed, and the number of species, reactions, and collision pairs. Species thermodynamic properties were computed using the RRHO model as described in Section 4.4.1 using the rotational, vibrational, and electronic characteristic temperatures and degeneracies provided by Gurvich *et al.* [173, 175]. The reaction mechanisms and rate constants employed for each mixture are detailed in the proceeding section followed by the collision integral data required to compute transport coefficients for each mixture.

Table D.1.: *Summary of the three mixtures used in Chapter 7.*

Mixture Name	Species	Noneq. Model	# Species / Reactions	# Collision Pairs
air	e^- N^+ O^+ NO^+ ${N_2}^+$ ${O_2}^+$ N O NO N_2 O_2	T, T^{ve}	11 / 22	66
air-ablation	e^- N^+ O^+ N O NO N_2 O_2 C C^+ H H^+ C_2 C_2H C_3 CO CO_2 CN HCN H_2	T, T^{ve}	20 / 25	210
Titan	N C H N_2 C H CN NH CH CH_2 CH_3 CH_4 HCN	T	13 / 27	91

D.2. Reaction Mechanisms

This section presents the reaction mechanisms used for each of the three mixtures summarized in the previous section. For each mechanism, the corresponding reactions, rate constants, and temperature dependencies are provided.

Table D.2.: *Gas phase chemical reactions used in this work for air simulations. Forward reaction rate coefficients are computed using the modified Arrhenius formula, $k_f(T_f) = AT_f^{\beta}\exp(-\theta/T_f)$. Backward reaction rate coefficients are computed in order to satisfy equilibrium at the temperature associated with the reverse reaction, $k_b = k_f(T_b)/k_{eq}(T_b)$. The sources for the listed rate constants are provided in the last column.*

No.	Reaction	A	β	θ	Ref.
		m, s, mol		K	
	associative ionization ($T_f = T, T_b = T^{ve}$)				
1.	$N + O \rightleftharpoons NO^+ + e^-$	5.30×10^{6}	0.00	31 900	[69]
2.	$O + O \rightleftharpoons {O_2}^+ + e^-$	7.10×10^{-4}	2.70	80 600	[67]
3.	$N + N \rightleftharpoons {N_2}^+ + e^-$	4.40×10^{1}	1.50	67 500	[69]
	charge exchange ($T_f = T, T_b = T$)				
4.	$NO^+ + O \rightleftharpoons N^+ + O_2$	1.00×10^{6}	0.50	77 200	[67]
5.	$N^+ + N_2 \rightleftharpoons {N_2}^+ + N$	1.00×10^{6}	0.50	12 200	[67]
6.	${O_2}^+ + N \rightleftharpoons N^+ + O_2$	8.70×10^{7}	0.14	28 600	[67]
7.	$O^+ + NO \rightleftharpoons N^+ + O_2$	1.40×10^{-1}	1.90	26 600	[67]
8.	${O_2}^+ + N_2 \rightleftharpoons {N_2}^+ + O_2$	9.90×10^{6}	0.00	40 700	[67]
9.	${O_2}^+ + O \rightleftharpoons O^+ + O_2$	4.00×10^{6}	0.09	18 000	[67]
10.	$NO^+ + N \rightleftharpoons O^+ + N_2$	3.40×10^{7}	−1.08	12 800	[67]
11.	$NO^+ + O_2 \rightleftharpoons {O_2}^+ + NO$	2.40×10^{7}	0.41	32 600	[67]
12.	$NO^+ + O \rightleftharpoons {O_2}^+ + N$	7.20×10^{7}	0.29	48 600	[67]
13.	$O^+ + N_2 \rightleftharpoons {N_2}^+ + O$	9.10×10^{7}	0.36	22 800	[67]
14.	$NO^+ + N \rightleftharpoons {N_2}^+ + O$	7.20×10^{7}	0.00	35 500	[67]
	electron impact dissociation ($T_f = T^{ve}, T_b = T^{ve}$)				
15.	$N_2 + e^- \rightleftharpoons N + N + e^-$	3.00×10^{18}	−1.60	113 200	[69]
	heavy particle impact dissociation ($T_f = \sqrt{TT^{ve}}, T_b = T$)				
16.	$N_2 + M \rightleftharpoons N + N + M$	7.00×10^{15}	−1.60	113 200	[69]
	$M = N\ O$	3.00×10^{16}			
17.	$O_2 + M \rightleftharpoons O + O + M$	2.00×10^{15}	−1.50	59 360	[69]
	$M = N\ O$	1.00×10^{16}			
18.	$NO + M \rightleftharpoons N + O + M$	5.00×10^{9}	0.00	75 500	[68]
	$M = N\ O\ NO$	1.00×10^{11}			
	exchange ($T_f = T, T_b = T$)				
19.	$NO + O \rightleftharpoons N + O_2$	8.40×10^{6}	0.00	19 400	[69]
20.	$N_2 + O \rightleftharpoons NO + N$	5.70×10^{6}	0.42	42 938	[69]
	electron impact ionization ($T_f = T^{ve}, T_b = T$)				
21.	$O + e^- \rightleftharpoons O^+ + e^- + e^-$	3.90×10^{27}	−3.78	158 500	[69]
22.	$N + e^- \rightleftharpoons N^+ + e^- + e^-$	2.50×10^{28}	−3.82	168 200	[69]

Table D.3.: *Gas phase chemical reactions used in this work for coupled air and ablation simulations. Forward reaction rate coefficients are computed using the modified Arrhenius formula, $k_f(T_f) = AT_f^{\beta}\exp(-\theta/T_f)$. Backward reaction rate coefficients are computed in order to satisfy equilibrium at the temperature associated with the reverse reaction, $k_b = k_f(T_b)/k_{eq}(T_b)$. The sources for the listed rate constants are provided in the last column.*

No.	Reaction	A m, s, mol	β	θ K	Ref.
	electron impact dissociation ($T_f = T^{ve}, T_b = T^{ve}$)				
1.	$N_2 + e^- \rightleftharpoons 2\,N + e^-$	1.00×10^{19}	-1.60	113 200	[305]
	heavy particle impact dissociation ($T_f = \sqrt{TT^{ve}}, T_b = T$)				
2.	$N_2 + M \rightleftharpoons 2\,N + M$	7.00×10^{15}	-1.60	113 200	[305]
	M = atoms	3.00×10^{16}			
3.	$O_2 + M \rightleftharpoons 2\,O + M$	2.00×10^{15}	-1.50	59 750	[305]
	M = H	0.00			
	M = atoms except H	1.00×10^{16}			
4.	$C_2 + M \rightleftharpoons C + C + M$	3.70×10^{8}	0.00	69 000	[305]
5.	$CN + M \rightleftharpoons C + N + M$	2.50×10^{8}	0.00	71 000	[305]
6.	$NO + M \rightleftharpoons N + O + M$	5.00×10^{9}	0.00	75 500	[305]
	M = atoms	1.10×10^{11}			
7.	$CO_2 + M \rightleftharpoons CO + O + M$	6.90×10^{15}	-1.50	63 275	[305]
	M = atomic ions and H	1.40×10^{16}			
	M = neutral ions except H	1.40×10^{16}			
8.	$CO + M \rightleftharpoons C + O + M$	2.30×10^{14}	-1.00	129 000	[305]
	M = atoms	3.40×10^{14}			
9.	$C_3 + M \rightleftharpoons C_2 + C + M$	6.30×10^{10}	-0.50	101 200	[305]
10.	$H_2 + M \rightleftharpoons H + H + M$	2.20×10^{8}	0.00	48 300	[305]
	exchange ($T_f = T, T_b = T$)				
11.	$N_2 + O \rightleftharpoons NO + N$	6.40×10^{11}	-1.00	38 370	[305]
12.	$NO + O \rightleftharpoons N + O_2$	8.40×10^{6}	0.00	19 450	[305]
13.	$CO + C \rightleftharpoons C_2 + O$	2.00×10^{11}	-1.00	58 000	[305]
14.	$CO + O \rightleftharpoons O_2 + C$	3.90×10^{7}	-0.18	69 200	[305]
15.	$CO + N \rightleftharpoons CN + O$	1.00×10^{8}	0.00	38 600	[305]
16.	$N_2 + C \rightleftharpoons CN + N$	1.10×10^{8}	-0.11	23 200	[305]
17.	$CN + O \rightleftharpoons NO + C$	1.60×10^{7}	0.10	14 600	[305]
18.	$CN + C \rightleftharpoons C_2 + N$	5.00×10^{7}	0.00	13 000	[305]
19.	$CO_2 + O \rightleftharpoons O_2 + CO$	2.10×10^{7}	0.00	27 800	[305]
20.	$HCN + H \rightleftharpoons CN + H_2$	8.00×10^{5}	0.02	85 537	[305]
21.	$C_2H + H \rightleftharpoons C_2 + H_2$	1.00×10^{6}	0.00	16 770	[69]
	electron impact ionization ($T_f = T^{ve}, T_b = T$)				
22.	$O + e^- \rightleftharpoons O^+ + e^- + e^-$	3.90×10^{27}	-3.78	158 500	[69]
23.	$N + e^- \rightleftharpoons N^+ + e^- + e^-$	2.50×10^{28}	-3.82	168 200	[69]
24.	$H + e^- \rightleftharpoons H^+ + e^- + e^-$	2.20×10^{24}	-2.80	157 800	[69]
25.	$C + e^- \rightleftharpoons C^+ + e^- + e^-$	6.35×10^{9}	0.00	130 700	[69]

Table D.4.: *Gas phase chemical reactions used in this work for Titan simulations. Forward reaction rate coefficients are computed using the modified Arrhenius formula, $k_f(T) = AT^{\beta}\exp(-\theta/T)$. Backward reaction rate coefficients are computed in order to satisfy equilibrium at the temperature associated with the reverse reaction, $k_b = k_f(T)/k_{eq}(T)$. The rate constants are taken from Gökçen [295].*

No.	Reaction	A m, s, mol	β	θ K
	heavy particle impact dissociation			
1.	$N_2 + M \rightleftharpoons 2\,N + M$	7.00×10^{15}	-1.60	113 200
	M = atoms	3.00×10^{16}		
2.	$CH_4 + M \rightleftharpoons CH_3 + H + M$	4.70×10^{41}	-8.20	59 200
3.	$CH_3 + M \rightleftharpoons CH_2 + H + M$	1.02×10^{10}	0.00	45 600
4.	$CH_3 + M \rightleftharpoons CH + H_2 + M$	5.00×10^{9}	0.00	42 800
5.	$CH_2 + M \rightleftharpoons CH + H + M$	4.00×10^{9}	0.00	41 800
6.	$CH_2 + M \rightleftharpoons C + H_2 + M$	1.30×10^{8}	0.00	29 700
7.	$CH + M \rightleftharpoons C + H + M$	1.90×10^{8}	0.00	33 700
8.	$C_2 + M \rightleftharpoons 2\,C + M$	1.50×10^{10}	0.00	71 600
9.	$H_2 + M \rightleftharpoons 2\,H + M$	2.23×10^{8}	0.00	48 350
10.	$CN + M \rightleftharpoons C + N + M$	2.53×10^{8}	0.00	78 000
11.	$NH + M \rightleftharpoons N + H + M$	1.80×10^{8}	0.00	37 600
12.	$HCN + M \rightleftharpoons CN + H + M$	3.57×10^{20}	-2.60	62 845
	exchange			
13.	$CH_3 + N \rightleftharpoons HCN + 2\,H$	7.00×10^{7}	0.00	0
14.	$CH_3 + H \rightleftharpoons CH_2 + H_2$	6.03×10^{7}	0.00	7600
15.	$CH_2 + N_2 \rightleftharpoons HCN + NH$	4.82×10^{6}	0.00	18 000
16.	$CH_2 + N \rightleftharpoons HCN + H$	5.00×10^{7}	0.00	0
17.	$CH_2 + H \rightleftharpoons CH + H_2$	6.03×10^{6}	0.00	-900
18.	$CH + N_2 \rightleftharpoons HCN + N$	4.40×10^{6}	0.00	11 060
19.	$CH + C \rightleftharpoons C_2 + H$	2.00×10^{8}	0.00	0
20.	$C_2 + N_2 \rightleftharpoons 2\,CN$	1.50×10^{7}	0.00	21 000
21.	$CN + H_2 \rightleftharpoons HCN + H$	2.95×10^{-1}	0.00	1130
22.	$CN + C \rightleftharpoons C_2 + N$	5.00×10^{7}	0.00	13 000
23.	$N + H_2 \rightleftharpoons NH + H$	1.60×10^{8}	0.00	12 650
24.	$C + N_2 \rightleftharpoons CN + N$	5.24×10^{7}	0.00	22 600
25.	$C + H_2 \rightleftharpoons CH + H$	4.00×10^{8}	0.00	11 700
26.	$H + N_2 \rightleftharpoons NH + N$	3.00×10^{6}	0.50	71 400
27.	$H + CH_4 \rightleftharpoons CH_3 + H_2$	1.32×10^{-2}	3.00	4045

D.3. Collision Integrals

Figs. (D.1 - D.3) present summaries of the collision integral data used for each collision pair in the three mixtures presented in Section D.1. Each cell corresponding to a collision pair is color-coded based on the type of collision represented. Depending on the type of collision, reference information is also given for each collision pair detailing the source of the required collision integral data. All attractive and repulsive charged collisions are treated as Coulomb interactions using the Debye-Hückel potential as described in Section 4.5.1. All other collision integrals are either explicitly taken from the given reference, or are computed using the Langevin (ion-neutral) or Lennard-Jones (neutral-neutral) potentials. Pure species Lennard-Jones parameters and species dipole polarizabilities used in this work are given in Table D.5. Lennard-Jones parameters for non-pure interactions can be obtained from the Lorentz and Berthelot combination rules as described in Section 4.5.1.

	e^-	N^+	O^+	N_2^+	O_2^+	NO^+	N	O	N_2	O_2	NO
e^-	-										
N^+	+	-									
O^+	+	-	-								
N_2^+	+	-	-	-							
O_2^+	+	-	-	-	-						
NO^+	+	-	-	-	-	-					
N	[201]	[213]	[213]	[213]	[213]	[213]	[201]				
O	[201]	[213]	[213]	[213]	[213]	[213]	[201]	[201]			
N_2	[201]	[213]	[213]	[213]	[213]	[213]	[201]	[201]	[201]		
O_2	[201]	[213]	[213]	[213]	[213]	[213]	[201]	[201]	[201]	[201]	
NO	[201]	[213]	[213]	[213]	[213]	[213]	[201]	[201]	[201]	[201]	[201]

Figure D.1.: *Summary of collision integral data for the air mixture used in this work. Cell colors represent type of collision (red : charged, orange : electron-neutral, green : ion-neutral, blue : neutral-neutral). Numbers indicate reference source for each collision pair. + : attractive, − : repulsive.*

	N	C	H	N_2	C_2	H_2	CN	NH	CH	CH_2	CH_3	CH_4	HCN
N	[201]												
C	[202]	[202]											
H	[208]	[208]	[203]										
N_2	[201]	[202]	[208]	[201]									
C_2	[208]	[208]	[208]	[208]	[208]								
H_2	[208]	[208]	[203]	[208]	[208]	[203]							
CN	[202]	[202]	[208]	[202]	[208]	[208]	[202]						
NH	LJ	LJ	LJ	LJ	LJ	LJ	LJ	LJ					
CH	LJ	LJ	LJ	LJ	LJ	LJ	LJ	LJ	LJ				
CH_2	LJ	LJ	LJ	LJ	LJ	LJ	LJ	LJ	LJ	LJ			
CH_3	LJ	LJ	LJ	LJ	LJ	LJ	LJ	LJ	LJ	LJ	LJ		
CH_4	LJ	LJ	LJ	LJ	LJ	LJ	LJ	LJ	LJ	LJ	LJ	LJ	
HCN	LJ	LJ	[208]	LJ	[208]	[208]	LJ	LJ	LJ	LJ	LJ	LJ	LJ

Figure D.2.: *Summary of collision integral data for the Titan mixture used in this work. Numbers indicate reference source for each collision pair. LJ : Lennard-Jones (12-6) potential.*

	e^-	O^+	N^+	C^+	H^+	N	O	NO	N_2	O_2	C_2	C_3	CN	CO	CO_2	C	H_2	HCN	H	C_2H
e^-	-																			
O^+	+	-																		
N^+	+	-	-																	
C^+	+	-	-	-																
H^+	+	-	-	-	-															
N	[201]	[213]	[213]	[202]	L	[201]														
O	[201]	[213]	[213]	[202]	L	[201]	[201]													
NO	[201]	[213]	[213]	L	L	[201]	[201]	[201]												
N_2	[201]	[213]	[213]	L	L	[201]	[201]	[201]	[201]											
O_2	[201]	[213]	[213]	[202]	L	[201]	[201]	[201]	[201]	[201]										
C_2	C	[208]	[208]	[208]	L	[208]	[208]	[208]	[208]	[208]	[208]									
C_3	C	[208]	[208]	[208]	[208]	[208]	[208]	[208]	[208]	[208]	[208]	[208]								
CN	[202]	L	L	L	L	[202]	[202]	[202]	[202]	[202]	[208]	[208]	[202]							
CO	[202]	[202]	[202]	[202]	L	[202]	[202]	[202]	[202]	[202]	[208]	[208]	[202]	[202]						
CO_2	[202]	L	L	L	L	[202]	[202]	[202]	[202]	[202]	[208]	[208]	[202]	[202]	[202]					
C	[202]	[202]	[202]	[202]	L	[202]	[202]	[202]	[202]	[202]	[208]	[208]	[202]	[202]	[202]	[202]				
H_2	[203]	[208]	[208]	[208]	[203]	[208]	[208]	[208]	[208]	[208]	[208]	[208]	[208]	[208]	[208]	[208]	[203]			
HCN	C	L	L	L	L	LJ	LJ	LJ	LJ	LJ	[208]	[208]	LJ	LJ	LJ	LJ	[208]	LJ		
H	[203]	[208]	[208]	[208]	L	[208]	[208]	[208]	[208]	[208]	[208]	[208]	[208]	[208]	[208]	[208]	[203]	[208]	[203]	
C_2H	C	[208]	[208]	[208]	[208]	[208]	[208]	[208]	[208]	[208]	[208]	[208]	[208]	[208]	[208]	[208]	[208]	[208]	[208]	[208]

Figure D.3.: *Summary of collision integral data for the coupled air and ablation mixture used in this work. Cell colors represent type of collision (red : charged, orange : electron-neutral, green : ion-neutral, blue : neutral-neutral). Numbers indicate reference source for each collision pair. + : attractive, − : repulsive, L : Langevin potential, LJ : Lennard-Jones (12-6) potential, C : copied from $e^- - C$ data.*

Table D.5.: *Pure species Lennard-Jones potential parameters and species dipole polarizabilities used in this work.*

Species	Lennard-Jones Parameters			Polarizabilities	
	σ Å	ϕ^0/k_B K	Ref.	α Å^3	Ref.
C	3.0	100.0	[306]	1.76	[202]
C_2	3.913	78.8	[69]	5.58	[208]
CH	2.750	80.0	[307]		
CH_2	3.8	144.0	[308]		
CH_3	3.8	144.0	[308]		
CH_4	4.010	143.8	[309]		
CN	3.856	75.0	[69]	2.00	[202]
CO	3.690	91.7	[69]	1.95	[202]
CO_2	3.763	244.0	[308]	2.91	[202]
H	2.4	40.0	[306]	0.667	[203]
H_2	2.827	59.7	[69]		
HCN	3.630	569.1	[310]	2.53	[306]
N	2.98	119.0	[306]	1.10	[202]
N_2	3.798	71.4	[69]	1.74	[202]
NH	2.650	80.0	[308]		
NO	3.599	91.0	[69]	1.70	[202]
O	2.660	70.0	[306]	0.80	[202]
O_2	3.467	106.7	[69]	1.58	[202]

Bibliography

Each reference is followed by the list of the pages where it is cited.

[1] John T. Howe. Hypervelocity atmospheric flight: Real gas flow fields. Technical Report RP 1249, National Aeronautics and Space Administration, 1990. 3

[2] Thomas Rivell. Notes on earth atmospheric entry for Mars sample return missions. Technical Report TP–2006-213486, National Aeronautics and Space Administration, 2006. 3

[3] Deepak Bose, Michael Olson, Bernard Laub, Todd White, Jay Feldman, Jose Santos, Milad Mahzari, Matthew MacLean, Aaron Dufrene, and Michael Holden. Initial Assessment of Mars Science Laboratory Heatshield Instrumentation and Flight Data. In *51st AIAA Aerospace Sciences Meeting Including the New Horizons Forum and Aerospace Exposition*, volume 2013-0908. AIAA, January 2013. 3

[4] B. Laub and E. Venkatapathy. Thermal protection system technology and facility needs for demanding future planetary missions. In *Proceedings of the Interntational Workshop Planetary Probe Atmospheric Entry and Descent Trajectory Analysis and Science*, ESA SP, Lisbon, Portugal, 6-9 October 2003. 4

[5] Carol Davies and Marla Arcadi. Planetary Mission Entry Vehicles Quick Reference Guide. Version 3.0. Technical Report 2006-3401, NASA, NASA Ames Research Center, January 2006. 5, 143

[6] R Goulard. The coupling of radiation and convection in detached shock layers. *Journal of Quantitative Spectroscopy and Radiative Transfer*, 1:249–257, 1961. 6

[7] T. E. Magin, L. Caillault, A. Bourdon, and C. O. Laux. Nonequilibrium radiative heat flux modeling for the Huygens entry probe. *Journal of Geophysical Research*, 111(E7), 2006. 7, 17, 130, 144, 158

[8] B. Helber, A. Turchi, O. Chazot, and T. E. Magin. Physico-chemistry of CN in the boundary layer of graphite in nitrogen plasmas. In *45th AIAA Thermophysics Conference*, AIAA paper 2015-2668, Dallas, TX, 2015. 8, 134

[9] Mairead Stackpoole, Steve Sepka, Ioana Cozmuta, and Dean Kontinos. Post-flight evaluation of Stardust Sample Return Capsule forebody heatshield material. *AIAA paper*, 1202:2008, 2008. 8

[10] Jason Rabinovitch, Vanessa M. Marx, and Guillaume Blanquart. Pyrolysis Gas Composition for a Phenolic Impregnated Carbon Ablator Heatshield. In *11th AIAA/ASME Joint Thermophysics and Heat Transfer Conference*, volume 2014-2246, 2014. 7

[11] George F. Sykes Jr. Decomposition Characteristics of a Char-Forming Phenolic Polymer Used for Ablative Composites. Technical Report TN D-3810, NASA, 1967. 7

[12] Hsi-Wu Wong, Jay Peck, Robin E. Bonomi, James Assif, Francesco Panerai, Guillaume Reinisch, Jean Lachaud, and Nagi N. Mansour. Quantitative determination of species production from phenol-formaldehyde resin pyrolysis. *Polymer Degradation and Stability*, 112:122–131, February 2015. 7

[13] Kimberly A. Trick and Tony E. Saliba. Mechanisms of the pyrolysis of phenolic resin in a carbon/phenolic composite. *Carbon*, 33(11):1509–1515, 1995. 7

[14] Hsi-Wu Wong, Jay Peck, James Assif, Jean Lachaud, and Nagi N. Mansour. Quantitative determination of species production from the pyrolysis of the Phenolic Impregnated Carbon Ablator (PICA). In *AIAA Science and Technology Forum and Exposition*, volume 2015-1447. AIAA, January 2015. 7

[15] Brody K. Bessire, Sridhar A. Lahankar, and Timothy K. Minton. Pyrolysis of Phenolic Impregnated Carbon Ablator (PICA). *ACS Applied Materials & Interfaces*, 7(3):1383–1395, January 2015. 7

[16] Christopher O. Johnston, Peter A. Gnoffo, and Kenneth Sutton. Influence of ablation on radiative heating for earth entry. *Journal of Spacecraft and Rockets*, 46(3):481–491, 2009. 9, 10, 25, 143, 158, 159, 166, 167

[17] Bernd Helber. *Material Response Characterization of Low-density Ablators in Atmopheric Entry Plasmas*. PhD thesis, von Karman Institute for Fluid Dynamics and Vrije Universiteit Brussel, Brussels, Belgium, January 2016. 10

[18] Pierre Schrooyen. *Numerical simulation of aerothermal flows through ablative thermal protection systems*. PhD thesis, von Karman Institute for Fluid Dynamics and Université Catholique de Louvain, Belgium, November 2015. 10, 171

[19] T. Gökçen and C. Park. The coupling of radiative transfer to quasi-1d flows with thermochemical nonequilibrium. In *AIAA 29th aerospace sciences meeting*, page 570, 1991. 10

[20] Lin C. Hartung, Robert A. Mitcheltree, and Peter A. Gnoffo. Coupled radiation effects in thermochemical nonequilibrium shock-capturing flowfield calculations. *Journal of Thermophysics and Heat Transfer*, 8(2):244–250, 1994.

[21] Michael J. Wright, Deepak Bose, and Joe Olejniczak. Impact of flowfield-radiation coupling on aeroheating for titan aerocapture. *Journal of Thermophysics and Heat Transfer*, 19(1):17–27, 2005. 10

[22] Scott A. Stanley and Leland A. Carlson. Effects of shock wave precursors ahead of hypersonic entry vehicles. *Journal of Spacecraft and Rockets*, 29(2):190–197, 1992. 10

[23] C. Park. Radiation enhancement by nonequilibrium in earth's atmosphere. *Journal of Spacecraft and Rockets*, 22(1):27–36, 1985. 10

[24] Lin C. Hartung. Development of a nonequilibrium radiative heating prediction method for coupled flowfield solutions. *Journal of Thermophysics and Heat Transfer*, 6(4):618–625, 1992. 10

[25] S. Sharma. Modeling of nonequilibrium radiation phenomena: an assessment. *Journal of Thermophysics and Heat Transfer*, 10:85âĂŞ396, 1996. 10

[26] Peter A. Gnoffo, Roop N. Gupta, and Judy L. Shinn. Conservation equations and physical models for hypersonic air flows in thermal and chemical nonequilibrium. Technical Paper 2867, NASA, February 1989. 10, 17, 23, 24, 42

[27] Graham V. Candler and Robert W. Maccormack. Computation of weakly ionized hypersonic flows in thermochemical nonequilibrium. *Journal of Thermophysics and Heat Transfer*, 5(3):266–273, July 1991. 10, 17, 43, 44, 131

[28] Graham V. Candler, Pramod K. Subbareddy, and Ioannis Nompelis. Decoupled Implicit Method for Aerothermodynamics and Reacting Flows. *AIAA Journal*, 51(5):1245–1254, May 2013. 10

[29] Jong-Hun Lee. Basic governing equations for the flight regimes of aeroassisted orbital transfer vehicles. In *19th Thermophysics Conference*, AIAA paper 84-1729, Snowmass, CO, 1984. 10, 15, 17

[30] Chul Park. *Nonequilibrium Hypersonic Aerothermodynamics*. Wiley, New York, 1990. LCCB: TL571.5 .P37 1990. 10, 41, 42

[31] Ellis E. Whiting, Chul Park, James O. Arnold, and John A. Paterson. NEQAIR96, nonequilibrium and equilibrium radiative transport and spectra program: User's manual. Technical Report NASA-RP-1389, NASA Ames Research Center, 1996. 10

[32] Brett A. Cruden and Aaron M. Brandis. Updates to the NEQAIR radiation solver. In *Proceedings of the 6th High Temperature Gas Radiation Workshop*, St. Andrews, UK, November 2014. ESA. 10

[33] K. Fujita and T. Abe. SPRADIAN, structural package for radiation analysis: theory and application. *ISAS Report No 669*, 1997. 10

[34] L. Kuznetsova and S. Surzhikov. Absorption cross sections of diatomic molecules for problems of radiative heat transfer in low-temperature plasma. *High Temperature*, 37(3):374–385, 1999. 10

[35] C. Laux. Radiation and nonequilibrium collisinal-radiative models. *VKI special course on physico-chemical models for high enthalpy and plasma flows modeling*, 2002. 10

[36] S. Chauveau, M.-Y. Perrin, Ph Rivière, and A. Soufiani. Contributions of diatomic molecular electronic systems to heated air radiation. *Journal of Quantitative Spectroscopy and Radiative Transfer*, 72(4):503–530, 2002. 10, 51, 52, 53, 55

[37] Sophie Chauveau, Christine Deron, Marie-Yvonne Perrin, Philippe Rivière, and Anouar Soufiani. Radiative transfer in LTE air plasmas for temperatures up to 15,000 K. *Journal of Quantitative Spectroscopy and Radiative Transfer*, 77:113–130, 2003. 51, 52, 53, 55, 57, 58, 59

[38] Y. Babou, Ph. Rivière, M.Y. Perrin, , and A. Soufiani. High-temperature and nonequilibrium partition function and thermodynamic data of diatomic molecules. *International Journal of Thermophysics*, 30(2):416–438, 2009.

[39] Y. Babou, Ph. Rivière, M.Y. Perrin, , and A. Soufiani. Spectroscopic data for the prediction of radiative transfer in CO_2âĂŞN_2 plasmas. *Journal of Quantitative Spectroscopy and Radiative Transfer*, 110:89–108, 2009. 51, 52, 55, 57, 58, 59

[40] A. Soufiani, Ph. Rivière, and M.Y. Perrin. High temperature gas radiation (HTGR) database and models. *Von Karman Institute Lecture Series*, STO-EN-AVT-218, 2013. 10, 51, 52, 55, 145

[41] A. Kramida, Yu Ralchenko, J. Reader, and NIST ASD Team. NIST Atomic Spectra Database (version 5.2), 2014. 10, 55

[42] W. Cunto, C. Mendoza, F. Ochsenbein, and C. J. Zeippen. TOPbase at the CDS. *Astronomy and Astrophysics*, 275, 1993. 10, 55, 57, 58

[43] Jean-Michel Lamet, Yacine Babou, Philippe Rivière, Marie-Yvonne Perrin, and Anouar Soufiani. Radiative transfer in gases under thermal and chemical nonequilibrium conditions: Application to earth atmospheric re-entry. *Journal of Quantitative Spectroscopy and Radiative Transfer*, 109(2):235–244, January 2008. 10, 16, 17, 56, 58

[44] Bruno Lopez, Marie Yvonne Perrin, Philippe Rivière, and Anouar Soufiani. Coupled Nonequilibrium Flowfield–Radiative Transfer Calculation Behind a Shock Wave. *Journal of Thermophysics and Heat Transfer*, 27(3):404–413, 2013. 10, 154

[45] A. M. Feldick, M. F. Modest, and D. A. Levin. Closely Coupled Flowfield-Radiation Interactions During Hypersonic Reentry. *Journal of Thermophysics and Heat Transfer*, 25(4):481–492, October 2011. 10

[46] C.O. Johnston, B.R. Hollis, and K. Sutton. Spectrum modeling for air shock-layer radiation at lunar-return conditions. *Journal of Spacecraft and Rockets*, 45(5):865–878, 2008. 10, 151

[47] M. K. Denison and B. W. Webb. The spectral-line-based weighted-sum-of-gray-gases model in nonisothermal nonhomogeneous media. *Journal of Heat Transfer*, 117:359–365, 1995. 10

[48] R. Goody, R. West, L. Chen, and D. Crisp. The correlated-k method for radiation calculations in nonhomogeneous atmospheres. *Journal of Quantitative Spectroscopy and Radiative Transfer*, 42:539–550, 1989. 10

[49] D. Mihalas and B. Weibel-Mihalas. *Foundations of radiation hydrodynamics*. Dover Publications, INC, Mineloa, 1999. 11

[50] Ph. Rivière, A. Soufiani, M. Y. Perrin, H. Riad, and A. Gleizes. Air mixture radiative property modelling in the temperature range 10,000-40,000 K. *Journal of Quantitative Spectroscopy and Radiative Transfer*, 56(1):29–45, 1996. 11

[51] A. Bansal and M. F. Modest. Multiscale Part-Spectrum k-Distribution Database for Atomic Radiation in Hypersonic Nonequilibrium Flows. *Journal of Heat Transfer*, 133(12):122701–122701, 2011. 11

[52] A. Bansal, M. F. Modest, and D. A. Levin. Multi-scale k-distribution model for gas mixtures in hypersonic nonequilibrium flows. *Journal of Quantitative Spectroscopy and Radiative Transfer*, 112:1213–1221, 2011. 11

[53] Ankit Bansal and M. F. Modest. Modeling of Radiative Heat Transfer in Carbonaceous Atmospheres Using k-Distribution Models. *Journal of Thermophysics and Heat Transfer*, 27(2):217–225, April 2013. 11, 152, 153

[54] M. F. Modest. *Radiative heat transfer*. Academic Press, third edition, 2013. 11

[55] Jean-Michel Lamet, Philippe Rivière, Marie-Yvonne Perrin, and Anouar Soufiani. Narrow-band model for nonequilibrium air plasma radiation. *Journal of Quantitative Spectroscopy and Radiative Transfer*, 111(1):87–104, January 2010. 11, 20, 52, 53, 57, 60, 61, 65, 68, 70, 145, 154

[56] W. G. Vincenti and Charles H. Kruger. *Introduction to Physical Gas Dynamics*. Krieger Pub Co, 1975. 13, 21, 26, 41

[57] Forrest R. Gilmore. Potential energy curves for N2, NO, O2 and corresponding ions. *Journal of Quantitative Spectroscopy and Radiative Transfer*, 5:369–390, 1965. 14

[58] C. Park. Assessment of two-temperature kinetic model for dissociating and weakly-ionizing nitrogen. In *4th Thermophysics and Heat Transfer Conference*, Boston, MA, June 1986. AIAA. 15, 17, 35, 37

[59] Chul Park. Convergence of Computation of Chemical Reacting Flows. In *Thermophysical Aspects of Re-Entry Flows*, pages 478–513. American Institute of Aeronautics and Astronautics, New York, January 1986.

[60] Chul Park. Assessment of two-temperature kinetic model for ionizing air. In *22nd Thermophysics Conference*, AIAA paper 87-1574, Honolulu, Hawaii, 1987. 15, 35, 37, 42

[61] Jong-Hun Lee. Basic Governing Equations for the Flight Regimes of Aeroassisted Orbital Transfer Vehicles. In H. F. Nelson, editor, *Thermal Design of Aeroassisted Orbital Transfer Vehicles*, pages 3–53. American Institute of Aeronautics and Astronautics, New York, January 1985. 15, 17

[62] M. Born and R. Oppenheimer. Zur Quantentheorie der Molekeln. *Annalen der Physik*, 389(20):457–484, 1927. 16

[63] Richard L. Jaffe. The calculation of high-temperature equilibrium and nonequilibrium specific heat data for N2, O2 and NO. In *22nd AIAA Thermophysics Conference*, AIAA paper 87-1633, Honolulu, HI, 1987. 16

[64] Thomas L. Eddy and K. Y. Cho. A multitemperature model for plasmas in chemical nonequilibrium. In *HTD*, volume 161, pages 195–210. ASME, 1991. 16

[65] D. Giordano. Hypersonic-flow governing equations with electromagnetic fields. In *Non-Equilibrium Gas Dynamics - From Physical Models to Hypersonic Flights*, volume EN-AVT-162, pages 1–68, Rhode St. Genèse, Belgium, 2009. NATO-STO/VKI Lecture Series. 16, 19, 21

[66] Chul Park and Seung-Ho Lee. Validation of multi-temperature nozzle flow code NOZNT. In *28th Therrnophysics Conference*, volume 93–2862. AIAA, 1993. 17

[67] Chul Park. Review of chemical-kinetic problems of future NASA missions, I: Earth entries. *Journal of Thermophysics and Heat Transfer*, 7(3):385–398, July-Sept. 1993. 42, 192

[68] Chul Park, John T. Howe, Richard L. Jaffe, and Graham V. Candler. Review of Chemical-Kinetic Problems of Future NASA Missions, II: Mars Entries. *Journal of Thermophysics and Heat Transfer*, 8(1):9–23, 1994. 192

[69] Chul Park, Richard L. Jaffe, and Harry Partridge. Chemical-Kinetic Parameters of Hyperbolic Earth Entry. *Journal of Thermophysics and Heat Transfer*, 15(1):76–90, 2001. 39, 133, 143, 192, 193, 197

[70] Andrea Lani, Marco Panesi, and Herman Deconinck. Conservative Residual Distribution Method for Viscous Double Cone Flows in Thermochemical Nonequilibrium. *Communications in Computational Physics*, 2012.

[71] Laurent Soucasse, James B. Scoggins, Thierry E. Magin, Philippe Rivière, and Anouar Soufiani. Flow-radiation coupling for atmospheric entries using a Hybrid Statistical Narrow Band model. *Journal of Quantitative Spectroscopy and Radiative Transfer*, 2016. in press. 17, 61

[72] A. Munafò, M. Panesi, and T. E. Magin. Boltzmann rovibrational collisional coarse-grained model for internal energy excitation and dissociation in hypersonic flows. *Physical Review E*, 89(2), February 2014. 17, 18, 19, 140, 170

[73] Jean-Luc Cambier and Stephane Moreau. Simulations of a molecular plasma in collisional-radiative nonequilibrium. In *AIAA 24th Plasmadynamics & Lasers Conference*, AIAA paper 93-3196, Orlando, FL, 1993. 17

[74] Laurent C. Pierrot, Christophe O. Laux, and Charles H. Kruger. Vibrationally-specific collisional-radiative model for nonequilibrium nitrogen plasmas. In *29th AIAA Plasmadynamics and Lasers Conference*, AIAA paper 98-2664, Albuquerque, NM, 1998. 17, 18

[75] Thierry E. Magin, Marco Panesi, Anne Bourdon, Richard L. Jaffe, and David W. Schwenke. Coarse-grain model for internal energy excitation and dissociation of molecular nitrogen. *Chemical Physics*, 398:90–95, April 2012. 17, 18

[76] M. G. Kapper and J.-L. Cambier. Ionizing shocks in argon. Part II: Transient and multi-dimensional effects. *Journal of Applied Physics*, 109(11):113309, 2011. 18

[77] M. G. Kapper and J.-L. Cambier. Ionizing shocks in argon. Part I: Collisional-radiative model and steady-state structure. *Journal of Applied Physics*, 109(11):113308, 2011.

[78] Marco Panesi, Richard L. Jaffe, David W. Schwenke, and Thierry E. Magin. Rovibrational internal energy transfer and dissociation of N2($1\Sigma g+$)-N(4Su) system in hypersonic flows. *The Journal of Chemical Physics*, 138(4):044312, 2013. 18

[79] Richard L. Jaffe, David W. Schwenke, and Marco Panesi. First principles calculations of heavy particle rate coefficients. In Timothy C. Lieuwen, editor, *Hypersonic Nonequilibrium Flows: Fundamentals and Recent Advances*, volume 247 of *Progress in Astronautics and Aeronautics*, pages 103–158. American Institute of Aeronautics and Astronautics, Reston, Virginia, 2015. 18, 34

[80] Galina Chaban, Richard Jaffe, David Schwenke, and Winifred Huo. Dissociation cross sections and rate coefficients for nitrogen from accurate theoretical calculations. In *46th AIAA Aerospace Sciences Meeting and Exhibit*, AIAA paper 2008-1209, Reno, NV, 2008. 18, 19

[81] Galina Chaban, Richard Jaffe, David Schwenke, and Winifred Huo. Dissociation cross sections and rates for nitrogen. In *Non-Equilibrium Gas Dynamics - from Physical Models to Hypersonic Flights*, NATO-STO/VKI LS RTO-EN-AVT-162, Rhode-Saint-Genèse, Belgium, 2009.

[82] Richard Jaffe, David Schwenke, and Galina Chaban. Theoretical analysis of N2 collisional dissociation and rotation-vibration energy transfer. In *47th AIAA Aerospace Sciences Meeting including The New Horizons Forum and Aerospace Exposition*, AIAA paper 2009-1569, Orlando, FL, 2009.

[83] Richard Jaffe, David Schwenke, and Galina Chaban. Vibration-rotation excitation and dissociation in N2-N2 collisions from accurate theoretical calculations. In *10th AIAA/ASME Joint Thermophysics and Heat Transfer Conference*, AIAA paper 2010-4517, Chicago, IL, 2010. 18, 19

[84] Gert Due Billing and Edward R. Fisher. VV and VT rate coefficients in H2 by a quantum-classical model. *Chemical Physics*, 18:225–232, 1976. 18

[85] Gert Due Billing and E. R. Fisher. VV and VT rate coefficients in N2 by a quantum-classical model. *Chemical Physics*, 43(3):395–401, 1979.

[86] Kenneth Haug, Donald G. Truhlar, and Normand C. Blais. Monte Carlo trajectory and master equation simulation of the nonequilibrium dissociation rate coefficient for Ar+H2→Ar+2H at 4500 K. *The Journal of Chemical Physics*, 86(5):2697, 1987.

[87] David W. Schwenke. A theoretical prediction of hydrogen molecule dissociation-recombination rates including an accurate treatment of internal state nonequilibrium effects. *The Journal of Chemical Physics*, 92(12):7267, 1990.

[88] Eswar Josyula and William F. Bailey. Vibration-Dissociation Coupling Using Master Equations in Nonequilibrium Hypersonic Blunt-Body Flow. *Journal of Thermophysics and Heat Transfer*, 15(2):157–167, April 2001.

[89] Eswar Josyula, William F. Bailey, and Stephen M. Ruffin. Reactive and nonreactive vibrational energy exchanges in nonequilibrium hypersonic flows. *Physics of Fluids*, 15(10):3223, 2003.

[90] F. Esposito, I. Armenise, and M. Capitelli. N–N2 state to state vibrational-relaxation and dissociation rates based on quasiclassical calculations. *Chemical Physics*, 331(1):1–8, December 2006. 35

[91] Fabrizio Esposito, Iole Armenise, Giulia Capitta, and Mario Capitelli. O–O2 state-to-state vibrational relaxation and dissociation rates based on quasiclassical calculations. *Chemical Physics*, 351(1-3):91–98, July 2008. 35

[92] Marco Panesi, Thierry Magin, Anne Bourdon, Arnaud Bultel, and O. Chazot. Fire II flight experiment analysis by means of a collisional-radiative model. *Journal of thermophysics and heat transfer*, 23(2):236–248, April-June 2009. 24, 154

[93] Marco Panesi, T. E. Magin, A. Bourdon, A. Bultel, and O. Chazot. Electronic Excitation of Atoms and Molecules for the FIRE II Flight Experiment. *Journal of Thermophysics and Heat Transfer*, 25(3):361–374, July 2011.

[94] Christophe O. Laux, Laurent Pierrot, and Richard J. Gessman. State-to-state modeling of a recombining nitrogen plasma experiment. *Chemical Physics*, 398:46–55, April 2012.

[95] Jae Gang Kim and Iain D. Boyd. State-resolved thermochemical nonequilibrium analysis of hydrogen mixture flows. *Physics of Fluids*, 24(8):086102, 2012. 18

[96] Hai P. Le, Ann R. Karagozian, and Jean-Luc Cambier. Complexity reduction of collisional-radiative kinetics for atomic plasma. *Physics of Plasmas*, 20(12):123304, December 2013. 18

[97] A. Munafò and T. E. Magin. Modeling of stagnation-line nonequilibrium flows by means of quantum based collisional models. *Physics of Fluids*, 26(9):097102, September 2014. 18, 19, 130, 131

[98] J. H. Ferziger and H. G. Kaper. *Mathematical Theory of Transport Processes in Gases*. North-Holland Publishing Company, 1972. 21, 29, 82

[99] Vincent Giovangigli. *Multicomponent Flow Modeling*. Birkhäuser, Boston, 1999. 21, 29, 33

[100] Benjamin Graille, Thierry E. Magin, and Marc Massot. Kinetic theory of plasmas: Translational energy. *Mathematical Models and Methods in Applied Sciences*, 19(04):527–599, 2009. 21, 29, 43, 171

[101] Ekaterina Nagnibeda and Elena Kustova. *Non-Equilibrium Reacting Gas Flows: Kinetic Theory of Transport and Relaxation Processes*. Heat and mass transfer. Springer, Berlin, 2009. OCLC: 382400436. 29

[102] Raymond Brun. *Introduction to reactive gas dynamics*. Oxford University Press, New York, 2009. 21

[103] B. Bottin, D. Vanden Abeele, M. Carbonaro, G. Degrez, and G.S.R. Sarma. Thermodynamic and transport properties for inductive plasma modeling. *Journal of Thermophysics and Heat Transfer*, 13(3):343–350, 1999. 25, 73, 109, 170

[104] John D. Anderson. *Hypersonic and High Temperature Gas Dynamics*. McGraw-Hill Book Company, New York, 1989. 28, 128

[105] M. Mitchner and H. Kruger Charles Jr. *Partially Ionized Gases*. John Wiley and Sons, Inc, 1973. 29

[106] Thierry E. Magin and Gérard Degrez. Transport algorithms for partially ionized and unmagnetized plasmas. *Journal of Computational Physics*, 198(2):424–449, August 2004. 29, 32, 90, 91, 92, 175

[107] Thierry Magin and Gérard Degrez. Transport properties of partially ionized and unmagnetized plasmas. *Physical Review E*, 70(4), October 2004. 29, 32, 43, 83, 106

[108] Domenico Bruno and Vincent Giovangigli. Relaxation of internal temperature and volume viscosity. *Physics of Fluids*, 23(9):093104, 2011. 29

[109] V Giovangigli, B Graille, T Magin, and M Massot. Multicomponent transport in weakly ionized mixtures. *Plasma Sources Science and Technology*, 19(3):034002, June 2010. 29

[110] A. F. Kolesnikov. The equations of motion of a multicomponent partially ionized two-tempertaure mixture of gases in an electromagnetic field with transport coefficients in higher approximations. Technical Report 1556, Moscow State University, 1974. in Russian. 30

[111] Vincent Giovangigli and Benjamin Graille. Kinetic theory of partially ionized reactive gas mixtures. *Physica A: Statistical Mechanics and its Applications*, 327(3-4):313–348, September 2003. 33

[112] I. Prigogine and E. Xhrouet. On the Perturbation of Maxwell Distribution Function by Chemical Reactions in Gases. *Physica*, 15(11-12):913–932, 1949. 33

[113] Ilya Prigogine and M. Mahieu. Sur la perturbation de la distribution de Maxwell par des réactions chimiques en phase gazeuse. *Physica*, 16(1):51–64, 1950.

[114] B. Shizgal and M. Karplus. Nonequilibrium Contributions to the Rate of Reaction. I. Perturbation of the Velocity Distribution Function. *The Journal of Chemical Physics*, 52(8):4262, 1970.

[115] B. Shizgal and M. Karplus. Nonequilibrium Contributions to the Rate of Reactions. II. Isolated Multicomponent Systems. *The Journal of Chemical Physics*, 54(10):4345, 1971.

[116] B. Shizgal and M. Karplus. Nonequilibrium Contribution to the Rate of Reaction. III. Isothermal Multicomponent Systems. *The Journal of Chemical Physics*, 54(10):4357, 1971. 33

[117] Kenneth K. Kuo. *Principles of Combustion*. John Wiley and Sons, Inc, second edition edition, 2005. 33, 109

[118] P. Hammerling, J. D. Teare, and B. Kivel. Theory of Radiation from Luminous Shock Waves in Nitrogen. *Physics of Fluids*, 2(4):422, 1959. 35, 37

[119] Paul V. Marrone and Charles E. Treanor. Chemical Relaxation with Preferential Dissociation from Excited Vibrational Levels. *Physics of Fluids*, 6(9):1215, 1963. 37, 44

[120] Surendra P. Sharma, Winifred M. Huo, and Chul Park. The rate parameters for coupled vibration-dissociation in a generalized SSH approximation. *AIAA paper*, 2714:1988, 1988. 37

[121] D. I. Ford and R. E. Johnson. Dependence of rate constants on vibrational temperatures: An Arrhenius description. In *AIAA Paper 88-0461, AIAA 26 Th Aerospace Sciences Meeting*, 1988.

[122] O. Knab, H. H. Fruhauf, and S. Jonas. Multiple temperature descriptions of reaction rate constants with regard to consistent chemical-vibrational coupling. In *27th Thermophysics Conference*, Nashville, TN, July 6-8, 1992. 38, 43

[123] S. O. Macheret and J. W. Rich. Theory of nonequilibrium dissociation rates behind strong shock waves. In *AIAA 28th Thermophysics Conference*, volume AIAA 93-2860, Orlando, Florida, July 6-9, 1993. 37

[124] S. O. Macheret, A. A. Fridman, I. V. Adamovich, J. W. Rich, and C. E. Treanor. Mechanisms of nonequilibrium dissociation of diatomic molecules. In *6th Joint Thermophysics and Heat Transfer Conference*, AIAA paper 94-1984, Colorado Springs, CO, 1994. 37

[125] O. Knab, T. H. Gogel, H.-H. Fruhauf, and E. W. Messerschmid. CVCV-Model Validation by Means of Radiative Heating Calculations. In *33rd Aerospace Sciences Meeting and Exhibit*, volume AIAA 95-0623, Reno, Nevada, January 9-12, 1995. 38

[126] S. Kanne, O. Knab, H. H. Frühauf, and E. W. Messerschmid. The influence of rotational excitation on vibration-chemistry-vibration-coupling. *AIAA-Paper 96-1802*, pages 18–21, 1996.

[127] Sergey O. Macheret. Molecular dissociation at high temperatures. In *32nd Thermophysics Conference*, volume AIAA 97–2501, Atlanta, Georgia, 1997. 35, 37

[128] Marco Panesi. *Physical Models for Nonequilibrium Plasma Flow Simulations at High Speed Re-Entry Conditions*. Ph.d. thesis, von Karman Institute for Fluid Dynamics and Universita degli Studi di Pisa, July 2009. 37, 43

[129] Jochen Marschall, Matthew MacLean, Paul E. Norman, and Thomas E. Schwartzentruber. Surface Chemistry in Non-equilibrium Flows. In *Hypersonic Nonequilibrium Flows: Fundamentals and Recent Advances*, volume 247 of *Progress in Astronautics and Aeronautics*, pages 239–327. American Institute of Aeronautics and Astronautics, Reston, Virginia, 2015. 38, 40

[130] L. Landau and E. Teller. Theory of sound dispersion. *Physikalische Zeitschrift der Sowjetunion*, 10:34, 1936. 41, 42

[131] Roger C. Millikan and Donald R. White. Systematics of Vibrational Relaxation. *The Journal of Chemical Physics*, 39(12):3209, 1963. 41

[132] E. E. Nikitin and J. Troe. 70 years of Landau–Teller theory for collisional energy transfer. Semiclassical three-dimensional generalizations of the classical collinear model. *Physical Chemistry Chemical Physics*, 10(11):1483, 2008. 42

[133] Jong-Hun Lee. Electron-Impact Vibrational Relaxation in High Temperature Nitrogen. In *30th Aerospace Sciences Meeting & Exhibit*, Reno, Nevada, 1992. AIAA Paper 92-0807. 43

[134] A. Bourdon and P. Vervisch. Electron-vibration energy exchange models in nitrogen plasma flows. *Physical Review E*, 55(4):4634–4641, April 1997.

[135] V. Laporta and D. Bruno. Electron-vibration energy exchange models in nitrogen-containing plasma flows. *The Journal of Chemical Physics*, 138(10):104319, 2013. 43

[136] R. M. Goody and Y. L. Yung. *Atmospheric Radiation: Theoretical Basis*. Oxford Univ. Press, New York, 2nd ed edition, 1995. 53, 61

[137] Sébastien Depraz, Philippe Rivière, Marie-Yvonne Perrin, and Anouar Soufiani. Band models for radiative transfer in non-LTE diatomic molecules of CO2-N2 plasmas. In *Proceedings of the 14th International Heat Transfer Conference*, page 6, Washington, USA, August 8-13, 2010. ASME. 52, 68, 70

[138] D. M. Cooper. An experimental determination of the cross section of the swings band system of C3. *Journal of Quantitative Spectroscopy and Radiative Transfer*, 22:201–208, 1979. 52, 56

[139] Laurent C. Pierrot, Christophe O. Laux, and Charles H. Kruger. Optical absorption of carbon and hydrocarbon species from shock heated acetylene and methane in the 135-220 nm wavelength range. In *AIAA 16th Thermophysics Conference*, AIAA paper 81-1189, Palo Alto, CA, 1981. 52, 56

[140] T. E. H. Walker and H. P. Kelly. The Photoionization Cross Section for Diatomic CH*. *Chemical Physics Letters*, 16(3), October 1972. 52, 58

[141] S.A. Tashkun and V.I. Perevalov. CDSD-4000: High-resolution, high-temperature carbon dioxide spectroscopic databank. *Journal of Quantitative Spectroscopy and Radiative Transfer*, 112(9):1403–1410, June 2011. 52, 55, 65, 68

[142] Philippe Rivière, Marie-Yvonne Perrin, and Anouar Soufiani. New developments for CO2 IR radiation: Comparison between experiments and spectroscopic database predictions, and updated band model parameters. In *5th International Workshop on Radiation of High Temperature Gases in Atmospheric Entry*, Barcelona, Spain, 16-19 October 2012. ESA. 52, 68

[143] S Prasanna, Ph Rivière, and A Soufiani. Modelling radiative properties of participating species in a microwave plasma reactor for diamond deposition. *Journal of Physics: Conference Series*, 550:012050, November 2014. 52, 55

[144] M. Yan, H. R. Sadeghpour, and A. Dalgarno. Photoionization cross sections of He and H2. *The Astrophysical Journal*, 496(2):1044, 1998. Erratum - [156]. 52, 58

[145] Michael F. Modest. *Radiative Heat Transfer*. Academic Press, 2. ed edition, 2003. 53, 54, 64

[146] S. Roland Drayson. Rapid computation of the Voigt profile. *Journal of Quantitative Spectroscopy and Radiative Transfer*, 16(7):611–614, 1976. 54

[147] J. Humlíček. Optimized computation of the voigt and complex probability functions. *Journal of Quantitative Spectroscopy and Radiative Transfer*, 27(4):437–444, April 1982.

[148] Kendra L. Letchworth and D. Chris Benner. Rapid and accurate calculation of the Voigt function. *Journal of Quantitative Spectroscopy and Radiative Transfer*, 107(1):173–192, September 2007.

[149] Franz Schreier. Optimized implementations of rational approximations for the Voigt and complex error function. *Journal of Quantitative Spectroscopy and Radiative Transfer*, 112(6):1010–1025, April 2011. 54

[150] E.E. Whiting. An empirical approximation to the Voigt profile. *Journal of Quantitative Spectroscopy and Radiative Transfer*, 8(6):1379–1384, June 1968. 54

[151] Ph. Rivière. Systematic semi-classical calculations of Stark broadening parameters of NI, OI, NII, OII multiplets for modelling the radiative transfer in atmospheric air mixture plasmas. *Journal of Quantitative Spectroscopy and Radiative Transfer*, 73:91–110, 2002. 55

[152] E. V. Zoby, K. Sutton, W. B. Olstand, and J. N. Moss. An approximate inviscid radiating flowfield analysis for outer planet entry probes. In *16th Aerospace Sciences Meeting*, AIAA paper 78-189, Huntsville, AL, 1978. 55

[153] R. Vaillon, M. Lallemand, and C. Stehle. Specific frequency integration method applied to thermally nonhomogeneous hydrogen-helium gas mixture. *Journal of Quantitative Spectroscopy and Radiative Transfer*, 58(3):301–328, 1997. 55

[154] Hervé Abgrall, Evelyne Roueff, Françoise Launay, Jean-Yves Roncin, and Jean-Louis Subtil. The Lyman and Werner band systems of molecular hydrogen. *Journal of Molecular Spectroscopy*, 157:512–523, 1993. 55

[155] I. Dabrowski. The Lyman and Werner bands of H2. *Canadian Journal of Physics*, 62(12):1639–1664, December 1984. 55

[156] M. Yan, H. R. Sadeghpour, and A. Dalgarno. Photoionization cross sections of He and H2 - Erratum. *The Astrophysical Journal*, 559:1194, 2001. 58, 208

[157] H. A. Kramers. XCIII. *On the theory of X-ray absorption and of the continuous X-ray spectrum*. *Philosophical Magazine Series 6*, 46(275):836–871, November 1923. 59

[158] Claus B. Ludwig, W. Malkmus, J. E. Reardon, and J. A. L. Thomson. Handbook of infrared radiation from combustion gases. Technical Report NASA SP-3080, Marshall Space Flight Center, 1973. 61, 150

[159] Stephen J. Young. Nonisothermal band model theory. *Journal of Quantitative Spectroscopy and Radiative Transfer*, 18:1–28, 1977. 63, 150

[160] Philippe Rivière and Anouar Soufiani. Generalized Malkmus line intensity distribution for CO2 infrared radiation in Doppler broadening regime. *Journal of Quantitative Spectroscopy and Radiative Transfer*, 112(3):475–485, February 2011. 63, 68

[161] James B. Scoggins, Laurent Soucasse, Philippe Riviere, Anouar Soufiani, and Thierry E. Magin. An adaptive hybrid statistical narrow band model for coupled radiative transfer in atmospheric entry flows. In *8th European Symposium on Aerothermodynamics of Space Vehicles*, Lisbon, Portugal, March, 2-6, 2015. 65

[162] M. Lino da Silva. An adaptive line-by-line—statistical model for fast and accurate spectral simulations in low-pressure plasmas. *Journal of Quantitative Spectroscopy and Radiative Transfer*, 108(1):106–125, November 2007. 66

[163] Thierry E. Magin. *A Model for Inductive Plasma Wind Tunnels*. PhD thesis, Université Libre de Bruxelles and von Karman Institute for Fluid Dynamics, Belgium, June 2004. 73, 170

[164] David G. Goodwin, Harry K. Moffat, and Raymond L. Speth. Cantera: An object-oriented software toolkit for chemical kinetics, thermodynamics, and transport processes, 2017. Version 2.3.0. 74

[165] R. J. Kee, F. M. Rupley, J. A. Miller, M. E. Coltrin, J. F. Grcar, E. Meeks, H. K. Moffat, A. E. Lutz, G. Dixon-Lewis, M. D. Smooke, J. Warnatz, G. H. Evans, R. S. Larson, R. E. Mitchell, L. R. Petzold, W. C. Reynolds, M. Caracotsios, W. E. Stewart, P. Glarborg, C. Wang, and O. Adigun. CHEMKIN collection, 2000. 74

[166] Sanford Gordon and Bonnie J. McBride. Computer program for calculation of complex chemical equilibrium compositions and applications: I. Analysis. Technical Report RP 1311, NASA, October 1994. 74, 78, 109, 119, 120

[167] A. Ern and V. Giovangigli. EGLIB: A General-Purpose Fortran Library for Multicomponent Transport Property Evaluation. Technical report, CERMICS, 1996. 74

[168] Bjarne Stroustrup. *The C++ Programming Language*. Addison-Wesley, Reading, Mass, 3rd ed edition, 1997. LCCB: QA76.73.C153 S77 1997. 74

[169] Erich Gamma, editor. *Design Patterns: Elements of Reusable Object-Oriented Software*. Addison-Wesley professional computing series. Addison-Wesley, Reading, Mass, 1995. LCCB: QA76.64 .D47 1995.

[170] Paul J. Deitel and Harvey M. Deitel. *C++ How to Program*. How to program series. Pearson, Boston, ninth edition edition, 2014. LCCB: QA76.73.C153 D45 2014. 74

[171] Andrea Lani. *An Object Oriented and High Performance Platform for Aerothermodynamics Simulation*. PhD thesis, Universite Libre de Bruxelles and von Karman Institute for Fluid Dynamics, April 2009. 75

[172] L. V. Gurvich, I. V. Veyts, and C. B. Alcock, editors. *Thermodynamic Properties of Individual Substatnces*, volume 1, Elements O, H(D, T), F, Cl, Br, I, He, Ne, Ar, Kr, Xe, Rn, S, N, P, and Their Compounds. Part One. Methods and Computation. Hemisphere Publishing Corporation, fourth edition, 1989. 78

[173] L. V. Gurvich, I. V. Veyts, and C. B. Alcock, editors. *Thermodynamic Properties of Individual Substatnces*, volume 1, Elements O, H(D, T), F, Cl, Br, I, He, Ne, Ar, Kr, Xe, Rn, S, N, P, and Their Compounds. Part Two. Tables. Hemisphere Publishing Corporation, fourth edition, 1989. 191

[174] L. V. Gurvich, I. V. Veyts, and C. B. Alcock, editors. *Thermodynamic Properties of Individual Substatnces*, volume 2, Elements C, Si, Ge, Sn, Pb, and Their Compounds. Part One. Methods and Computation. Hemisphere Publishing Corporation, fourth edition, 1991.

[175] L. V. Gurvich, I. V. Veyts, and C. B. Alcock, editors. *Thermodynamic Properties of Individual Substatnces*, volume 2, Elements C, Si, Ge, Sn, Pb, and Their Compounds. Part Two. Tables. Hemisphere Publishing Corporation, fourth edition, 1991. 191

[176] L. V. Gurvich, I. V. Veyts, and C. B. Alcock, editors. *Thermodynamic Properties of Individual Substatnces*, volume 3, Elements B, Al, Ga, In, Tl, Be, Mg, Ca, Sr, Ba and Their Compounds. Part One. Methods and Computation. CRC Press, Inc., 1994.

[177] L. V. Gurvich, I. V. Veyts, and C. B. Alcock, editors. *Thermodynamic Properties of Individual Substatnces*, volume 3, Elements B, Al, Ga, In, Tl, Be, Mg, Ca, Sr, Ba and Their Compounds. Part Two. Tables. CRC Press, Inc., 1994. 78

[178] B. J. McBride, S. Gordon, and M. J. Reno. Thermodynamic Data for Fifty Reference Elements. Technical Report TP 3287, NASA, 1993. 78

[179] Bonnie J. McBride, S. Gordon, and M. J. Reno. Coefficients for Calculating Thermodynamic and Transport Properties of Individual Species. Technical Report TM 4513, NASA, 1993.

[180] S. Gordon and B. J. McBride. Thermodynamic Data to 20 000 K for Monatomic Gases. Technical Report TP 208523, NASA, 1999.

[181] Bonnie J. McBride, Michael J. Zehe, and Sanford Gordon. NASA Glenn Coefficients for Calculating Thermodynamic Properties of Individual Species. Technical Report 211556, NASA, 2002. 78, 109, 120

[182] Bonnie J. McBride and Sanford Gordon. Computer program for calculation of complex chemical equilibrium compositions and applicaitons: II. Users Manual and Program Description. Technical Report RP 1311, NASA, June 1996. 78, 109, 120

[183] L. V. Gurvich, I. V. Veyts, and C. B. Alcock. *Thermodynamic Properties of Individual Substances*. Hemisphere Pub. Corp., 4th edition, 1989. 78

[184] TRC. TRC Thermodynamic Tables, Non-Hydrocarbons and TRC Thermodynamic Tables, Hydrocarbons, extent 2001 (loose-leaf tables with individual dates). 78

[185] M. W. Chase and National Institute of Standards and Technology (U.S.), editors. *NIST-JANAF Thermochemical Tables*. American Chemical Society: American Institute of Physics for the National Institute of Standards and Technology, Washington, DC : New York, 4th ed edition, 1998. 78

[186] O. V. Dorofeeva, Vladimir P. Novikov, and David B. Neumann. NIST-JANAF thermochemical tables. I. Ten organic molecules related to atmospheric chemistry. *Journal of Physical and Chemical Reference Data*, 30(2):475–513, 2001. 78

[187] Branko Ruscic, Reinhardt E. Pinzon, Melita L. Morton, Gregor von Laszevski, Sandra J. Bittner, Sandeep G. Nijsure, Kaizar A. Amin, Michael Minkoff, and Albert F. Wagner. Introduction to Active Thermochemical Tables: Several "Key" Enthalpies of Formation Revisited. *The Journal of Physical Chemistry A*, 108(45):9979–9997, November 2004. 79

[188] Branko Ruscic, Reinhardt E Pinzon, Gregor von Laszewski, Deepti Kodeboyina, Alexander Burcat, David Leahy, David Montoy, and Albert F Wagner. Active Thermochemical Tables: Thermochemistry for the 21st century. *Journal of Physics: Conference Series*, 16:561–570, January 2005. 79

[189] B. Ruscic. Active Thermochemical Tables (ATcT) values based on ver. 1.112 of the Thermochemical Network, 2013. 79

[190] Alexander Burcat and Branko Ruscic. Third millenium ideal gas and condensed phase thermochemical database for combustion with updates from active thermochemical tables. Technical Report ANL-05/20, Argonne National Laboratory, 2005. 79, 80

[191] Guillaume Blanquart and Heinz Pitsch. Thermochemical Properties of Polycyclic Aromatic Hydrocarbons (PAH) from G3MP2B3 Calculations. *The Journal of Physical Chemistry A*, 111(28):6510–6520, July 2007. 80

[192] G. Blanquart, P. Pepiot-Desjardins, and H. Pitsch. Chemical mechanism for high temperature combustion of engine relevant fuels with emphasis on soot precursors. *Combustion and Flame*, 156(3):588–607, March 2009.

[193] K. Narayanaswamy, G. Blanquart, and H. Pitsch. A consistent chemical mechanism for oxidation of substituted aromatic species. *Combustion and Flame*, 157(10):1879–1898, October 2010.

[194] Guillaume Blanquart. Effects of spin contamination on estimating bond dissociation energies of polycyclic aromatic hydrocarbons. *International Journal of Quantum Chemistry*, 115(12):796–801, June 2015. 80

[195] C. Franklin Goldsmith, Gregory R. Magoon, and William H. Green. Database of Small Molecule Thermochemistry for Combustion. *The Journal of Physical Chemistry A*, 116(36):9033–9057, September 2012. 80

[196] James B. Scoggins, Jason Rabinovich, Benjamin Barros-Fernandez, Alexandre Martin, Jean Lachaud, Richard L. Jaffe, Nagi N. Mansour, Guillaume Blanquart, and Thierry E. Magin. Thermodynamic properties of carbon-phenolic gas mixtures. *Aerospace Science and Technology*, March 2017. 80

[197] A. D'Angola, G. Colonna, C. Gorse, and M. Capitelli. Thermodynamic and transport properties in equilibrium air plasmas in a wide pressure and temperature range. *The European Physical Journal D*, 46(1):129–150, January 2008. 80, 81, 95, 96, 97, 101, 102, 106

[198] Joseph O. Hirschfelder, Charles F. Curtiss, and R. Byron Bird. *Molecular Theory of Gases and Liquids*. John Wiley & Sons, Inc., 1954. 82, 83, 84, 91

[199] Sydney Chapman and T. G. Cowling. *The Mathematical Theory of Non-Uniform Gases: An Account of the Kinetic Theory of Viscosity, Thermal Conduction and Diffusion in Gases*. Cambridge mathematical library. Cambridge Univ. Press, Cambridge, 3. ed., transferred to digital printing edition, 1998. OCLC: 246384286. 82

[200] R. S. Devoto. Transport coefficients of ionized argon. *Physics of Fluids*, 16(5):616, 1973. 83, 87

[201] Michael J. Wright, Deepak Bose, Grant E. Palmer, and Eugene Levin. Recommended collision integrals for transport property computations part 1: Air species. *AIAA journal*, 43(12):2558–2564, 2005. 83, 86, 87, 88, 195, 196

[202] Michael J. Wright, Helen H. Hwang, and David W. Schwenke. Recommended Collision Integrals for Transport Property Computations Part II: Mars and Venus Entries. *AIAA Journal*, 45(1):281–288, January 2007. 83, 87, 88, 196, 197

[203] D. Bruno, C. Catalfamo, M. Capitelli, G. Colonna, O. De Pascale, P. Diomede, C. Gorse, A. Laricchiuta, S. Longo, D. Giordano, and F. Pirani. Transport properties of high-temperature Jupiter atmosphere components. *Physics of Plasmas*, 17(11):112315, November 2010. 83, 87, 90, 95, 97, 196, 197

[204] Louis Monchick and E. A. Mason. Transport properties of polar gases. *The Journal of Chemical Physics*, 35(5):1676–1697, 1961. 84

[205] Chang Lyoul Kong. Combining rules for intermolecular potential parameters. II. Rules for the Lennard-Jones (12–6) potential and the Morse potential. *The Journal of Chemical Physics*, 59(5):2464–2467, September 1973. 84

[206] Adolf A. Abrahamson. Born-Mayer-type interatomic potential for neutral ground-state atoms with Z= 2 to Z= 105. *Physical Review*, 178(1):76, 1969. 85

[207] I. Sokolova and Thierry Magin. Potential models for transport property calculations of dissociated and ionized mixtures for Mars atmosphere. Technical note, von Karman Institute for Fluid Dynamics, 2002. 85

[208] Aurélie Bellemans and Thierry Magin. Calculation of collision integrals for ablation species. In *8th European Conference on Aerodynamics for Space Vehicles*, Lisbon, Portugal, March, 2-6, 2015. 85, 107, 171, 196, 197

[209] F. Pirani, M. Albertı, A. Castro, M. Moix Teixidor, and D. Cappelletti. Atom–bond pairwise additive representation for intermolecular potential energy surfaces. *Chemical Physics Letters*, 394(1-3):37–44, August 2004. 85

[210] Fernando Pirani, Glauciete S. Maciel, David Cappelletti, and Vincenzo Aquilanti. Experimental benchmarks and phenomenology of interatomic forces: Open-shell and electronic anisotropy effects. *International Reviews in Physical Chemistry*, 25(1-2):165–199, January 2006.

[211] M. Capitelli, D. Cappelletti, G. Colonna, C. Gorse, A. Laricchiuta, G. Liuti, S. Longo, and F. Pirani. On the possibility of using model potentials for collision integral calculations of interest for planetary atmospheres. *Chemical Physics*, 338(1):62–68, September 2007. 85

[212] A. Laricchiuta, G. Colonna, D. Bruno, R. Celiberto, C. Gorse, F. Pirani, and M. Capitelli. Classical transport collision integrals for a Lennard-Jones like phenomenological model potential. *Chemical Physics Letters*, 445(4-6):133–139, September 2007. 85

[213] Eugene Levin and Michael J. Wright. Collision integrals for ion-neutral interactions of nitrogen and oxygen. *Journal of Thermophysics and Heat Transfer*, 18(1):143–147, 2004. 86, 195, 196

[214] M. Capitelli. Transport properties of partially ionized gases. *Le Journal de Physique Colloques*, 38(C3):C3–227–C3–237, August 1977. 86

[215] A. B. Murphy. Transport coefficients of air, argon-air, nitrogen-air, and oxygen-air plasmas. *Plasma Chemistry and Plasma Processing*, 15(2):279–307, 1995. 86, 100, 101, 102

[216] E. A. Mason, R. J. Munn, and Francis J. Smith. Transport Coefficients of Ionized Gases. *Physics of Fluids*, 10(8):1827, 1967. 87

[217] Roop N. Gupta, Jerrold M. Yos, Richard A. Thompson, and Kam-Pui Lee. A review of reaction rates and thermodynamic and transport properties for an 11-species air model for chemical and thermal nonequilibrium calculations to 3000K. Reference Publication RP-1232, NASA, 1990. 91

[218] C. R. Wilke. A Viscosity Equation for Gas Mixtures. *The Journal of Chemical Physics*, 18(4):517, 1950. 91

[219] Alexandre Ern and Vincent Giovangigli. Fast and accurate multicomponent transport property evaluation. *Journal of Computational Physics*, 120:105–116, 1995. 91, 92

[220] Vincent Giovangigli. Multicomponent transport algorithms for partially ionized mixtures. *Journal of Computational Physics*, 229(11):4117–4142, June 2010. 91

[221] Alexandre Ern and Vincent Giovangigli. Projected iterative algorithms with application to multicomponent transport. *Linear Algebra and its Applications*, 250:289–315, 1997. 92

[222] Youcef Saad and Martin H. Schultz. GMRES: A generalized minimal residual algorithm for solving nonsymmetric linear systems. *SIAM Journal on scientific and statistical computing*, 7(3):856–869, 1986. 92

[223] Thierry Magin, Gérard Degrez, and Irina Sokolova. Thermodynamics and transport properties of Martian atmosphere for space entry application. In *33rd Plasmadynamics and Lasers Conference*, Maui, Hawaii, 2002. AIAA. 96

[224] James N. Butler and Richard S. Brokaw. Thermal Conductivity of Gas Mixtures in Chemical Equilibrium. *The Journal of Chemical Physics*, 26(6):1636–1643, June 1957. 95, 99

[225] Andrea Lani, Janos Molnar, D. Vanden Abeele, Pietro Rini, Thierry Magin, and Gérard Degrez. Numerical Study of Elemental Demixing in Atmospheric Entry Flow Regimes near Local Thermodynamic Equilibrium. In *ECCOMAS CFD 2006: Proceedings of the European Conference on Computational Fluid Dynamics*, Egmond aan Zee, The Netherlands, September 5-8, 2006. Delft University of Technology; European Community on Computational Methods in Applied Sciences (ECCOMAS). 95

[226] Richard S. Brokaw. Thermal Conductivity of Gas Mixtures in Chemical Equilibrium. II. *The Journal of Chemical Physics*, 32(4):1005–1006, April 1960. 99, 100

[227] G. A. Tirsky. Up-to-date gasdynamic models of hypersonic aerodynamics and heat transfer with real gas properties. *Annual Review of Fluid Mechanics*, 25:151–181, 1993. 101

[228] M. Capitelli, C. Gorse, S. Longo, and D. Giordano. Collision integrals of high-temperature air species. *Journal of Thermophysics and Heat Transfer*, 14(2):259–268, 2000. 101, 102

[229] E. I. Asinovsky, A. V. Kirillin, E. P. Pakhomov, and V. I Shabashov. Experimental investigation of transport properties of low-temperature plasma by means of electric arc. *IEEE Proc*, 69(4):592–601, 1971. 101, 102

[230] Wei-Yin Loh. Classification and regression trees. *Wiley Interdisciplinary Reviews: Data Mining and Knowledge Discovery*, 1(1):14–23, January 2011. 102

[231] J. Lachaud, J.B. Scoggins, T.E. Magin, M.G. Meyer, and N.N. Mansour. A Generic Local Thermal Equilibrium Model for Porous Reactive Materials Submitted to High Temperatures. *International Journal of Heat and Mass Transfer*, 108:1406–1417, May 2017. 107, 171

[232] G. Bellas-Chatzigeorgis, P. F. Barbante, and T. E. Magin. Development of Detailed Chemistry Models for Boundary Layer Catalytic Recombination. In *8th European Symposium on Aerothermodynamics for Space Vehicles*, Lisbon, Portugal, 2015. 107, 171

[233] Bruno Dias, Alessandro Turchi, and Thierry E. Magin. Stagnation-line simulations of meteor ablation. In *45th AIAA Thermophysics Conference*, AIAA paper 2015-2349, Dallas, TX, 2015. 107, 171

[234] Bruno Dias, Federico Bariselli, Alessandro Turchi, Aldo Frezzotti, Philippe Chatelain, and Thierry Magin. Development of a melting model for meteors. In *AIP Conference Proceedings*, 1786, page 160004, 2016. 107, 171

[235] Ana Isabel del Val Benıtez, Thierry E. Magin, Bruno Dias, and Olivier Chazot. Characterization of Ground Testing Conditions in High Enthalpy and Plasma Wind Tunnels for Aerospace Missions. In *8th European Symposium on Aerothermodynamics for Space Vehicles*, Lisbon, Portugal, 2015. 107, 171

[236] S. H. Chan and C. C. Tan. Complex equilibrium calculations by Simplex and Duality theories with applications to liquid metal fuel propulsion systems. *Combustion and Flame*, 88(2):123–136, 1992. 109

[237] Risto Pajarre, Peter Blomberg, and Pertti Koukkari. Thermochemical multi-phase models applying the constrained gibbs energy method. *Comput.-Aided Chem. Eng.*, 25:883–888, 2008.

[238] Pertti Koukkari and Risto Pajarre. A Gibbs energy minimization method for constrained and partial equilibria. *Pure Appl. Chem.*, 83(6):1243–1254, 2011. 109, 110

[239] F. S. Milos and Y. K. Chen. Comprehensive model for multi-component ablation thermochemistry. In *35th Aerospace Sciences Meeting and Exhibit*, volume 97-0141. AIAA, 1997. 109

[240] Ben F. Blackwell and Micah A. Howard. An Element Potential Based Chemical Equilibrium Solver for Gas/Surface Thermochemistry. In *50th AIAA Aerospace Sciences Meeting Including the New Horizons Forum and Aerospace Exposition*. American Institute of Aeronautics and Astronautics, January 2012.

[241] Jason Rabinovitch. *Advancing EDL Technologies for Future Space Missions: From Ground Testing Facilities to Ablative Heatshields*. PhD thesis, California Institute of Technology, 2014. 109

[242] F. Van Zeggeren and S. H. Storey. *The Computation of Chemical Equilibria*. Cambridge at the University Press, 1970. 109

[243] W. R. Smith and R. W. Missen. *Chemical Reaction Equilibrium Analysis: Theory and Algorithms*. Krieger, Malabar, FL, 1991. 109

[244] W. B. White, S. M. Johnson, and G. B. Dantzig. Chemical Equilibrium in Complex Mixtures. *The Journal of Chemical Physics*, 28(5):751, 1958. 109

[245] W. B. White. Numerical Determination of Chemical Equilibrium and the Partitioning of Free Energy. *The Journal of Chemical Physics*, 46(11):4171, 1967. 109

[246] W. C. Reynolds. The element potential method for chemical equilibrium analysis: Implementation in the interactive program STANJAN version 3. Technical report, Department of Mechanical Engineering, Stanford University, January 1986. 109, 112

[247] James C. Keck and David Gillespie. Rate-controlled partial-equilibrium method for treating reacting gas mixtures. *Combustion and Flame*, 17(2):237–241, 1971. 109

[248] A.R. Morr and J.B. Heywood. Partial equilibrium model for predicting concentration of CO in combustion. *Acta Astronautica*, 1(7-8):949–966, July 1974.

[249] M. Delichatsios and J. C. Keck. Rate-controlled constrained-equilibrium calculations of CO and NO freezing in internal combustion engines. In *ACS Division of Petroleum Chemistry Symposium on Chemistry of Combustion in Engines*, volume 20, pages 105–113, Philadelphia, PA, April 1975.

[250] Robert Law, Mohamad Metghalchi, and James C. Keck. Rate-controlled constrained equilibrium calculation of ignition delay times in hydrogen-oxygen mixtures. *Symposium (International) on Combustion*, 22(1):1705–1713, January 1989.

[251] James C. Keck. Rate-controlled constrained-equilibrium theory of chemical reactions in complex systems. *Prog. Energy Combust. Sci.*, 16:125–154, 1990.

[252] V. Yousefian. A rate-controlled constrained-equilibrium thermochemistry algorithm for complex reacting systems. *Combustion and Flame*, 115(1-2):68–80, 1998.

[253] Djamel Hamiroune, Partha Bishnu, Mohamad Metghalchi, and James C. Keck. Rate-controlled constrained-equilibrium method using constraint potentials. *Combustion Theory and Modelling*, 2:81–94, 1998.

[254] Q. Tang and S. B. Pope. A more accurate projection in the rate-controlled constrained-equilibrium method for dimension reduction of combustion chemistry. *Combust. There. Model*, 8:255–279, 2004.

[255] W.P. Jones and Stelios Rigopoulos. Rate-controlled constrained equilibrium: Formulation and application to nonpremixed laminar flames. *Combustion and Flame*, 142(3):223–234, August 2005.

[256] Mohammad Janbozorgi, Sergio Ugarte, Hameed Metghalchi, and James. C. Keck. Combustion modeling of mono-carbon fuels using the rate-controlled constrained-equilibrium method. *Combustion and Flame*, 156(10):1871–1885, October 2009.

[257] Mohammad Janbozorgi and Hameed Metghalchi. Rate-controlled constrained-equilibrium theory applied to expansion of combustion products in the power stroke of an internal combustion engine. *Int. J. Thermodyn*, 12(1):44–50, 2009.

[258] Varun Hiremath, Zhuyin Ren, and Stephen B. Pope. A greedy algorithm for species selection in dimension reduction of combustion chemistry. *Combustion Theory and Modelling*, 14(5):619–652, September 2010.

[259] Varun Hiremath, Zhuyin Ren, and Stephen B. Pope. Combined dimension reduction and tabulation strategy using ISAT–RCCE–GALI for the efficient implementation of combustion chemistry. *Combustion and Flame*, 158(11):2113–2127, November 2011. 110

[260] Gian Paolo Beretta, James C. Keck, Mohammad Janbozorgi, and Hameed Metghalchi. The Rate-Controlled Constrained-Equilibrium Approach to Far-From-Local-Equilibrium Thermodynamics. *Entropy*, 14(12):92–130, January 2012. 110

[261] Salem Elbahloul and Stelios Rigopoulos. Rate-Controlled Constrained Equilibrium (RCCE) simulations of turbulent partially premixed flames (Sandia D/E/F) and comparison with detailed chemistry. *Combustion and Flame*, 162(5):2256–2271, 2015. 109

[262] Partha S. Bishnu, Djamel Hamiroune, Mohamad Metghalchi, and James C. Keck. Constrained-equilibrium calculations for chemical systems subject to generalized linear constraints using the NASA and STANJAN equilibrium programs. *Combustion Theory and Modelling*, 1(3):295–312, 1997. 110, 120

[263] P. S. Bishnu, D. Hamiroune, and M. Metghalchi. Development of constrained equilibrium codes and their applications in nonequilibrium thermodynamics. *J. Energy Resour. Technol.*, 123(3):214–220, 2001. 110

[264] Stephen B. Pope. The computation of constrained and unconstrained equilibrium compositions of ideal gas mixtures using Gibbs function continuation. *FDA03-02, Cornell University, http://eccentric. mae. cornell. edu/∼ pope/Reports/CEQ_ FDA. pdf*, 2003. 110, 115

[265] S Pope. Gibbs function continuation for the stable computation of chemical equilibrium. *Combustion and Flame*, 139(3):222–226, November 2004. 110, 117

[266] Zhuyin Ren, Graham M. Goldin, Varun Hiremath, and Stephen B. Pope. Simulations of a turbulent non-premixed flame using combined dimension reduction and tabulation for combustion chemistry. *Fuel*, 105:636–644, March 2013. 110

[267] Jian Cai, Masato Handa, and Michael F. Modest. Eulerian-eulerian multi-fluid methods for pulverized coal flames with nongray radiation. *Combustion and Flame*, 162(4):1550–1565, April 2015. 110

[268] Mahdi Kooshkbaghi, Christos E. Frouzakis, Eliodoro Chiavazzo, Konstantinos Boulouchos, and Iliya V. Karlin. The global relaxation redistribution method for reduction of combustion kinetics. *The Journal of Chemical Physics*, 141(4):044102, July 2014. 110

[269] James B. Scoggins and Thierry E. Magin. Gibbs function continuation for linearly constrained multiphase equilibria. *Combustion and Flame*, 162(12):4514–4522, December 2015. 110

[270] T. C. Kelley. *Iterative Methods for Linear and Nonlinear Equations*. Society for Industrial and Applied Mathematics, 1995. 113

[271] David B. Shear. Stability and Uniqueness of the Equilibrium Point in Chemical Reaction Systems. *The Journal of Chemical Physics*, 48(9):4144, 1968. 114

[272] William H. Press, Saul A. Teukolsky, William T. Vetterling, and Brian P. Flannery. *Numerical Recipes in C: The Art of Scientific Computing*. Cambridge University Press, 2nd edition, 1992. 114

[273] J. W. Gibbs. The equilibrium of heterogeneous substances. *Transactions of the Connecticut Academy of Arts and Sciences*, 111:198–248, 1874-1879. 115

[274] James B. Scoggins and Thierry E. Magin. Development of Mutation++: Multicomponent thermodynamic and transport properties for ionized plasmas written in C++. In *11th AIAA/ASME Joint Thermophysics and Heat Transfer Conference*, AIAA paper 2014-2966, Atlanta, GA, 2014. 120

[275] B. Helber, C. O. Asma, Y. Babou, A. Hubin, O. Chazot, and T. E. Magin. Material response characterization of a low-density carbon composite ablator in high-enthalpy plasma flows. *J. Mater. Sci.*, 49(13):4530 – 4543, 2014. 121

[276] Arno Klomfass and Siegfried Müller. Calculation of stagnation streamline quantities in hypersonic blunt body flows. *Shock Waves*, 7(1):13–23, 1997. 127

[277] Alessandro Turchi, J. J. Matesanz Saiz, Thierry E. Magin, and Olivier Chazot. On the Flight Extrapolation of Stagnation-Point Ablative Material Plasma Wind Tunnel Tests. In *Proceedings of 8th European Symposium on Aerothermodynamics for Space Vehicles*, 2015. 127

[278] Chul Park. Stagnation-Point Radiation for Apollo 4. *Journal of Thermophysics and Heat Transfer*, 18(3):349–357, July-September 2004. 128, 143, 166

[279] P. L. Roe. Approximate Riemann solvers, parameter vectors and difference schemes. *Journal of Computational Physics*, 43(2):357–372, 1981. 130

[280] Ramadas K. Prabhu. An approximate Riemann solver for thermal and chemical nonequilibrium flows. Contractor Report 195003, NASA, 1994. 130

[281] C. Hirsch. *Numerical Computation of Internal and External Flows*. John Wiley & Sons, Inc., New York, NY, 1990. 130, 132, 133, 134

[282] B. van Leer. Towards the ultimate conservative difference scheme. *Journal of Computational Physics*, 32(1):101–136, 1979. 131

[283] G. D. van Albada, B. van Leer, and W. W. Roberts. A comparative study of computational methods in cosmic gasdynamics. *Astronomy and Astrophysics*, 108(1):76–84, 1982. 131

[284] J. Blazek. *Computational Fluid Dynamics: Principles and Applications*. Elsevier, Amsterdam, 2. ed., 6. reprint edition, 2008. 131

[285] M.-S Liou and B. van Leer. Choice of implicit and explicit operators for the upwind differencing method. In *26th AIAA Aerospace Sciences Meeting*, volume AIAA Paper 1988-624, Reno, Nevada, 1988. 132

[286] J. D. Ramshaw and C. H. Chang. Friction-weighted self-consistent effective binary diffusion approximation. *Journal of Non-Equilibrium Thermodynamics*, 21(3):223–232, 1996. 132

[287] Alessandro Turchi, Bernd Helber, Alessandro Munafò, and Thierry E. Magin. Development and testing of an ablation model based on plasma wind tunnel experiments. In *11th AIAA/ASME Joint Thermophysics and Heat Transfer Conference*, AIAA paper 2014-2125, Atlanta, GA, 2014. 133, 160

[288] Toshiyuki Suzuki, Masahito Mizuno, Kazuhisa Fujita, and Takeharu Sakai. Experimental and numerical study of thermal response of ablator in an arc-jet facility. In *45th Aerospace Sciences Meeting and Exhibit, Reno*, 2007. 133

[289] James B. Scoggins, Laurent Soucasse, Philippe Rivière, Anouar Soufiani, and Thierry Magin. Coupled flow, radiation, and ablation simulations of atmospheric entry vehicles using the hybrid statistical narrow band model. In *45th AIAA Thermophysics Conference*, AIAA paper 2015-3112, Dallas, TX, 2015. 140

[290] Elden S. Cornette. Forebody temperatures and calorimeter heating rates measured during project fire ii reentry at 11.35 kilometers per second. Technical Report NASA TM X-1305, NASA Langley Research Center, 1966. 141, 143, 145

[291] Dona L. Cauchon. Radiative heating results from the Fire II flight experiment at a reentry velocity of 11.4 kilometers per second. Technical Report TM X-1402, National Aeronautics and Space Administration, Washington, D.C., July 1967. 141, 145

[292] R. C. Ried Jr., W. C. Rochelle, and J. D. Milhoan. Radiative heating to the Apollo command module: Engineering prediction and flight measurement. Technical Report TM X-58091, NASA, 1972. 143, 166

[293] H. B. Niemann, S. K. Atreya, S. J. Bauer, G. R. Carignan, J. E. Demick, R. L. Frost, D. Gautier, J. A. Haberman, D. N. Harpold, D. M. Hunten, G. Israel, J. I. Lunine, W. T. Kasprzak, T. C. Owen, M. Paulkovich, F. Raulin, E. Raaen, and S. H. Way. The abundances of constituents of Titan's atmosphere from the GCMS instrument on the Huygens probe. *Nature*, 438(7069):779–784, December 2005. 144

[294] L. Caillault, L. Walpot, T. E. Magin, A. Bourdon, and C. O. Laux. Radiative heating predictions for Huygens entry. *Journal of Geophysical Research*, 111(E9), 2006. 144, 158

[295] Tahir Gokcen. N2-CH4-Ar Chemical Kinetic Model for Simulations of Atmospheric Entry to Titan. *Journal of Thermophysics and Heat Transfer*, 21(1):9–18, January 2007. 144, 194

[296] Grant E. Palmer, Todd White, and Alexander Pace. Direct coupling of the NEQAIR radiation and DPLR CFD codes. *Journal of Spacecraft and Rockets*, 48(5):836–845, 2011. 145

[297] Christopher O. Johnston. *Nonequilibrium Shock-Layer Radiative Heating for Earth and Titan Entry*. PhD thesis, Virginia Polytechnic Institute and State University, 2006. 152, 153, 154, 158, 167

[298] Deepak Bose, Michael Wright, David Bogdanoff, George Raiche, and Gary A. Allen. Modeling and Experimental Assessment of CN Radiation Behind a Strong Shock Wave. *Journal of Thermophysics and Heat Transfer*, 20(2):220–230, April 2006. 152

[299] Olivier Rouzaud, Anouar Soufiani, Philippe Rivière, and David Zeitoun. Influence of radiative heating on a martian orbiter. *Journal of Thermophysics and Heat Transfer*, 22(1):10–19, 2008. 171

[300] J.M. Lamet, Ph. Rivière, L. Tessé, A. Soufiani, and M.Y. Perrin. Radiation modelling of air plasma in nonequilibrium conditions: application to earth atmospheric re-entry. In *Proceedings of the 3rd International Workshop on Radiation of High Temperature Gases in Atmospheric Entry*, Heraklion, Greece, 30 September-3 October 2008. 171

[301] S. I. Braginskii. Transport processes in plasma. *Reviews of Plasma Physics*, 1:205, 1965. 171

[302] A. Alvarez Laguna, A. Lani, H. Deconinck, N.N. Mansour, and S. Poedts. A fully-implicit finite-volume method for multi-fluid reactive and collisional magnetized plasmas on unstructured meshes. *Journal of Computational Physics*, 318:252–276, August 2016. 171

[303] Yana G. Maneva, Alejandro Alvarez Laguna, Andrea Lani, and Stefaan Poedts. Multi-fluid Modeling of Magnetosonic Wave Propagation in the Solar Chromosphere: Effects of Impact Ionization and Radiative Recombination. *The Astrophysical Journal*, 836(2):197, February 2017. 171

[304] James B. Scoggins, Carleton P. Knisely, and Thierry E. Magin. Crossed contributions to electron and heavy-particle transport fluxes for magnetized plasmas in the continuum regime. *AIP Conference Proceedings*, 1786:130002, 2016. 171

[305] David Olynick, Y.-K. Chen, and Michael E. Tauber. Aerothermodynamics of the Startdust Sample Return Capsule. *Journal of Spacecraft and Rockets*, 36(3):442–462, 1999. 193

[306] P. André, J. Aubreton, S. Clain, M. Dudeck, E. Duffour, M. F. Elchinger, B. Izrar, D. Rochette, R. Touzani, and D. Vacher. Transport coefficients in thermal plasma. Applications to Mars and Titan atmospheres. *The European Physical Journal D*, 57(2):227–234, April 2010. 197

[307] Mechanical San Diego Mechanism web page and University of California at San Diego Aerospace Engineering (Combustion Research). Chemical-kinetic mechanisms for combustion applications. `http://combustion.ucsd.edu`. 197

[308] Gregory P. Smith, David M. Golden, Michael Frenklach, Nigel W. Moriarty, Boris Eiteneer, Mikhail Goldenberg, C. Thomas Bowman, Ronald K. Hanson, Soonho Song, William C. Gardiner, Jr., Vitali V. Lissianski, and Zhiwei Qin. GRI-Mech 3.0. `http://www.me.berkeley.edu/gri_mech`. 197

[309] F. Cuadros, I. Cachadiña, and W. Ahumada. Determination of lennard-jones interaction parameters using a new procedure. *Molecular Engineering*, 6:319–325, 1996. 197

[310] Chun Yang, Jeanna Buldyreva, Iouli E. Gordon, François Rohart, Arnaud Cuisset, Gaël Mouret, Robin Bocquet, and Francis Hindle. Oxygen, nitrogen and air broadening of hcn spectral lines at terahertz frequencies. *Journal of Quantitative Spectroscopy & Radiative Transfer*, 109:2857–2868, 2008. 197

université PARIS-SACLAY
ÉCOLE DOCTORALE
Sciences mécaniques et énergétiques, matériaux et géosciences (SMEMAG)

Titre : Développement de méthodes numériques et étude des phénomènes couplés d'écoulement, de rayonnement, et d'ablation dans les problèmes d'entrée atmosphérique

Mots clés : entrée atmosphérique, hypersonique, aerothermodynamique, rayonnement, ablation, équilibre multiphase

Résumé : Cette thèse est centrée sur le couplage entre les phénomènes d'écoulement, d'ablation et de rayonnement au voisinage du point d'arrêt de véhicules d'entrée atmosphérique pourvus d'un système de protection thermique de type carbone-phénolique. La recherche est divisée en trois parties : 1) le développement de méthodes numériques et d'outils pour la simulation d'écoulements hypersoniques hors équilibre autour de corps émoussés, 2) la mise en œuvre d'un nouveau modèle de transport du rayonnement hors équilibre dans ces écoulements, y compris dans les couches limites contaminées par les produits d'ablation, et 3) l'application de ces outils à des conditions réelles de vol.

Les effets du couplage entre l'ablation et le rayonnement sont étudiés pour les rentrées terrestres. Il est démontré que les produits d'ablation dans la couche limite peuvent augmenter le blocage radiatif à la surface du véhicule. Pour les conditions de flux maximum d'Apollo 4, les effets de couplage entre le rayonnement et l'ablation réduisent le flux conductif de 35%. L'accord avec les données radiométriques est excellent, ce qui valide partiellement la méthode de couplage et la base de données radiatives. L'importance d'une modélisation précise du soufflage du carbone dans la couche limite est également établie.

Title : Development of numerical methods and study of coupled flow, radiation, and ablation phenomena for atmospheric entry

Keywords : atmospheric entry, hypersonics, aerothermodynamics, radiation, ablation, coupling, multiphase equilibrium

Abstract : This thesis focuses on the coupling between flow, ablation, and radiation phenomena encountered in the stagnation region of atmospheric entry vehicles with carbon-phenolic thermal protection systems. The research is divided into three parts : 1) development of numerical methods and tools for the simulation of hypersonic, non equilibrium flows over blunt bodies, 2) implementation of a new radiation transport model for calculating nonequilibrium radiative heat transfer in atmospheric entry flows, including ablation contominated boundary layers, and 3) application of these tools to study real flight conditions.
The effects of coupled ablation and radiation are studied for Earth entries. It's shown that ablation products in the boundary layer can increase the radiation blockage to the surface of the vehicle. An analysis of the Apollo 4 peak heating condition shows coupled radiation and ablation effects reduce the conducted heat flux by as much as 35% for a fixed wall temperature of 2500 K. Comparison with the radiometer data shows excellent agreement, partially validating the coupling methodology and radiation database. The importance of accurately modeling the amount of carbon blown into the boundary layer is demonstrated by contrasting the results of other researchers.

Université Paris-Saclay
Espace Technologique / Immeuble Discovery
Route de l'Orme aux Merisiers RD 128 / 91190 Saint-Aubin, France